



**Functional analysis of ion channels and neuronal networks  
in 2D and 3D *in vitro* cell culture models**

**Funktionelle Analyse von Ionenkanälen und neuronalen  
Netzwerken in 2D und 3D *in vitro* Zellkulturmodellen**

Doctoral thesis for a doctoral degree  
at the Graduate School of Life Sciences,  
Julius-Maximilians-Universität Würzburg,  
Section Neuroscience

submitted by

**Dieter Janzen**

from

**Podolsk**

Würzburg 2021

**Submitted on:** .....

Office stamp

## **Members of the Thesis Committee**

**Chairperson:** Prof. Dr. Georg Gasteiger

**Primary Supervisor:** Prof. Dr. Carmen Villmann

**Second Supervisor:** Prof. Dr. Paul Dalton

**Third Supervisor:** PD Dr. Pamela Strissel

**Date of Public Defense:** .....

**Date of Receipt of Certificates:** .....

“All we have to decide is what to do with the time that is given us.”

— J.R.R. Tolkien, *The Fellowship of the Ring*

# Acknowledgements

I owe my deepest gratitude to my supervisor Prof. Dr. Carmen Villmann for accepting me as a PhD student and making it possible for me to work on such interesting and successful projects. Thank you for always being available for discussion of new results as well as failures.

I would like to extend my gratitude to my second supervisor Prof. Dr. Paul Dalton for valuable advice and practical suggestions, especially during our project meetings.

I would also like to thank my third supervisor PD Dr. Pamela Strissel for her advice and positivity during our meetings.

Many thanks to Prof. Dr. Georg Gasteiger for chairing my thesis committee.

I am grateful to Prof. Dr. Reiner Strick, Annalena Wieland, and Ezgi Bakirci for making our project B01 such a success. Special thanks to Ezgi for always supplying me with enough scaffolds for my experiments.

Many thanks to all other co-authors for making our publications possible, especially Benedikt Slavik for giving a steady supply of good-smelling compounds and Dr. Corinna Martin for introducing me to calcium imaging.

I had a great pleasure working with the Villmann lab, including Dr. Natascha Schäfer, Dr. Vera Römer, Dr. Alexandra Kitzenmaier, Dr. Sinem Milanos, Anna-Lena Eckes, Dana Wegmann, Christine Schmitt, and Nadine Vornberger. Thank you for supporting my work, fruitful discussions, and all the good times in the lab.

I would like to thank the team of the animal facility of the Institute for Clinical Neurobiology, including Regine Sendtner, Viktor Buterus, Franziska Wagner, and Sebastian Rose, for the good cooperation.

Thanks also to all other members of the Institute for Clinical Neurobiology for the good working atmosphere and support.

Many thanks to the collaborative research center TRR225 and all its members for collaborations and discussions during our events and meetings.

Finally, I would like to thank my parents for always supporting and believing in me.

# Abstract

In the central nervous system, excitatory and inhibitory signal transduction processes are mediated by presynaptic release of neurotransmitters, which bind to postsynaptic receptors. Glycine receptors (GlyRs) and GABA<sub>A</sub> receptors (GABA<sub>A</sub>Rs) are ligand-gated ion channels that enable synaptic inhibition. One part of the present thesis elucidated the role of the GlyR $\alpha$ 1  $\beta$ 8- $\beta$ 9 loop in receptor expression, localization, and function by means of amino acid substitutions at residue Q177. This residue is underlying a startle disease phenotype in the spontaneous mouse model *shaky* and affected homozygous animals are dying 4-6 weeks after birth. The residue is located in the  $\beta$ 8- $\beta$ 9 loop and thus part of the signal transduction unit essential for proper ion channel function. Moreover, residue Q177 is involved in a hydrogen network important for ligand binding. We observed no difference in ion channel trafficking to the cellular membrane for GlyR $\alpha$ 1<sup>Q177</sup> variants. However, electrophysiological measurements demonstrated reduced glycine, taurine, and  $\beta$ -alanine potency in comparison to the wildtype protein. Modeling revealed that some GlyR $\alpha$ 1<sup>Q177</sup> variants disrupt the hydrogen network around residue Q177. The largest alterations were observed for the Q177R variant, which displayed similar effects as the Q177K mutation present in *shaky* mice. Exchange with structurally related amino acids to the original glutamine preserved the hydrogen bond network. Our results underlined the importance of the GlyR  $\beta$ 8- $\beta$ 9 loop for proper ion channel gating.

GlyRs as well as GABA<sub>A</sub>Rs can be modulated by numerous allosteric substances. Recently, we focused on monoterpenes from plant extracts and showed positive allosteric modulation of GABA<sub>A</sub>Rs. Here, we focused on the effect of 11 sesquiterpenes and sesquiterpenoids (SQTs) on GABA<sub>A</sub>Rs. SQTs are compounds naturally occurring in plants. We tested SQTs of the volatile fractions of hop and chamomile, including their secondary metabolites generated during digestion. Using the patch-clamp technique on transfected cells and neurons, we were able to observe significant GABA<sub>A</sub>R modulation by some of the compounds analyzed. Furthermore, a possible binding mechanism of SQTs to the neurosteroid binding site of the GABA<sub>A</sub>R was revealed by modeling and docking studies. We successfully demonstrated GABA<sub>A</sub>R modulation by SQTs and their secondary metabolites.

The second part of the thesis investigated three-dimensional (3D) *in vitro* cell culture models which are becoming more and more important in different part of natural sciences. The third dimension allows developing of complex models closer to the natural environment of cells, but also requires materials with mechanical and biological properties comparable to the native tissue of the encapsulated cells. This is especially challenging for 3D *in vitro* cultures of primary neurons and astrocytes as the brain is one of the softest tissues found in the body. Ultra-soft matrices that mimic the neuronal *in vivo* environment are difficult to handle. We have overcome these challenges using fiber scaffolds created by melt electrowriting to reinforce ultra-soft matrigel. Hence, the scaffolds enabled proper handling of the whole composites and thus structural and functional characterizations requiring movement of the composites to different experimental setups. Using these scaffold-matrigel composites, we successfully established methods necessary for the characterization of neuronal network formation. Before starting with neurons, a mouse fibroblast cell line was seeded in scaffold-matrigel composites and transfected with the GlyR. 3D cultured cells displayed high viability, could be immunocytochemically stained, and electrophysiologically analyzed.

In a follow-up study, primary mouse cortical neurons in fiber-reinforced matrigel were grown for up to 21 days *in vitro*. Neurons displayed high viability, and quantification of neurite lengths and synapse density revealed a fully formed neuronal network already after 7 days in 3D culture. Calcium imaging and patch clamp experiments demonstrated spontaneous network activity, functional voltage-gated sodium channels as well as action potential firing. By combining ultra-soft hydrogels with fiber scaffolds, we successfully created a cell culture model suitable for future work in the context of cell-cell interactions between primary cells of the brain and tumor cells, which will help to elucidate the molecular pathology of aggressive brain tumors and possibly other disease mechanisms.

# Zusammenfassung

Im zentralen Nervensystem wird die exzitatorische und inhibitorische Signaltransduktion durch die präsynaptische Ausschüttung von Neurotransmittern, die an postsynaptische Rezeptoren binden, gesteuert. Glycinrezeptoren (GlyRs) und GABA<sub>A</sub>-Rezeptoren (GABA<sub>A</sub>Rs) sind ligandengesteuerte Ionenkanäle, die die synaptische Inhibition ermöglichen. Ein Teil der vorliegenden Arbeit beschäftigt sich mit dem Einfluss des GlyR $\alpha$ 1  $\beta$ 8- $\beta$ 9-Loops auf Expression, Lokalisation und Funktion des Rezeptors. Dazu wurde ein Aminosäureaustausch an Position Q177 durchgeführt, welche dem Startle-Krankheits-Phänotyp des spontanen Mausmodells *shaky* zugrunde liegt. Betroffene homozygote Tiere versterben 4-6 Wochen nach Geburt. Die Position befindet sich im  $\beta$ 8- $\beta$ 9-Loop und ist damit Teil einer Signaltransduktionseinheit, die essenziell für die korrekte Rezeptorfunktion ist. Zudem ist Position Q177 Teil eines Wasserstoffbrückennetzwerks, welches für die Ligandenbindung erforderlich ist. Wir konnten keinen Einfluss der GlyR $\alpha$ 1<sup>Q177</sup>-Varianten auf den Transport des Rezeptors zur Zellmembran feststellen. Allerdings zeigten elektrophysiologische Messungen eine verringerte Wirksamkeit von Glycin, Taurin und  $\beta$ -Alanin verglichen mit dem Wildtyp-Protein. Mithilfe von Proteinmodellierung konnte gezeigt werden, dass manche der GlyR $\alpha$ 1<sup>Q177</sup>-Varianten das Wasserstoffbrückennetzwerk im Umfeld von Position Q177 stören. Die größten Effekte wurden bei der Q177R-Variante beobachtet, die sich ähnlich zur Q177K-Mutation der *shaky*-Maus verhielt. Der Austausch zu einer Aminosäure, die strukturell ähnlich zum ursprünglichen Glutamin ist, störte das Wasserstoffbrückennetzwerk hingegen nicht. Unsere Ergebnisse zeigen, wie wichtig der GlyR  $\beta$ 8- $\beta$ 9-Loop für die Aufrechterhaltung der Rezeptorfunktion ist.

Sowohl GlyRs als auch GABA<sub>A</sub>Rs können durch verschiedenste allosterische Substanzen moduliert werden. Zuletzt zeigten wir positive allosterische Modulation von GABA<sub>A</sub>Rs durch Monoterpene aus Pflanzenextrakten. Hier haben wir uns auf den Effekt von 11 Sesquiterpenen und Sesquiterpenoiden (SQTs) auf GABA<sub>A</sub>Rs fokussiert. SQTs sind natürlich in Pflanzen vorkommende Stoffe. Wir testeten SQTs aus dem flüchtigen Anteil von Hopfen und Kamille, sowie deren sekundäre Metaboliten, die während der Verdauung entstehen. Mithilfe der Patch-Clamp-Methode konnten wir in transfizierten Zellenlinien und neuronalen Primärzellen signifikante Modulation von GABA<sub>A</sub>Rs durch einige der SQTs beobachten. Außerdem wurde mithilfe von Docking-Simulationen eine mögliche Bindung von SQTs in der Neurosteroid-Bindungstasche gezeigt. Zusammengefasst haben wir



erfolgreich die Modulation von GABA<sub>A</sub>Rs durch SQTs und deren sekundäre Metaboliten demonstriert.

Der zweite Teil der vorliegenden Arbeit beschäftigt sich mit dreidimensionalen (3D) *in vitro* Zellkulturmodellen, die zunehmend an Bedeutung gewinnen. Die dritte Dimension erlaubt die Entwicklungen von komplexen Modellen, die sich der natürlichen Umgebung von Zellen annähern. Dafür werden Materialien benötigt, deren mechanische und biologische Eigenschaften denen des ursprünglichen Gewebes der eingeschlossenen Zellen ähneln. Dies ist insbesondere eine Herausforderung bei 3D *in vitro* Kulturen von primären Neuronen und Astrozyten, da das Gehirn eines der weichsten Gewebe des Körpers ist. Ultraweiche Matrizen, welche die neuronale Umgebung nachahmen, sind schwer zu handhaben. Wir haben dieses Problem gelöst, indem wir ultraweiches Matrigel mit Fasergerüsten verstärkten, die mithilfe von Melt Electrowriting gedruckt wurden. Somit können diese Matrigel-Faser-Komposite für strukturelle und funktionelle Experimente benutzt werden, die häufige Bewegung und Transport der Proben voraussetzen. Mit diesen Matrigel-Faser-Kompositen haben wir Methoden etabliert, die für die Charakterisierung von neuronalen Netzwerken erforderlich sind. Anstelle von Neuronen haben wir dafür eine Mausfibroblasten-Zelllinie benutzt und mit dem GlyR transfiziert. Zellen in den Matrigel-Faser-Komposite zeigten eine hohe Viabilität, konnten immunocytochemisch angefärbt werden, und mithilfe von elektrophysiologischen Methoden gemessen werden.

Darauf aufbauend haben wir primäre kortikale Mausneurone in faserverstärktem Matrigel für bis zu 21 Tage wachsen lassen. Die Neurone zeigten eine hohe Viabilität und durch Quantifikation von Neuritenlänge und Synapsendichte konnte ein vollständig ausgeformtes Netzwerk nach 7 Tagen in 3D-Kultur demonstriert werden. Mithilfe von Calcium-Imaging und Patch-Clamp-Experimenten wurden spontane Netzwerkaktivität, funktionelle spannungsgesteuerte Natriumkanäle, sowie Aktionspotentiale nachgewiesen. Somit konnten wir durch Kombination von einem ultraweichen Hydrogel mit Fasergerüsten erfolgreich ein Zellkulturmodell entwickeln, das zukünftig für die Erforschung von Zell-Zell-Interaktionen zwischen primären Gehirnzellen und Tumorzellen benutzt werden kann. Damit kann die molekulare Pathologie von aggressiven Hirntumoren und möglicherweise anderen Krankheitsmechanismen weiter aufgeklärt werden.

# Contents

<b>Introduction .....</b>	<b>1</b>
The Mammalian Central Nervous System.....	1
The Glycine Receptor .....	1
Glycine Receptor Structure .....	2
The <i>shaky</i> Mouse Model and the Role of the $\beta 8$ - $\beta 9$ Loop.....	4
The GABA <sub>A</sub> Receptor.....	5
GABA <sub>A</sub> Receptor Structure.....	6
GABA <sub>A</sub> Receptor Modulation by Natural Compounds .....	7
Biofabrication.....	9
The Brain Extracellular Matrix.....	9
Commonly Used Hydrogels.....	11
Melt Electrowriting.....	12
Ultra-soft matrix composites for 3D neuroglia <i>in vitro</i> research .....	13
<b>Materials and Methods .....</b>	<b>15</b>
Transfection of HEK293 cells.....	15
Biotinylation of cell surface proteins .....	15
Western Blot .....	16
Isolation of mouse cortical and hippocampal neurons.....	18
<b>Publications .....</b>	<b>19</b>
The GlyR Extracellular $\beta 8$ - $\beta 9$ Loop - A Functional Determinant of Agonist Potency .....	19
Sesquiterpenes and Sesquiterpenoids Harbor Modulatory Allosteric Potential and Affect Inhibitory GABA <sub>A</sub> Receptor Function <i>in vitro</i> .....	34

3D Electrophysiological Measurements on Cells Embedded within Fiber-Reinforced Matrigel .....	54
Cortical Neurons Form a Functional Neuronal Network in a 3D Printed Reinforced Matrix.....	62
<b>Discussion .....</b>	<b>69</b>
The GlyR Extracellular $\beta$ 8- $\beta$ 9 Loop.....	69
GABA <sub>A</sub> R Modulation by Sesquiterpenes and Sesquiterpenoids .....	73
3D Cell Culture in Fiber-Reinforced Hydrogel.....	76
<b>References .....</b>	<b>81</b>

# Introduction

## The Mammalian Central Nervous System

In the mammalian central nervous system (CNS), excitation and inhibition are enabled by presynaptic release of neurotransmitters which bind at postsynaptic receptors. Neurotransmitter receptors are classified into metabotropic and ionotropic receptors. While metabotropic receptors modulate cell activity via signal transduction mechanisms such as G proteins, ionotropic receptors form ion channels themselves and open upon neurotransmitter binding, allowing ions to pass through the cellular membrane. The resulting difference in charge either lead to a depolarization of the cell, possibly reaching the threshold for an action potential, or to hyperpolarization of the cell and thus an inhibition of neuronal firing. Due to those mechanisms, ionotropic receptors are also called ligand-gated ion channels (LGICs). The major neurotransmitters in the CNS are glutamate and acetylcholine at excitatory synapses, and  $\gamma$ -aminobutyric acid (GABA) and glycine at inhibitory synapses.

LGICs are grouped into three superfamilies: ionotropic glutamate receptors (GluRs), Cys-loop receptors (CLRs), and ATP-gated channels. The tetrameric GluRs are further divided into four subtypes: AMPA receptors, NMDA receptors, kainate receptors, and  $\delta$  receptors. AMPA and NMDA receptors are the most common GluRs (Traynelis et al. 2010). AMPA receptors enable cellular depolarization through sodium ion influx. In addition, NMDA receptors modulate synaptic plasticity via calcium ion permeability. CLRs are subdivided into cationic 5-HT<sub>3</sub> serotonin receptors, nicotinic acetylcholine receptors, and zinc-activated ion channels, and into the anionic GABA<sub>A</sub> receptors (GABA<sub>A</sub>Rs) and glycine receptors (GlyRs) (Nys et al. 2013). All CLRs share a pentameric structure. The name-giving 13-amino-acid loop is enclosed by a pair of disulfide-bonded cysteine residues in the extracellular domain (ECD) (Thompson et al. 2010). The first part of this thesis including two publications will focus on the inhibitory GlyRs and GABA<sub>A</sub>Rs.

## The Glycine Receptor

GlyRs are predominantly expressed in the spinal cord and brain stem, where they enable fast synaptic inhibition and play an important role in feedback control of the motor circuit. Motoneurons are excited via glutamatergic input, resulting in release of acetylcholine at the

neuromuscular junction, which causes muscle contraction. Simultaneously, inhibitory interneurons are excited by cholinergic collateral axons of motoneurons or glutamatergic primary afferents of dorsal root ganglia. Upon excitation, the interneurons release glycine which binds to GlyRs located at the motoneuronal membrane, resulting in hyperpolarization, and therefore balancing excitation of the muscle contraction (Rajendra et al. 1997).

Glycine is a full agonist of the GlyR. Taurine and  $\beta$ -alanine and taurine are partial agonists and hence bind with lower affinity (Lewis et al. 2003). The alkaloid strychnine is the main antagonist and is able to replace glycine in the binding pocket, thus blocking the ion channel (Young & Snyder 1974). Other modulators include alcohols and anesthetics (Mihic et al. 1997), endocannabinoids (Yevenes & Zeilhofer 2011),  $Zn^{2+}$  (Laube et al. 2000), picrotoxin (Pribilla et al. 1992), ivermectin (Shan et al. 2001), and glucose (Breitinger et al. 2015).

Defects in mammalian glycinergic neurotransmission are associated with hyperekplexia (startle disease; stiff baby syndrome; OMIM #149400) (Zhou et al. 2002), pain (Harvey et al. 2004), panic disorders (Deckert et al. 2017), and autism (Pilorge et al. 2016). Mutations in other proteins important for glycinergic synapse formation, e.g., glycine transporter 2, gephyrin, and collybistin are also associated with hyperekplexia (Harvey et al. 2008).

## **Glycine Receptor Structure**

GlyRs are homo- or heteropentameric chloride channels composed of five subunits which assemble pseudo-symmetrically around an ion channel pore. Four  $\alpha$  subunits  $\alpha$ 1-4 and one  $\beta$  subunit have been identified in mammals. All  $\alpha$  subunits can form functional homomeric receptors without presence of the  $\beta$  subunit (Kuhse et al. 1991; Nikolic et al. 1998; Harvey et al. 2000). Heteromeric receptors, with  $\alpha$ 1 $\beta$  GlyRs being the most common one, are composed of two  $\alpha$  and three  $\beta$  or three  $\alpha$  and two  $\beta$  subunits (Langosch et al. 1988; Grudzinska et al. 2005; Durisic et al. 2012; Patrizio et al. 2017). Homo- and heteromeric GlyRs can be differentiated using picrotoxin, which acts as non-competitive antagonist in absence of the  $\beta$  subunit (Pribilla et al. 1992). Expression of the  $\alpha$ 1 subunit, the most common adult  $\alpha$  subunit, starts immediately after birth and is highest in spinal cord and brain stem, while lower expression has been observed in the superior and inferior colliculi, thalamus, and hypothalamus (Sato et al. 1991).  $\alpha$ 2 is predominantly expressed at embryonic stages, however expression declines as  $\alpha$ 1 and  $\beta$  expression are increased after birth (Becker et al. 1988; Malosio et al. 1991; Lynch 2009). Some expression persists in adult retina, cortex, cerebellum, and auditory brain stem (Piechotta et al. 2001; Nobles et al. 2012; Avila et al.

2013). The  $\alpha 3$  subunit is expressed in several brain regions, e.g., the retina, where it is associated with neurons of the cone pathway, or in the spinal cord dorsal horn, where it is involved in inflammatory pain sensitization processes (Haverkamp et al. 2003; Haverkamp et al. 2004; Harvey et al. 2004; Harvey et al. 2009). GlyR $\alpha 3$  has also been identified in the cochlea, where it modulates auditory processing like signal-in-noise detection (Dlugaiczky et al. 2008; Tziridis et al. 2017). The  $\alpha 4$  subunit gene is a pseudo-gene in humans (Simon et al. 2004). However,  $\alpha 4$  is expressed in the mouse retina with unknown function, as well as in zebrafish spinal cord and hindbrain, where it seems to contribute to escape behavior (Heinze et al. 2007; Leacock et al. 2018). The  $\beta$ -subunit has been found distributed in the whole CNS and also in non-neuronal tissues (Malosio et al. 1991).

Each GlyR subunit consists of a long N-terminal ECD, four transmembrane  $\alpha$ -helices M1-4, a large intracellular domain between M3 and M4, and a short extracellular C-terminus. The ECD is formed by a short  $\alpha$ -helix followed by 10  $\beta$ -sheets connected by short loop structures. The ion channel pore is formed by the M2 helices of all five subunits. In recent years, the GlyR structure has been more and more elucidated by cryogenic electron microscopy (Figure 1) (Du et al. 2015; Huang et al. 2015; Huang et al. 2017a; Huang et al. 2017b; Kumar et al. 2020; Yu et al. 2021). Previously, only partial structures or homology models of related CLRs were available (Althoff et al. 2014; Moraga-Cid et al. 2015).

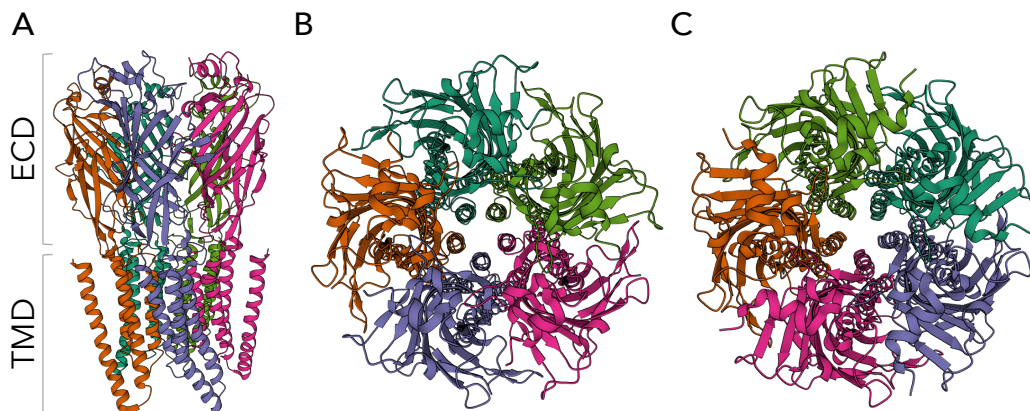


**Figure 1: Glycine receptor structure.** A) Side view of a homopentameric GlyRa1. ECD: extracellular domain, TMD: transmembrane domain. B) Top view of the same GlyRa1 in the unbound/closed state. C) Top view of the glycine-bound state. Note the tilted TMD in the central ion channel pore. Each subunit in A, B, C is shown in a different color. Structures (6pxd, 6pm6) were obtained from the Protein structure comparison service PDBeFold at European Bioinformatics Institute (Krissinel & Henrick 2004).

The ligand-binding interface is formed by loops A, B, and C from the principal (+) site and loops D, E, and F (also called  $\beta 8$ - $\beta 9$  loop) from the complementary (-) site (Hibbs & Gouaux 2011). Residues F159 (loop B), T204 and F207 (loop C), R65 ( $\beta 2$ ) and S129 ( $\beta 6$ ) directly participate in glycine binding (Du et al. 2015; Yu et al. 2021). Upon ligand binding, loop C undergoes a conformational change and transmits the activation signal to the rest of the channel, resulting in tilting of the M2 domains and thus opening of the ion channel pore (Althoff et al. 2014; Du et al. 2015). The large intracellular M3-4 loop has the highest diversity and plays an essential role in cell surface trafficking of the receptor (Sadtlir et al. 2003; Villmann et al. 2009a; Haeger et al. 2010). Truncations of the M3-4 loop also affect receptor desensitization and maximum responses to agonists, hinting at participation in channel opening (Langlhofer et al. 2015; Ivica et al. 2021). However, almost no information about M3-4 movement during ligand binding and channel opening are available. The GlyR  $\beta$  subunit M3-4 loop harbors a binding motif for the scaffold protein gephyrin, which anchors GlyRs and GABA<sub>A</sub>Rs to the postsynaptic membranes of neurons (Fritschy et al. 2008; Kasaragod & Schindelin 2019).

## The *shaky* Mouse Model and the Role of the $\beta 8$ - $\beta 9$ Loop

*Shaky* is a novel spontaneous mouse mutant that carries a missense mutation resulting in an amino acid substitution of glutamine to lysine at position 177 (Q177K, number refers to mature protein), located in the  $\beta 8$ - $\beta 9$  loop of the GlyR $\alpha 1$  ECD (Schaefer et al. 2017). Affected homozygous mice suffer from progressively worsening neuromotor deficits from postnatal day 14 on until death around 4-6 weeks after birth.

At the neuronal level, a decreased synaptic localization and concomitantly an increased expression of GlyR $\alpha 1$ <sup>Q177K</sup> was observed, most likely a failed attempt of compensation. Electrophysiological recordings revealed reduced current amplitudes, frequencies, and decay times. Furthermore, structural modeling exhibited a disrupted hydrogen bond network, that enables, in the non-mutated situation, glycine binding to the neighboring residue R65. These results suggest an important role of the  $\beta 8$ - $\beta 9$  loop in GlyR clustering at the membrane as well as ion channel gating (Schaefer et al. 2017).

During the time of the first publication included in this dissertation, knowledge of the GlyR  $\beta 8$ - $\beta 9$  loop was limited. *In vitro* studies of this loop were so far only investigated in other CLRs. In the GABA<sub>A</sub>R  $\gamma$  subunit, changes to the  $\beta 8$ - $\beta 9$  loop affects diazepam potentiation (Padgett & Lummis 2008). In the 5-HT<sub>3</sub> serotonin receptor, residues in the  $\beta 8$ - $\beta 9$  loop are critical for antagonist binding (Thompson et al. 2006). Interactions of full and partial agonist

with the  $\beta 8$ - $\beta 9$  have been shown in the nicotinic acetylcholine receptors (Hibbs et al. 2009). Furthermore, the involvement of the  $\beta 8$ - $\beta 9$  loop in a hydrogen network important for ligand-binding was discovered (Padgett & Lummis 2008; Khatri & Weiss 2010; Nys et al. 2013). Newly published GlyR structures revealed that the  $\beta 8$ - $\beta 9$  loop is part of the signal transduction unit. Upon ligand binding, the  $\beta 8$ - $\beta 9$  loop together with preM1-M1, M2, Cys-loop,  $\beta 10$ , M2-3 loop, and  $\beta 1$ -2 loop transfer the closed receptor into the open configuration and back (Hassaine et al. 2014; Du et al. 2015; Huang et al. 2015). Taken together, these results clearly demonstrate the important role of the  $\beta 8$ - $\beta 9$  loop in GlyR function. Experiments in the *shaky* mouse model could show how the Q177K mutation disturbs a hydrogen network and thus ligand binding (Schaefer et al. 2017). The aim of the publication “**The GlyR Extracellular  $\beta 8$ - $\beta 9$  Loop – A Functional Determinant of Agonist Potency**” was to analyze the effect of other amino acid substitutions at position Q177 of the GlyR $\alpha 1$  subunit on receptor expression, localization, and function to further elucidate the role of the  $\beta 8$ - $\beta 9$  loop within the ECD of GlyRs. We could demonstrate that GlyR $\alpha 1$ <sup>Q177</sup> variants do not affect ion channel trafficking to the cellular membrane, but reduce glycine, taurine, and  $\beta$ -alanine potency in comparison to the wildtype protein. The largest alterations were observed for the GlyR $\alpha 1$ <sup>Q177R</sup> variant, which disrupts the hydrogen network around residue Q177, similar to the Q177K mutation in *shaky* mice. This study underlined the importance of the GlyR  $\beta 8$ - $\beta 9$  loop for proper ion channel function.

## The GABA<sub>A</sub> Receptor

GABA<sub>A</sub>Rs are the major inhibitory LGICs in the central nervous system and enable phasic synaptic as well as tonic perisynaptic and extrasynaptic inhibition. They are expressed in brain areas like cortex, hippocampus, and olfactory bulb, where they inhibit incoming action potentials through chloride ion influx, thus helping to balance excitatory and inhibitory neurotransmission (Sieghart 2006; Mortensen et al. 2012). Dysfunction of the GABA<sub>A</sub>R, manifesting most commonly as reduced activity, can cause serious neurological disorders like epilepsy, anxiety disorders, schizophrenia, and insomnia (Mohler 2006). This makes GABA<sub>A</sub>Rs a prime target for drug research, resulting in an extensive list of agonists that includes both natural compounds and synthesized drugs (Olsen 2018).

GABA is the primary agonist. Prominent agonists with positive modulatory function include the benzodiazepine diazepam, barbiturates, and propofol (Olsen 2018). Diazepam is used for broad treatment of, e.g., epilepsy and anxiety. Barbiturates are used for sedation and treatment of insomnia, seizures, and headaches. Propofol is mainly used for general



anesthesia. Due to the widespread distribution of GABA<sub>A</sub>Rs in the brain, most drugs targeting them can cause strong side effects (Janhsen et al. 2015; Choi et al. 2014). Like for the GlyR, GABA<sub>A</sub>Rs are also positively modulated by ethanol (Forstera et al. 2016). The GABA analog gaboxadol is a selective ligand for extrasynaptic GABA<sub>A</sub>Rs (Meera et al. 2011). GABA<sub>A</sub>Rs can be blocked by the antagonists picrotoxin and bicuculline.

## GABA<sub>A</sub> Receptor Structure

Like the other CLR<sub>s</sub>, GABA<sub>A</sub>Rs are heteropentameric receptors consisting of two to three different subunits that are encoded by 19 genes ( $\alpha$ 1-6,  $\beta$ 1-3,  $\gamma$ 1-3,  $\delta$ ,  $\epsilon$ ,  $\theta$ ,  $\pi$ ,  $\rho$ 1-3,) (Simon et al. 2004). Most GABA<sub>A</sub>Rs are formed by two  $\alpha$ , two  $\beta$ , and a single  $\gamma/\delta$  subunit, with  $\alpha$ 1 $\beta$ 2 $\gamma$ 2 and  $\alpha$ 1 $\beta$ 3 $\gamma$ 2 receptors being the most abundant configurations in the brain (Fritschy & Mohler 1995). An arrangement of  $\alpha$ - $\beta$ - $\alpha$ - $\beta$ - $\gamma/\delta$  in a clockwise manner seems most likely (Lavery et al. 2017; Lavery et al. 2019; Masiulis et al. 2019). Receptor configurations with just  $\alpha$  and  $\beta$  subunits are also possible. Functional homomeric  $\beta$ 3 and heteromeric  $\beta$ 3 $\gamma$ 2 receptors have also been reported (Hoerbelt et al. 2015). The multitude of possible receptor combinations allows for distinct physiological roles of GABA<sub>A</sub>Rs in the CNS.  $\alpha$ 1 containing receptors seem to be involved in sedative pathways, while  $\alpha$ 2 containing receptors play a part in mediating anxiety pathways (McKernan et al. 2000; Low et al. 2000). Extrasynaptic, tonic  $\delta$ ,  $\epsilon$ , or  $\theta$ -containing receptors display a high affinity but low efficacy to GABA, enabling them to sense low GABA concentrations of synaptic spillover (Brickley & Mody 2012).

Like other CLR<sub>s</sub>, each GABA<sub>A</sub>R subunit consists of a long N-terminal ECD, four transmembrane domains M1-4, with M2 forming the ion channel pore, and a short C-terminus. The large intracellular M3-4 loop has a high sequence variability between different subunit types and holds binding sites for structural proteins like gephyrin (Kasaragod & Schindelin 2019). Detailed structural data became available in recent years (Zhu et al. 2018; Nakane et al. 2020; Miller & Aricescu 2014; Miller et al. 2017). GABA binds at the  $\beta$ - $\alpha$  interface, while benzodiazepines, like the allosteric modulator diazepam, bind to a cavity at the  $\alpha$ - $\gamma$  interface (Whiting et al. 1995). Recently, a second binding site for benzodiazepines was discovered between the transmembrane domains at the  $\beta$ - $\alpha$  interface. Furthermore, neurosteroid binding to a hydrophobic pocket between adjacent transmembrane domains was found (Alvarez & Estrin 2015; Miller et al. 2017; Alvarez & Pecci 2018).

## GABA<sub>A</sub> Receptor Modulation by Natural Compounds

Other than the multitude of GABA<sub>A</sub>R modulators used in clinical therapy and research, more and more natural compounds with modulatory effects are being found in plants and products containing plant material (Johnston et al. 2006). These compounds belong to the groups of flavonoids, terpenoids, phenols, and polyacetylenic alcohols, which can be found in herbs, fruits, vegetables, and therefore also in cosmetics and beverages, like tea, coffee, whisky, and red wine (Hossain et al. 2002). Plants have been used for thousands of years for medical treatment and wellbeing of humans. Nowadays enhancement of GABA<sub>A</sub>R inhibition is a well-used therapy for many diseases of the CNS. Thus, it makes sense to search for more modulatory compounds.

Terpenoids are the largest group of natural products and contribute to scent and color of plants. Terpenoids are categorized into different subclasses, depending on the number of carbon atoms and acyclic or cyclic structure. Their partly high hydrophobicity allows binding to transmembrane subunit interfaces or modulation of the surrounding lipids (Manayi et al. 2016; Silva et al. 2019). Volatile bicyclic and monoterpenoids myrtenol and verbenol, found in various Mediterranean tea preparations that are known for calming and sedating effects, have been described as positive allosteric modulators at  $\alpha 1\beta 2\gamma 2$  and  $\alpha 1\beta 2$  GABA<sub>A</sub>Rs (Kessler et al. 2012; Kessler et al. 2014). The sesquiterpenoid valerenic acid, found in valerian, a plant commonly used to promote sleep, has been shown to positively modulate GABA<sub>A</sub> receptors (Khom et al. 2007). Other sesquiterpenes and sesquiterpenoids (SQTs) have also been described as GABA<sub>A</sub>R modulators, e.g., artemisinins, which are commonly used for treatment of malaria (Manayi et al. 2016; Kasaragod et al. 2019).

Many of these modulating natural compounds share structural similarities, such as the presence of a hydroxy group and a mono- or bicyclic character. Previous studies have shown that digestion and metabolization processes lead to structural changes in natural components (Adams et al. 2011; Heinlein & Buettner 2012). These processes may create secondary metabolites that gain the ability to modulate GABA<sub>A</sub>Rs, prompting to not just look at natural compounds, but also their metabolites.

In the publication “**Sesquiterpenes and sesquiterpenoids harbor modulatory allosteric potential and affect inhibitory GABA<sub>A</sub> receptor function in vitro**” we investigated the effect of 11 SQTs on GABA<sub>A</sub>Rs. The SQTs tested include major compounds of the volatile fractions of hop and chamomile and secondary metabolites created by an *in vitro* digestion model (Figure 2). In the human embryonic kidney 293

(HEK293) cell line, we could observe significant GABA<sub>A</sub>R modulation by some SQTs, including secondary metabolites. However, due to the presence of both phasic and tonic GABA<sub>A</sub>Rs in hippocampal neurons, different results were obtained compared to the overexpression of a distinct GABA<sub>A</sub>R configuration in HEK293 cells. Modeling and docking studies revealed a possible binding mechanism of SQTs to the neurosteroid binding site of the GABA<sub>A</sub>R. Taken together, we could successfully demonstrate GABA<sub>A</sub>R modulation by SQTs and that digested SQTs do not lose neurotrophic activity.

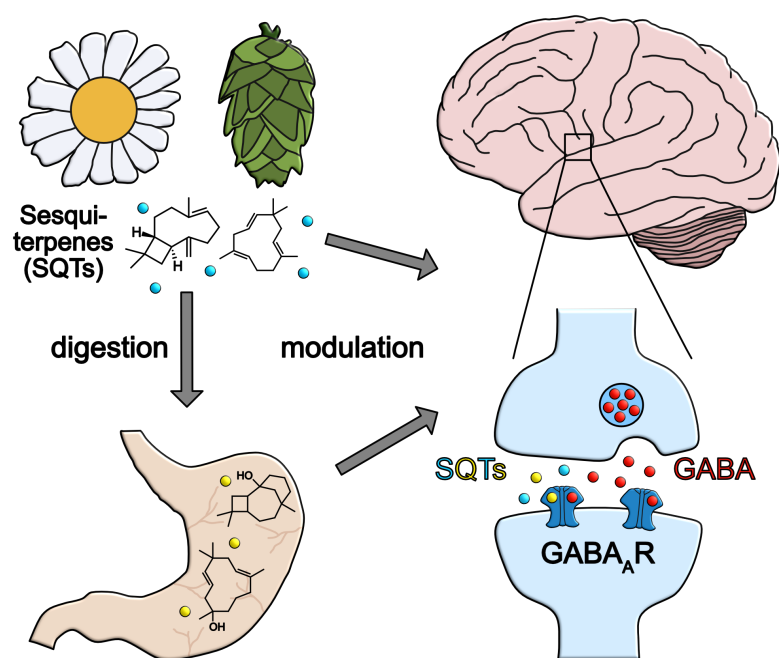


**Figure 2: Digestion of SQTs creates secondary metabolites.** SQTs are major compounds of the volatile fraction of chamomile and hop. Digestive processes transform them into secondary metabolites with altered neurotrophic potential on GABA<sub>A</sub>Rs. Reprinted from Janzen et al. (2021). © 2021 The Authors. Published by John Wiley & Sons Ltd. Licensed under CC BY 4.0.

## **Biofabrication**

Biofabrication is the use of additive manufacturing (AM), commonly called three-dimensional (3D) printing, to arrange cells and materials to create hierarchical tissue-analogous structures (Groll et al. 2016). The term biofabrication is used by many scientific disciplines and its definition can change accordingly, e.g., the fabrication of materials by living organisms can also be called biofabrication. Here, biofabrication is described according to the definition used by the tissue engineering and regenerative medicine field that aims to create implantable materials for treatment of injuries and diseases (Berthiaume et al. 2011). Tissue-appropriate cells generally are arranged in such a way that they resemble the native issue, often by placing the cells on tissue scaffolds. However, tissue engineering has their limitations as research progresses slowly and translation into clinical studies is difficult (Ikada 2006).

In recent years, AM technologies have progressed rapidly, leading to a drastic increase in quality and availability of established and new techniques while simultaneously reducing their costs. New advancements allow automatic arrangement of cells and material, separate or together, to create standardized functional tissue models that can be used for implanting or as replacement for animal experiments in drug research. However, there is still a need for cell-compatible and printable materials. Each cell type of the human body has its own microenvironment and thus needs suitable equipment and material. For example, when printing a hydrogel (or matrix) containing cells (called bioink), the cells are exposed to shear stress which has significant impact on cell viability, morphology, as well as proliferation (Blaeser et al. 2016). 3D culture models can generally be classified into scaffold or scaffold-free cultures. In scaffold-based cultures, cells are seeded on solid scaffolds, encapsulated in hydrogels, or in a composite consisting of multiple material types. In contrast, scaffold free cultures allow cells to self-assemble into spheroids using hanging drop cultures, spinning bioreactors, magnetic levitation, or other techniques that prevent cell growth on surfaces (Edmondson et al. 2014; Langhans 2018). In the present study, scaffold-based cultures were used.

## **The Brain Extracellular Matrix**

Multiple factors need to be considered when creating scaffold-based cell culture models. The mechanical properties of the cell environment play a significant role in cell differentiation, survival, and function. For example, mesenchymal stem cells can differentiate into several

cell types depending on the stiffness of the surrounding hydrogel, e.g., 20 kPa for nerve cells and 80 kPa for chondrocytes (Oh et al. 2016). Through mechanotransduction, tissue stiffness can influence cell morphology, migration, proliferation and other cell behavior (Eyckmans et al. 2011). These mechanisms are especially important in the developing brain, where stiffness gradients, next to chemical cues, guide growing axons to their destination (Koser et al. 2016). The brain is one of the softest tissues in the body with elastic moduli between 30-500 Pa, depending on the developmental stage and brain region (Christ et al. 2010; Iwashita et al. 2014). The low elastic modulus of the brain is due to its unique extracellular matrix (ECM), which contains low amounts of matrix proteins, such as collagens, laminins, and fibronectin. In addition, the brain ECM predominantly contains glycosaminoglycans, in particular high portions of hyaluronic acid, as well as tenascins, and proteoglycans (Lau et al. 2013). Neurons and glia form cell-ECM interactions using a wide range of brain-specific receptors that bind to ECM proteins (Barros et al. 2011). The brain ECM can be divided into three main components: the basal lamina, perineuronal nets, and the interstitial matrix (Figure 3) (Kim et al. 2018).

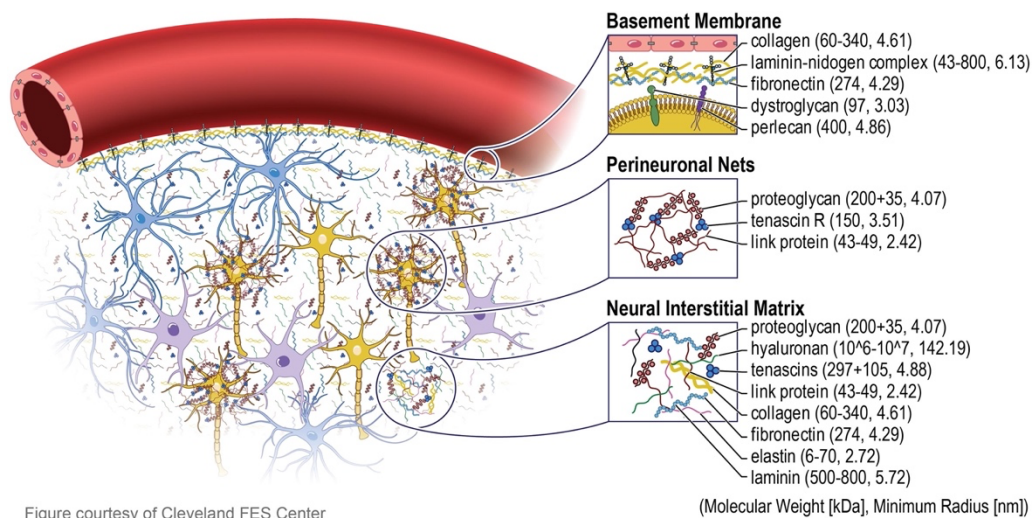


**Figure 3: The brain extracellular matrix.** The extracellular matrix of the brain is divided into three components: basement membrane, perineuronal nets, and interstitial matrix. Each component contains a unique protein composition that facilitate structural and regulatory functions. Neurons are depicted as yellow, astrocytes as blue, and microglia as purple cells. Reprinted from Kim et al. (2018). © 2018 The Authors. Published by Frontiers Media SA. Licensed under CC BY 4.0.

The basal lamina separates cerebral vasculature and brain tissue and is composed of collagen, laminin, nidogen, perlecan (LeBleu et al. 2007). Perineuronal nets, which contain hyaluronan, chondroitin sulfate proteoglycans, and tenascins surround the soma and dendrites, thus helping to enable synapse formation and thus regulate neuronal plasticity

(Fawcett et al. 2019). The interstitial matrix is made up of various ECM proteins connecting neuronal networks with the vascular system. This matrix is also important for signal transmission and substance transport (Lei et al. 2017).

Brain tissue stiffness does not only change during development but have also been described for various neurological disorders, e.g., neurodegenerative diseases such as Alzheimer's and Parkinson's (Bonneh-Barkay & Wiley 2009). Stiffening of the ECM has been observed for brain tumors, in particular glioblastoma multiforme (GBM), the most aggressive and deadly type of brain cancer, for which stiffer tumor ECM has been associated with poor prognosis (Holland 2000; Miroshnikova et al. 2016). GBM cells migrate along blood vessels and white matter tracts and infiltrate the brain, but rarely metastasize outside the brain (Cuddapah et al. 2014). Recently it has been demonstrated, that GBM can form chemical so called pseudo-synapses with neurons. Stimulated by presynaptic neurons, postsynaptic AMPA receptors present on GBM cells generate calcium transients that increase tumor invasiveness (Venkataramani et al. 2019). Neurons, glia, and brain tumor cells affect each other not just by modulating the surrounding ECM, but also form cell-cell interactions that can have extensive effects on brain functions and tumor progression. Therefore, *in vitro* cell culture models that mimic the *in vivo* environment are needed to further elucidate these mechanisms and to develop new approaches for therapy of these aggressive brain tumors.

## Commonly Used Hydrogels

3D *in vitro* cell cultures models are of special interest to the neuroscience field as the third dimension offers more space for neuronal outgrowth and network formation than traditional 2D cultures. Therefore, 3D complexity of neuronal cultures represents a suitable alternative to *in vivo* models like brain slices. Many factors need to be considered when creating 3D *in vitro* cell culture models of the brain. For example, the matrix needs to have the right mechanical properties. As it has been pointed out already, neurons prefer softer environments and form more extensive networks in ultra-soft hydrogels (Palazzolo et al. 2015). The multitude of ECM proteins present in brain tissue needs to be considered to develop 3D *in vitro* model systems. On the one hand, hydrogels can be supplemented with such proteins. Recently, hydrogels were created by addition of decellularized brain ECM (Medberry et al. 2013). Decellularized ECM has the advantage of retaining its native composition, however obtaining large quantities is difficult as significant amounts of source tissue are required (Hoshiya et al. 2016). Another popular hydrogel for all kinds of 3D cultures is matrigel, an ECM mixture secreted by Engelbreth-Holm-Swarm mouse sarcoma

cells. Matrigel is composed mostly of laminin, collagen IV and entactin, but also contains perlecan and various growth factors, which in sum allow growth of almost all cell types in matrigel (Hughes et al. 2010). However, its tumor origin prevents its use in clinical applications and lot-to-lot variations in protein concentrations make reproducibility challenging. Therefore, research on synthetic alternatives to matrigel is increasing. Synthetic hydrogels of natural and unnatural origin have many advantages. They have defined formulas that can be adapted to desired stiffness and porosity and can easily be functionalized with adhesive motives and ECM proteins, allowing the creation of cell-specific hydrogels. However, especially unnatural hydrogels lack common adhesive sites, are not biocompatible, and disable cell growth when used in their pure form. Hence, finding the right formula is a highly time-consuming process. The glycosaminoglycan hyaluronic acid is one of the best characterized natural hydrogels and, due to its natural occurrence in the brain ECM, a prime candidate for 3D *in vitro* models of the brain (Burdick & Prestwich 2011; Seidlits et al. 2010). Just recently the advantage of peptide-modified, hyaluronic-acid based 3D cultures over conventional 2D cultures has been demonstrated for human neural stem/progenitor cells (Seidlits et al. 2019). Other hydrogels successfully used for neuronal cultures are alginate, a natural polymer obtained from brown seaweed, or collagen (Frampton et al. 2011; Palazzolo et al. 2015; Xu et al. 2009). Recently, Distler et al. demonstrated that oxidized alginate-gelatin-laminin hydrogels facilitate differentiation and growth of stem cell derived neurospheres (Distler et al. 2021). Furthermore, many hydrogel formulations based on polyacrylamide or polyethylene glycol are being developed as alternatives to matrigel (Aisenbrey & Murphy 2020).

## **Melt Electrowriting**

In addition to the hydrogel matrix, 3D scaffolds made of biodegradable polymers are popular in the tissue engineering field. Various 3D-printing techniques are available, e.g., fused deposition modeling, inkjet printing, and selective laser sintering (Bártolo et al. 2009). Another commonly used technique is solution electrospinning, which is often used to create random meshes of fibers with sub-micrometer fibers, which can be used as substrate for cell growth (Cipitria et al. 2011). However, these random meshes can be too tight for cells to pass through, making them unsuitable for real 3D cultures.

A relatively new technique, which solves this problem, is melt electrowriting (MEW). MEW deposits polymer melt fibers in the micrometer range on an automated laterally translating collection system in a controlled manner (Brown et al. 2011). This allows the creation of

complex shapes and structures, like porous tubes (Figure 4) (McColl et al. 2018; Robinson et al. 2019). An ideal polymer for MEW is polycaprolactone (PCL), a biodegradable, non-toxic polyester with a low melting point (60 °C) that is approved for use in the human body (Brown et al. 2011). MEW PCL scaffolds have successfully been used for cartilage and vascular applications (Visser et al. 2015; Saïdy et al. 2019). The use of MEW is especially of interest for reinforcement of soft hydrogels, as already low volumes of ordered fibers can significantly increase overall mechanical stability and handling of scaffold-hydrogel composites (Visser et al. 2015; Mekhileri et al. 2018). Furthermore, MEW fibers can possibly influence cell behavior and growth through mechanotransductive or haptotactic cues, e.g., as guidance for neuronal outgrowth (Smeal et al. 2005; Baker & Chen 2012). Taken together, MEW has the potential to provide essential support for ultra-soft matrices used in creating 3D *in vitro* brain models.

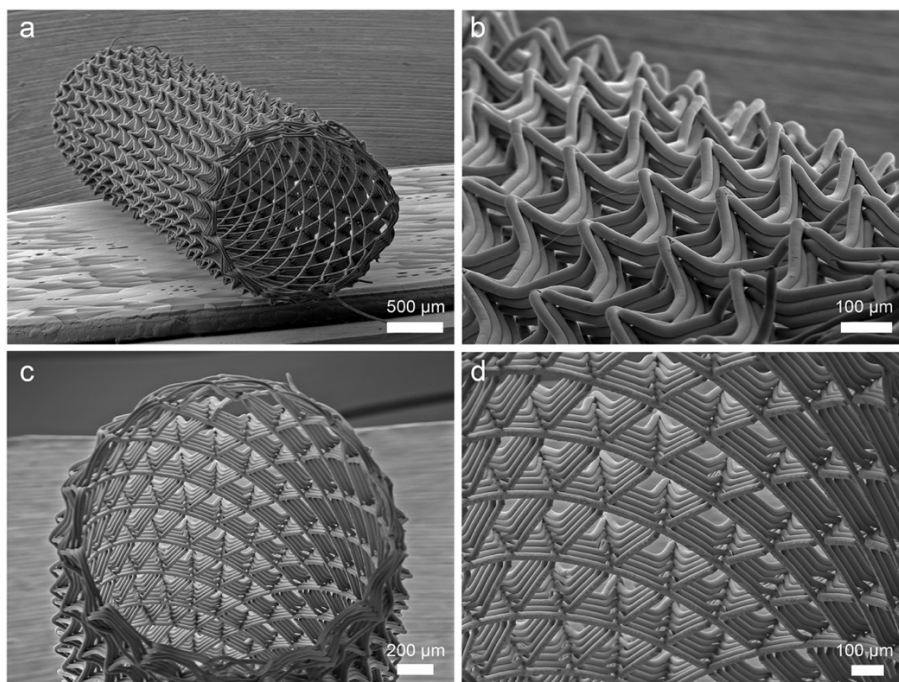


**Figure 4: Melt electrowritten tube.** Melt electrowriting can be used to create complex structures. Reprinted from McColl et al. (2018). © 2018 The Authors. Published by Elsevier Ltd. Licensed under CC BY-NC-ND 4.0.

## Ultra-soft matrix composites for 3D neuroglia *in vitro* research

In 2018, the collaborative research center TRR225 „From the fundamentals of biofabrication towards functional tissue models” was established as a cooperation of the Universities of Würzburg, Erlangen, and Bayreuth, to develop new (bio)materials, methods, and study cell behavior in 3D culture models. The following two publications result of the



work of TRR225's sub-project B01 "Ultra-soft matrix composites for 3D neuroglia *in vitro* research". The goal of sub-project B01 was to use ultra-soft matrices to create 3D models that mimic the neuronal *in vivo* environment. As these matrices are difficult to handle, melt electrowritten fiber scaffolds were used to reinforce the matrix, which enabled proper handling for experiments, e.g., immunocytochemical stainings and electrophysiological measurements. Co-cultures of neurons, astrocytes, and glioblastoma cells in these matrix composites were used to study neuronal differentiation, network formation, as well as glioblastoma migration and interaction with healthy cells.

In the publication "**3D Electrophysiological Measurements on Cells Embedded within Fiber-Reinforced Matrigel**" we successfully established methods necessary for the characterization of neuronal network formation at the structural and functional level. Out of three designs, MEW scaffolds with 200  $\mu\text{m}$  pore spacings were chosen and used to reinforce soft matrigel, which was rheologically analyzed. The reinforcement enabled handling of an ultra-soft matrix. As a first cell line, mouse fibroblasts were transfected with the ligand-gated ion channel GlyR and seeded in scaffold-matrigel composites. Cells displayed high viability and could be immunocytochemically stained for the GlyR. Using the patch clamp technique, glycine efficacy and potency were characterized for the GlyR in a 3D culture system. Moreover, we created a 3D cell culture model that did not lead to functional alterations of the GlyR using electrophysiological measurements as well as other commonly used techniques and can further be adapted for the culture of neuronal cells.

In the follow-up publication "**Cortical Neurons Form a Functional Neuronal Network in a 3D Printed Reinforced Matrix**" we continued our work by culturing primary mouse cortical neurons in fiber-reinforced matrigel. Neurons were cultured up to 21 days and displayed higher viability than conventional 2D culture on coated glass coverslips. Neurite lengths and synapse density were quantified using immunocytochemical stainings of dendritic and synaptic markers. Calcium imaging revealed spontaneous network activity around day 14 in culture and patch clamp experiments demonstrated functional voltage-gated sodium channels as well as action potential firing. Taken together, we successfully advanced our previous 3D cell culture model for the use with primary neurons, thus creating a new model that can be used to study neuronal networks in 3D. Future experiments will focus on replacing matrigel with other matrix formulations that are not of tumor origin and provide optimal support for neuronal cultures.

# Materials and Methods

The following materials and methods were published in an abridged version and are described here in more detail to allow easier replication of experiments. All chemical used were purchased from Carl Roth (Karlsruhe, Germany) or Merck/Sigma-Aldrich (Darmstadt, Germany) unless stated otherwise.

## Transfection of HEK293 cells

HEK293 were transfected using a calcium phosphate protocol. DNA, 0.1X TRIS/EDTA (A0973.0500; AppliChem, Darmstadt, Germany) and 2.5 M CaCl<sub>2</sub> pH 7.0 were thoroughly mixed before 2X HEPES buffered saline (HBS; 50 mM HEPES; 12 mM glucose; 10 mM KCl; 280 mM NaCl; 1.5 mM Na<sub>2</sub>HPO<sub>4</sub>; pH 6.95) was added (see Table 1). The transfection mixture was incubated for 20 min at room temperature and then pipetted onto the cells. Cell medium was exchanged after 5-6 h and cells were used for experiments 24-72 h after transfection.

Table 1: Transfection mixture for HEK293 cells

Reagent	35 mm cell culture dish	100 mm cell culture dish
DNA	1-3 µg	10-30 µg
0.1X TRIS/EDTA	ad 90 µl	ad 450 µl
2.5 M CaCl <sub>2</sub>	10 µl	50 µl
2X HBS	100 µl	500 µl

## Biotinylation of cell surface proteins

A biotinylation assay was used to separate membrane-bound and intracellular proteins. Buffers used are shown in Table 2. HEK293 cells in 100 mm dishes were washed once with cold PBS (phosphate buffered saline) and incubated with 1 ml of 1 mg/ml EZ-Link Sulfo-NHS-LC-Biotin (21335; Thermo Fisher Scientific, Waltham, MA, USA) in PBS for 30 min, 4 °C on a tumbling shaker. Cells were washed twice with cold PBS, once with quenching buffer, and incubated for 10 min, 4 °C with quenching buffer. Using a cell scraper, the cells were detached and transferred in 2 ml PBS to a reaction tube. Samples were centrifuged for

1 min at 1,000 x g, 4 °C, the pellets merged with 1 ml lysis buffer, homogenized, and centrifuged again for 1 min at 20,000 x g, 4 °C. 80 µl of the supernatant was stored at -80 °C (whole cell fraction). The remaining supernatant was incubated for 2 h, 4 °C with 50 µl streptavidin agarose beads (20353; Thermo Fisher Scientific, Waltham, MA, USA) on an overhead shaker and then centrifuged for 1 min at 12,000 x g, room temperature. The supernatant was stored at -20 °C (intracellular fraction). The remaining beads, bound to the membrane proteins, were washed three times with lysis buffer, resuspended in 60 µl of 95 °C hot 2X SDS buffer, and heated for 5 min at 95 °C. The membrane fraction was stored at -80 °C. Before Western Blot analysis, whole cell fraction samples were also diluted in 2X SDS buffer and heated for 5 min at 95 °C.

**Table 2: Biotinylation assay buffers**

<b>Buffer</b>	<b>Composition</b>
PBS	137 mM NaCl, 3 mM KCl, 6.5 mM Na <sub>2</sub> HPO <sub>4</sub> x H <sub>2</sub> O, 1.5 mM KH <sub>2</sub> PO <sub>4</sub> x H <sub>2</sub> O; pH 8
Quenching buffer	192 mM glycine, 25 mM TRIS
TBS (TRIS buffered saline)	50 mM TRIS; 150 mM NaCl; pH 8
Lysis buffer	1% Triton X-100; 2 mM EDTA; 0.1 mM PMSF; 10 mg/ml protease inhibitor (04693132001, Roche, Basel, Switzerland); in TBS
2X SDS sample buffer	90 mM TRIS-HCl; 20% (v/v) glycerol; 2% (w/v) SDS; 0.02% (w/v) bromophenol blue

## Western Blot

The sodium dodecyl sulfate polyacrylamide gel electrophoresis (SDS-PAGE), followed by Western Blotting, was used to separate and stain proteins for analysis. Buffers and solutions used are shown in Table 3. Protein samples and Blue Prestained Protein Standard, Broad Range (P7718; New England Biolabs, Ipswich, MA, USA) were loaded into an 11% discontinuous polyacrylamide gel (Table 4). The electrophoresis in SDS buffer was performed for 20 min at 80 V and followed by 90-110 min at 160 V. Afterwards, proteins were transferred from the gel to a nitrocellulose membrane (GE Healthcare, Freiburg,

Germany) using the wet blot transfer method. Blotting was performed for 1 h at 200 mA, 4 °C (proteins <100 kDa) or overnight at 100 mA, 4 °C (proteins >100 kDa). After transfer, the membrane was incubated with blocking solution for 1 h at room temperature and incubated with the primary antibody in blocking solution overnight at 4 °C on a tumbling shaker. On the next day, the membrane was washed three times with TBS-T for 20 min each, incubated with a secondary horse radish peroxidase-coupled antibody (Dianova, Hamburg, Germany) in blocking solution for 1 h at room temperature, and washed three times with TBS-T for 20 min each. Protein signals were detected using SuperSignal West Pico or Femto (Thermo Fisher Scientific, Waltham, MA, USA), captured on X-ray films (Super RX-N; Fujifilm, Tokyo, Japan), and developed by a CP1000 film processor (AGFA, Mortsel, Belgium).

**Table 3: Buffers and solutions used for SDS-PAGE and Western Blot**

<b>Buffer</b>	<b>Composition</b>
TBS	50 mM TRIS, 150 mM NaCl
TBS-T	50 mM TRIS, 150 mM NaCl, 0.1% tween 20
Blocking solution	TBS-T, 3% (w/v) bovine serum albumin
SDS buffer	25 mM TRIS, 192 mM glycine, 0.1% (w/v) SDS, pH 8.3
Wet blot transfer buffer	25 mM TRIS, 192 mM glycine, 10% ethanol
Separating gel buffer	1.5 M TRIS-HCl, 0.4% (w/v) SDS, pH 8.8
Stacking gel buffer	0.5 M TRIS-HCl, 0.4% (w/v) SDS, pH 6.8

**Table 4: Composition of an 11% discontinuous polyacrylamide gel**

<b>Gel</b>	<b>Composition</b>
Stacking gel	325 µl 30% polyacrylamide, 625 µl stacking gel buffer; 1.52 ml H <sub>2</sub> O; 2.5 µl TEMED, 12.5 µl 10% ammonium persulfate
11% separating gel	3.3 ml 30% polyacrylamide, 2.24 ml separating gel buffer, 3.45 ml H <sub>2</sub> O; 6 µl TEMED; 30 µl 10% ammonium persulfate

## Isolation of mouse cortical and hippocampal neurons

Cortical and hippocampal neurons were prepared from mouse embryos at embryonic day 16-18 from pregnant wild type CD1 mice (Strain code 022; Charles River, Sulzfeld, Germany). Experiments were authorized by the local veterinary authority and Committee on the Ethics of Animal Experiments (Regierung von Unterfranken). Material used is shown in Table 5. After euthanasia of the pregnant mouse with CO<sub>2</sub>, embryos were transferred to a 100 mm dish with minimum essential medium. The uterus and amniotic sacs were removed, embryos were decapitated, and heads collected in a separate dish. Brains were carefully extracted and transferred to a cooled dish. Cortices were cut off, so no corpus callosum and no olfactory bulbs remained. After removal of the meninges, the hippocampus, visible as a crescent shaped structure on the inside of the cortex, was cut out. Depending on which neuronal subculture was desired, the following steps were continued either with hippocampi or cortices. Tissue was transferred to a 15 ml tube, the supernatant removed, and 0.5 mg/mL trypsin, 0.2 mg/mL EDTA and 10 µg/µL DNase I in PBS were added. After 30 min incubation at 37 °C, 10% fetal bovine serum was added, and neurons were dissociated by trituration with flame-polished Pasteur pipettes. After two 10 min centrifugation steps at 95 x g and resuspension in 1 ml neurobasal medium, neurons were counted and seeded either on poly-L-lysine coated coverslips or mixed with hydrogel to be used in 3D cultures. Neurons were cultured under standard growth conditions at 37 °C and 5% CO<sub>2</sub> in neurobasal medium containing 2 mM GlutaMAX and 2% (v/v) B27 supplement. 50% of the medium was exchanged every week.

Table 5: Materials used for neuronal isolation

Material	Product number, manufacturer
Minimum essential medium	21090055; Thermo Fisher Scientific, Waltham, MA, USA
Neurobasal medium	21103049, Thermo Fisher Scientific
B27 supplement	17504044; Thermo Fisher Scientific
GlutaMAX	35050038; Thermo Fisher Scientific
Fetal bovine serum	10270106; Thermo Fisher Scientific
DNase I recombinant	04536282001; Merck, Darmstadt, Germany
Trypsin/EDTA in PBS	P10-023500; PAN-Biotech, Aidenbach, Germany

# Publications

## The GlyR Extracellular $\beta 8$ - $\beta 9$ Loop - A Functional Determinant of Agonist Potency

Dieter Janzen<sup>1†</sup>, Natascha Schaefer<sup>1†</sup>, Carolyn Delto<sup>2</sup>, Hermann Schindelin<sup>2</sup>,  
Carmen Villmann<sup>1</sup>

<sup>1</sup> Institute for Clinical Neurobiology, University of Würzburg,  
Würzburg, Germany

<sup>2</sup> Rudolf Virchow Center for Experimental Biomedicine,  
University of Würzburg, Würzburg, Germany

† Shared authorship

Published in  
**Frontiers in Molecular Neuroscience**

October 09, 2017

# The GlyR Extracellular $\beta 8$ – $\beta 9$ Loop – A Functional Determinant of Agonist Potency

Dieter Janzen<sup>1†</sup>, Natascha Schaefer<sup>1†</sup>, Carolyn Delto<sup>2</sup>, Hermann Schindelin<sup>2</sup> and Carmen Villmann<sup>1\*</sup>

<sup>1</sup> Institute for Clinical Neurobiology, University of Würzburg, Würzburg, Germany, <sup>2</sup> Rudolf Virchow Center for Experimental Biomedicine, University of Würzburg, Würzburg, Germany

## OPEN ACCESS

### Edited by:

Piotr Bregestovski,  
Aix-Marseille University, France

### Reviewed by:

Alexey Rossokhin,  
Research Center of Neurology, Russia  
Timothy Lynagh,  
University of Copenhagen, Denmark

### \*Correspondence:

Carmen Villmann  
villmann\_c@ukw.de

<sup>†</sup>These authors have contributed  
equally to this work.

**Received:** 05 August 2017

**Accepted:** 22 September 2017

**Published:** 09 October 2017

### Citation:

Janzen D, Schaefer N, Delto C,  
Schindelin H and Villmann C (2017)  
The GlyR Extracellular  $\beta 8$ – $\beta 9$  Loop –  
A Functional Determinant of Agonist  
Potency.  
*Front. Mol. Neurosci.* 10:322.  
doi: 10.3389/fnmol.2017.00322

Ligand-binding of Cys-loop receptors results in rearrangements of extracellular loop structures which are further translated into the tilting of membrane spanning helices, and finally opening of the ion channels. The cryo-EM structure of the homopentameric  $\alpha 1$  glycine receptor (GlyR) demonstrated an involvement of the extracellular  $\beta 8$ – $\beta 9$  loop in the transition from ligand-bound receptors to the open channel state. Recently, we identified a functional role of the  $\beta 8$ – $\beta 9$  loop in a novel startle disease mouse model *shaky*. The mutation of residue GlyR $\alpha 1$ <sup>Q177</sup> to lysine present in *shaky* mice resulted in reduced glycine potency, reduced synaptic expression, and a disrupted hydrogen network at the structural level around position GlyR $\alpha 1$ <sup>Q177</sup>. Here, we investigated the role of amino acid volume, side chain length, and charge at position Q177 to get deeper insights into the functional role of the  $\beta 8$ – $\beta 9$  loop. We used a combined approach of *in vitro* expression analysis, functional electrophysiological recordings, and GlyR modeling to describe the role of Q177 for GlyR ion channel function. GlyR $\alpha 1$ <sup>Q177</sup> variants do not disturb ion channel transport to the cellular surface of transfected cells, neither in homomeric nor in heteromeric GlyR configurations. The EC<sub>50</sub> values were increased for all GlyR $\alpha 1$ <sup>Q177</sup> variants in comparison to the wild type. The largest decrease in glycine potency was observed for the variant GlyR $\alpha 1$ <sup>Q177R</sup>. Potencies of the partial agonists  $\beta$ -alanine and taurine were also reduced. Our data are further supported by homology modeling. The GlyR $\alpha 1$ <sup>Q177R</sup> variant does not form hydrogen bonds with the surrounding network of residue Q177 similar to the substitution with a basic lysine present in the mouse mutant *shaky*. Among all investigated Q177 mutants, the neutral exchange of glutamine to asparagine as well as the introduction of the closely related amino acid glutamic acid preserve the hydrogen bond network. Introduction of amino acids with small side chains or larger volume resulted in a loss of their hydrogen bonds to neighboring residues. The  $\beta 8$ – $\beta 9$  loop is thus an important structural and functional determinant of the inhibitory GlyR.

**Keywords:** glycine receptor,  $\beta 8$ – $\beta 9$  loop, side chain length, side chain volume, ligand potency, gating, startle disease

**Abbreviations:** ECD, extracellular domain; GlyR, glycine receptor; TMs, transmembrane domains; WT, wild type.

## INTRODUCTION

Glycine receptors (GlyRs) are predominantly expressed in the adult brain stem and spinal cord, where they represent the major component in inhibitory neurotransmission. GlyRs localized in motoneuron membranes in the spinal cord get activated upon glycine release from neighboring inhibitory interneurons. The chloride ion influx leads to hyperpolarization of motoneurons, balancing excitation of the muscle contraction (Rajendra et al., 1997). Disturbances in glycinergic inhibition are associated with rare disorders such as startle disease (OMIM 149400, hyperekplexia, stiff baby syndrome), pain (Harvey et al., 2004), autism spectrum disorders (Harvey and Yee, 2013; Pilorge et al., 2015), and panic disorders (Deckert et al., 2017). Human startle disease is caused by mutations in the *GLRA1*, *GLRB*, and *SLC6A5* genes encoding GlyR subunits  $\alpha 1$  and  $\beta$  and the glycine transporter 2 (GlyT2).

Glycine receptors are described as homo- and heteropentameric ligand-gated ion channels of the superfamily of Cys-loop receptors (Lynch, 2004). For heteromeric GlyR complexes, five adjacent subunits are arranged around an ion channel pore composed of two  $\alpha$  and three  $\beta$  subunits or three  $\alpha$  and two  $\beta$  subunits (Grudzinska et al., 2005; Durisic et al., 2012; Yang et al., 2012). Each GlyR subunit consists of four TM helices, which are connected via intra- or extracellular loop structures. TM2 helices of all five subunits form the inner wall of the ion channel pore. The GlyR ECD is organized into an immunoglobulin-like structure and comprised of a short  $\alpha$ -helix and 10  $\beta$ -strands connected by loop structures (Du et al., 2015; Huang et al., 2015; Moraga-Cid et al., 2015). All Cys-loop receptors share the location of the agonist and antagonist-binding sites in the ECD formed by loops A, B, C from one subunit and loops D, E, F, G from an adjacent subunit (F loop in the following referred to as  $\beta 8$ - $\beta 9$  loop) (Brams et al., 2011). Ligands of the GlyR, starting with the highest affinity, are glycine,  $\beta$ -alanine, and taurine (Lynch, 2004). Antagonist of the GlyR is the alkaloid strychnine ( $C_{21}H_{22}N_2O_2$ ) (Breitinger and Becker, 1998). Upon ligand binding, Cys-loop receptors get activated and undergo a variety of conformational changes and transition processes leading to tilts and slight turns of the TM helices and thus opening of the ion pore (Althoff et al., 2014).

Several *in vitro* studies revealed distinct contributions of ECD loop structures for receptor function. It was shown that phenylalanine 159 localized in the loop B contributes to a cation- $\pi$  interaction with the incoming ligand, which is essential prior to channel opening (Pless et al., 2011). Moreover, loop C plays a role in transmitting the activation signal to the rest of the channel and exhibits a rearrangement upon ligand binding (Althoff et al., 2014). Mutations in the  $\beta 2$ - $\beta 3$  loop interfere with the maturation process of the protein and contribute to ligand specificity (Schaefer et al., 2015). Furthermore, loops  $\beta 2$ - $\beta 3$  and loop D determine ligand efficacy and play a role in ligand-induced desensitization or channel opening (Nys et al., 2013). The  $\beta 8$ - $\beta 9$  loop affects diazepam potentiation of the GABA<sub>A</sub>Rs (Padgett and Lummis, 2008). Loop  $\beta 8$ - $\beta 9$  has been suggested to play a major role in linking ligand binding to channel opening (Khatri and Weiss, 2010). Recently published structural models showed a

coupling of movements within the ECDs, including the  $\beta 8$ - $\beta 9$  loop, proceeding to the TM helices resulting in their tilting and enabling ion channel opening and closing (Hassaine et al., 2014; Du et al., 2015; Huang et al., 2015).

We recently published the first *in vivo* model carrying a mutation within the  $\beta 8$ - $\beta 9$  loop (Schaefer et al., 2017). A single amino acid exchange GlyR $\alpha 1^{Q177K}$  in the mouse mutant *shaky* resulted in premature death of homozygous animals. *In vivo*, synaptic GlyRs are decreased generating disturbed glycinergic signal transmission (Schaefer et al., 2017). At the structural level the hydrogen bond network around residue Q177 was disrupted.

Here, we investigated the role of side chain length, volume, and charge at amino acid position 177 in the  $\beta 8$ - $\beta 9$  loop of the GlyR $\alpha 1$ . Our aim was to understand the importance of  $\beta 8$ - $\beta 9$  structural changes with respect to GlyR potency and gating. Our hypothesis is that neutral exchanges and amino acids that preserve the hydrogen network only marginally affect GlyR function. Therefore, we introduced the conservative amino acid exchange GlyR $\alpha 1^{Q177N}$ . The original mutation in the mouse mutant *shaky* was GlyR $\alpha 1^{Q177K}$ . We further generated the mutation of glutamine to arginine which is similar to the mutation in *shaky*, but the side chain volume is increased. The series was completed by introduction of small residues, e.g., glycine and alanine, or very large residues such as tryptophan. All residues preserving the hydrogen bond network around residue glutamine 177 had almost no effect on GlyR function. In contrast, residues that were unable to preserve the hydrogen bond network generated functional ion channels with impaired glycine potency. Thus, our data provide further evidence of the GlyR  $\beta 8$ - $\beta 9$  loop as a structurally but also functionally important element facilitating inhibitory neurotransmission in the adult organism.

## MATERIALS AND METHODS

### Site-Directed Mutagenesis

PCR-mutagenesis was used to introduce the mutations (Q177A, Q177C, Q177D, Q177E, Q177G, Q177K, Q177N, Q177R, Q177W) at position 177 (numbering refers to mature protein). The murine GlyR $\alpha 1$  cDNA in the vector pRK7 was used as parental clone and refers to WT. Mutation-carrying amplicons were digested with Pst I and Bam HI and subcloned into the GlyR $\alpha 1$  WT sequence. All mutations were verified by sequencing (LGC Genomics, Berlin, Germany).

### Cell Lines

HEK293 human embryonic kidney cells CRL-1573, purchased from ATCC (Manassas, VA, United States) were grown in minimal essential medium (MEM) supplemented with 10% fetal calf serum, 200 mM GlutaMAX, 100 mM sodium pyruvate, and 50 U/ml penicillin/streptomycin (Thermo Fisher Scientific, Waltham, MA, United States) under standard growth conditions at 37°C and 5% CO<sub>2</sub>.

### Transfection

HEK293 cells were transiently transfected using a modified calcium phosphate precipitation method. A mixture of plasmid



DNA,  $\text{CaCl}_2$ , 0.1x TE buffer and 2x HBS (50 mM HEPES, 12 mM glucose, 10 mM KCl, 280 mM NaCl, 1.5 mM  $\text{Na}_2\text{HPO}_4$ ) was applied onto the cells. A GlyR $\alpha 1$  to GlyR $\beta$  ratio of 1:2 was used for co-expression. For GlyR $\alpha 1$ :GlyR $\beta$ :GFP co-expression, a ratio of 1:2:1 was transfected. The same amount of DNA was used for GlyR $\alpha 1$  WT and mutants. Media were exchanged after 6–24 h. Immunocytochemical stainings and electrophysiological experiments were always done 24 h after transfection, biotinylation experiments were performed 48 h after transfection.

### Cell Lysates

Whole cell lysates of transfected HEK293 cells transiently expressing the GlyR $\alpha 1$  variants and GlyR $\beta$  were acquired by using the CytoBuster Protein Extraction Reagent (Merck Millipore, Billerica, MA, United States) according to the manufacturer's protocol. Forty micrograms of protein were diluted in 2x SDS sample buffer and heated for 5 min at 95°C before use in SDS-PAGE and Western blot.

### Biotinylation of Cell Surface Proteins

For biotinylation, transfected HEK293 cells transiently expressing the GlyR $\alpha 1$  variants or co-expressing GlyR $\beta$  were used. Medium was aspirated 48 h after transfection and cells were washed once with ice-cold PBS. To label surface proteins, cells were incubated with 1 mg/ml EZ-Link Sulfo-NHS-LC-Biotin (sulfo-succinimidyl-6-[biotin-amido]hexanoate) (Thermo Fisher Scientific, Waltham, MA, United States) for 30 min at 4°C. Cells were washed twice with ice-cold PBS, once with quenching buffer (192 mM glycine, 25 mM TRIS, in PBS pH 8.0) and incubated with quenching buffer for 10 min at 4°C. Cells were scraped into ice-cold PBS, centrifuged for 1 min at  $1000 \times g$ , 4°C, and lysed with 1% Triton X-100, 2 mM EDTA, 0.1 mM PMSE, and 10 mg/ml protease inhibitor (Roche, Basel, Switzerland) in TBS pH 8.0. The lysate was centrifuged again for 1 min at  $17000 \times g$ , 4°C. The supernatant (whole cell fraction, WC) was incubated with 50  $\mu\text{l}$  of streptavidin agarose beads (Thermo Fisher Scientific, Waltham, MA, United States) using an overhead shaker for 2 h at 4°C. The supernatant (intracellular protein fraction) was removed and beads (surface protein fraction, SF) were washed three times with TBS buffer. The 60  $\mu\text{l}$  2x SDS sample buffer was added and the samples were heated 5 min at 95°C before use in SDS-PAGE and Western blot. Before gel loading, the protein amounts of the WC fraction were determined and 40  $\mu\text{g}$  of protein loaded to each lane of the gel. For SF samples, the same volume (30  $\mu\text{l}$ ) was loaded.

### SDS-PAGE and Western Blotting

For protein separation, 11% PAM (polyacrylamide) gels were used. Gels were run at 150 V for 90 min. Proteins were transferred to nitrocellulose (GE Healthcare, Freiburg, Germany) using a wet blot transfer system (transfer buffer: 25 mM TRIS, 192 mM glycine, 10% ethanol) (Bio-Rad, Hercules, CA, United States). For GlyR protein transfer, 2 h at 200 mA were used. For larger proteins, e.g., cadherin, overnight blotting at 100 mA was performed. Membranes were blocked for 1 h with 5% BSA in TBS-T (TBS with 1% Tween 20). Primary antibodies were

incubated overnight at 4°C. Proteins were detected with the pan- $\alpha$  antibody for GlyRs (mAb4a, Synaptic Systems, Göttingen, Germany, Cat. No. 146 011, 1:500) and pan-cadherin (Cell Signaling Technology, Danvers, MA, United States, Cat. No 4068, 1:1500) served as loading control. Signals were detected using the SuperSignal West (Thermo Fisher Scientific, Waltham, MA, United States).

### Immunocytochemical Staining

To stain GlyR surface receptors, GlyR $\alpha 1$  variants, and pDsRed-Monomer-Mem [Takara Bio (formerly Clontech), Mountain View, CA, United States] were co-transfected into HEK293 cells. All steps were performed at room temperature. After fixation for 20 min with 50  $\mu\text{l}$  4% paraformaldehyde, 4% sucrose solution, cells were washed three times with PBS and blocked for 30 min with 5% (v/v) goat serum in PBS. Afterward, cells were incubated for 1 h with the GlyR $\alpha 1$ -specific primary antibody mAb2b (1:500 in blocking solution; epitope amino acids 1–10 of mature GlyR $\alpha 1$ ; Synaptic Systems, Göttingen, Germany). Cells were washed three times with PBS and incubated for 45 min with the secondary Alexa488-coupled goat-anti-mouse antibody (1:500 in blocking solution; Dianova, Hamburg, Germany). Then, cells were washed three times with PBS, incubated for 5 min with DAPI (1:5000 in PBS; Thermo Fisher Scientific, Waltham, MA, United States) and mounted on glass slides with Mowiol 4-88 (Carl Roth, Karlsruhe, Germany). Imaging was performed using an Olympus IX-81 inverted fluorescence microscope (Olympus, Tokyo, Japan).

### Confocal Microscopy, Image Acquisition, and Analysis

Images were acquired using an inverted Olympus IX81 microscope equipped with an Olympus FV1000 confocal laser scanning system, a FVD10 SPD spectral detector and diode lasers of 495 nm (Alexa488) and 550 nm (Cy3) (Olympus, Tokyo, Japan). All images shown were acquired with an Olympus UPLSAPO 60x (oil, numerical aperture: 1.35) objective. The images were further developed and organized by Adobe Photoshop (Adobe, San Jose, CA, United States) or ImageJ (1.51)/Fiji<sup>1</sup>.

### Electrophysiology

The patch clamp technique was used to measure current amplitudes (I) of transfected HEK293 cells. Currents were amplified using an EPC-9 amplifier and the software Patchmaster (HEKA, Lambrecht, Germany). Cells were patched 24 h after transfection in a whole-cell configuration mode. To measure glycine-evoked chloride currents, 1 mM or 100  $\mu\text{M}$  glycine were applied. For  $\text{EC}_{50}$  measurements, glycine,  $\beta$ -alanine and taurine concentrations ranging from 1–3000  $\mu\text{M}$  (glycine) or 3–10000  $\mu\text{M}$  ( $\beta$ -alanine and taurine) were applied. All agonist and antagonists were applied using an Octaflo II system (ALA Scientific Instruments, Farmingdale, NY, United States). The extracellular buffer consisted of (in mM): 137 NaCl, 5.4 KCl, 1.8  $\text{CaCl}_2$ , 1  $\text{MgCl}_2$ , 5 HEPES, pH adjusted to 7.4 with NaOH. The

<sup>1</sup><https://imagej.net/ImageJ>

intracellular buffer contained (in mM): 120 CsCl, 20 N(Et)<sub>4</sub>Cl, 1 CaCl<sub>2</sub>, 2 MgCl<sub>2</sub>, 11 EGTA, 10 HEPES, pH adjusted to 7.2 with CsOH. Recording pipettes with an open resistance of 4–6 M $\Omega$  were manufactured from borosilicate capillaries using a P97 horizontal puller (Sutter Instrument, Novato, CA, United States). Cells were held at –60 mV and fast capacitances were in range of 11–13 pF. All experiments were performed at room temperature.

### Statistical Analysis

Data analysis of Western blots: The image quantification was performed using ImageJ (1.51)/Fiji<sup>2</sup>. The data were analyzed using Student's *t*-test (analysis of variance) and values below \**p* < 0.05 were considered significant, \*\**p* < 0.01, \*\*\**p* < 0.001. The values are displayed as means  $\pm$  standard error of the mean ( $\pm$ SEM) or as otherwise noted. The graphs were generated using Origin 9.4 software (OriginLab, Northampton, MA, United States).

For the analysis of electrophysiological data, a non-linear algorithm (Origin, OriginLab, Northampton, MA, United States) was used to construct concentration-response curves from peak current amplitudes obtained with eight appropriately spaced concentrations in the range of 1–3000  $\mu$ M glycine or 3–10000  $\mu$ M  $\beta$ -alanine, and taurine. The following Hill equation was used:  $I = I_{max} * c^{n_{Hill}} / (c^{n_{Hill}} + EC_{50}^{n_{Hill}})$ . *I* refers to the current amplitude at the given agonist concentration *c*, *I*<sub>max</sub> is the current amplitude at a saturating agonist, *EC*<sub>50</sub> refers to the agonist concentration evoking half-maximal current responses and *n*<sub>Hill</sub> is the Hill coefficient.

Images were processed with ImageJ (1.51)/Fiji<sup>2</sup> (Schindelin et al., 2012, 2015; Schneider et al., 2012) and Adobe Photoshop (Adobe, San Jose, CA, United States).

### Computational Methods

The effect of different mutations was predicted based on the recent structure of the human homopentameric GlyR $\alpha 3$  in complex with AM-3607 and glycine (Huang et al., 2017). Mutations were introduced *in silico* in the structure and the side chains were positioned in preferred rotamer conformations while minimizing steric overlaps as well as optimizing hydrogen-bonding capabilities using the software Coot (Emsley et al., 2010). Images were made using The PyMOL Molecular Graphics System, Version 1.8 Schrödinger, LLC.

For the alignment the sequences of human GlyR $\alpha 1$ , murine GlyR $\alpha 1/\alpha 2/\alpha 3/\beta$ , and GABA<sub>A</sub>  $\alpha 1/\gamma 2$  were aligned with Clustal Omega using the default settings<sup>3</sup> (Sievers et al., 2011).

## RESULTS

Our current understanding of GlyR ion channel opening and closing suggests concerted movements within the ECD (loops  $\beta 9$ – $\beta 10$ ,  $\beta 1$ – $\beta 2$ , and  $\beta 6$ – $\beta 7$ ) upon ligand-binding that are transmitted to elements of the ECD-TMD interface ( $\beta 10$ -pre-M1,

<sup>2</sup><https://imagej.net/ImageJ>

<sup>3</sup><http://www.ebi.ac.uk/Tools/msa/clustalo/>

the M2-3 loop) (Du et al., 2015). The  $\beta 8$ – $\beta 9$  loop is part of the ligand-binding site by its localization underneath the ligand-binding pocket (Brejc et al., 2001; Hansen et al., 2005). Recently, we found in a novel startle disease mouse model that a  $\beta 8$ – $\beta 9$  loop alteration disrupts GlyR ligand-binding site stability and ion channel gating (Schaefer et al., 2017).

Here, we investigated the role of side chain volume and charge at position Q177 within the  $\beta 8$ – $\beta 9$  loop for GlyR expression, agonist potency and structural consequences within the hydrogen bond network of the GlyR ECD.

### GlyR $\alpha 1$ Amino Acid Substitutions at Position Glutamine 177 in the $\beta 8$ – $\beta 9$ Loop

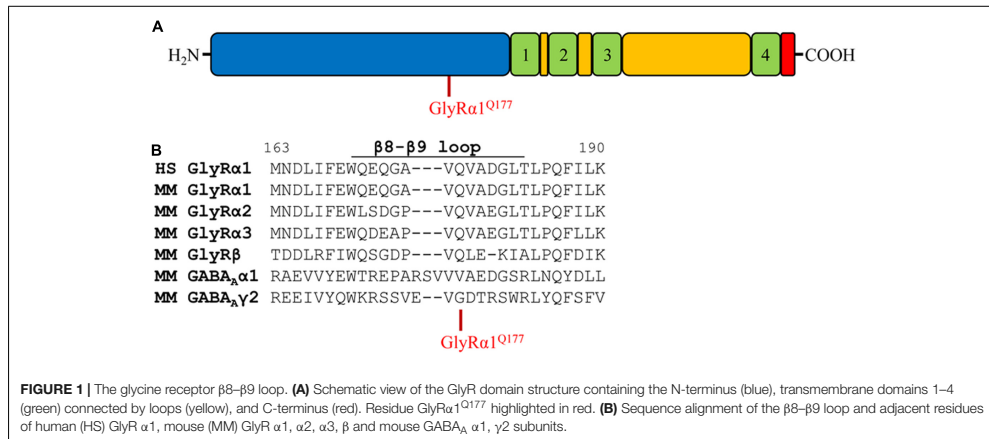
Glycine receptors share a large organized N-terminal domain (ECD) with other Cys-loop receptors. The ECD consists of an  $\alpha$ -helix, followed by 10  $\beta$ -strands connected by loop structures important for transmitting conformational changes upon ligand-binding. Residue 177 is localized in the  $\beta 8$ – $\beta 9$  loop and occupied by a glutamine in all murine GlyR $\alpha$  subunits, GlyR $\beta$  as well as human GlyR $\alpha 1$  (Figures 1A,B). The closely related GABA<sub>A</sub> receptor subunits  $\alpha 1$  and  $\gamma 2$  carry a valine ( $\alpha 1$ ) or a glycine ( $\gamma 2$ ) at the corresponding residue in the  $\beta 8$ – $\beta 9$  loop (Figure 1B). Mutations within GlyR subunits are associated with human hyperekplexia (Startle disease). The amino acid exchange of Q177 into a lysine resulted in severe startle disease in the mouse mutant *shaky* (Schaefer et al., 2017).

Apart from the GlyR $\alpha 1$ <sup>Q177K</sup> mutation in the mouse mutant *shaky*, the following amino acids were introduced at position 177: arginine (GlyR $\alpha 1$ <sup>Q177R</sup>) carrying a positively charged side chain similar to lysine in the *shaky* mutant; asparagine (GlyR $\alpha 1$ <sup>Q177N</sup>) with a hydrophilic side chain and similar to the original glutamine; aspartate and glutamate (GlyR $\alpha 1$ <sup>Q177D</sup>, GlyR $\alpha 1$ <sup>Q177E</sup>) both negatively charged; glycine (GlyR $\alpha 1$ <sup>Q177G</sup>) a neutral and small amino acid (present in GABA receptor  $\gamma 2$ ); alanine (GlyR $\alpha 1$ <sup>Q177A</sup>) with a small hydrophobic side chain; cysteine (GlyR $\alpha 1$ <sup>Q177C</sup>) with a thiol side chain; and tryptophan (GlyR $\alpha 1$ <sup>Q177W</sup>) carrying a sterically demanding side chain.

### $\beta 8$ – $\beta 9$ Loop Alterations with Positive Charged Side Chains at Position Q177 Reduce Surface Expression *In Vitro*

Glycine receptor mutants associated with startle disease affect either GlyR expression or GlyR function. Mutation of GlyR $\alpha 1$ <sup>Q177K</sup> resulted in reduced  $\alpha 1$  expression *in vitro* [33  $\pm$  5% of wild-type  $\alpha 1\beta$  (Schaefer et al., 2017)].

Analysis of crude protein lysates (Figures 2A,B) showed protein expression of all GlyR $\alpha 1$ <sup>Q177</sup> variants with no overall differences whether co-expressed with GlyR $\beta$  or when expressed alone. In addition, cell stainings for surface expression also revealed no obvious differences between GlyR $\alpha 1$  WT and GlyR $\alpha 1$ <sup>Q177</sup> variants (Figure 2C). GAP-43 expressed as a fusion protein with dsRed encoded on a co-transfected plasmid was used as membrane marker and for control of transfection efficiency. All GlyR $\alpha 1$ <sup>Q177</sup> variants exhibited colocalization with GAP-43 and thus cellular surface expression.



Protein quantification from Western blots after pull-down of biotinylated surface proteins by streptavidin-beads concomitantly demonstrated no significant differences in whole cell (WC) expression for GlyRa1<sup>Q177</sup> variants (Figures 3A upper panel, C and Table 1) or GlyRa1<sup>Q177</sup> variants coexpressed with GlyR $\beta$  subunit (Figures 3B upper panel, D and Table 1). The biotinylation method also allows a direct comparison between WC and surface protein fraction (SF) (Figures 3A,B lower panel and Table 1). Note, in the surface fractions of variants GlyRa1 enhanced degradation is visible but also for WT receptors. Only the upper band was used for calculation of the surface protein amount. Degradation might result from maturation deficits, showing that GlyRa1<sup>Q177</sup> variants seem to get stuck on their way to the cell surface, most probably in the ER compartment as shown previously for other recessive GlyRa1 variants (Schaefer et al., 2015). However, significant differences of SF protein level were observed for some GlyRa1<sup>Q177</sup> variants without or with co-expression with GlyR $\beta$  (Figures 3C,D). The GlyR expression of the Q177 variants was normalized to expression of pan-cadherin in the same sample serving as a membrane marker control protein. The resulting relative expression of GlyRa1WT was set to 1 (corresponding to 100%) and the relative expression of the GlyRa1 variants calculated accordingly (Figures 3C,D lower panels and Table 1).

In single expression studies, the SF protein level for GlyRa1<sup>Q177A</sup> (61 ± 6%), GlyRa1<sup>Q177C</sup> (16 ± 8%), GlyRa1<sup>Q177D</sup> (52 ± 14%), GlyRa1<sup>Q177K</sup> (12 ± 2%), GlyRa1<sup>Q177R</sup> (37 ± 8%), and GlyRa1<sup>Q177W</sup> (30 ± 15%) were significantly reduced compared to  $\alpha 1$ WT (Figure 3C and Table 1). Variants GlyRa1<sup>Q177E</sup>, GlyRa1<sup>Q177G</sup>, GlyRa1<sup>Q177N</sup> exhibited surface expression indistinguishable from GlyRa1WT (Table 1).

In co-expressions with GlyR $\beta$ , the surface expression levels were lower compared to single expressions. The GlyR complex consists of two  $\alpha$  and three  $\beta$  subunits (Grudzinska et al., 2005) which coassemble within the endoplasmic reticulum.

We coexpressed  $\alpha 1$  and  $\beta$  in a 1:2 ratio. The low amount of the  $\beta$  subunit during transfection was probably the reason for the lower expression of GlyRa1 variants at the cell surface in  $\alpha 1\beta$  co-expressions (Figures 3C,D).

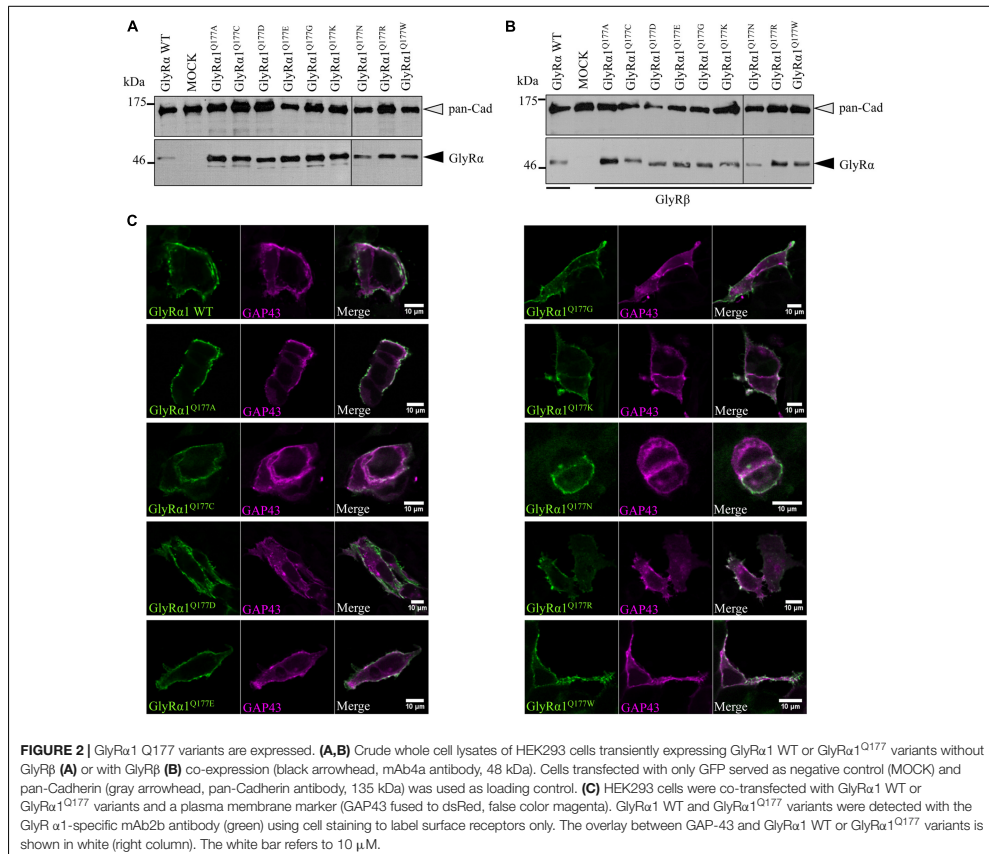
Surface fraction protein level for co-expression with GlyR $\beta$  demonstrated significant changes: GlyRa1<sup>Q177C</sup> (13 ± 6%), GlyRa1<sup>Q177K</sup> (9 ± 1%), and GlyRa1<sup>Q177W</sup> (13 ± 3%) (Figure 3D and Table 1). Interestingly, the conservative exchange of an asparagine instead of the GlyRa1 WT glutamine had no impact on whole cell and surface expression. The expression of variant GlyRa1<sup>Q177E</sup> was also similar to GlyRa1 WT and also did not lead to significant differences in GlyR expression level at the cell surface.

### $\beta 8$ - $\beta 9$ Loop Variants Reduce Potency of the Agonist Glycine

Changes in the integrity of the  $\beta 8$ - $\beta 9$  loop have been determined to reduce glycine potency and modify the function as a gating element of this receptor class (Schaefer et al., 2017).

Glycine receptor physiology of the mutant receptors coexpressed with the GlyR $\beta$  subunit was determined by electrophysiological measurements using whole-cell recordings following transient expression in HEK293 cells. As a preliminary screen, absolute currents values (I) were determined at saturating concentrations of glycine (1 mM) and at a glycine concentration around the EC<sub>50</sub> value of the GlyR $\alpha 1\beta$  WT (100  $\mu$ M). No significant differences in  $I_{max}$  values for all GlyRa1<sup>Q177</sup> $\beta$  variants in comparison to GlyR $\alpha 1\beta$  WT were observed (Figure 4A) but significant reductions in glycine-induced currents at 100  $\mu$ M glycine (Figure 4B and Table 2).

These measurements were followed by a determination of a dose-response curve using eight different glycine concentrations (1, 3, 10, 30, 100, 300, 1000, and 3000  $\mu$ M) to determine changes in glycine potency for GlyRa1<sup>Q177</sup> $\beta$  variants. An EC<sub>50</sub> of 58 ± 4  $\mu$ M for GlyR $\alpha 1\beta$  WT was estimated in transfected

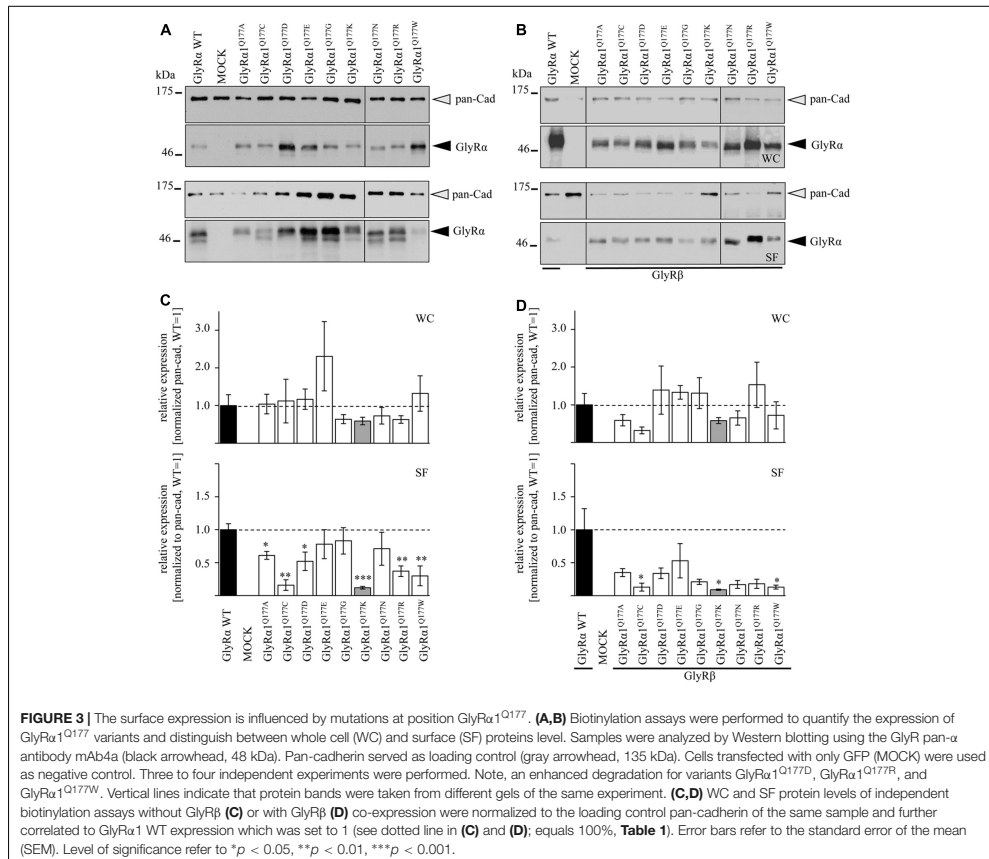


HEK293 cells (ratio of 1:2  $\alpha$ 1: $\beta$ , **Figure 4C**). The glycine EC<sub>50</sub> values for GlyR $\alpha$ 1<sup>Q177</sup> $\beta$  variants differed in a range between a two-fold (GlyR $\alpha$ 1<sup>Q177N</sup> $\beta$  or GlyR $\alpha$ 1<sup>Q177C</sup> $\beta$ ) up to a six-fold increase (GlyR $\alpha$ 1<sup>Q177K</sup> $\beta$ ) (**Figures 4C–E** and **Table 2**). Variants were grouped according to structural characteristics. Group one is comprised of GlyR $\alpha$ 1<sup>Q177K</sup> $\beta$  and GlyR $\alpha$ 1<sup>Q177R</sup> $\beta$ , both positive amino acids which showed a large increase in EC<sub>50</sub> when compared to GlyR $\alpha$ 1 $\beta$  WT (GlyR $\alpha$ 1<sup>Q177K</sup> $\beta$  312  $\pm$  7  $\mu$ M, a 5.3-fold increase and GlyR $\alpha$ 1<sup>Q177R</sup> $\beta$  231  $\pm$  4  $\mu$ M, a 4-fold increase) (**Figure 4C**). The second group consists of the aspartate mutant (negatively charged), the glutamic acid mutant (negatively charged) and the conservative asparagine (polar). The observed increase in EC<sub>50</sub>, was minor for GlyR $\alpha$ 1<sup>Q177D</sup> $\beta$  137  $\pm$  4  $\mu$ M, a 2.3-fold increase; GlyR $\alpha$ 1<sup>Q177E</sup> $\beta$  109  $\pm$  7  $\mu$ M, a 1.8-fold increase; GlyR $\alpha$ 1<sup>Q177N</sup> $\beta$  96  $\pm$  1  $\mu$ M, a 1.6-fold increase) (**Figure 4D**). The third group includes GlyR $\alpha$ 1<sup>Q177A</sup> $\beta$ , GlyR $\alpha$ 1<sup>Q177C</sup> $\beta$ , GlyR $\alpha$ 1<sup>Q177G</sup> $\beta$ , GlyR $\alpha$ 1<sup>Q177W</sup> $\beta$  which all showed

increased EC<sub>50</sub> values: GlyR $\alpha$ 1<sup>Q177A</sup> $\beta$  208  $\pm$  22  $\mu$ M, a 3.6-fold increase; GlyR $\alpha$ 1<sup>Q177G</sup> $\beta$  262  $\pm$  13  $\mu$ M, a 4.5-fold increase and GlyR $\alpha$ 1<sup>Q177W</sup> $\beta$  130  $\pm$  12  $\mu$ M, a 2.2-fold increase) (**Figure 4E**). Interestingly, the substituted cysteine with an overall size close to glutamine but rather different to the small residues glycine and alanine or the bulky tryptophan exhibited only a slight shift in glycine potency (88  $\pm$  3  $\mu$ M, a 1.5-fold increase).

To further discriminate between agonist potency and gating defects, we used the GlyR $\alpha$ 1 asparagine mutant (GlyR $\alpha$ 1<sup>Q177N</sup>), which is closely related to the original glutamine and the arginine mutant (GlyR $\alpha$ 1<sup>Q177R</sup>) similar to the lysine mutants in the mouse mutant *shaky*. These mutants were analyzed upon application of the partial GlyR agonists  $\beta$ -alanine and taurine.

A concentration of 100  $\mu$ M for both partial agonists generated non-significant changes in agonist-induced inward currents with 1.3  $\pm$  0.3 nA for GlyR $\alpha$ 1 $\beta$  WT, 0.87  $\pm$  0.4 nA for GlyR $\alpha$ 1<sup>Q177N</sup> $\beta$ ,



and  $0.2 \pm 0.07$  nA for GlyR $\alpha 1^{Q177R}\beta$  at 100  $\mu$ M  $\beta$ -alanine and  $0.13 \pm 0.06$  nA for GlyR $\alpha 1\beta$  WT,  $0.02 \pm 0.001$  nA for GlyR $\alpha 1^{Q177N}\beta$ , and  $0 \pm 0$  nA for GlyR $\alpha 1^{Q177R}\beta$  at 100  $\mu$ M taurine (**Figures 5A,C**).

The application of 10 mM  $\beta$ -alanine did not result in significant differences between GlyR $\alpha 1\beta$  WT ( $5.3 \pm 2$  nA,  $n = 3$ ) and GlyR $\alpha 1^{Q177N}\beta$  ( $4.1 \pm 0.8$  nA,  $n = 3$ ) or GlyR $\alpha 1^{Q177R}\beta$  ( $4.5 \pm 0.9$  nA,  $n = 3$ ) (**Figure 5A**). In contrast, taurine application at 10 mM significantly reduced GlyR efficacy with GlyR $\alpha 1\beta$  WT  $5.7 \pm 0.4$  nA,  $n = 3$ ; GlyR $\alpha 1^{Q177N}\beta$   $2.7 \pm 0.5$  nA,  $n = 3$ ; and GlyR $\alpha 1^{Q177R}\beta$   $3.1 \pm 0.4$  nA,  $n = 3$  (**Figure 5C**). Although, the GlyR $\alpha 1\beta$  WT reached saturation at 10 mM taurine, it is obvious that the mutants probably not completely reached saturation.

Hence, we further examined  $\beta$ -alanine potency in comparison to GlyR $\alpha 1$  WT, which exhibited a slight increase of the EC<sub>50</sub> for  $\beta$ -alanine (GlyR $\alpha 1\beta$  WT  $157 \pm 7$   $\mu$ M; GlyR $\alpha 1^{Q177N}\beta$   $203 \pm 17$   $\mu$ M a 1.3-fold increase; GlyR $\alpha 1^{Q177R}\beta$   $359 \pm 19$   $\mu$ M,

a 2.3-fold increase) (**Figure 5B** and **Table 2**). For taurine potency, the EC<sub>50</sub> for the arginine and asparagine GlyR $\alpha 1$  variants showed the following results in comparison to GlyR $\alpha 1\beta$  WT (GlyR $\alpha 1\beta$  WT  $593 \pm 18$   $\mu$ M; GlyR $\alpha 1^{Q177N}\beta$   $1254 \pm 72$   $\mu$ M, a 2.1-fold increase; and GlyR $\alpha 1^{Q177R}\beta$   $2982 \pm 183$   $\mu$ M, a 5-fold increase) (**Figure 5D** and **Table 2**).

In conclusion, the physiological data point to a mixed phenotype affecting agonist/partial agonist potency and most probably partial agonist efficacy at least for taurine.

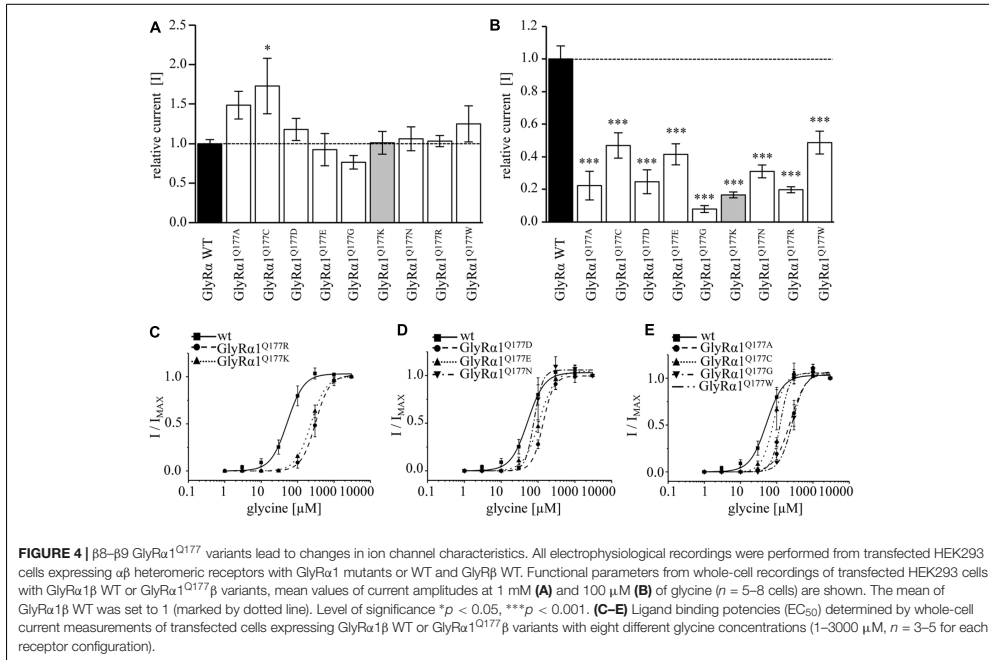
### Structural Modeling Revealed Changes in the Hydrogen Bonding Pattern of $\beta 8$ - $\beta 9$ Mutants

Earlier studies reported the importance of the hydrogen bond network within the GlyR ECD or the closely related GABA<sub>A</sub> receptor for stabilization of the structure (Padgett and Lummis,

**TABLE 1** | Protein expression profile of GlyR $\alpha 1$ <sup>Q177</sup> variants.

Construct	Number (n)	Whole cell rel. expression normalized to pan-cad [%]	Significance * <i>p</i> < 0.05, ** <i>p</i> < 0.01, *** <i>p</i> < 0.001	Whole cell rel. expression normalized to pan-cad [%]	Number (n)	Surface rel. expression normalized to pan-cad	Significance * <i>p</i> < 0.05, ** <i>p</i> < 0.01, *** <i>p</i> < 0.001	Surface rel. expression normalized to pan-cad [%]
<b>Single expression</b>								
<b>mAb4a signal (N-domain)</b>								
GlyR $\alpha 1$ WT	4	0.78 ± 0.23		100 ± 30	4	3.02 ± 0.28		100 ± 9
GlyR $\alpha 1$ <sup>Q177A</sup>	4	0.81 ± 0.2	n.s.	102 ± 25	3	1.85 ± 0.19	*	61 ± 6
GlyR $\alpha 1$ <sup>Q177C</sup>	4	0.87 ± 0.45	n.s.	112 ± 58	3	0.47 ± 0.24	**	16 ± 8
GlyR $\alpha 1$ <sup>Q177D</sup>	4	0.91 ± 0.21	n.s.	116 ± 27	4	1.57 ± 0.43	*	52 ± 14
GlyR $\alpha 1$ <sup>Q177E</sup>	4	1.8 ± 0.72	n.s.	230 ± 92	3	2.35 ± 0.65	n.s.	78 ± 22
GlyR $\alpha 1$ <sup>Q177G</sup>	4	0.5 ± 0.09	n.s.	64 ± 12	3	2.51 ± 0.61	n.s.	84 ± 20
<b>GlyR<math>\alpha 1</math><sup>Q177K</sup></b>	4	0.46 ± 0.08	n.s.	59 ± 10	3	0.36 ± 0.06	***	12 ± 2
GlyR $\alpha 1$ <sup>Q177N</sup>	4	0.57 ± 0.17	n.s.	73 ± 22	3	2.13 ± 0.76	n.s.	71 ± 25
GlyR $\alpha 1$ <sup>Q177R</sup>	4	0.49 ± 0.08	n.s.	63 ± 10	4	1.12 ± 0.23	**	37 ± 8
GlyR $\alpha 1$ <sup>Q177W</sup>	4	1.03 ± 0.37	n.s.	132 ± 46	3	0.91 ± 0.44	**	30 ± 15
<b>Co-expression with GlyRP WT</b>								
<b>mAb4a signal (N-domain)</b>								
GlyR $\alpha 1$ WT	5	0.97 ± 0.29		100 ± 30	3	3.36 ± 1.09		100 ± 33
GlyR $\alpha 1$ <sup>Q177A</sup>	4	0.57 ± 0.15	n.s.	59 ± 15	3	1.17 ± 0.19	n.s.	35 ± 6
GlyR $\alpha 1$ <sup>Q177C</sup>	4	0.31 ± 0.09	n.s.	31 ± 9	3	0.44 ± 0.2	*	13 ± 6
GlyR $\alpha 1$ <sup>Q177D</sup>	4	1.35 ± 0.62	n.s.	139 ± 64	3	1.13 ± 0.27	n.s.	33 ± 8
GlyR $\alpha 1$ <sup>Q177E</sup>	4	1.29 ± 0.17	n.s.	133 ± 17	3	1.79 ± 0.88	n.s.	54 ± 27
GlyR $\alpha 1$ <sup>Q177G</sup>	4	1.27 ± 0.4	n.s.	130 ± 41	3	0.71 ± 0.13	n.s.	22 ± 4
<b>GlyR<math>\alpha 1</math><sup>Q177K</sup></b>	4	0.56 ± 0.08	n.s.	56 ± 8	3	0.30 ± 0.03	*	9 ± 1
GlyR $\alpha 1$ <sup>Q177N</sup>	4	0.63 ± 0.18	n.s.	65 ± 18	3	0.56 ± 0.21	n.s.	17 ± 6
GlyR $\alpha 1$ <sup>Q177R</sup>	4	1.48 ± 0.58	n.s.	152 ± 60	3	0.59 ± 0.23	n.s.	18 ± 7
GlyR $\alpha 1$ <sup>Q177W</sup>	4	0.7 ± 0.35	n.s.	72 ± 36	3	0.44 ± 0.11	*	13 ± 3

To calculate the relative expression in percent (%), the WT expression was set to 100%. All other estimated relative expression values were calculated accordingly. n.s., non-significant.



2008; Yu et al., 2014). The mutation GlyR $\alpha 1^{Q177K}$  disrupts the hydrogen bond network around residue Q177 (Figures 6A,B). Similarly, the introduction of an arginine at position 177 resulted in lack of hydrogen bonds to neighboring residues such as N42, R65, and N203 (Figure 6C). Interestingly residues that marginally affect GlyR function, such as GlyR $\alpha 1^{Q177E}$  and GlyR $\alpha 1^{Q177N}$  were still able to form a hydrogen bond, arguing for minor structural changes to the GlyR structure (Figures 6D,E). Not in line with a direct correlation between a lack of the hydrogen bond network and large changes in glycine potency are the data on GlyR $\alpha 1^{Q177C}$ . This residue is predicted to lack the hydrogen bonds to R65 and N203 (data not shown), but exhibited only small changes in glycine potency. From its size, cysteine is similar to asparagine. One might therefore argue that size and side chain property underlie the observed effects on glycine potency.

The large side chain volume of GlyR $\alpha 1^{Q177W}$  is expected to completely disrupt the hydrogen bond network (Figure 6F). Similarly, this amino acid exchange resulted in an increased  $EC_{50}$  for the agonist glycine. The correct side chain volume of glutamine at position 177 seems to be critical since tryptophan, the bulkiest side chain, and glycine, the smallest residue, behaved similarly. Glycine most probably is too small and lacks side chain atoms which can engage in the formation of hydrogen bonds, while in the larger residues, the bulkier side chain is no longer able to interact with N42, R65, and N203 (Figure 6F).

## DISCUSSION

Signal transduction from ligand-binding into channel opening in Cys-loop receptors involves concerted conformational changes of defined structures of the ECD at both the principle (+) and the complementary (-) site of the intersubunit interface (Hilf and Dutzler, 2008; Hibbs and Gouaux, 2011; Du et al., 2015; Morales-Perez et al., 2016). The involvement of the  $\beta 8$ - $\beta 9$  loop in these conformational rearrangements was first described in the cryo-EM structure of the GlyR $\alpha 1$  subunit analyzing transitions between the closed receptor configuration and the open states (Du et al., 2015).

Previous studies on Cys-loop receptors determined a hydrogen bond network of the  $\beta 8$ - $\beta 9$  loop with residues close to the ligand binding site as important for transitions between different receptor states (Padgett and Lummis, 2008; Nys et al., 2013; Yu et al., 2014). Disruptions in structurally important GlyR elements may underlie disease pathology of startle disease (Bode and Lynch, 2014). Several mutations distributed all over the GlyR structure have been correlated to disease mechanisms (Chung et al., 2010).

Within the  $\beta 8$ - $\beta 9$  loop one human mutation was so far identified GlyR $\alpha 1^{W170S}$  (Al-Futaisi et al., 2012; Zhou et al., 2013). An RNA-editing variant P185L of the GlyR $\alpha 3 \beta 8$ - $\beta 9$  loop detected in patients with mesial temporal lobe epilepsy (TLE) has been described to increase glycine potency *in vitro* (Meier et al.,

TABLE 2 | Electrophysiological properties of GlyR $\alpha 1^{Q177}$  variants.

$\alpha 1$ construct co-expressed with GlyR $\beta$	Number of cells (n)	Mean $I_{gly}$ / 100 $\mu M$ [nA] $\pm$ SEM	Number of cells for EC <sub>50</sub> glycine	EC <sub>50</sub> glycine [ $\mu M$ $\pm$ SEM]	$n_H$ glycine	Number of cells for EC <sub>50</sub> $\beta$ -alanine	EC <sub>50</sub> $\beta$ -alanine [ $\mu M$ $\pm$ SEM]	$n_H$ $\beta$ -alanine	Number of cells for EC <sub>50</sub> taurine	EC <sub>50</sub> taurine [ $\mu M$ $\pm$ SEM]	$n_H$ taurine
GlyR $\alpha 1$ WT	30	3.8 $\pm$ 0.3	5	58 $\pm$ 4	1.9	3	157 $\pm$ 7	2.6	3	593 $\pm$ 18	2.3
GlyR $\alpha 1^{Q177A}$	6	0.8 $\pm$ 0.3***	4	208 $\pm$ 22	2.0		ND			ND	
GlyR $\alpha 1^{Q177C}$	8	1.8 $\pm$ 0.3***	3	88 $\pm$ 3	2.1		ND			ND	
GlyR $\alpha 1^{Q177D}$	6	0.9 $\pm$ 0.3***	5	137 $\pm$ 4	3.4		ND			ND	
GlyR $\alpha 1^{Q177E}$	5	1.6 $\pm$ 0.2**	4	109 $\pm$ 7	2.6		ND			ND	
GlyR $\alpha 1^{Q177G}$	5	0.3 $\pm$ 0.08***	3	262 $\pm$ 13	2.5		ND			ND	
<b>GlyR<math>\alpha 1^{Q177K}</math></b>	<b>5</b>	<b>0.6 <math>\pm</math> 0.07***</b>	<b>3</b>	<b>312 <math>\pm</math> 7</b>	<b>2.2</b>		<b>ND</b>			<b>ND</b>	
GlyR $\alpha 1^{Q177N}$	5	1.2 $\pm$ 0.2**	4	96 $\pm$ 1	3.0	3	203 $\pm$ 17	1.7	3	1254 $\pm$ 72	1.6
GlyR $\alpha 1^{Q177R}$	5	0.8 $\pm$ 0.07***	4	231 $\pm$ 4	2.0	3	359 $\pm$ 19	1.9	3	2382 $\pm$ 183	1.5
GlyR $\alpha 1^{Q177W}$	5	1.8 $\pm$ 0.3***	3	130 $\pm$ 12	3.7		ND			ND	

Significance values =  $p$ , \*\*\* $p$  < 0.001, n, number of cells recorded,  $n_H$  Hill coefficient, SEM, standard error of the mean; ND, not determined.

2005; Eichler et al., 2009). The murine GlyR $\alpha 1$  startle disease mutant *shaky* (Q177K) resulted in lethality of homozygous animals due to a complex functional pattern including reduced synaptic expression, decreased agonist potency and accelerated ion channel closure (Schaefer et al., 2017). Moreover, glutamine 177 is part of the hydrogen bond network important for ion channel function. Here, we investigated the side chain volume and charge of Q177 with regard to expression and ion channel functionality.

In startle disease, depending on the type of mutation either ion channel function (dominant trait) or expression and transport (recessive mutation) is disabled (Chung et al., 2010; Bode and Lynch, 2014). Although GlyR $\alpha 1^{Q177K}$  leads to decreased expression *in vitro*, there is still enough protein expressed to generate functional ion channels (Schaefer et al., 2017).

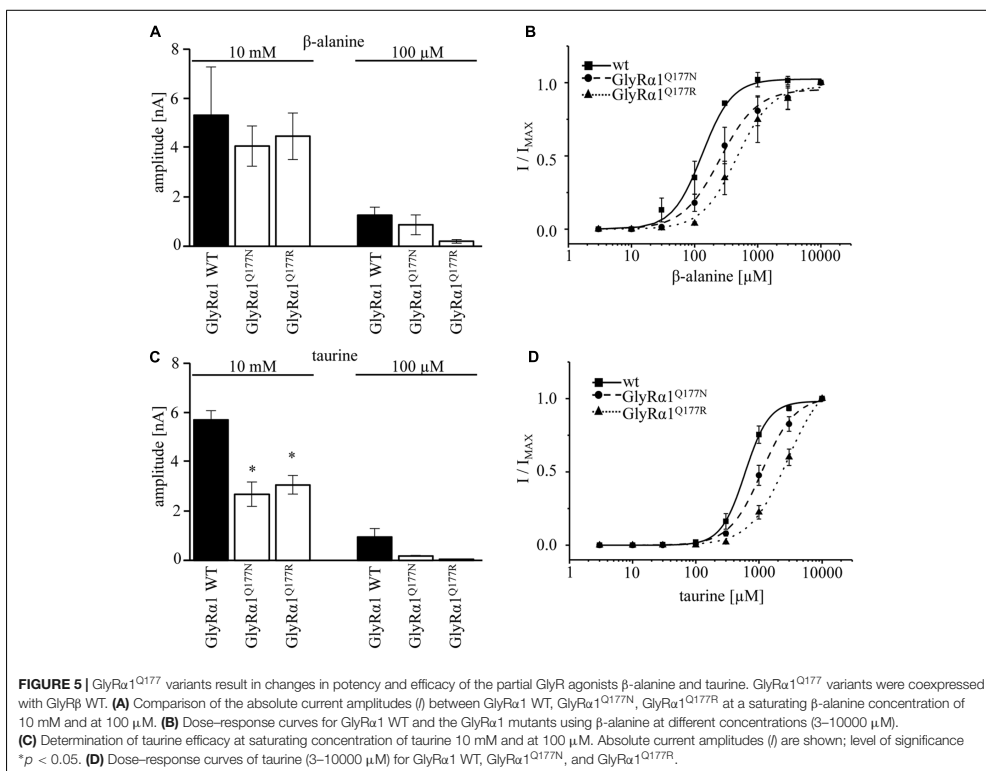
For all GlyR $\alpha 1^{Q177}$  variants, the overall expression levels were indistinguishable from  $\alpha 1$ WT. Using protein quantification analyses combined with discrimination between whole cell and surface protein, differences between GlyR $\alpha 1$  WT and the mutants were identified. In contrast to no significant differences in the whole cell protein amount of all GlyR $\alpha 1^{Q177}$  variants, surface expression levels differed between WT and mutants.

Similar to the *shaky* variant, GlyR $\alpha 1^{Q177K}$ , the mutant GlyR $\alpha 1^{Q177R}$  showed a decreased expression when expressed alone or in co-expression with GlyR $\beta$ . The conservative exchange of glutamine 177 to asparagine, however, did not result in a different expression pattern in comparison to GlyR $\alpha 1$  WT. Interestingly, the introduction of a negative charge, such as in GlyR $\alpha 1^{Q177E}$  which is a structurally similar amino acid residue to the original glutamine resulted in a similar expression pattern like GlyR $\alpha 1$  WT. The introduction of neutral amino acid residues either small (glycine, alanine, and cysteine) or bulky (tryptophan) resulted in reduced surface receptor levels, independent of the presence of the  $\beta$ -subunit.

A reduction of cell surface receptors argues for differences of maximal currents upon application of saturating glycine concentration. Earlier reports on recessive hyperekplexia mutants demonstrated that a reduction of cellular membrane expression revealed smaller  $I_{max}$  values in electrophysiological recordings (Villmann et al., 2009; Chung et al., 2010). The *shaky* mutant GlyR $\alpha 1^{Q177K}$ , however, did not result in changes at glycine-induced currents at saturating glycine concentrations although the surface expression was reduced *in vitro* (Schaefer et al., 2017). Here, at a saturating concentration of glycine, all GlyR $\alpha 1^{Q177}$  variants exhibited maximal current amplitudes almost indistinguishable from WT. The estimated reduction of cell surface expression for the GlyR $\alpha 1^{Q177}$  mutants is thus not sufficient to change the maximal current amplitudes in the HEK293 cell overexpression system.

Due to decreased glycinergic currents at lower glycine concentrations observed for all GlyR $\alpha 1^{Q177}$  mutants, a reduction of glycine potency was suggested. Glycine potency was differently affected in GlyR $\alpha 1$  variants. A lower glycine potency was exhibited by GlyR $\alpha 1^{Q177R}$ . The determined four-fold decrease of glycine potency was similar to the *shaky* mutation GlyR $\alpha 1^{Q177K}$  (Schaefer et al., 2017). Small changes were observed for the conservative exchange of glutamine to asparagine (1.6-fold) as





well as to the charged glutamate (1.8-fold). The presence of the smallest amino acids glycine and alanine at position 177 revealed higher  $EC_{50}$  values for the agonist glycine which were similar to the  $EC_{50}$  of the very bulky residue tryptophan.

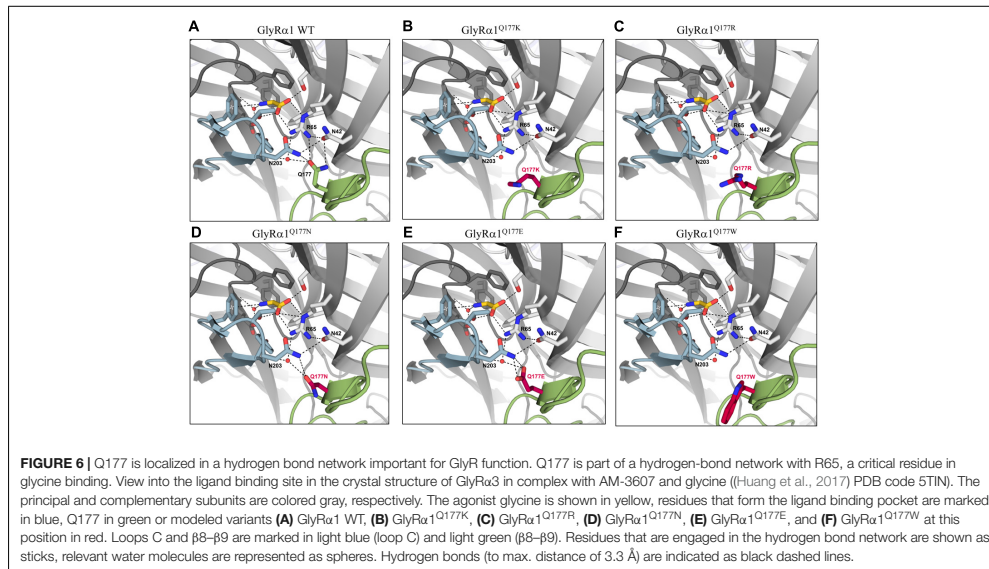
The  $\beta 8$ - $\beta 9$  loop is not directly involved in ligand binding but in structural transitions between agonist bound receptor and the open state of the ion channel (Althoff et al., 2014; Du et al., 2015). No changes in agonist/antagonist affinities have been observed in the *shaky* mouse carrying the GlyR $\alpha 1^{Q177K}$  mutation. Glycine and strychnine bound with the same efficiency to the mutated receptor compared to GlyR $\alpha 1$  WT (Schaefer et al., 2017). The observed glycine potency has been determined to correlate with changes in the hydrogen bond network around residue Q177.

In the variants GlyR $\alpha 1^{Q177K}$  or GlyR $\alpha 1^{Q177R}$  the hydrogen bond with residue R65 is disrupted. In the modeled GlyR $\alpha 1$  WT, the oxygen of the amide at the side chain of glutamine acts as the hydrogen bond acceptor. The side chains of lysine and arginine lack this oxygen, which in turn hinder GlyR $\alpha 1^{Q177K}$  or GlyR $\alpha 1^{Q177R}$  to form a hydrogen bond with R65. Furthermore, the side chains of lysine and arginine are longer compared to glutamine, arguing for steric effects that might be transferred

to conformational changes to the ligand-binding site and thus explain differences in glycine potency.

Asparagine is almost identical in structure to the original glutamine (Q177) in the  $\beta 8$ - $\beta 9$  loop with the side chain missing one methylene unit, so one would expect results similar to the GlyR $\alpha 1$  WT. The shorter side-chain of asparagine is predicted to result in a weaker hydrogen bond between GlyR $\alpha 1^{Q177N}$  and R65, as shown in the structural modeling, resulting in a different conformation of the ligand-binding site which probably destabilizes the glycine binding pocket.

While glutamine features an amide, in contrast, glutamic acid carries a carboxyl group. Aspartic acid also features a carboxyl group instead of an amide and misses a methylene unit compared to glutamine. A hydrogen bond between R65 and GlyR $\alpha 1^{Q177D}$  or GlyR $\alpha 1^{Q177E}$  should be possible with an oxygen of the carboxyl group acting as acceptor. However, the negative side chain charge may affect the strength of the hydrogen bond and also the interaction with other nearby structural elements, e.g., N42. Modeling of the putative position of the glutamate side chain showed an orientation toward the amide group of N203, to which it can form tight hydrogen bonds. In contrast, this repositioning



moves the side chain further away from R65 and thereby a second hydrogen bond is lost.

Although, the amino acids glycine and tryptophan differ the most in side chain volume, the determined glycine potency was similarly affected. Glycine has no side chain. Hence, no hydrogen bond between R65 and GlyR $\alpha 1$ <sup>Q177G</sup> is possible. Characterization of G160 variants, localized in loop B, revealed that replacing glycine with two other small amino acids alanine and serine results in a 6- to 10-fold decrease in glycine potency (Atak et al., 2015). These data indicate that even the small difference between glycine and alanine can have a big impact on the conformation of the ligand-binding pocket. In contrast, characterization of P250 variants, a residue located in the short intracellular TM1-2 loop, has shown that short side chains gave rise to WT-like channels (Breitinger et al., 2001). Hence, the observed effects depend on the origin of the amino acid at a determined position in the protein.

The introduction of a cysteine at position 177 is also predicted to result in disturbed hydrogen network formation which is in line with a slight rightward shift in glycine EC<sub>50</sub> values. Free cysteine residues share the ability for disulfide bridge formation. However, this is unlikely as C138-C152 and C198-C209 already form stable disulfide bridges in the GlyR (James et al., 2013). A disruption of those disulfide bridges would probably have stronger negative effects on ion channel function or even lead to non-functionality (Vogel et al., 2009). Sterically the effect of GlyR $\alpha 1$ <sup>Q177C</sup> is less detrimental which might explain the observed small effects on glycine potency. Tryptophan (W) is the largest amino acid and contains an aromatic indole ring. Because of the indole side chain, no hydrogen bond between

GlyR $\alpha 1$ <sup>Q177W</sup> and R65 is possible. The original glutamine 177 forms a hydrogen bond with R65, which is located in the glycine binding pocket. Mutation of R65 to lysine and alanine revealed a 200- and 1250-fold decrease in glycine EC<sub>50</sub>, demonstrating that R65 is an important residue for ligand binding (Grudzinska et al., 2005).

The analysis of partial agonist efficacy and potency implies changes in agonist efficacy at least for taurine and changes in partial agonist potencies. These data indicate that Q177 influences the formation of the agonist/partial agonist binding sites possibly by differences in hydrogen bond network formation. Moreover, taurine measurements verified that structural changes in the  $\beta 8$ - $\beta 9$  loop also affect GlyR gating similar to findings for the *shaky* mouse mutant (Schaefer et al., 2017). In summary, the number of contacts to the hydrogen bond network and a mutual stabilization of the conformation seems to be reduced.

Since, the first description of the large movements the  $\beta 8$ - $\beta 9$  loop undergoes upon transition from the agonist-bound GlyR structure to the open conformation in the cryo-EM structure of GlyR $\alpha 1$  (Du et al., 2015), similar observations have been explored in the  $\alpha 4\beta 2$  crystal structure of the nicotinic acetylcholine receptor (Morales-Perez et al., 2016). The  $\beta 8$ - $\beta 9$  loop is connected to loop C covering the binding pocket but also is located underneath the binding pocket, thus it indirectly participates in the binding pocket. Furthermore, it is involved in the coupling of conformational changes of the ECD following ligand binding to finally ion channel opening and closing. During GlyR ion channel opening, the C loop switches from open to closed and displaces the  $\beta 8$ - $\beta 9$  loop which concomitantly induces

rotation of the pre-M1 and M1 and finally movement of the M2 elements (Du et al., 2015). The analysis of the first mouse mutant carrying an amino acid transition in the  $\beta 8$ - $\beta 9$  loop further revealed the importance of this loop structure for GlyR function and survival. The mutant mouse showed no changes in agonist affinity but the ensuing signal transduction resulting in ion channel opening was almost completely abolished (Schaefer et al., 2017). We showed that all mutations at residue Q177 lack the potential to form hydrogen bonds with residue R65. Thus, the hydrogen bond to R65 is critical for the stabilization of the glycine-binding pocket, which is in agreement with the observed decrease in glycine potencies. A further impact on GlyR gating as suggested by the observed reduced efficacy of the partial agonist taurine is in line with the displacement  $\beta 8$ - $\beta 9$  undergoes during GlyR ion channel opening and closing and glycinergic signaling toward the pore forming unit (Du et al., 2015).

Moreover, the  $\beta 8$ - $\beta 9$  loop harbors a structural potential for allosteric modulation. Nys et al. (2016) argued that chlorpromazine bound to ELIC, a member of the Cys-loop receptor family, undergoes hydrophobic interaction with  $\beta 8$ - $\beta 9$  loop residues and is part of a multisite model for allosteric modulation in a continuous stretch from the top to the bottom of the receptor. A modulatory role of the  $\beta 8$ - $\beta 9$  loop has also been determined for GABA<sub>A</sub> receptors. Tricyclic oxazole-2,3-benzodiazepines bind to the interface between  $\alpha$  and  $\beta$  subunits to residues <sup>172</sup>REPAR<sup>176</sup> within the GABA<sub>A</sub> receptor  $\beta 8$ - $\beta 9$  loop. These residues undergo interactions with residues R66 and F45 located close to the agonist binding site (Mihalik et al., 2017). The  $\beta 8$ - $\beta 9$  of the GlyR and other Cys-loop

receptors might also harbor allosteric potential for yet unknown modulators.

## CONCLUSION

The  $\beta 8$ - $\beta 9$  loop is an important contributor to the hydrogen bond network in the ligand-bound state thus stabilizing the glycine-binding pocket.

## AUTHOR CONTRIBUTIONS

CV participated in research design. CV and DJ conducted experiments. CD, HS, CV, NS, and DJ performed data analysis. CV and NS wrote the manuscript.

## FUNDING

This work was supported by DFG VI586 (CV) and Schi425/8-1 (HS), NS is supported by the SCIENTIA program University Würzburg and DJ is supported by the GSLS Würzburg.

## ACKNOWLEDGMENT

Gudrun Schell and Nadine Vornberger are highly acknowledged for their excellent technical assistance.

## REFERENCES

- Al-Futaisi, A. M., Al-Kindi, M. N., Al-Mawali, A. M., Koul, R. L., Al-Adawi, S., and Al-Yahyaee, S. A. (2012). Novel mutation of *GLRA1* in Omani families with hyperekplexia and mild mental retardation. *Pediatr. Neurol.* 46, 89–93. doi: 10.1016/j.pediatrneurol.2011.11.008
- Althoff, T., Hibbs, R. E., Banerjee, S., and Gouaux, E. (2014). X-ray structures of GluCl in apo states reveal a gating mechanism of Cys-loop receptors. *Nature* 512, 333–337. doi: 10.1038/nature13669
- Atak, S., Langhofer, G., Schaefer, N., Kessler, D., Meiselbach, H., Delto, C., et al. (2015). Disturbances of ligand potency and enhanced degradation of the human glycine receptor at affected positions G160 and T162 originally identified in patients suffering from hyperekplexia. *Front. Mol. Neurosci.* 8:79. doi: 10.3389/fnmol.2015.00079
- Bode, A., and Lynch, J. W. (2014). The impact of human hyperekplexia mutations on glycine receptor structure and function. *Mol. Brain* 7:2. doi: 10.1186/1756-6606-7-2
- Brams, M., Pandya, A., Kuzmin, D., van Elk, R., Krijnen, L., Yakel, J. L., et al. (2011). A structural and mutagenic blueprint for molecular recognition of strychnine and d-tubocurarine by different cys-loop receptors. *PLoS Biol.* 9:e1001034. doi: 10.1371/journal.pbio.1001034
- Breitinger, H. G., and Becker, C. M. (1998). The inhibitory glycine receptor: prospects for a therapeutic orphan? *Curr. Pharm. Des.* 4, 315–334.
- Breitinger, H. G., Villmann, C., Becker, K., and Becker, C. M. (2001). Opposing effects of molecular volume and charge at the hyperekplexia site alpha 1(P250) govern glycine receptor activation and desensitization. *J. Biol. Chem.* 276, 29657–29663. doi: 10.1074/jbc.M100446200
- Brejck, K., van Dijk, W. J., Klaassen, R. V., Schuurmans, M., van Der Oost, J., Smit, A. B., et al. (2001). Crystal structure of an ACh-binding protein reveals the ligand-binding domain of nicotinic receptors. *Nature* 411, 269–276. doi: 10.1038/35077011
- Chung, S. K., Vanbellighen, J. F., Mullins, J. G., Robinson, A., Hantke, J., Hammond, C. L., et al. (2010). Pathophysiological mechanisms of dominant and recessive *GLRA1* mutations in hyperekplexia. *J. Neurosci.* 30, 9612–9620. doi: 10.1523/JNEUROSCI.1763-10.2010
- Deckert, J., Weber, H., Villmann, C., Lonsdorf, T. B., Richter, J., Andreatta, M., et al. (2017). *GLRB* allelic variation associated with agoraphobic cognitions, increased startle response and fear network activation: a potential neurogenetic pathway to panic disorder. *Mol. Psychiatry* 22, 1431–1439. doi: 10.1038/mp.2017.2
- Du, J., Lu, W., Wu, S., Cheng, Y., and Gouaux, E. (2015). Glycine receptor mechanism elucidated by electron cryo-microscopy. *Nature* 526, 224–229. doi: 10.1038/nature14853
- Duriscic, N., Godin, A. G., Wever, C. M., Heyes, C. D., Lakadamyali, M., and Dent, J. A. (2012). Stoichiometry of the human glycine receptor revealed by direct subunit counting. *J. Neurosci.* 32, 12915–12920. doi: 10.1523/JNEUROSCI.2050-12.2012
- Eichler, S. A., Förstera, B., Smolinsky, B., Jüttner, R., Lehmann, T. N., Föhling, M., et al. (2009). Splice-specific roles of glycine receptor  $\alpha 3$  in the hippocampus. *Eur. J. Neurosci.* 30, 1077–1091. doi: 10.1111/j.1460-9568.2009.06903.x
- Emsley, P., Lohkamp, B., Scott, W. G., and Cowtan, K. (2010). Features and development of Coot. *Acta Crystallogr. D Biol. Crystallogr.* 66, 486–501. doi: 10.1107/S0907444910007493
- Grudzinska, J., Schemm, R., Haeger, S., Nicke, A., Schmalzing, G., Betz, H., et al. (2005). The beta subunit determines the ligand binding properties of synaptic glycine receptors. *Neuron* 45, 727–739. doi: 10.1016/j.neuron.2005.01.028
- Hansen, S. B., Sulzenbacher, G., Huxford, T., Marchot, P., Taylor, P., and Bourne, Y. (2005). Structures of *Aplysia* AChBP complexes with nicotinic agonists and antagonists reveal distinctive binding interfaces and conformations. *EMBO J.* 24, 3635–3646. doi: 10.1038/sj.emboj.7600828
- Harvey, R. J., Depner, U. B., Wassle, H., Ahmadi, S., Heindl, C., Reinold, H., et al. (2004). GlyR alpha3: an essential target for spinal PGE2-mediated

- inflammatory pain sensitization. *Science* 304, 884–887. doi: 10.1126/science.1094925
- Harvey, R. J., and Yee, B. K. (2013). Glycine transporters as novel therapeutic targets in schizophrenia, alcohol dependence and pain. *Nat. Rev. Drug Discov.* 12, 866–885. doi: 10.1038/nrd3893
- Hassaine, G., Deluz, C., Grasso, L., Wyss, R., Tol, M. B., Hovius, R., et al. (2014). X-ray structure of the mouse serotonin 5-HT<sub>3</sub> receptor. *Nature* 512, 276–281. doi: 10.1038/nature13552
- Hibbs, R. E., and Gouaux, E. (2011). Principles of activation and permeation in an anion-selective Cys-loop receptor. *Nature* 474, 54–60. doi: 10.1038/nature10139
- Hilf, R. J., and Dutzler, R. (2008). X-ray structure of a prokaryotic pentameric ligand-gated ion channel. *Nature* 452, 375–379. doi: 10.1038/nature06717
- Huang, X., Chen, H., Michelsen, K., Schneider, S., and Shaffer, P. L. (2015). Crystal structure of human glycine receptor- $\alpha 3$  bound to antagonist strychnine. *Nature* 526, 277–280. doi: 10.1038/nature14972
- Huang, X., Shaffer, P. L., Ayube, S., Bregman, H., Chen, H., Lehto, S. G., et al. (2017). Crystal structures of human glycine receptor  $\alpha 3$  bound to a novel class of analgesic potentiators. *Nat. Struct. Mol. Biol.* 24, 108–113. doi: 10.1038/nsmb.3329
- James, V. M., Bode, A., Chung, S. K., Gill, J. L., Nielsen, M., Cowan, F. M., et al. (2013). Novel missense mutations in the glycine receptor beta subunit gene (GLRB) in startle disease. *Neurobiol. Dis.* 52, 137–149. doi: 10.1016/j.nbd.2012.12.001
- Khatri, A., and Weiss, D. S. (2010). The role of Loop F in the activation of the GABA receptor. *J. Physiol.* 588, 59–66. doi: 10.1113/jphysiol.2009.179705
- Lynch, J. W. (2004). Molecular structure and function of the glycine receptor chloride channel. *Physiol. Rev.* 84, 1051–1095. doi: 10.1152/physrev.00042.2003
- Meier, J. C., Henneberger, C., Melnick, I., Racca, C., Harvey, R. J., Heinemann, U., et al. (2005). RNA editing produces glycine receptor  $\alpha 3^{P185L}$ , resulting in high agonist potency. *Nat. Neurosci.* 8, 736–744. doi: 10.1038/nn1467
- Mihalik, B., Palvolgyi, A., Bogar, F., Megyeri, K., Ling, I., Barkoczy, J., et al. (2017). Loop-F of the alpha-subunit determines the pharmacologic profile of novel competitive inhibitors of GABA<sub>A</sub> receptors. *Eur. J. Pharmacol.* 798, 129–136. doi: 10.1016/j.ejphar.2017.01.033
- Moraga-Cid, G., Sauguet, L., Huon, C., Malherbe, L., Girard-Blanc, C., Petres, S., et al. (2015). Allosteric and hyperekplexic mutant phenotypes investigated on an  $\alpha 1$  glycine receptor transmembrane structure. *Proc. Natl. Acad. Sci. U.S.A.* 112, 2865–2870. doi: 10.1073/pnas.1417864112
- Morales-Perez, C. L., Noviello, C. M., and Hibbs, R. E. (2016). X-ray structure of the human  $\alpha 4\beta 2$  nicotinic receptor. *Nature* 538, 411–415. doi: 10.1038/nature19785
- Nys, M., Kesters, D., and Ulens, C. (2013). Structural insights into Cys-loop receptor function and ligand recognition. *Biochem. Pharmacol.* 86, 1042–1053. doi: 10.1016/j.bcp.2013.07.001
- Nys, M., Wijckmans, E., Farinha, A., Yoluk, O., Andersson, M., Brams, M., et al. (2016). Allosteric binding site in a Cys-loop receptor ligand-binding domain unveiled in the crystal structure of ELIC in complex with chlorpromazine. *Proc. Natl. Acad. Sci. U.S.A.* 113, E6696–E6703. doi: 10.1073/pnas.1603101113
- Padgett, C. L., and Lumms, S. C. (2008). The F-loop of the GABA A receptor gamma2 subunit contributes to benzodiazepine modulation. *J. Biol. Chem.* 283, 2702–2708. doi: 10.1074/jbc.M705699200
- Pilorge, M., Fassier, C., Le Corronc, H., Potey, A., Bai, J., De Gois, S., et al. (2015). Genetic and functional analyses demonstrate a role for abnormal glycinergic signaling in autism. *Mol. Psychiatry* 21, 936–945. doi: 10.1038/mp.2015.139
- Pless, S. A., Hanek, A. P., Price, K. L., Lynch, J. W., Lester, H. A., Dougherty, D. A., et al. (2011). A cation- $\pi$  interaction at a phenylalanine residue in the glycine receptor binding site is conserved for different agonists. *Mol. Pharmacol.* 79, 742–748. doi: 10.1124/mol.110.069583
- Rajendra, S., Lynch, J. W., and Schofield, P. R. (1997). The glycine receptor. *Pharmacol. Ther.* 73, 121–146. doi: 10.1016/S0163-7258(96)00163-5
- Schaefer, N., Berger, A., van Brederode, J., Zheng, F., Zhang, Y., Leacock, S., et al. (2017). Disruption of a structurally important extracellular element in the glycine receptor leads to decreased synaptic integration and signaling resulting in severe startle disease. *J. Neurosci.* 37, 7948–7961. doi: 10.1523/JNEUROSCI.0009-17.2017
- Schaefer, N., Kluck, C. J., Price, K. L., Meiselbach, H., Vornberger, N., Schwarzinger, S., et al. (2015). Disturbed neuronal ER-golgi sorting of unassembled glycine receptors suggests altered subcellular processing is a cause of human hyperekplexia. *J. Neurosci.* 35, 422–437. doi: 10.1523/JNEUROSCI.1509-14.2015
- Schindelin, J., Arganda-Carreras, I., Frise, E., Kaynig, V., Longair, M., Pietzsch, T., et al. (2012). Fiji: an open-source platform for biological-image analysis. *Nat. Methods* 9, 676–682. doi: 10.1038/nmeth.2019
- Schindelin, J., Rueden, C. T., Hiner, M. C., and Eliceiri, K. W. (2015). The ImageJ ecosystem: an open platform for biomedical image analysis. *Mol. Reprod. Dev.* 82, 518–529. doi: 10.1002/mrd.22489
- Schneider, C. A., Rasband, W. S., and Eliceiri, K. W. (2012). NIH Image to ImageJ: 25 years of image analysis. *Nat. Methods* 9, 671–675. doi: 10.1038/nmeth.2089
- Sievers, F., Wilm, A., Dineen, D., Gibson, T. J., Karplus, K., Li, W., et al. (2011). Fast, scalable generation of high-quality protein multiple sequence alignments using Clustal Omega. *Mol. Syst. Biol.* 7, 539. doi: 10.1038/msb.2011.75
- Villmann, C., Oertel, J., Melzer, N., and Becker, C. M. (2009). Recessive hyperekplexia mutations of the glycine receptor  $\alpha 1$  subunit affect cell surface integration and stability. *J. Neurochem.* 111, 837–847. doi: 10.1111/j.1471-4159.2009.06372.x
- Vogel, N., Kluck, C. J., Melzer, N., Schwarzinger, S., Breiting, U., Seeber, S., et al. (2009). Mapping of disulfide bonds within the amino-terminal extracellular domain of the inhibitory glycine receptor. *J. Biol. Chem.* 284, 36128–36136. doi: 10.1074/jbc.M109.043448
- Yang, Z., Taran, E., Webb, T. I., and Lynch, J. W. (2012). Stoichiometry and subunit arrangement of  $\alpha 1\beta 2$  glycine receptors as determined by atomic force microscopy. *Biochemistry* 51, 5229–5231. doi: 10.1021/bi300063m
- Yu, R., Hurdiss, E., Greiner, T., Lape, R., Sivilotti, L., and Biggin, P. C. (2014). Agonist and antagonist binding in human glycine receptors. *Biochemistry* 53, 6041–6051. doi: 10.1021/bi500815f
- Zhou, N., Wang, C. H., Zhang, S., and Wu, D. C. (2013). The GLRA1 missense mutation W170S associates lack of Zn<sup>2+</sup> potentiation with human hyperekplexia. *J. Neurosci.* 33, 17675–17681. doi: 10.1523/JNEUROSCI.3240-13.2013

**Conflict of Interest Statement:** The authors declare that the research was conducted in the absence of any commercial or financial relationships that could be construed as a potential conflict of interest.

Copyright © 2017 Janzen, Schaefer, Delto, Schindelin and Villmann. This is an open-access article distributed under the terms of the Creative Commons Attribution License (CC BY). The use, distribution or reproduction in other forums is permitted, provided the original author(s) or licensor are credited and that the original publication in this journal is cited, in accordance with accepted academic practice. No use, distribution or reproduction is permitted which does not comply with these terms.

# Sesquiterpenes and Sesquiterpenoids Harbor Modulatory Allosteric Potential and Affect Inhibitory GABA<sub>A</sub> Receptor Function *in vitro*

Dieter Janzen<sup>1</sup>, Benedikt Slavik<sup>2</sup>, Markus Zehe<sup>3</sup>, Christoph Sotriffer<sup>3</sup>, Helene M. Loos<sup>2,4</sup>, Andrea Buettner<sup>2,4</sup>, Carmen Villmann<sup>1</sup>

<sup>1</sup> Institute for Clinical Neurobiology, University Hospital Würzburg, University of Würzburg, Würzburg, Germany

<sup>2</sup> Chair of Aroma and Smell Research, Department of Chemistry and Pharmacy, University of Erlangen-Nürnberg, Erlangen, Germany

<sup>3</sup> Institute of Pharmacy and Food Chemistry, University of Würzburg, Würzburg, Germany

<sup>4</sup> Fraunhofer Institute for Process Engineering and Packaging IVV, Freising, Germany

Published in  
**Journal of Neurochemistry**  
July 15, 2021

## Sesquiterpenes and sesquiterpenoids harbor modulatory allosteric potential and affect inhibitory GABA<sub>A</sub> receptor function in vitro

Dieter Janzen<sup>1</sup>  | Benedikt Slavik<sup>2</sup>  | Markus Zehe<sup>3</sup> | Christoph Sotriffer<sup>3</sup> | Helene M. Loos<sup>2,4</sup>  | Andrea Buettner<sup>2,4</sup>  | Carmen Villmann<sup>1</sup> 

<sup>1</sup>Institute for Clinical Neurobiology, University Hospital, Julius-Maximilians-University Würzburg, Würzburg, Germany

<sup>2</sup>Chair of Aroma and Smell Research, Department of Chemistry and Pharmacy, Friedrich-Alexander-University Erlangen-Nürnberg (FAU), Erlangen, Germany

<sup>3</sup>Institute of Pharmacy and Food Chemistry, Julius-Maximilians-University Würzburg, Würzburg, Germany

<sup>4</sup>Fraunhofer Institute for Process Engineering and Packaging IVV, Freising, Germany

### Correspondence

Carmen Villmann, Institute for Clinical Neurobiology, Julius-Maximilians-University Würzburg, Versbacherstr. 5, D-97078 Würzburg, Germany.  
Email: villmann\_c@ukw.de

### Funding information

Graduate School for Life Sciences Würzburg; Deutsche Forschungsgemeinschaft, Grant/Award Number: V1586/8 and BU1351/11; INST 90/979-1 FUGG

### Abstract

Naturally occurring compounds such as sesquiterpenes and sesquiterpenoids (SQTs) have been shown to modulate GABA<sub>A</sub> receptors (GABA<sub>A</sub>Rs). In this study, the modulatory potential of 11 SQTs at GABA<sub>A</sub>Rs was analyzed to characterize their potential neurotropic activity. Transfected HEK293 cells and primary hippocampal neurons were functionally investigated using electrophysiological whole-cell recordings. Significantly different effects of β-caryophyllene and α-humulene, as well as their respective derivatives β-caryolanol and humulol, were observed in the HEK293 cell system. In neurons, the concomitant presence of phasic and tonic GABA<sub>A</sub>R configurations accounts for differences in receptor modulation by SQTs. The in vivo presence of the γ<sub>2</sub> and δ subunits is important for SQT modulation. While phasic GABA<sub>A</sub> receptors in hippocampal neurons exhibited significantly altered GABA-evoked current amplitudes in the presence of humulol and guaiol, negative allosteric potential at recombinantly expressed α<sub>1</sub>β<sub>2</sub>γ<sub>2</sub> receptors was only verified for humulol. Modeling and docking studies provided support for the binding of SQTs to the neurosteroid-binding site of the GABA<sub>A</sub>R localized between transmembrane segments 1 and 3 at the (α) interface. In sum, differences in the modulation of GABA<sub>A</sub>R isoforms between SQTs were identified. Another finding is that our results provide an indication that nutritional digestion affects the neurotropic potential of natural compounds.

### KEYWORDS

allosteric modulation, GABA<sub>A</sub> receptor, patch clamp recording

**Abbreviations:** GABA, γ-aminobutyric acid; GABA<sub>A</sub>R, γ-aminobutyric acid type A receptor; GFP, green fluorescent protein; HEK293, human embryonic kidney cells; M1-4, transmembrane domains 1-4; PTX, picrotoxinin; RRID, Research Resource Identifier; SQTs, sesquiterpenes and sesquiterpenoids.

This is an open access article under the terms of the Creative Commons Attribution License, which permits use, distribution and reproduction in any medium, provided the original work is properly cited.

© 2021 The Authors. *Journal of Neurochemistry* published by John Wiley & Sons Ltd on behalf of International Society for Neurochemistry

## 1 | INTRODUCTION

GABA<sub>A</sub>Rs represent the major inhibitory ligand-gated chloride ion channels in the central nervous system. GABA<sub>A</sub>Rs mediate fast phasic synaptic inhibition as well as tonic perisynaptic and extrasynaptic inhibition, and are expressed in brain areas, for example, cortex, hippocampus, and olfactory bulb. They contribute to the balance between excitatory and inhibitory neurotransmission processes by inhibiting incoming action potentials through chloride ion influx (Mortensen et al., 2012; Sieghart, 2006).

GABA<sub>A</sub>Rs are heteropentameric receptors that belong to the superfamily of Cys-loop receptors also including glycine receptors, the 5HT<sub>3</sub> receptor, and nicotinic acetylcholine receptors (nAChRs). Common to all Cys-loop receptors is their large N-terminal domain followed by four transmembrane domains (M1-4) with M2 representing the ion channel pore, and a short extracellular C-terminus. The large intracellular loop between M3 and M4 is of the highest variability between Cys-loop receptors bearing binding sites for other structural proteins (Kasaragod & Schindelin, 2019).

GABA<sub>A</sub>R subunits are encoded by 19 genes ( $\alpha$ 1-6,  $\beta$ 1-3,  $\gamma$ 1-3,  $\delta$ ,  $\epsilon$ ,  $\theta$ ,  $\rho$ 1-3,  $\pi$ ) (Simon et al., 2004). Most GABA<sub>A</sub>Rs are formed by  $\alpha$ ,  $\beta$ , and  $\gamma$ / $\delta$  subunits with the  $\alpha_1\beta_2\gamma_2$  configurations representing the most abundant receptor subtypes in the brain (Fritschy & Mohler, 1995). Recent structures revealed an arrangement of  $\alpha$ - $\beta$ - $\alpha$ - $\beta$ - $\gamma$ / $\delta$  in a clockwise manner (Laverty et al., 2017; Masiulis et al., 2019). The large extracellular N-terminus harbors the ligand-binding site for GABA at the interface of two adjacent subunits ( $\alpha$  and  $\beta$ ). The ion channel can be blocked by the antagonist picrotoxinin (PTX) which binds to residues located in M2 constricting the ion channel pore to about 1.5 Å. Following the binding of another antagonist, bicuculline, to the orthosteric-binding site, the GABA<sub>A</sub>Rs turn into a closed conformation similar to the PTX-bound state (Masiulis et al., 2019). Diazepam, a benzodiazepine, is a potent allosteric modulator of GABAergic function binding specifically to the orthosteric-binding site at the interface of  $\alpha_1$  and  $\gamma_2$  subunits. Diazepam is an established drug used as a muscle relaxant and a sedative substance (Rudolph & Knoflach, 2011). Recently, a second binding site for benzodiazepines was demonstrated responsible for the observed biphasic GABA<sub>A</sub>R potentiation at higher diazepam concentrations (Olsen, 2018; Walters et al., 2000). This binding site is localized between the transmembrane domains at the interface of subunits  $\beta$  ( $\beta_3$ ) and  $\alpha$  ( $\alpha_1$ ). Similarly, neurosteroid binding has been demonstrated within a hydrophobic-binding pocket between adjacent transmembrane domains (Alvarez & Estrin, 2015; Alvarez & Pecci, 2018; Miller et al., 2017).

Several studies describe modulation of GABA<sub>A</sub>Rs by natural compounds taken up via nutrition or used in aroma therapy, however, most lack receptor subtype specificity (Johnston et al., 2006). Positive and negative allosteric modulation of GABA<sub>A</sub>Rs has been shown, for instance, for flavonoids, terpenoids, phenols, and polyacetylenic alcohols, bearing convulsive, anticonvulsive, sedative or anxiolytic potential. Because of the partly high hydrophobicity of terpenoids, binding to the transmembrane subunit interfaces or

modulation of the lipid surrounding have been postulated as underlying mechanisms (Manayi et al., 2016; Silva et al., 2019). Among different terpene subtypes, volatile bicyclic monoterpenoids carrying a hydroxy group revealed positive allosteric modulators at  $\alpha_1\beta_2\gamma_2$  but also at  $\alpha_1\beta_2$  GABA<sub>A</sub>Rs (Kessler et al., 2012, 2014). Modulation of GABAergic function has also been ascribed to sesquiterpenes and sesquiterpenoids (SQTs) (Kasaragod et al., 2019; Manayi et al., 2016).

In this study, we investigated the modulatory effects of 11 SQTs occurring in different plants like hop and chamomile on GABA<sub>A</sub>R configurations present in the human brain. Therefore, the GABA<sub>A</sub>Rs expressed in transfected HEK293 cells and primary hippocampal neurons were characterized by electrophysiological whole-cell recordings. Our functional data were accompanied by structural modeling and molecular docking studies to further investigate possible binding modes of the SQTs studied. We found significant differences in the modulation of GABA<sub>A</sub>R isoforms between different SQTs as well as between transfected cells and hippocampal neurons. The results also indicate that structural changes because of digestion and biotransformation processes may affect the neurotropic potential of natural compounds.

## 2 | MATERIALS AND METHODS

### 2.1 | Chemical Information

GABA, ZnCl<sub>2</sub>, picrotoxinin, diazepam, and gaboxadol were acquired from Sigma-Aldrich. Stock solutions of GABA (1 M) and ZnCl<sub>2</sub> (100 mM) were prepared in water. Picrotoxinin (50 mM), diazepam (10 mM), and gaboxadol (100 mM) were dissolved in ethanol. Guaiol,  $\alpha$ -humulene,  $\alpha$ -bisabolol,  $\beta$ -caryophyllene, and nootkatone were purchased from Sigma-Aldrich.  $\beta$ -Caryolanol and humulol were synthesized according to Heinlein & Buettner, (2012). Spathulenol,  $\alpha$ -bisabolone oxide A,  $\alpha$ -bisabolol oxide A, and  $\alpha$ -bisabolol oxide B were isolated by a combination of different extraction and isolation steps. In short, dried chamomile flower heads were extracted with dichloromethane and the volatile fraction was isolated by means of solvent-assisted flavor evaporation (Engel et al., 1999). Centrifugal partition chromatography resulted in the direct isolation of  $\alpha$ -bisabolone oxide A. Silica gel chromatography and size exclusion chromatography provided further purification of spathulenol,  $\alpha$ -bisabolol oxide A, and  $\alpha$ -bisabolol oxide B. Additionally,  $\alpha$ -bisabolol oxide A was isolated by preparative two-dimensional GC. SQT stock solutions (100 mM) were prepared in ethanol. All stock solutions were stored at -20°C. Fresh solutions were prepared from stock solutions on the day of recording (final concentration of ethanol 0.6%).

### 2.2 | Extraction and isolation of SQTs from chamomile and hop for GC-MS analyses

Dried hop cones (2.43 g) and dried chamomile flower heads (2.62 g), both purchased from a local company (Wurdies Kräuter GmbH & Co.

KG), were finely chopped for 1 min with a mini chopper (Kenwood CH180, Kenwood Limited). Solvent extraction was performed with dichloromethane (DCM, 50 ml, 30 min). After drying over sodium sulfate, the extracts were applied to solvent-assisted flavor evaporation (SAFE) at 60°C in a vacuum (Engel et al., 1999). The distillates were concentrated to 100  $\mu$ l by Vigreux and subsequent micro distillation at 50°C (Bemelmans, 1979). As the last step, the distillates were diluted 1:10 (DCM) for GC-MS analysis.

### 2.3 | GC-MS analyses of the hop and chamomile distillates

The analyses were performed on a GC 6,890 (Agilent Technologies, Santa Clara, CA, USA) connected to a MSD 5,973 (Hewlett-Packard, Palo Alto, CA, USA), equipped with a GERSTEL MPS 2 multipurpose sampler and a GERSTEL CIS 3 injection system (GERSTEL GmbH & Co. KG, Mülheim an der Ruhr, Germany). An uncoated fused silica capillary pre-column (3 m  $\times$  0.53 mm i.D.) was fixed to a DB-5 capillary column (30  $\times$  0.25 mm i.D., film thickness 0.25  $\mu$ m; both from Agilent J&W Scientific). The oven program was started at 60°C and was raised at 3°C/min until 246°C. The carrier gas (helium) flow was set to 1 ml/min. A split of 20:1 was used for the application of the sample (2  $\mu$ l). EI mass spectra were recorded in full scan mode (40.0–400.0 amu) using 70 eV.

### 2.4 | Cell lines

HEK293 human embryonic kidney cells (CRL-1573, RRID:CVCL\_0045, ATCC; passages 33 lot 70016364 and 34 lot 61714301) were grown in minimal essential medium (MEM) supplemented with 10% fetal calf serum, 200 mM GlutaMAX, 100 mM sodium pyruvate, 100 U/ml penicillin, and 100  $\mu$ g/ml streptomycin (Thermo Fisher Scientific) under standard growth conditions at 37°C and 5% CO<sub>2</sub>. Following thawing, cells used for experiments were between passages 6 and 20. The cell line is not listed as a commonly misidentified cell line by the International Cell Line Authentication Committee.

### 2.5 | Transfection

HEK293 cells were transiently transfected using a modified calcium-phosphate precipitation method. Plasmid DNAs of  $\alpha_1$ ,  $\alpha_4$ ,  $\alpha_6$ ,  $\beta_2$ ,  $\beta_3$ ,  $\gamma_2$ ,  $\delta$  subunits, and GFP were mixed with the following combinations and ratios:  $\alpha_1$ : $\beta_2$ :GFP 1:1:1,  $\alpha_1$ : $\beta_2$ : $\gamma_2$ :GFP 1:1:0.5:1,  $\alpha_4$ : $\beta_3$ : $\delta$ :GFP 1:1:0.5:1,  $\alpha_6$ : $\beta_3$ : $\delta$ :GFP 1:1:0.5:1. DNA was mixed with 0.1 $\times$  TE buffer, 2.5 M CaCl<sub>2</sub>, and 2 $\times$  HBS buffer (50 mM HEPES, 12 mM glucose, 10 mM KCl, 280 mM NaCl, 1.5 mM Na<sub>2</sub>HPO<sub>4</sub>, pH 6.98) and applied to the cells. Cell medium was exchanged after 6 hr to reduce transfection stress. Electrophysiological recordings were performed 24–48 hr post-transfection.

### 2.6 | Neuronal preparation and culture

Hippocampal neurons were prepared from mouse embryos at embryonic day 17 (E17) from pregnant female wild-type CD1 mice (Strain code: 022, RRID:IMSR\_CRL:022, Charles River). Female pregnant mice were subjected to a 10-min-deep CO<sub>2</sub> anesthesia. Experiments were authorized by the local veterinary authority and Committee on the Ethics of Animal Experiments (Regierung von Unterfranken, license FBVVL 568/200-324/13). In short, hippocampi from all embryos (n = 10–16) were pooled and trypsinated for 30 min by incubation in 0.5 mg/ml trypsin, 0.2 mg/ml EDTA, and 10  $\mu$ g/ $\mu$ l DNase I in PBS for 30 min at 37°C. After adding 10% fetal calf serum, neurons were dissociated by trituration, counted, and seeded on poly-L-lysine-coated coverslips. Hippocampal neurons were cultured under standard growth conditions at 37°C and 5% CO<sub>2</sub> in a neurobasal medium containing 2 mM GlutaMAX and 2% (v/v) B27 supplement (Thermo Fisher Scientific). Neurons were used for patch clamp experiments after 18–21 days in culture.

### 2.7 | Electrophysiology

Whole-cell recordings of transfected HEK293 cells and hippocampal neurons were obtained using the patch clamp technique. A Sutter P97 horizontal puller (Sutter Instrument) was used to pull recording pipettes (3–5 M $\Omega$ ) from thin-walled borosilicate capillaries (TW150-F4; World Precision Instruments, Sarasota, FL, USA). Recordings were obtained with an EPC10 USB amplifier operated with Patchmaster software (HEKA Elektronik). Currents were low-pass filtered at 2.9 kHz and digitized at 20 kHz. Cells were held at –60 mV. An Octaflow II system (ALA Scientific Instruments) was used to apply agonist solutions directly on patched cells for 50 ms with a pressure of 1 bar. The intracellular buffer contained (in mM) 120 CsCl, 20 N(Et)<sub>4</sub>Cl, 1 CaCl<sub>2</sub>, 2 MgCl<sub>2</sub>, 11 EGTA, 10 HEPES; pH 7.3, adjusted with CsOH (295  $\pm$  1.5 mOsm/L) and the extracellular solution consisted of (in mM) 137 NaCl, 5.4 KCl, 1.8 CaCl<sub>2</sub>, 1 MgCl<sub>2</sub>, 5 HEPES pH 7.3, adjusted with NaOH (320  $\pm$  1.5 mOsm/L). All measurements were performed at 21°C.

### 2.8 | Molecular modeling and docking

The docking study was performed at two different locations at the transmembrane domain of the GABA<sub>A</sub>-receptor: the diazepam-binding site in the  $\beta^+\alpha^-$ -interface and the pregnanolone-binding site in the  $\alpha\alpha$ -interface. For the former, a CryoEM structure of the human full-length  $\alpha_1\beta_3\gamma_2$ -GABA<sub>A</sub>-receptor was used (PDB: 6HUP) (Masiulis et al., 2019), for the latter (i.e., the pregnanolone-binding site) the crystal structure of an  $\alpha_6\beta_3$ -chimera (PDB: 5O8F) (Miller et al., 2017). The preparation of the structures as well as the setup of the docking calculations with AutoDock (Morris et al., 1998) are described in detail in the Supplemental Information.



## 2.9 | Statistical analysis

GraphPad Prism 9.0.0 (GraphPad Software) was used to calculate mean values, standard deviation, standard error of the mean, and statistical significance. The two-tailed paired *t* test was used to estimate significance values with \**p* < .05, \*\**p* < .01, \*\*\**p* < .001, \*\*\*\**p* < .0001. Data were not assessed for normality, no test for outliers was conducted, and no sample size calculation was done. The sample size is based on previous studies of a similar design (Milanos et al., 2018).

## 2.10 | Study and experimental design

This study was not a pre-registered study. Therefore, no randomization was performed to allocate subjects in the study. Moreover, this study did not include animal experiments. Hippocampal cultures were obtained from pooled hippocampi of embryos from pregnant female CD1. Three independent cultures were used for the electrophysiological recordings from mature neurons between DIV 18–21 in culture. No blinding of the experimenter was performed in the electrophysiological data acquisition and analysis.

Exclusion criteria for transfected HEK293 cells used for electrophysiological measurements: We defined exclusion criteria as transfected cells might not have picked up all plasmids (3 to express a defined type of GABA<sub>A</sub>R). Among the cells measured, one cell did not show a picrotoxinin block arguing that the expression of the GABA<sub>A</sub>R was not achieved. Thus, this cell was excluded from analysis (8 of 9 cells were used for analysis). For neurons,

not all neurons in the hippocampal culture represent GABAergic cells. Picrotoxinin blocks GABAergic neurons and was used as a selection criterion. Synaptic GABA<sub>A</sub>Rs were verified by potentiation with diazepam. Gaboxadol, a superagonist at tonic GABA<sub>A</sub>Rs, was used to show that cells express tonic GABA<sub>A</sub>Rs. Using these criteria, we excluded two cells from our initial recordings from hippocampal neurons not exhibiting a picrotoxin block and concomitantly no diazepam potentiation.

## 3 | RESULTS

### 3.1 | Positive and negative allosteric modulation of GABA<sub>A</sub>Rs of the α1β2 subtype by SQTs

In this study, the modulatory effect of 11 different SQTs was investigated on GABA<sub>A</sub>Rs (Figure 1a). β-Caryophyllene and α-humulene are major compounds of the volatile fraction of hop. In previous studies it was shown, that they are transformed into β-caryolanol and humulol, respectively, when applied to an in vitro digestion model (Heinlein & Buettner, 2012) (Figure 1b, left side). (E)-β-Farnesene, spathulenol, α-bisabolol, α-bisabolol oxide A, α-bisabolol oxide B, and α-bisabolone oxide A are major constituents of the volatile fraction of chamomile. (Figure 1b, right side). Guaiol is a major constituent in valerian (*Valeriana officinalis* L.) and was chosen because of its structural similarity to spathulenol. SQTs were diluted in ethanol, which resulted in final ethanol concentrations of 0.6% for single modulator measurements and 1% for co-application of two modulators in the patch solutions.

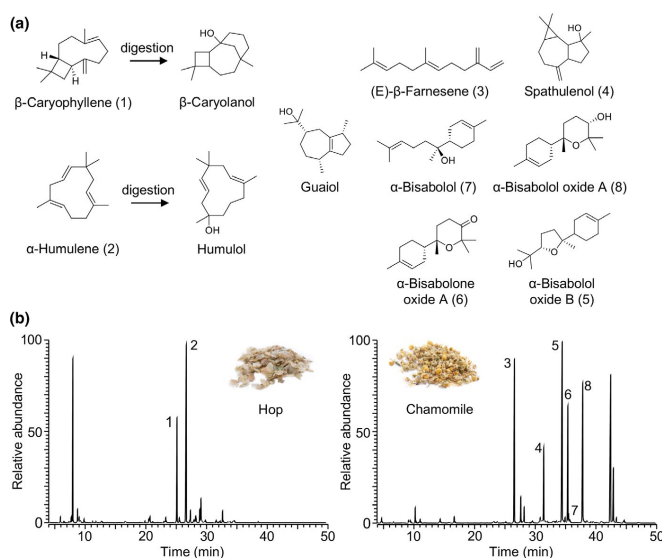


**FIGURE 1** Structures of SQTs and chromatograms of distillates obtained from hop and chamomile. (a) Chemical structures of all modulators used in this study. (b) Total ion chromatograms of the distillates of hop (left) and chamomile (right) obtained after solvent-assisted flavor evaporation. The target SQTs are marked with the numbers according to a

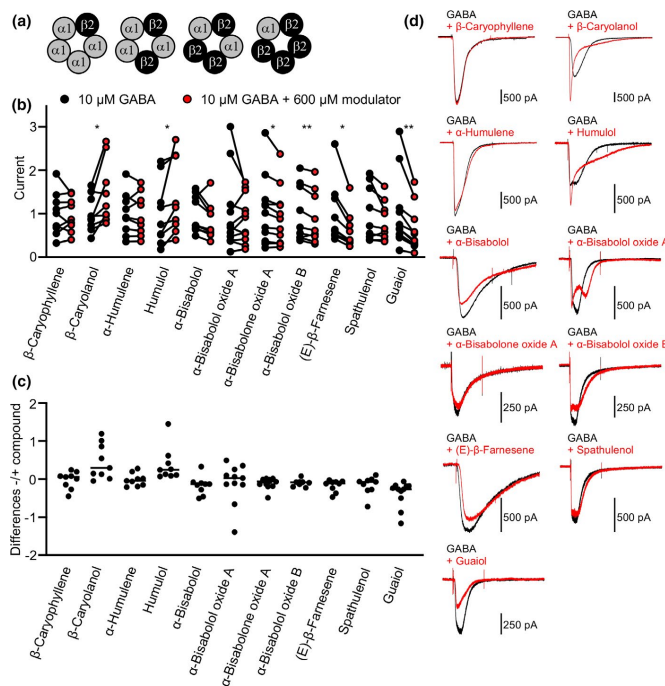


**FIGURE 2** Positive and negative allosteric modulation of  $\alpha_1\beta_2$  GABA<sub>A</sub>Rs by SQTs. (a) Possible receptor configurations for  $\alpha_1\beta_2$  GABA<sub>A</sub>Rs. (b) Normalized currents of patch clamp recordings from transfected HEK293 cells during application of 10  $\mu$ M GABA (black dots) or with co-application of 600  $\mu$ M of the appropriate modulator (red dots). Each pair of dots represents one cell. Patch clamp experiments were performed on at least 3 days with independent cell batches and transfections, total number of cells recorded was  $n = 9-12$ . \* $p \leq .05$ , \*\* $p \leq .01$ . (c) Differences +/- compound in b are shown. (d) Example current traces for each recording are shown in b. Black traces, 10  $\mu$ M GABA; red traces, 10  $\mu$ M GABA + 600  $\mu$ M modulator

A matching ethanol concentration was used for control measurements without a modulator.

Previous studies demonstrated that GABAergic modulation by terpenoids is most probably independent of the presence of the  $\gamma_2$  subunit in the pentameric GABA<sub>A</sub>R complex (Kessler et al., 2014). Therefore, the modulatory effect of SQTs was first analyzed on heteromeric GABA<sub>A</sub>Rs composed of  $\alpha_1$  and the  $\beta_2$  subunits. Cells were co-transfected with a green fluorescent protein (GFP) to distinguish transfected from untransfected cells during patch clamp experiments by using a fluorescence microscope.

Multiple receptor configurations in the pentameric receptor complex are possible resulting from  $\alpha_1\beta_2$  subunit transfection (Figure 2a). Their effects on agonist potency are unknown, but expression differences seem to influence receptor stoichiometry, with 2:3 being the most likely one (Wagoner & Czajkowski, 2010). For analysis of SQT modulation, 10  $\mu$ M GABA (referring to EC<sub>10-30</sub>, (Milanos et al., 2018) was applied for 50 ms, followed by a 50 ms co-application with 600  $\mu$ M of the appropriate modulator (Figure 2b, c). A concentration of 600  $\mu$ M for the SQTs was chosen because of

previous results on other terpenes starting with modulation at concentrations of 100  $\mu$ M and being most effective between 300  $\mu$ M and 1 mM (van Brederode et al., 2016; Kessler et al., 2014; Milanos et al., 2018). Obtained maximum current ( $I_{max}$ ) values were divided by the mean GABA current for better comparability. Co-application with  $\beta$ -caryophyllene (146  $\pm$  24%,  $p = .017$ ) and humulol (138  $\pm$  29%,  $p = .033$ ) resulted in significantly increased  $I_{max}$ , whereas  $\alpha$ -bisabolone oxide A (89  $\pm$  22%,  $p = .023$ ),  $\alpha$ -bisabolone oxide B (90  $\pm$  20%,  $p = .009$ ), (E)- $\beta$ -farnesene (83  $\pm$  19%,  $p = .010$ ), and guaial (62  $\pm$  16%,  $p = .0039$ ) significantly reduced GABA-induced  $I_{max}$  values (Table 1). Representative current traces for these recordings are shown in Figure 2d. The significantly different effects of  $\beta$ -caryophyllene and  $\alpha$ -humulene and their respective derivatives  $\beta$ -caryolanol and humulol suggest that the additional hydroxy group may account for the observed differences in receptor modulation. Furthermore,  $\alpha$ -bisabolone oxide A,  $\alpha$ -bisabolone oxide B, (E)- $\beta$ -farnesene, and guaial exhibited a negative allosteric modulatory effect independent of the presence of a hydroxy group. As a single concentration of 600  $\mu$ M SQTs was used for recordings, we

Compound	c [ $\mu$ M]	$I_{rel} \pm SEM$ [%]	$I_{abs} \pm SEM$ [nA]	p-values	n
GABA	10	100 $\pm$ 17	1.84 $\pm$ 0.30	0.7600	9
$\beta$ -Caryophyllene	600	98 $\pm$ 13	1.80 $\pm$ 0.24		
GABA	10	100 $\pm$ 14	1.19 $\pm$ 0.16	0.0172*	9
$\beta$ -Caryolanol	600	146 $\pm$ 24	1.73 $\pm$ 0.28		
GABA	10	100 $\pm$ 16	2.56 $\pm$ 0.42	0.7578	9
$\alpha$ -Humulene	600	98 $\pm$ 16	2.51 $\pm$ 0.41		
GABA	10	100 $\pm$ 25	1.33 $\pm$ 0.33	0.0336*	9
Humulol	600	138 $\pm$ 29	1.84 $\pm$ 0.38		
GABA	10	100 $\pm$ 14	0.71 $\pm$ 0.10	0.0720	9
$\alpha$ -Bisabolol	600	83 $\pm$ 14	0.59 $\pm$ 0.10		
GABA	10	100 $\pm$ 27	0.67 $\pm$ 0.18	0.5244	10
$\alpha$ -Bisabolol oxide A	600	90 $\pm$ 17	0.60 $\pm$ 0.11		
GABA	10	100 $\pm$ 26	0.33 $\pm$ 0.09	0.0236*	12
$\alpha$ -Bisabolone oxide A	600	89 $\pm$ 22	0.29 $\pm$ 0.07		
GABA	10	100 $\pm$ 21	0.75 $\pm$ 0.16	0.0097**	9
$\alpha$ -Bisabolol oxide B	600	90 $\pm$ 20	0.67 $\pm$ 0.15		
GABA	10	100 $\pm$ 24	0.39 $\pm$ 0.09	0.0101*	9
(E)- $\beta$ -Farnesene	600	83 $\pm$ 19	0.32 $\pm$ 0.07		
GABA	10	100 $\pm$ 21	0.68 $\pm$ 0.14	0.0746	9
Spathulenol	600	83 $\pm$ 15	0.56 $\pm$ 0.10		
GABA	10	100 $\pm$ 25	0.58 $\pm$ 0.15	0.0039**	10
Guaiol	600	62 $\pm$ 16	0.36 $\pm$ 0.09		
GABA	10	100 $\pm$ 13	1.03 $\pm$ 0.13		9
$\beta$ -Caryolanol + Humulol	500 + 500	108 $\pm$ 9	1.11 $\pm$ 0.10	0.4388	
$\beta$ -Caryolanol + $\alpha$ -Bisabolol	500 + 500	56 $\pm$ 7	0.57 $\pm$ 0.07	0.0004***	
$\beta$ -Caryolanol + Guaiol	500 + 500	52 $\pm$ 7	0.53 $\pm$ 0.07	0.0002***	

TABLE 1 Electrophysiological data obtained from  $\alpha_1\beta_2$  GABA<sub>A</sub>Rs expressed in HEK293 cells

Note: c, concentration; SEM, standard error of the mean; levels of significance with p-values \* $p \leq .05$ , \*\* $p \leq .01$ , \*\*\* $p \leq .001$ ; n, number of recorded cells.

cannot exclude maximal positive or negative allosteric modulation at lower or higher concentrations of the GABAergic modulators.

In our initial screen, a modulator concentration of 600  $\mu$ M was used. As it is known that hydrophobic chemicals can bind to plastic tubes (Heinlein et al., 2014) as used in the application system of the electrophysiological setup, samples of the applied solutions were taken before and after passage through the application system. These samples were analyzed by GC-MS to reveal concentration differences between the start and end of the recording session (Supporting information Figure S1). Our data revealed a reduction of the used substances by a mean of 52% (~300  $\mu$ M released by the application system) while transported through the tubing system, suggesting that the real modulatory effect is probably much more pronounced. With a reduction of the concentration of the substances released by the perfusion system, a concentration ~300  $\mu$ M should still be sufficient to modulate GABA<sub>A</sub> receptors (Milanos et al., 2018).

### 3.2 | Modulation of the GABAergic response by co-applied SQTs is difficult to predict

As some SQTs modulate GABA<sub>A</sub>Rs of the  $\alpha_1\beta_2$  subtype positively and others modulate negatively, we hypothesized additive or neutralizing effects for co-applications of two modulators.  $\beta$ -Caryolanol showed the largest positive modulation. It was co-applied with humulol, another positive modulator to investigate additive effects. A second round of co-application analyzed competing effects between SQTs, respectively. Here,  $\beta$ -caryolanol together with the negative modulators  $\alpha$ -bisabolol and guaiol, were used (Figure 3a, b). 10  $\mu$ M GABA were co-applied with 500  $\mu$ M of each modulator. Interestingly, co-application of  $\beta$ -caryolanol and humulol showed no additive modulatory effect (108  $\pm$  9%,  $p = .43$ ). In contrast, co-application of  $\beta$ -caryolanol and  $\alpha$ -bisabolol (56  $\pm$  7%,  $p = .0004$ ) or guaiol (52  $\pm$  7%,  $p = .0002$ ; Table 1) showed significantly enhanced negative modulation of the maximal GABA-induced chloride current.

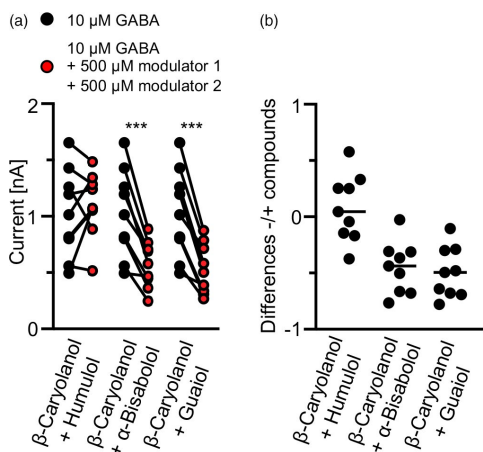


**FIGURE 3** Co-application of two SQTs generates competitive rather than additive modulation at GABA<sub>A</sub>Rs. (a) Currents acquired by patch clamp recordings from HEK293 cells expressing  $\alpha_1\beta_2$  GABA<sub>A</sub>Rs. Currents were recorded during the application of 10  $\mu$ M GABA (black dots) or with co-application of two modulators with a concentration of 500  $\mu$ M per modulator (red dots). Each pair of dots represents one patched HEK293 cell. Experiments from 3 recording sessions using independent cell batches and transfections are shown, number of cells recorded was 9 for every condition, significance level \*\*\* $p \leq .001$ . (b) Differences between each current pair in a are shown

These data argue that the modulatory effect upon co-application of multiple SQTs is difficult to predict and might result from different affinities to the receptor protein.

### 3.3 | The GABA<sub>A</sub>R subunit $\gamma_2$ plays a major role in the modulation by SQTs

SQTs modulate  $\alpha_1\beta_2$  GABA<sub>A</sub>Rs in transfected HEK293 cells, but they might have a different effect in vivo, where multiple GABA receptor configurations are present in the same neuron (phasic receptors containing the  $\gamma_2$  subunit and tonic receptors containing a  $\delta$  subunit). Among possible GABA<sub>A</sub>R subunit combinations,  $\alpha_1\beta_2\gamma_2$  is the most abundant receptor configuration in the brain (Figure 4a) (Whiting, 2003). Patch clamp recordings were performed on hippocampal neurons at day in vitro 18–21 (DIV18–21) to check if endogenous GABA<sub>A</sub>R configurations are affected by SQTs. No significant effects on  $I_{max}$  were observed for  $\beta$ -caryophyllene ( $94 \pm 22\%$ ),  $\beta$ -caryolanol ( $79 \pm 21\%$ ), and  $\alpha$ -humulene ( $93 \pm 19\%$ ) when co-applied with 10  $\mu$ M GABA (Figure 4b–g). However, a significant decrease in current for 10  $\mu$ M GABA + humulol ( $78 \pm 19\%$ ,  $p = .0056$ , Table 2) as well as a significant increase for guaiol ( $120 \pm 27\%$ ,  $p = .0008$ ). These data are in contrast to the effects observed for  $\alpha_1\beta_2$  receptors in transfected HEK293 cells and might argue for differences in GABAergic modulation by

GABA<sub>A</sub>Rs containing  $\gamma$  or also possibly  $\delta$  subunits or other  $\alpha/\beta$  subunits than  $\alpha_1/\beta_2$ . At GABA concentrations of 10  $\mu$ M, tonic GABA<sub>A</sub> receptors including the  $\delta$  subunit are saturated and may less contribute to the observed effects than synaptic receptor compositions including the  $\gamma$  subunit (Karim et al., 2013; Mortensen et al., 2012). Therefore, GABA<sub>A</sub>R modulation was generally tested in hippocampal neurons by diazepam, a positive allosteric modulator, the antagonist picrotoxinin, or the agonist gaboxadol. Diazepam ( $138 \pm 33\%$ ,  $p \leq 0.0001$ ) and gaboxadol ( $176 \pm 41\%$ ,  $p = .0025$ ) application resulted in significantly increased currents and hint for the presence of  $\gamma$  and  $\delta$  containing receptors (Chua & Chebib, 2017). In contrast, GABAergic currents were significantly reduced by co-application of GABA and picrotoxinin to 41%–59% (Figure 4c, f, h–j). These data suggest that the presence of different GABA<sub>A</sub>R configurations in one neuron harboring  $\gamma$  and  $\delta$  subunits may play a role in GABA<sub>A</sub>R modulation by SQTs. GABA<sub>A</sub>Rs containing the  $\gamma_2$  subunit enable phasic inhibition, receptors harboring a  $\delta$  subunit mediate tonic inhibition (Olsen & Sieghart, 2009).

To investigate the SQT modulation on phasic GABA<sub>A</sub>Rs, HEK293 cells were transfected with  $\alpha_1\beta_2\gamma_2$  receptors to see if the presence of the  $\gamma_2$  subunit is responsible for the observed effects in hippocampal neurons (Figure 5a). Similar to the result obtained from whole-cell recordings on primary neurons,  $\beta$ -caryophyllene ( $90 \pm 37\%$ ),  $\beta$ -caryolanol ( $72 \pm 27\%$ ),  $\alpha$ -humulene ( $97 \pm 28\%$ ), and guaiol ( $100 \pm 32\%$ ) had no significant effect on the currents evoked by 10  $\mu$ M GABA, whereas co-application of humulol ( $84 \pm 26\%$ ,  $p = .016$ , Table 3) significantly reduced maximum currents (Figure 5b–g). In transfected HEK293 cells with the  $\alpha_1\beta_2\gamma_2$  subunits, diazepam ( $111 \pm 35\%$ ) elicited increased currents ( $p = .0596$ ). Application of ZnCl<sub>2</sub> ( $92 \pm 36\%$ ) had no significant effect, verifying the presence of the  $\gamma_2$  subunit in the receptor complexes. Picrotoxinin blocked GABA-induced currents by 55%–68%. Representative traces are shown in Figure 5h–j. Taken together, these results indicate that the  $\gamma_2$  subunit plays a major role in the modulation of GABA<sub>A</sub>Rs by SQTs.

### 3.4 | SQTs exhibited rather negative allosteric modulatory potential at tonic GABA<sub>A</sub>Rs

Next, tonic  $\alpha_4\beta_3\delta$  and  $\alpha_6\beta_3\delta$  GABA<sub>A</sub>Rs expressed in HEK293 cells were analyzed (Figure 6a, h). Here again, 10  $\mu$ M GABA together with different SQTs were co-applied. Application of 10  $\mu$ M GABA together with the SQTs saturates tonic receptors (Karim et al., 2013; Mortensen et al., 2012). Therefore, the modulatory potential obtained might differ from SQT effects under non-saturating conditions. All SQTs significantly reduced the maximal current response at  $\alpha_4\beta_3\delta$  receptors (Figure 6b–g, Table 3), with guaiol ( $65 \pm 23\%$ ,  $p = .0075$ ) having the strongest effect. Similar results were obtained for  $\alpha_6\beta_3\delta$  receptors with  $\beta$ -caryophyllene ( $76 \pm 26\%$ ,  $p = .0029$ ) and guaiol ( $75 \pm 33\%$ ,  $p = .0078$ ) significantly reducing GABA-induced  $I_{max}$  values.  $\alpha_4\beta_3\delta$  receptors subtypes were significantly blocked by co-application of GABA and picrotoxinin while picrotoxinin block was less pronounced for  $\alpha_6\beta_3\delta$  not reaching significance ( $p = .0558$ ) in one block of measurements. The presence of the expression of tonic receptors was verified by

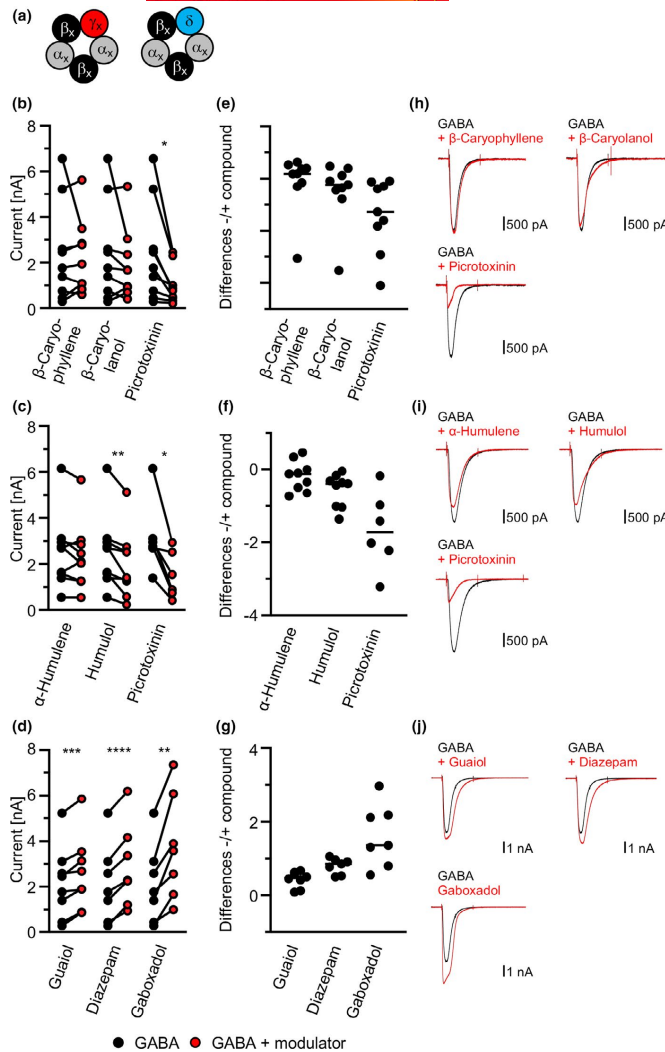


**FIGURE 4** The modulatory potential of SQTs at GABA<sub>A</sub>Rs differs between transfected cells and primary hippocampal neurons. (a) Possible receptor configurations for GABA<sub>A</sub>Rs in hippocampal neurons. Subunits marked with x have multiple subtypes contributing to various receptor combinations, with  $\alpha_1\beta_2\gamma_2$  being the major isoform. (b–d) Absolute currents of patch clamp recordings during application of 10  $\mu$ M GABA (black dots) or with co-application of 600  $\mu$ M modulator (red dots). Furthermore, 10  $\mu$ M GABA was co-applied with 10  $\mu$ M diazepam or 100  $\mu$ M picrotoxinin. 1 mM gaboxadol was applied without co-application of GABA. Each pair of dots represents one patched hippocampal neuron at DIV18–21 in culture. Patch clamp experiments were performed on at least 3 days with cells isolated from different mice ( $n = 3$ ), number of recorded cells varied between 6 and 9 (see also Table 2), significance level \* $p \leq .05$ , \*\* $p \leq .01$ , \*\*\* $p \leq .001$ , \*\*\*\* $p \leq .0001$ . (e–g) Differences between each current pair in b–d are shown. (h–j) Representative current traces for each modulator in b–d are shown. Black traces: 10  $\mu$ M GABA; red traces: 10  $\mu$ M GABA + 600  $\mu$ M modulator/ 10  $\mu$ M diazepam/ 100  $\mu$ M picrotoxinin; 1 mM gaboxadol

gaboxadol which increased current amplitudes for  $\alpha_6\beta_3\delta$  receptors. In sum,  $\delta$ -subunit containing GABA<sub>A</sub>Rs are most probably rather negatively modulated by SQTs.

### 3.5 | SQTs with their lipophilic scaffold fit well to the binding sites of neurosteroids and diazepam localized in the transmembrane segment of GABA<sub>A</sub>Rs

A binding site for SQTs is not described, yet. SQTs are highly hydrophobic. Hence, they might favor a localization within the

transmembrane segment of the GABA<sub>A</sub>R in the lipid bilayer neighborhood. The low-affinity-binding site for diazepam and the neurosteroid-binding site have been described between transmembrane domains of GABA<sub>A</sub>Rs (Masiulis et al., 2019; Miller et al., 2017). Molecular modeling and docking studies were performed for five SQTs investigated in detail in this study, namely  $\beta$ -caryophyllene,  $\beta$ -caryolanol,  $\alpha$ -humulene, humulol, and guaiaiol.  $\beta$ -Caryolanol and humulol are derivatives of  $\beta$ -caryophyllene and  $\alpha$ -humulene (Figure 1a) and differed in modulatory potential at  $\alpha_1\beta_2$  GABA<sub>A</sub>Rs compared to the non-metabolized substances (Figure 2). To determine whether and how the SQTs prefer binding

TABLE 2 Electrophysiological data obtained from hippocampal neurons

Compound	c [ $\mu$ M]	$I_{rel} \pm SEM$ [%]	$I_{abs} \pm SEM$ [nA]	p-values	n
GABA	10	100 $\pm$ 30	2.39 $\pm$ 0.72		9
$\beta$ -Caryophyllene	600	94 $\pm$ 22	2.25 $\pm$ 0.54	0.7294	
$\beta$ -Caryolanol	600	79 $\pm$ 21	1.90 $\pm$ 0.51	0.2557	
Picrotoxinin	100	41 $\pm$ 11	0.98 $\pm$ 0.28	0.0163*	
GABA	10	100 $\pm$ 21	2.54 $\pm$ 0.54		9
$\alpha$ -Humulene	600	93 $\pm$ 19	2.36 $\pm$ 0.49	0.2238	
Humulol	600	78 $\pm$ 19	1.97 $\pm$ 0.49	0.0056**	
Picrotoxinin	100	59 $\pm$ 16	1.51 $\pm$ 0.42	0.0119*	6
GABA	10	100 $\pm$ 26	2.16 $\pm$ 0.56		8
Guaiol	600	120 $\pm$ 27	2.59 $\pm$ 0.58	0.0008***	
Diazepam	10	138 $\pm$ 33	2.92 $\pm$ 0.69	<0.0001****	7
Gaboxadol	1,000	176 $\pm$ 41	3.73 $\pm$ 0.87	0.0025**	

Note: c, concentration; SEM, standard error of the mean; levels of significance with p-values \* $p \leq .05$ , \*\* $p \leq .01$ , \*\*\* $p \leq .001$ , \*\*\*\* $p \leq .0001$ ; n, number of recorded cells.

to the low-affinity diazepam site or the neurosteroid site, a docking to the complete  $\alpha\beta$ - or  $\alpha\alpha$ -interface, respectively, was first performed. Since two possible interfaces can be formed between the  $\alpha$ - and the  $\beta$ -domain, namely  $\beta_3^+ \alpha_1^-$  (diazepam site) and  $\alpha_1^+ \beta_3^-$  (an alternative site), both were studied together. Although all substances were found in the diazepam site, often showing an extensive and reasonable overlap with the benzodiazepine-scaffold,  $\alpha$ -humulene, and  $\beta$ -caryophyllene leave several hydrogen bonding groups of the pocket unsaturated. The hydroxylated compounds humulol (S-humulol but not R-humulol; both might be present in the humulol fraction) and  $\beta$ -caryolanol form hydrogen bonds to the  $\beta_3$ M2 or M3 side chains ( $\beta_3^+$ ) within the diazepam-binding site, guaiol to helix  $\alpha_1$ M1 ( $\alpha_1^-$ ), all fitting nicely into this pocket. With exception of R-humulol, the binding modes of the SQTs in the alternative  $\alpha_1^+ \beta_3^-$ -site are less preferred.

In the case of docking to the entire  $\alpha\alpha$ -interface, all compounds could be found in the location analogous to the diazepam site, but only for the three compounds with hydroxy groups binding modes were obtained in the neurosteroid-binding site. A focused docking to this particular site showed that  $\alpha$ -humulene and  $\beta$ -caryophyllene cannot form particularly favorable interactions here, whereas humulol,  $\beta$ -caryolanol, and also guaiol are able to form at least one of the two polar interactions of the endogenous ligand pregnanolone to the receptor backbone and fit well with their lipophilic scaffold (Figure 7). Thus, binding to both, the diazepam- and the pregnanolone-binding site can be suggested, with the poses in the first one scored better.

#### 4 | DISCUSSION

GABA<sub>A</sub>Rs facilitate inhibitory neurotransmission in the central nervous system. They present a potential target for anticonvulsive and anesthetic drugs (Chua & Chebib, 2017; Krall et al., 2015; Kreuzer et al., 2019; Laverty et al., 2017; Zhu et al., 2018).

Moreover, naturally occurring substances, such as terpenoids, are able to modulate GABAergic function (Manayi et al., 2016). In this study, SQTs isolated from chamomile were found to harbor allosteric potential at GABA<sub>A</sub>Rs in transfected cell lines and primary neurons. Previously, we have identified odoriferous monoterpene structures from *Sideritis* extracts with a preference of a bicyclic character in combination with the presence of a hydroxy group harboring positive allosteric potential at GABA<sub>A</sub>Rs of the  $\alpha_1\beta_2$  configuration in vitro (Kessler et al., 2012, 2014). Terpenoids represent a diverse group of natural compounds formed by the condensation of isoprene units with the potential to modulate GABA<sub>A</sub>Rs and thus discussed for treatment of CNS disorders (Manayi et al., 2016). Valerenic acid, a sesquiterpenoid from *Valeriana officinalis* L., is used to treat anxiety and sleep disorders. It binds to the GABA<sub>A</sub>Rs dependent on the  $\beta$  isotype present in the complex (Khom et al., 2007). For bilobalide, present in *Ginkgo biloba*, different actions at the GABA<sub>A</sub>R have been described. Anticonvulsant but also antagonistic action at  $\alpha_1\beta_2\gamma_{2L}$  GABA<sub>A</sub>Rs similar to bicuculline and picrotoxin have been found (Huang et al., 2003; Kiewert et al., 2007). Here, we studied the neurotropic potential of SQTs assumed to be taken up by nutrition and digested in the human body. Biotransformation processes might alter the modulatory potential, for example, gastrointestinal processes were identified to modulate the chemical composition of ingested aroma constituents thus changing bioactivity of essential oils (Heinlein & Buettner, 2012). However, about the underlying mechanism of the gut-brain axis there is little systematized effort.

$\alpha$ -humulene, a monocyclic, and  $\beta$ -caryophyllene, a bicyclic sesquiterpene, are major components of the volatile fraction of hop but also part of many other essential oils. As shown in previous studies, metabolization processes taking place during intake and digestion of these compounds lead to changes in the structure. Both,  $\alpha$ -humulene and  $\beta$ -caryophyllene are hydroxylated because of the low pH in the gastric phase of digestion which

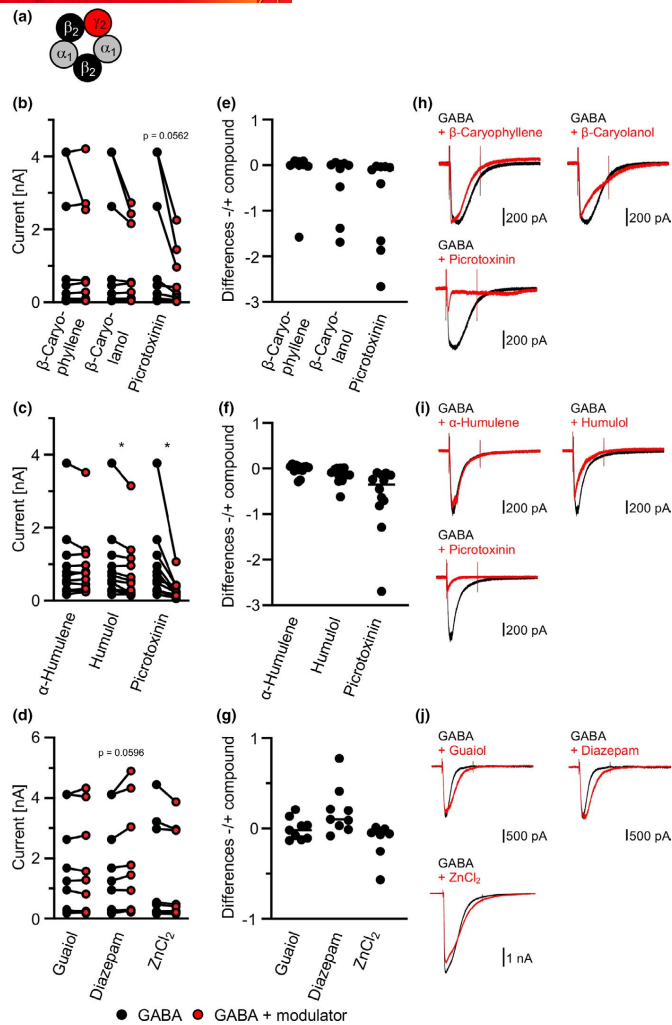


**FIGURE 5** SQT modulation of phasic  $\alpha_1\beta_2\gamma_2$  GABA<sub>A</sub>Rs. (a–d) Absolute currents of patch clamp recordings during application of 10  $\mu$ M GABA (black dots) or with co-application of 600  $\mu$ M modulator (red dots), recorded from HEK293 cells transfected with  $\alpha_1\beta_2\gamma_2$  GABA<sub>A</sub>Rs. 10  $\mu$ M GABA was co-applied with 10  $\mu$ M diazepam, 10  $\mu$ M  $ZnCl_2$ , or 100  $\mu$ M picrotoxinin. Each pair of dots represents one patched HEK293 cell. Patch clamp experiments were performed on at least 3 days with different cell batches, total numbers of recorded cells ( $n = 8$ –12) are shown in Table 3. \* $p \leq .05$ , \*\* $p \leq .01$ . (e–g) Differences between each current pair in b–d are shown. (h–j) Example traces for each modulator in b–d are shown. Black traces: 10  $\mu$ M GABA; red traces: 10  $\mu$ M GABA + 600  $\mu$ M modulator/ 10  $\mu$ M diazepam/ 10  $\mu$ M  $ZnCl_2$ / 100  $\mu$ M picrotoxinin

may affect the modulatory potential of the substance (Heinlein & Buettner, 2012). Indeed, in transfected HEK293 cells with GABA<sub>A</sub>Rs of the  $\alpha_1\beta_2$  subtype, the hydroxylated metabolites humulol and  $\beta$ -caryolanol showed positive allosteric potential by significantly increasing the GABAergic current upon co-application

of GABA in a low concentration. In contrast, the parent compounds  $\alpha$ -humulene and  $\beta$ -caryophyllene had no effect on GABAergic current. These data are in line with previous reports showing positive allosteric modulation of the GABAergic currents by terpenes and terpenoids harboring a hydroxy group (Kessler

TABLE 3 Electrophysiological data obtained from  $\alpha_1\beta_2\gamma_2$ ,  $\alpha_4\beta_3\delta$ , and  $\alpha_6\beta_3\delta$  GABA<sub>A</sub>Rs

GABA <sub>A</sub> R configuration	Compound	c [ $\mu$ M]	$I_{rel} \pm SEM$ [%]	$I_{obs} \pm SEM$ [nA]	p-values	n
$\alpha_1\beta_2\gamma_2$	GABA	10	100 $\pm$ 42	1.38 $\pm$ 0.58		9
	$\beta$ -Caryophyllene	600	90 $\pm$ 37	1.24 $\pm$ 0.51	0.4508	
	$\beta$ -Caryolanol	600	72 $\pm$ 27	0.99 $\pm$ 0.37	0.1230	
	Picrotoxinin	100	45 $\pm$ 19	0.62 $\pm$ 0.26	0.0562	
$\alpha_1\beta_2\gamma_2$	GABA	10	100 $\pm$ 31	0.93 $\pm$ 0.29		12
	$\alpha$ -Humulene	600	97 $\pm$ 28	0.90 $\pm$ 0.26	0.4655	
	Humulol	600	84 $\pm$ 26	0.78 $\pm$ 0.25	0.0162*	
	Picrotoxinin	100	32 $\pm$ 9	0.30 $\pm$ 0.08	0.0137*	
$\alpha_1\beta_2\gamma_2$	GABA	10	100 $\pm$ 31	1.72 $\pm$ 0.52		9
	Guaiol	600	100 $\pm$ 32	1.71 $\pm$ 0.54	0.8838	
	Diazepam	10	111 $\pm$ 35	1.91 $\pm$ 0.59	0.0596	
	ZnCl <sub>2</sub>	10	92 $\pm$ 36	1.41 $\pm$ 0.55	0.1079	8
$\alpha_4\beta_3\delta$	GABA	10	100 $\pm$ 38	0.98 $\pm$ 0.38		9
	$\beta$ -Caryophyllene	600	80 $\pm$ 33	0.78 $\pm$ 0.32	0.0118*	
	$\beta$ -Caryolanol	600	72 $\pm$ 32	0.70 $\pm$ 0.31	0.0049**	
	Picrotoxinin	100	27 $\pm$ 8	0.26 $\pm$ 0.08	0.0421*	
$\alpha_4\beta_3\delta$	GABA	10	100 $\pm$ 27	0.78 $\pm$ 0.21		10
	$\alpha$ -Humulene	600	77 $\pm$ 21	0.60 $\pm$ 0.16	0.0248*	
	Humulol	600	69 $\pm$ 17	0.53 $\pm$ 0.13	0.0199*	
	Picrotoxinin	100	32 $\pm$ 9	0.25 $\pm$ 0.07	0.0178*	
$\alpha_4\beta_3\delta$	GABA	10	100 $\pm$ 31	1.27 $\pm$ 0.39		9
	Guaiol	600	65 $\pm$ 23	0.83 $\pm$ 0.29	0.0075**	
	Gaboxadol	1,000	90 $\pm$ 30	1.15 $\pm$ 0.38	0.3296	
$\alpha_6\beta_3\delta$	GABA	10	100 $\pm$ 30	0.52 $\pm$ 0.16		9
	$\beta$ -Caryophyllene	600	76 $\pm$ 26	0.39 $\pm$ 0.14	0.0029**	
	$\beta$ -Caryolanol	600	96 $\pm$ 35	0.50 $\pm$ 0.18	0.6095	
	Picrotoxinin	100	24 $\pm$ 6	0.12 $\pm$ 0.03	0.0225*	
$\alpha_6\beta_3\delta$	GABA	10	100 $\pm$ 33	0.17 $\pm$ 0.06		8
	$\alpha$ -Humulene	600	86 $\pm$ 27	0.15 $\pm$ 0.05	0.2121	
	Humulol	600	98 $\pm$ 30	0.17 $\pm$ 0.05	0.8655	
	Picrotoxinin	100	43 $\pm$ 16	0.07 $\pm$ 0.03	0.0558	
$\alpha_6\beta_3\delta$	GABA	10	100 $\pm$ 37	0.50 $\pm$ 0.18		8
	Guaiol	600	75 $\pm$ 33	0.37 $\pm$ 0.16	0.0078**	
	Gaboxadol	1,000	166 $\pm$ 69	0.83 $\pm$ 0.34	0.0918	

Note: c, concentration; SEM, standard error of the mean; levels of significance with p-values \* $p \leq .05$ , \*\* $p \leq .01$ ; n, number of recorded cells.

et al., 2014). Guaiol, however, a sesquiterpenoid also bearing one hydroxy group like  $\beta$ -caryolanol and humulol exhibited a negative allosteric effect at the same receptor type. Attempts to predict additive or neutralizing effects using co-application of two sesquiterpenes harboring positive allosteric potential or with contrary potential failed. Thus, a prediction of the neurotropic activity seems to be difficult from the observed functional data following single application. Contrary actions at GABA<sub>A</sub>Rs have been observed for bilobalide but also for other substances such as ethanol, arguing for affinity, subtype-specific, and possibly cell-specific effects (Forstera et al., 2016; Kiewert et al., 2007).

The lipophilicity of SQTs does allow binding to the lipid environment of GABA<sub>A</sub>Rs. Structural similarities to diazepam and neurosteroids point also to binding in a hydrophobic pocket formed between transmembrane domains of the GABA<sub>A</sub>R (Lavery et al., 2017; Masiulis et al., 2019). Computational docking studies at the neurosteroid and the diazepam-binding sites, which are localized in a lipophilic surrounding, indicated possible binding modes in both sites. Nevertheless, the diazepam site as well as the alternative  $\alpha_1^+\beta_3$ -site also contain some polar amino acids. As these would presumably interact with water molecules in the unbound state, binding at these sites would be expected to result in a strong desolvation penalty,



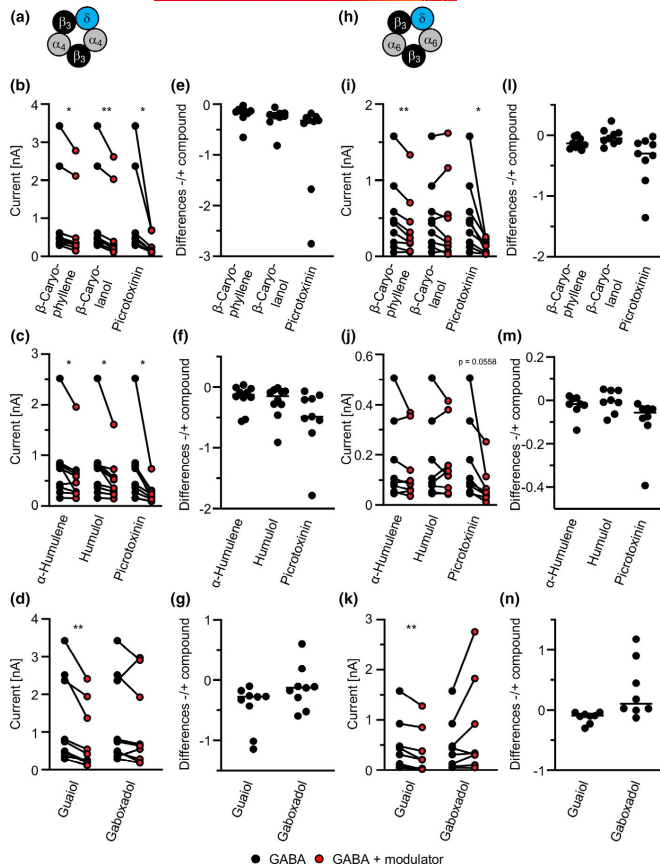


**FIGURE 6** Modulation of tonic  $\alpha_4\beta_3\delta$  and  $\alpha_6\beta_3\delta$  GABA<sub>A</sub>Rs by SQTs. (a–g) Measurements on  $\alpha_4\beta_3\delta$  GABA<sub>A</sub>Rs. (h–n) Measurements on  $\alpha_6\beta_3\delta$  GABA<sub>A</sub>Rs. B–d, i–k) Absolute currents of patch clamp recordings from HEK293 cells transfected with  $\alpha_4\beta_3\delta$  or  $\alpha_6\beta_3\delta$  GABA<sub>A</sub>Rs, respectively, during application of 10  $\mu$ M GABA (black dots) or following co-application of 600  $\mu$ M modulator (red dots). Furthermore, 10  $\mu$ M GABA was co-applied with 100  $\mu$ M picrotoxinin. 1 mM gaboxadol was applied without co-application of GABA. Each pair of dots represents one patched HEK293 cell. Patch clamp experiments were performed on at least 3 days with different cell batches, number of recorded cells were between 8 and 10. \* $p \leq .05$ , \*\* $p \leq .01$ . (e–g, l–m) Differences between each current pair in b–d, i–k are shown

which is not sufficiently considered by the scoring functions. Even though humulol and  $\beta$ -caryolanol can form polar interactions here, the binding modes of these otherwise completely hydrophobic molecules always show an unfavorably positioned methyl group, for instance, near the negatively charged Asp272 of helix  $\beta_3$ M3. The pregnanolone-binding site, on the other hand, is composed entirely of lipophilic amino acids except at the extreme ends, where the endogenous ligand forms polar interactions with the receptor. In addition, this binding site is rather surface-exposed. This is reflected by a comparison of buried surfaces: whereas diazepam is completely buried and shows no solvent accessible surface area in the complex, for pregnanolone only 69% of the ligand surface area are buried upon binding to the receptor. However, the remaining 31% of the apolar ligand surface are not directed toward the aqueous solution, but rather toward the lipid bilayer, which is energetically attractive. This difference in burial is markedly reflected in the scoring, which favors direct interactions, but does not consider favorable exposure to a lipophilic environment. Accordingly, better scores of the poses

in the diazepam-binding site should not be overinterpreted. Rather, the structure of the neurosteroid-binding site would better match the scaffold of hydroxylated SQTs, which is also supported by the observation that the hydroxylated SQTs, when docked to the entire  $\alpha\alpha$ -interface, were located in the neurosteroid-binding site, whereas the non-hydroxylated ones were not found at that location. Hence, binding to the lipophilic interface forming the neurosteroid-binding site is possibly preferred over the diazepam-binding site, especially for humulol and  $\beta$ -caryolanol. In addition, it is known that the hydroxy group of neurosteroids is crucially involved in their GABA-potential effects (Miller et al., 2017), which could possibly explain the effects of SQTs. Nevertheless, an interaction to other modulatory proteins of the GABA<sub>A</sub>R cannot be excluded.

Previous data on monoterpenoids suggested positive allosteric potential at GABA<sub>A</sub>Rs independent of the  $\gamma_2$  subunit (Kessler et al., 2014). Our initial comparisons of  $\alpha$ -humulene and  $\beta$ -caryophyllene versus their respective derivatives humulol and  $\beta$ -caryolanol, suggested a similar pattern. However, other tested

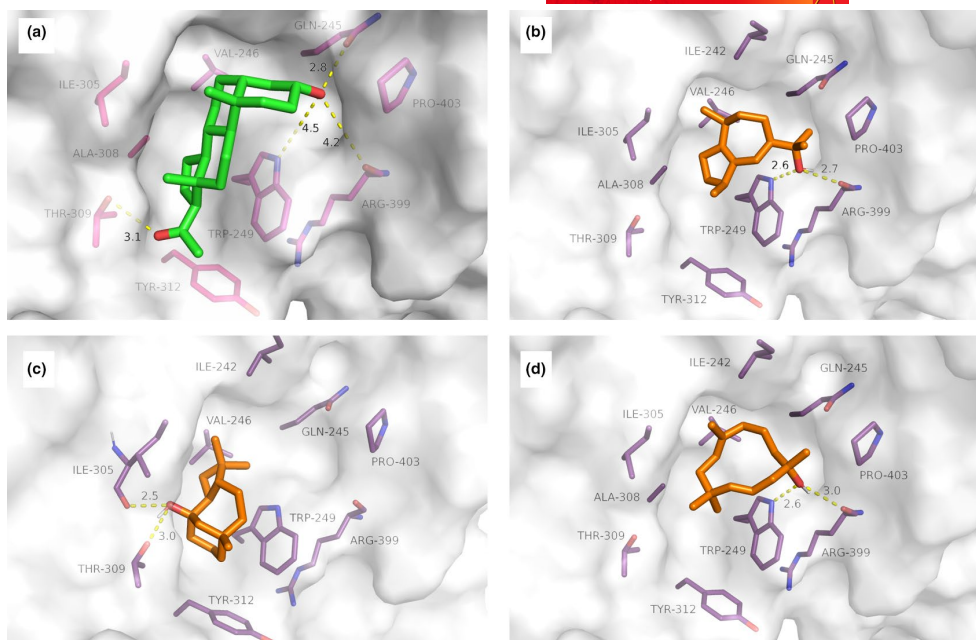


**FIGURE 7** Molecular docking results at the neurosteroid-binding site localized in the TM domain of the GABA<sub>A</sub>R. As a reference, the experimentally observed binding mode of pregnanolone in the  $\alpha$ -interface (PDB: 5O8F) is shown in (a). Binding modes proposed by docking of the SQTs gauiol (b),  $\beta$ -caryolanol (c), and S-humulol (d) are illustrated based on the top-scoring docking solutions

sesquiterpenoids also harboring a hydroxy group, for example, bisabolol, bisabolol oxide B, and spathulenol did not follow this pattern. Therefore, we investigated sesquiterpene modulation at isolated primary neurons of the hippocampus rich in GABAergic interneurons (Pelkey et al., 2017). The main receptor configuration is the  $\alpha_1\beta_2\gamma_2$  subtype (Olsen & Sieghart, 2008). Those GABA<sub>A</sub>Rs enable phasic inhibition whereas subtypes including the  $\alpha_4$ ,  $\alpha_6$ , or  $\delta$  subunit regulate long-lasting inhibition and thereby control the excitability of the neurons (Lee & Maguire, 2014). The neurotropic activity of the SQTs was different on primary hippocampal neurons in comparison to the controlled over-expression of the  $\alpha_1\beta_2$  subtype in HEK293 cells. While  $\beta$ -caryolanol showed no longer a significant modulatory effect, humulol turned into a negative and gauiol into a positive allosteric modulator. Control measurements using the superagonist gaboxadol and the benzodiazepine agonist diazepam confirmed the presence of phasic as well as tonic GABA<sub>A</sub>Rs in the hippocampal neurons. Back to controlled over-expression, the presence of the  $\gamma_2$  subunit in the  $\alpha_1\beta_2\gamma_2$  subunit composition led to the same observation as in hippocampal neurons with humulol as a negative allosteric modulator. Hence, the presence of the  $\gamma_2$  subunit in the majority of GABA<sub>A</sub>Rs (65%) in primary neurons is an important component for sesquiterpene modulation. At tonic GABA<sub>A</sub>Rs in the  $\alpha_4\beta_3\delta$  configuration,  $\beta$ -caryophyllene and  $\alpha$ -humulene as well as the sesquiterpenoids humulol and

$\beta$ -caryolanol but also gauiol exhibited negative allosteric modulation. However, all data were obtained under GABA-saturating conditions. At  $\alpha_6\beta_3\delta$  receptors,  $\beta$ -caryophyllene and gauiol but not  $\beta$ -caryolanol, humulene and humulol decreased GABAergic currents. As both tonic receptor configurations ( $\alpha_4\beta_3\delta$ ,  $\alpha_6\beta_3\delta$ ) harbor  $\beta_3$ , the observed effects are most probably independent of the  $\beta$  subunit and therefore dissimilar to modulation of GABA<sub>A</sub>Rs by valerianic acid remarkably dependent on the  $\beta$  subunit isotype ( $\beta_3 < \beta_2 < \beta_1$ ) (Khom et al., 2007).

Positive allosteric modulation of tonic GABA<sub>A</sub>Rs has been reported for monoterpene structures, verbenol and myrtenol, measured on hippocampal slices (van Brederode et al., 2016). In contrast to monoterpenes, our results show the negative modulatory potential of SQTs at GABA<sub>A</sub>Rs mainly at tonic receptor subtypes. Bilobalide, a sesquiterpene lactone, antagonizes GABA<sub>A</sub>Rs similar to bicuculline and picrotoxinin and the SQTs used here, but also exerts anticonvulsant activity via a presynaptic route maintaining the GABA levels and thus the GAD (glutamate decarboxylase) activity in the hippocampus and cerebral cortex (Sasaki et al., 2000). The action of sesquiterpenes at postsynaptic GABA<sub>A</sub>Rs but also at presynaptic sites regulating the activity of the GABA synthesizing enzyme GAD has been supported recently for the malaria drugs artemisinins. Artemisinins modulate GABA<sub>A</sub>Rs via targeting the binding epitope of the scaffold protein gephyrin by hindering the critical interaction of gephyrin and GABA<sub>A</sub>Rs



and thus decreasing GABAergic inhibition (Kasaragod et al., 2019). Moreover, sesquiterpenes interact with PDXK (pyridoxal kinase), an enzyme regulating the synthesis of GABA via GAD activity in presynaptic terminals (Kasaragod et al., 2020). Both of the abovementioned actions, however, require a longer presence of the SQTs enabling uptake into the cell to facilitate their action.

Based on a qualitative analysis of the binding modes obtained from our docking studies, preferential binding of the hydroxy group carrying SQTs to the neurosteroid-binding site and the diazepam site seems possible. Furthermore, we cannot exclude an indirect interaction of SQTs with associated proteins of the GABA<sub>A</sub>R or interactions with presynaptic enzymes and thereby modulating GABAergic activity. In our approach, the SQTs were co-applied together with the neurotransmitter GABA enabling monitoring of short and direct effects on receptor opening and closing only. Together with the recently observed shared potential of SQTs at postsynaptic and presynaptic sites, short-term and long-term aspects at GABAergic neurotransmission in the presence of SQTs should be investigated in more detail in the future, combined with affinity and binding studies to differentiate direct from indirect actions of SQTs on GABAergic inhibition processes. A better understanding of these mechanisms will further define their therapeutic potential for CNS disorders.

#### ACKNOWLEDGMENTS

This work was supported by DFG VI586/8-1 to C.V. and DFG BU 1351/17-1 and INST 90/979-1 FUGG to A.B. B.S. is grateful to Julian Nehr and Patrick Ballin for their support in laboratory work related to the identification and isolation of SQTs. D.J. is supported by the GSLS Würzburg.

All experiments were conducted in compliance with the ARRIVE guidelines.

#### CONFLICT OF INTEREST

The authors declare no conflict of interest.

#### AUTHORS' CONTRIBUTIONS

CV and AB participated in research design. Electrophysiology was performed by DJ. GC-MS and isolation of SQTs was performed by BS. DJ, CV, BS, and HL carried out data analysis. MZ and CS carried out modeling and docking analysis. CV, DJ, and BS contributed to the writing of the manuscript.

#### DATA AVAILABILITY STATEMENT

The data that support the findings of this study are available from the corresponding author upon reasonable request.

#### ORCID

Dieter Janzen  <https://orcid.org/0000-0001-7258-9043>

Benedikt Slavik  <https://orcid.org/0000-0002-6237-8012>

Helene M. Loos  <https://orcid.org/0000-0002-9112-5735>

Andrea Buettner  <https://orcid.org/0000-0002-6205-5125>

Carmen Villmann  <https://orcid.org/0000-0003-1498-6950>

#### REFERENCES

- Alvarez, L. D., & Estrin, D. A. (2015). Exploring the molecular basis of neurosteroid binding to the beta3 homopentameric GABA<sub>A</sub> receptor. *Journal of Steroid Biochemistry and Molecular Biology*, 154, 159–167.
- Alvarez, L. D., & Pecci, A. (2018). Structure and dynamics of neurosteroid binding to the alpha1beta2gamma2 GABA<sub>A</sub> receptor. *Journal of Steroid Biochemistry and Molecular Biology*, 182, 72–80.
- Bemelmans, J. (1979). *Progress in flavour research* (pp. 79–98). Applied Science Publishers Ltd.
- Chua, H. C., & Chebib, M. (2017). GABA<sub>A</sub> receptors and the diversity in their structure and pharmacology. *Advances in Pharmacology*, 79, 1–34.
- Engel, W., Bahr, W., & Schieberle, P. (1999). Solvent assisted flavour evaporation - a new and versatile technique for the careful and direct isolation of aroma compounds from complex food matrices. *European Food Research and Technology*, 209, 237–241. <https://doi.org/10.1007/s002170050486>
- Forstera, B., Castro, P. A., Moraga-Cid, G., & Aguayo, L. G. (2016). Potentiation of gamma aminobutyric acid receptors (GABA<sub>A</sub>R) by ethanol: How are inhibitory receptors affected? *Frontiers in Cellular Neuroscience*, 10, 114. <https://doi.org/10.3389/fncel.2016.00114>
- Fritschy, J. M., & Mohler, H. (1995). GABA<sub>A</sub>-receptor heterogeneity in the adult rat brain: Differential regional and cellular distribution of seven major subunits. *The Journal of Comparative Neurology*, 359, 154–194. <https://doi.org/10.1002/cne.903590111>
- Heinlein, A., & Buettner, A. (2012). Monitoring of biotransformation of hop aroma compounds in an in vitro digestion model. *Food & Function*, 3, 1059–1067. <https://doi.org/10.1039/c2fo30061c>
- Heinlein, A., Metzger, M., Walles, H., & Buettner, A. (2014). Transport of hop aroma compounds across Caco-2 monolayers. *Food Function*, 5, 2719–2730. <https://doi.org/10.1039/C3FO60675A>
- Huang, S. H., Duke, R. K., Chebib, M., Sasaki, K., Wada, K., & Johnston, G. A. (2003). Bilobalide, a sesquiterpene trilactone from Ginkgo biloba, is an antagonist at recombinant alpha1beta2gamma2L GABA(A) receptors. *European Journal of Pharmacology*, 464, 1–8.
- Johnston, G. A., Hanrahan, J. R., Chebib, M., Duke, R. K., & Mewett, K. N. (2006). Modulation of ionotropic GABA receptors by natural products of plant origin. *Advances in Pharmacology*, 54, 285–316.
- Karim, N., Wellendorph, P., Absalom, N., Johnston, G. A., Hanrahan, J. R., & Chebib, M. (2013). Potency of GABA at human recombinant GABA(A) receptors expressed in *Xenopus* oocytes: A mini review. *Amino Acids*, 44, 1139–1149. <https://doi.org/10.1007/s00726-012-1456-y>
- Kasaragod, V. B., Hausrat, T. J., Schaefer, N., Kuhn, M., Christensen, N. R., Tessmer, I., Maric, H. M., Madsen, K. L., Sotriuffer, C., Villmann, C., Kneussel, M., & Schindelin, H. (2019). Elucidating the molecular basis for inhibitory neurotransmission regulation by artemisinins. *Neuron*, 101(673–689), e611. <https://doi.org/10.1016/j.neuron.2019.01.001>
- Kasaragod, V. B., Pacios-Michelena, A., Schaefer, N., Zheng, F., Bader, N., Alzheimer, C., Villmann, C., & Schindelin, H. (2020). Pyridoxal kinase inhibition by artemisinins down-regulates inhibitory neurotransmission. *Proc Natl Acad Sci U S A*, 117, 33235–33245. <https://doi.org/10.1073/pnas.2008695117>
- Kasaragod, V. B., & Schindelin, H. (2019). Structure of heteropentameric GABA<sub>A</sub> receptors and receptor-anchoring properties of Gephyrin. *Frontiers in Molecular Neuroscience*, 12, 191. <https://doi.org/10.3389/fnmol.2019.00191>
- Kessler, A., Sahin-Nadeem, H., Lummis, S. C., Weigel, I., Pischetsrieder, M., Buettner, A., & Villmann, C. (2014). GABA(A) receptor modulation by terpenoids from *Sideritis* extracts. *Molecular Nutrition & Food Research*, 58, 851–862.
- Kessler, A., Villmann, C., Sahin-Nadeem, H., Pischetsrieder, M., & Buettner, A. (2012). GABA<sub>A</sub> receptor modulation by the volatile

- fractions of *Sideritis* species used as 'Greek' or 'Turkish' mountain tea. *Flavour and Fragrance Journal*, 27, 297–303.
- Khom, S., Baburin, I., Timin, E., Hohaus, A., Trauner, G., Kopp, B., & Hering, S. (2007). Valerianic acid potentiates and inhibits GABA(A) receptors: Molecular mechanism and subunit specificity. *Neuropharmacology*, 53, 178–187. <https://doi.org/10.1016/j.neuropharm.2007.04.018>
- Kiewert, C., Kumar, V., Hildmann, O., Rueda, M., Hartmann, J., Naik, R. S., & Klein, J. (2007). Role of GABAergic antagonism in the neuroprotective effects of bilobalide. *Brain Research*, 1128, 70–78. <https://doi.org/10.1016/j.brainres.2006.10.042>
- Krall, J., Balle, T., Krogsgaard-Larsen, N., Sorensen, T. E., Krogsgaard-Larsen, P., Kristiansen, U., & Frolund, B. (2015). GABA<sub>A</sub> receptor partial agonists and antagonists: Structure, binding mode, and pharmacology. *Advances in Pharmacology*, 72, 201–227.
- Kreuzer, M., Garcia, P. S., Brucklacher-Waldert, V., Claassen, R., Schneider, G., Antkowiak, B., & Drexler, B. (2019). Diazepam and ethanol differently modulate neuronal activity in organotypic cortical cultures. *BMC Neuroscience*, 20, 58. <https://doi.org/10.1186/s12868-019-0540-6>
- Laverty, D., Thomas, P., Field, M., Andersen, O. J., Gold, M. G., Biggin, P. C., Gielen, M., & Smart, T. G. (2017). Crystal structures of a GABA<sub>A</sub>-receptor chimera reveal new endogenous neurosteroid-binding sites. *Nature Structural & Molecular Biology*, 24, 977–985. <https://doi.org/10.1038/nsmb.3477>
- Lee, V., & Maguire, J. (2014). The impact of tonic GABA<sub>A</sub> receptor-mediated inhibition on neuronal excitability varies across brain region and cell type. *Frontiers in Neural Circuits*, 8, 3. <https://doi.org/10.3389/fncir.2014.00003>
- Manayi, A., Nabavi, S. M., Daglia, M., & Jafari, S. (2016). Natural terpenoids as a promising source for modulation of GABAergic system and treatment of neurological diseases. *Pharmacological Reports*, 68, 671–679. <https://doi.org/10.1016/j.pharep.2016.03.014>
- Masiulis, S., Desai, R., Uchański, T., Serna Martin, I., Laverty, D., Karia, D., Malinauskas, T., Zivanov, J., Pardon, E., Kotecha, A., Steyaert, J., Miller, K. W., & Aricescu, A. R. (2019). GABA<sub>A</sub> receptor signaling mechanisms revealed by structural pharmacology. *Nature*, 565, 454–459. <https://doi.org/10.1038/s41586-018-0832-5>
- Milanos, S., Kuenzel, K., Gilbert, D. F., Janzen, D., Sasi, M., Buettner, A., Frimurer, T. M., & Villmann, C. (2018). Structural changes at the myrtenol backbone reverse its positive allosteric potential into inhibitory GABA<sub>A</sub> receptor modulation. *Biological Chemistry*, 399, 549–563.
- Miller, P. S., Scott, S., Masiulis, S., De Colibus, L., Pardon, E., Steyaert, J., & Aricescu, A. R. (2017). Structural basis for GABA<sub>A</sub> receptor potentiation by neurosteroids. *Nature Structural & Molecular Biology*, 24, 986–992. <https://doi.org/10.1038/nsmb.3484>
- Morris, G. M., Goodsell, D. S., Halliday, R. S., Huey, R., Hart, W. E., Belew, R. K., & Olson, A. J. (1998). Automated docking using a Lamarckian genetic algorithm and an empirical binding free energy function. *Journal of Computational Chemistry*, 19, 1639–1662. [https://doi.org/10.1002/\(SICI\)1096-987X\(199811\)19:14<1639::AID-JCC10>3.0.CO;2-B](https://doi.org/10.1002/(SICI)1096-987X(199811)19:14<1639::AID-JCC10>3.0.CO;2-B)
- Mortensen, M., Patel, B., & Smart, T. G. (2012). GABA potency at GABA(A) receptors found in synaptic and extrasynaptic zones. *Frontiers in Cellular Neuroscience*, 6, 1. <https://doi.org/10.3389/fncel.2012.00001>
- Olsen, R. W. (2018). GABA<sub>A</sub> receptor: Positive and negative allosteric modulators. *Neuropharmacology*, 136, 10–22. <https://doi.org/10.1016/j.neuropharm.2018.01.036>
- Olsen, R. W., & Sieghart, W. (2008). International Union of Pharmacology. LXX. Subtypes of gamma-aminobutyric acid(A) receptors: Classification on the basis of subunit composition, pharmacology, and function. Update. *Pharmacological Reviews*, 60, 243–260.
- Olsen, R. W., & Sieghart, W. (2009). GABA<sub>A</sub> receptors: Subtypes provide diversity of function and pharmacology. *Neuropharmacology*, 56, 141–148. <https://doi.org/10.1016/j.neuropharm.2008.07.045>
- Pelkey, K. A., Chittajallu, R., Craig, M. T., Tricoire, L., Wester, J. C., & McBain, C. J. (2017). Hippocampal GABAergic inhibitory interneurons. *Physiological Reviews*, 97, 1619–1747. <https://doi.org/10.1152/physrev.00007.2017>
- Rudolph, U., & Knoflach, F. (2011). Beyond classical benzodiazepines: Novel therapeutic potential of GABA<sub>A</sub> receptor subtypes. *Nature Reviews Drug Discovery*, 10, 685–697. <https://doi.org/10.1038/nrd3502>
- Sasaki, K., Hatta, S., Wada, K., Ohshika, H., & Haga, M. (2000). Bilobalide prevents reduction of gamma-aminobutyric acid levels and glutamic acid decarboxylase activity induced by 4-O-methylpyridoxine in mouse hippocampus. *Life Sciences*, 67, 709–715.
- Sieghart, W. (2006). Structure, pharmacology, and function of GABA<sub>A</sub> receptor subtypes. *Advances in Pharmacology*, 54, 231–263.
- Silva, A. R., Grosso, C., Delerue-Matos, C., & Rocha, J. M. (2019). Comprehensive review on the interaction between natural compounds and brain receptors: Benefits and toxicity. *European Journal of Medicinal Chemistry*, 174, 87–115. <https://doi.org/10.1016/j.ejmech.2019.04.028>
- Simon, J., Wakimoto, H., Fujita, N., Lalande, M., & Barnard, E. A. (2004). Analysis of the set of GABA(A) receptor genes in the human genome. *Journal of Biological Chemistry*, 279, 41422–41435. <https://doi.org/10.1074/jbc.M401354200>
- van Brederode, J., Atak, S., Kessler, A., Pischetsrieder, M., Villmann, C., & Alzheimer, C. (2016). The terpenoids myrtenol and verbenol act on delta subunit-containing GABA<sub>A</sub> receptors and enhance tonic inhibition in dentate gyrus granule cells. *Neuroscience Letters*, 628, 91–97.
- Wagoner, K. R., & Czajkowski, C. (2010). Stoichiometry of expressed alpha(4)beta(2)delta gamma-aminobutyric acid type A receptors depends on the ratio of subunit cDNA transfected. *Journal of Biological Chemistry*, 285, 14187–14194.
- Walters, R. J., Hadley, S. H., Morris, K. D., & Amin, J. (2000). Benzodiazepines act on GABA<sub>A</sub> receptors via two distinct and separable mechanisms. *Nature Neuroscience*, 3, 1274–1281. <https://doi.org/10.1038/81800>
- Whiting, P. J. (2003). GABA-A receptor subtypes in the brain: A paradigm for CNS drug discovery? *Drug Discovery Today*, 8, 445–450. [https://doi.org/10.1016/S1359-6446\(03\)02703-X](https://doi.org/10.1016/S1359-6446(03)02703-X)
- Zhu, S., Novello, C. M., Teng, J., Walsh, R. M., Jr, Kim, J. J., & Hibbs, R. E. (2018). Structure of a human synaptic GABA<sub>A</sub> receptor. *Nature*, 559, 67–72. <https://doi.org/10.1038/s41586-018-0255-3>

#### SUPPORTING INFORMATION

Additional supporting information may be found online in the Supporting Information section.

**How to cite this article:** Janzen, D., Slavik, B., Zehe, M., Sotriffer, C., Loos, H. M., Buettner, A., & Villmann, C. (2021). Sesquiterpenes and sesquiterpenoids harbor modulatory allosteric potential and affect inhibitory GABA<sub>A</sub> receptor function in vitro. *Journal of Neurochemistry*, 00, 1–15. <https://doi.org/10.1111/jnc.15469>

## SUPPORTING INFORMATION

### MATERIALS AND METHODS:

#### QUANTIFICATION OF SQTs APPLIED IN THE ELECTROPHYSIOLOGICAL EXPERIMENTS

The SQT concentrations applied to the patched cells (see below) were cross-checked by GC-MS measurements. From each test solution, samples were taken before the first addition to the application system (start) and after the last application (end) during three independent measurements. The samples (100 or 200  $\mu\text{L}$ ) were extracted with diethyl ether and dried over sodium sulfate. Nootkatone was chosen as standard and was added (in concentrations ranging from 1.22 to 4.89  $\mu\text{g}/\text{mL}$ , according to the quantification requirements) right before the extraction. Depending on the available amount of sample obtained from the measurements, quantification could partly be performed in duplicates. For (*E*)- $\beta$ -farnesene and  $\alpha$ -bisabolol an analyte/standard (nootkatone) 5-point-calibration curve was prepared ( $y = 3,8385x - 0,1498$ ,  $R^2 = 0,9989$  and  $y = 2,3403x + 0,0132$ ,  $R^2 = 0,9999$ , respectively), and the concentrations were calculated accordingly. In few cases, extrapolation was necessary. The relative amounts of the other analytes were determined via the peak area ratio of analyte/standard. The GC-MS analyses were performed on a GC 7890A connected to a MSD 5975C (Agilent Technologies, Santa Clara, CA, USA), equipped with a GERSTEL MPS 2-XL multipurpose sampler and a CIS 4 injection system (GERSTEL GmbH & Co. KG, Mülheim an der Ruhr, Germany). An uncoated fused silica capillary pre-column (3 m x 0.53 mm i.D.) was fixed to a DB-FFAP capillary column (30 x 0.25 mm i.D., film thickness 0.25  $\mu\text{m}$ ; Agilent J&W Scientific, Santa Clara, CA, USA). The oven program was started at 40  $^{\circ}\text{C}$  with a hold time of 1 min and raised with 8  $^{\circ}\text{C}/\text{min}$  until 240  $^{\circ}\text{C}$ . The carrier gas (helium) flow was set to 1 mL/min. The samples (2  $\mu\text{L}$ ) were applied with the cold on-column technique. EI mass spectra were recorded with

selected ion monitoring (SIM) using 70 eV. The following ions were selected:  $\alpha$ -Humulene (SIM 93),  $\beta$ -caryophyllene (SIM 133),  $\beta$ -caryolanol (SIM 111), humulol (SIM 82);  $\alpha$ -bisabolol (SIM 109);  $\alpha$ -bisabolol oxide A (SIM 143); (*E*)- $\beta$ -farnesene (SIM 69); guaiol (SIM 161);  $\alpha$ -bisabolol oxide B (SIM 143); spathulenol (SIM 205);  $\alpha$ -bisabolone oxide A (SIM 141) and nootkatone (SIM 147).

### MOLECULAR MODELING AND DOCKING

The docking study was performed at two different locations of the transmembrane domains of the GABA<sub>A</sub>-receptor: the diazepam binding site in the  $\beta^+\alpha^-$ -interface and the pregnanolone binding site in the  $\alpha\alpha$ -interface. For the investigation of the diazepam binding site the CryoEM structure of the human full-length  $\alpha_1\beta_3\gamma_2$ -GABA<sub>A</sub>-receptor (PDB code 6HUP, (Masiulis *et al.* 2019) was used, whereas the analysis of the pregnanolone binding site was based on the crystal structure of an  $\alpha_5\beta_3$ -chimera (PDB code 5O8F, (Miller *et al.* 2017). Using MOE (Molecular Operating Environment), the extracellular part as well as all small molecules present in the experimental structure were removed and chain breaks were capped. Polar hydrogens were added with the program PROTONATE of the AMBER software package (Case *et al.* 2016; Case *et al.* 2005). Kollman charges and solvation parameters were assigned to generate the PDBQS-files required for the calculation of the docking grids (cf. below).

The coordinates of diazepam and pregnanolone were taken from the corresponding PDB-files. Addition of hydrogen atoms and Gasteiger charges, as well as energy minimization with the MMFF94 forcefield (gradient: 0.001 kcal/mol/Å), were performed with MOE. The coordinates of three of the five SQTs of interest were taken from the Cambridge Structural Database (CSD):  $\beta$ -Caryophyllene (CSD: JICSIX), guaiol (CSD: GEMRAT01) and  $\alpha$ -humulene (CSD: HULAGN). Ligand preparation of these molecules was performed in the same way as described for diazepam and pregnanolone.  $\beta$ -Caryolanol was modelled using the CSD structure of a

chloro-derivative (CSD: GEMRATO1) as a template. The chlorine atom was changed to a hydroxy group and the carbon-oxygen bond was energy-minimized with the above-mentioned settings. S-humulol and R-humulol were modelled based on  $\alpha$ -humulene. These ligand preparations were carried out with MOE.

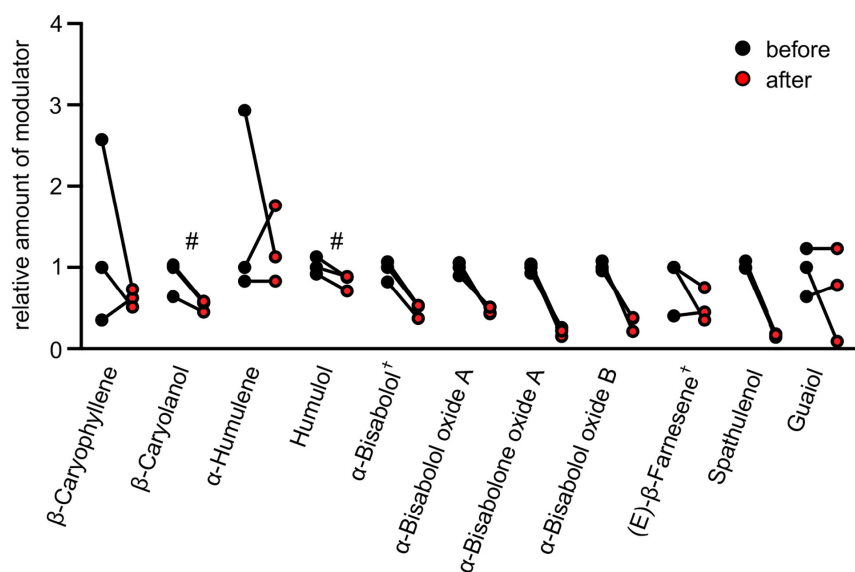
Docking studies were performed with AutoDock (Morris *et al.* 1998). Atomic affinity grids were calculated with AutoGrid based on the protein PDBQS-files. For the docking on the whole interfaces, the grids were centred approximately between the respective domains, covering a volume of 62 x 62 x 90 grid points with a default spacing of 0.375 Å. Based on the observation that in the  $\alpha\alpha$ -interface only the OH-containing ligands were found in the neurosteroid site, a second docking was performed, focussed on this binding site (grid size 88 x 60 x 108 points, grid spacing 0.188 Å). All dockings used the Lamarckian Genetic Algorithm with  $6.0 \times 10^6$  energy evaluations, a population size of 300 individuals, a maximum of 27,000 generations as well as 300 iterations in Solis & Wets local search. A total number of 50 GA runs was performed for each ligand. These settings resulted in a very accurate reproduction of the experimentally observed binding modes of diazepam (90% top poses with RMS-deviations < 1 Å) and pregnanolone (100% of poses with RMSD-deviations < 2 Å), respectively.

## REFERENCES

- Case, D., Betz, R., Cerutti, D. S. et al. (2016) *Amber 16, University of California, San Francisco*.
- Case, D. A., Cheatham III, T. E., Darden, T. et al. (2005) The Amber biomolecular simulation programs. *J Comput Chem* **26**, 1668-1688.
- Masiulis, S., Desai, R., Uchanski, T. et al. (2019) GABAA receptor signalling mechanisms revealed by structural pharmacology. *Nature* **565**, 454-459.
- Miller, P. S., Scott, S., Masiulis, S., De Colibus, L., Pardon, E., Steyaert, J. and Aricescu, A. R. (2017) Structural basis for GABAA receptor potentiation by neurosteroids. *Nat Struct Mol Biol* **24**, 986-992.

Morris, G. M., Goodsell, D. S., Halliday, R. S., Huey, R., Hart, W. E., Belew, R. K. and Olson, A. J. (1998) Automated docking using a Lamarckian genetic algorithm and an empirical binding free energy function. *J Comput Chem* **19**, 1639-1662.

**SUPPORTING INFORMATION FIGURE S1**



**SUPPORTING FIGURE S1** Normalized amounts (mean values) of SQTs applied in the patch clamp application system. Solutions containing 10  $\mu$ M GABA and 600  $\mu$ M modulator were used for patch clamp experiments. Samples were taken before and after passing through the solution application system and the relative modulator concentration (indicated by †) or ratio of peak areas was measured using GC-MS. Nootkatone was chosen as standard. All samples were analyzed twice except for the ones marked by a hash (#), which were only analyzed once.



# 3D Electrophysiological Measurements on Cells Embedded within Fiber-Reinforced Matrigel

Natascha Schaefer<sup>1†</sup>, Dieter Janzen<sup>1†</sup>, Ezgi Bakirci<sup>2</sup>, Andrei Hrynevich<sup>2</sup>,  
Paul D. Dalton<sup>2</sup>, Carmen Villmann<sup>1</sup>

<sup>1</sup> Institute for Clinical Neurobiology, University Hospital Würzburg,  
Würzburg, Germany

<sup>2</sup> Department of Functional Materials in Medicine and Dentistry,  
University Hospital Würzburg, Würzburg, Germany

† Shared authorship

Published in

**Advanced Healthcare Materials**

January 13, 2019

Reprinted with permission from John Wiley and Sons

## 3D Electrophysiological Measurements on Cells Embedded within Fiber-Reinforced Matrigel

Natascha Schaefer, Dieter Janzen, Ezgi Bakirci, Andrei Hrynevich, Paul D. Dalton, and Carmen Villmann\*

2D electrophysiology is often used to determine the electrical properties of neurons. In the brain however, neurons form extensive 3D networks. Thus, performing electrophysiology in a 3D environment provides a closer situation to the physiological condition and serves as a useful tool for various applications in the field of neuroscience. In this study, 3D electrophysiology is established within a fiber-reinforced matrix to enable fast readouts from transfected cells, which are often used as model systems for 2D electrophysiology. Using melt electrowriting (MEW) of scaffolds to reinforce Matrigel, 3D electrophysiology is performed on a glycine receptor-transfected Ltk-11 mouse fibroblast cell line. The glycine receptor is an inhibitory ion channel associated when mutated with impaired neuromotor behavior. The average thickness of the MEW scaffold is  $141.4 \pm 5.7 \mu\text{m}$ , using  $9.7 \pm 0.2 \mu\text{m}$  diameter fibers, and square pore spacings of 100, 200, and  $400 \mu\text{m}$ . For the first time, the electrophysiological characterization of glycine receptor-transfected cells is demonstrated with respect to agonist efficacy and potency in a 3D matrix. With the MEW scaffold reinforcement not interfering with the electrophysiological measurement, this approach can now be further adapted and developed for different kinds of neuronal cultures to study and understand pathological mechanisms under disease conditions.

3D matrices and scaffolds are an essential part of numerous areas of biomedical research, including tissue engineering,<sup>[1]</sup> cancer research,<sup>[2]</sup> cell expansion,<sup>[3]</sup> and stem-cell research.<sup>[4]</sup> In addition, the field of biofabrication is introducing an increasing number of ways to create hierarchical structures<sup>[5]</sup> to better recapitulate the in vivo environment. These include 3D-cell loaded structures with neurons, that are highly sensitive to changes within their environment, e.g., growth factor gradients,<sup>[6]</sup> extracellular matrix (ECM)-derived peptides,<sup>[7,8]</sup> or the stiffness

of the matrix.<sup>[9]</sup> Mechanical properties such as the stiffness of the 3D surrounding environment are known to affect differentiation of certain cells,<sup>[10]</sup> and are believed to be critical for neuronal maturation and neurotransmission.<sup>[9]</sup>


More discrete and higher resolved structures, such as those made with additive manufacturing (AM)<sup>[11]</sup> and electrojetting technology,<sup>[12]</sup> are promising to provide reproducible conditions. Electrojetting uses electrostatic forces to fabricate monodispersed, nanomicro particles in a simple, versatile, and cost-effective method for drug delivery and tissue engineering applications.<sup>[13]</sup> Electrospinning allows processability for polymer solutions and polymer melts.<sup>[14]</sup> In addition, polymer melts can be directly written using a programmable path in a technique known as melt electrowriting (MEW).<sup>[15]</sup> The precise placement of low-micrometer diameter fibers that are stackable using additive manufacturing principles are achievable using MEW (Figure 1a,b). The advantages of MEW include solvent-free processing and

avoidance of the chaotic fiber deposition often seen in electrospinning. Bioprinting approaches for cell hierarchy have been reinforced with extruded, stiffer structures<sup>[16]</sup> that reinforce the bioink and aid with in vitro handling<sup>[17]</sup> and extend a processing window for such hydrogels.<sup>[16,17]</sup> The reinforcing of matrices and bioinks with much smaller, low-micrometer scale fibers on matrices has recently been of particular interest.<sup>[18,19]</sup> Using MEW,<sup>[15]</sup> well-ordered, small diameter fibers can be distributed throughout a matrix in low volume fractions and provide significant increase in overall mechanical properties.<sup>[18-20]</sup> Furthermore, the mechanics of MEW fiber-reinforced hydrogels can be modulated further with sinusoidal direct-writing of the fibers.<sup>[18]</sup> Since the fiber diameter made using MEW can be readily changed with the nozzle mass flow rate and/or the collection speed, the diameter of the printed fiber can be significantly altered.<sup>[21]</sup> Therefore, MEW reinforcement of matrices (such as Matrigel shown here) have the potential to regulate the environment of cells through both mechanotransductive<sup>[22]</sup> or haptotactic<sup>[23]</sup> cues.

An experimentally designed in vitro 3D structure for electrophysiological studies requires a relevant receptor model, with the inhibitory glycine receptor (GlyR) used in this study. The GlyR is a pentameric, ligand gated ion channel, which belongs to the superfamily of Cys-loop receptors.<sup>[24]</sup> Upon binding of

Dr. N. Schaefer, D. Janzen, Prof. C. Villmann  
Institute for Clinical Neurobiology  
University Hospital Würzburg  
Versbacherstr. 5, 97078 Würzburg, Germany  
E-mail: Villmann\_C@ukw.de

E. Bakirci, A. Hrynevich, Prof. P. D. Dalton  
Department of Functional Materials in Medicine and Dentistry  
and Bavarian Polymer Institute  
University Hospital Würzburg  
Pleichenwall 2, 97070 Würzburg, Germany

 The ORCID identification number(s) for the author(s) of this article can be found under <https://doi.org/10.1002/adhm.201801226>.

DOI: 10.1002/adhm.201801226

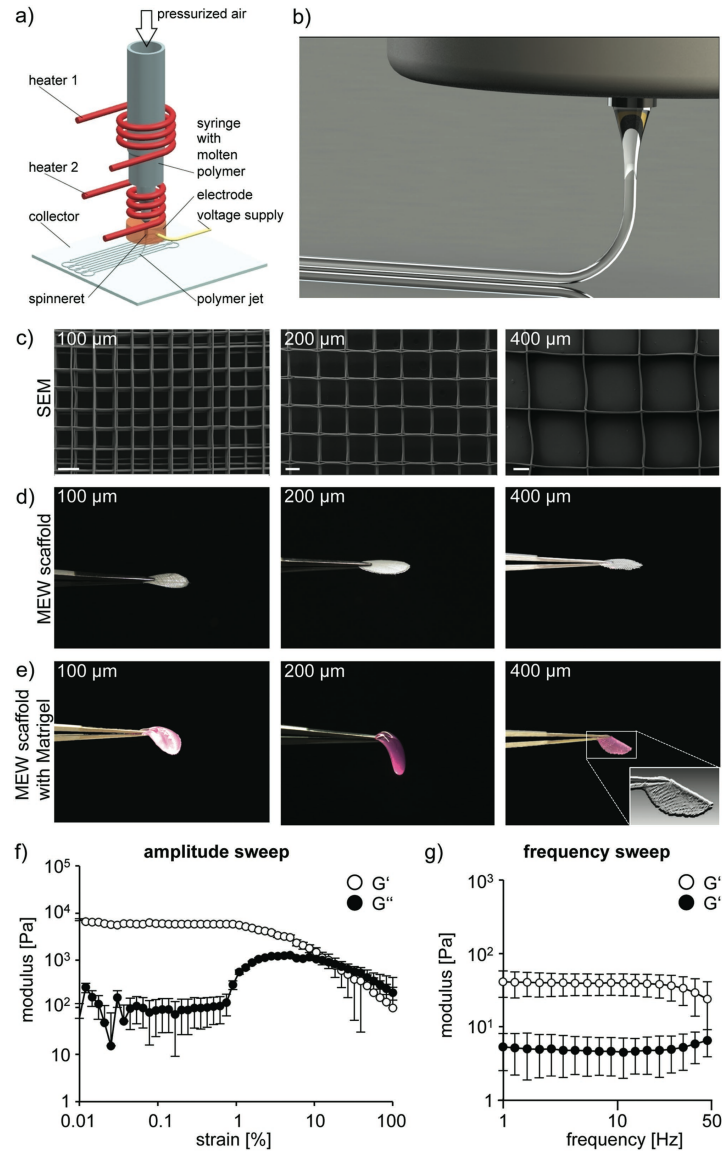


**Figure 1.** Handling of different MEW scaffolds with and without matrix. a) Schematic of the MEW head depicting how the polymer melt is heated and the nozzle directed over the surface. b) Rendering of the electrified molten jet as it comes out of the nozzle and forms a fiber that is direct-written layer-by-layer for the reinforcing MEW scaffold. c) Scanning electron microscopy images of MEW scaffold with different pores of 100, 200, and 400  $\mu\text{m}$ ; diameter of scaffolds is 9.8 mm. d) Same scaffolds as in (c) held with forceps to investigate stability during handling. e) Scaffolds as in (c) and (d) reinforced with Matrigel. Note, MEW scaffolds allow handling of ultra-weak matrices, but handling becomes difficult if the pore size increases, e.g., 400  $\mu\text{m}$ . The collapse of the 400  $\mu\text{m}$  scaffold is enlarged in lower right image; basrelief filter used. f) Amplitude and g) frequency sweep, from  $n = 4$  independent experiments, error bars represent standard deviation (S.D.).

its ligand glycine, the ion channel undergoes conformational changes, which lead to opening of the ion channel pore.<sup>[25]</sup> Changes in chloride conductance can be measured with electrophysiological recordings and provide a reliable readout about functional characteristics of the GlyR, e.g., channel opening/closing, ligand potency, and efficacy.<sup>[26]</sup> In this study, the mouse fibroblast Ltk-11 cell line was used as the underlying cellular model. MEW scaffolds have previously been infiltrated with fibroblasts<sup>[27]</sup> while the Ltk-11 cells are well-suited for transfection and 2D electrophysiology.<sup>[28]</sup> A fast readout technique that provides the 3D perspective to study cellular proteins under disease conditions as well as an adaption to the more complex neuronal system would be highly useful.

MEW scaffolds with different z-directional pore sizes were investigated and analyzed for their mechanical properties with and without Matrigel (Figure 1c). The fiber diameter of the MEW scaffolds was  $9.7 \pm 0.2 \mu\text{m}$  while the thickness was  $141.4 \pm 5.7 \mu\text{m}$  without Matrigel. The force-handling of the dry scaffolds were similar (Figure 1d), but the  $400 \mu\text{m}$  pore size became difficult to handle (Figure 1e) when Matrigel was included. The  $400 \mu\text{m}$  pore scaffolds rolled up when picked up by forceps and collapsed (Figure 1e, right image), while the  $100$  and  $200 \mu\text{m}$  pore scaffolds were more stable. An amplitude sweep was performed to determine the linear viscoelastic region of Matrigel (Figure 1f) which was 1% strain. A lower strain 0.1% was therefore selected for frequency sweep and confirmed a crosslinked hydrogel (Figure 1g).<sup>[29,30]</sup>

The estimation of living and dead cells of Ltk-11 cells grown in 2D compared to 3D embedded Ltk-11 cells in MEW scaffold reinforced Matrigel revealed no significant differences in the number of live and dead cells (2D live 98.5%, dead 1.5%; 3D live 98.9%, dead 1.1%; Figure 2a,b). Cell division in 3D starts 48 h postseeding, which is around 24 h later compared to 2D (data not shown), possibly due to the mechanical properties of the Matrigel. Smaller pores harbor less cells ( $100 \mu\text{m}$ ; Figure 2c, upper images), more cells were present in a  $200$  and  $400 \mu\text{m}$  scaffolds (Figure 2c, middle and lower panel). Following 24 h in scaffold, most Ltk-11 cells still form clustered structures (Figure 2c). This might be explained by better growth of cells when in contact with neighboring cells.<sup>[31]</sup> Comparing the cell number 24 h postseeding with 9 days after seeding, cells colonized and thus crossed each pore due to increase in cell division within the MEW scaffold/Matrigel complex independent of the pore size used (Figure 2c, right magnified images). Hence, our data are in line with previous results that fibroblasts are able to infiltrate MEW scaffolds.<sup>[27]</sup>

During cell seeding, transfection, and immunostaining procedures, the  $200 \mu\text{m}$  scaffold turned out to be the most appropriate scaffold for cell biological assays. Ltk-11 cells can be easily transfected in 2D cultures. In 3D, neither the calcium phosphate precipitation method based on complex formation of plasmid DNA and calcium phosphate nor lipofectamine transfection based on a hydrophobic complex were successful.<sup>[32]</sup> The calcium phosphate precipitates were unable to enter the Matrigel and remained at the matrix surface. Similarly, the DNA–lipofectamine complex did not diffuse into the Matrigel to target the Ltk-11 cells. Therefore, Ltk-11 cells were transfected in 2D cell cultures and transferred 24 h posttransfection together with Matrigel into the scaffold (Figure 2d). Enhanced

green fluorescent protein (eGFP) served as internal control for transfection efficiency. The GlyR  $\alpha 1$  subunit was chosen due to its ability to form homomeric ligand-gated ion channels. Note, every cell which shows green fluorescence successfully expresses eGFP. It is assumed that cells expressing eGFP have also taken up the plasmid DNA for the GlyR. As a proof, immunocytochemical staining was performed to analyze the expression of the GlyR  $\alpha 1$  subunit and eGFP in the 3D environment. Colocalization of eGFP and GlyR  $\alpha 1$  was observed in the same transfected Ltk-11 cell (Figure 2e). Therefore, electrophysiological experiments were only performed on green fluorescent cells. For electrophysiological purposes, the pore size of  $100 \mu\text{m}$  impacted the movements of the pipette tip to reach the cell of interest. Because of this, we continued with the  $200 \mu\text{m}$  pore scaffolds for all following experiments. Transfected Ltk-11 cells were used in parallel for studies in 2D or 3D to enable comparison.

Scaffolds were transferred into a recording chamber filled with extracellular buffer (ECS) to enable measurements under physiological conditions (Figure 3a,b). ECS is specific for each cell type. The soft cell/Matrigel/scaffold construct required fixation with an O-ring<sup>[33]</sup> to facilitate electrophysiological recordings (Figure 3a). The cells were approached with a glass pipette with positive pressure continuously applied to avoid plugging of the patch pipette with Matrigel. Following attachment of the cellular membrane (on-cell configuration), a negative membrane potential of  $-60 \text{ mV}$  was applied. The cellular membrane was disrupted and whole-cell measurements were performed applying a concentration series of glycine to determine the glycine concentration ( $\text{EC}_{50}$ ) where half of the ion channels are open. A pressure-based application system was used to apply the agonist for 250 ms with a pressure of 1 bar (Octaflow II, ALA Scientific Instruments, Farmingdale, NY, United States) as glycine would otherwise take too long to reach the cell through the viscous Matrigel. After applying glycine, a washing step with ECS for 7250 ms with a pressure of 1 bar was necessary, otherwise the glycine would stick to the cell surrounding. For comparison with 2D measurements, transfected Ltk-11 cells grown on glass coverslips surrounded by ECS were used. The glycine-induced current at saturating glycine concentration ( $1 \times 10^{-3} \text{ M}$ ) in 2D does not differ in shape to 3D arguing for similar onset and recovery of the ion channels (Figure 3c). However,  $I_{\text{max}}$  currents at  $1 \times 10^{-3} \text{ M}$  glycine are smaller in 3D than in 2D ( $I_{\text{max}}$  2D:  $3.3 \pm 0.6 \text{ nA}$ ;  $I_{\text{max}}$  3D:  $2.2 \pm 0.5 \text{ nA}$ ) (Figure 3c–e and Table 1), which can be explained by the viscous Matrigel preventing glycine from reaching GlyRs around the whole cell especially those on the opposite site of the application system. Therefore, not all GlyR channels of the approached cell open at the same time, leading to less chloride ion influx. Measured  $\text{EC}_{50}$  values showed a slight rightward shift compared to 2D ( $\text{EC}_{50}$  2D:  $110.5 \pm 17.6 \times 10^{-6} \text{ M}$ ) and 3D ( $\text{EC}_{50}$  3D:  $174.7 \pm 34.3 \times 10^{-6} \text{ M}$ ) (Figure 3e). At  $300 \times 10^{-6} \text{ M}$  of glycine,  $I_{300}$  differed significantly (Figure 3d and Table 1). In sum, we have successfully established a 3D electrophysiology approach based on embedded transfected Ltk-11 cells in Matrigel reinforced with MEW scaffolds. This protocol can now be adapted to other cell types. Our data demonstrate small changes in glycine-induced currents as well as for glycine potency. The comparison of 2D and 3D cultures of

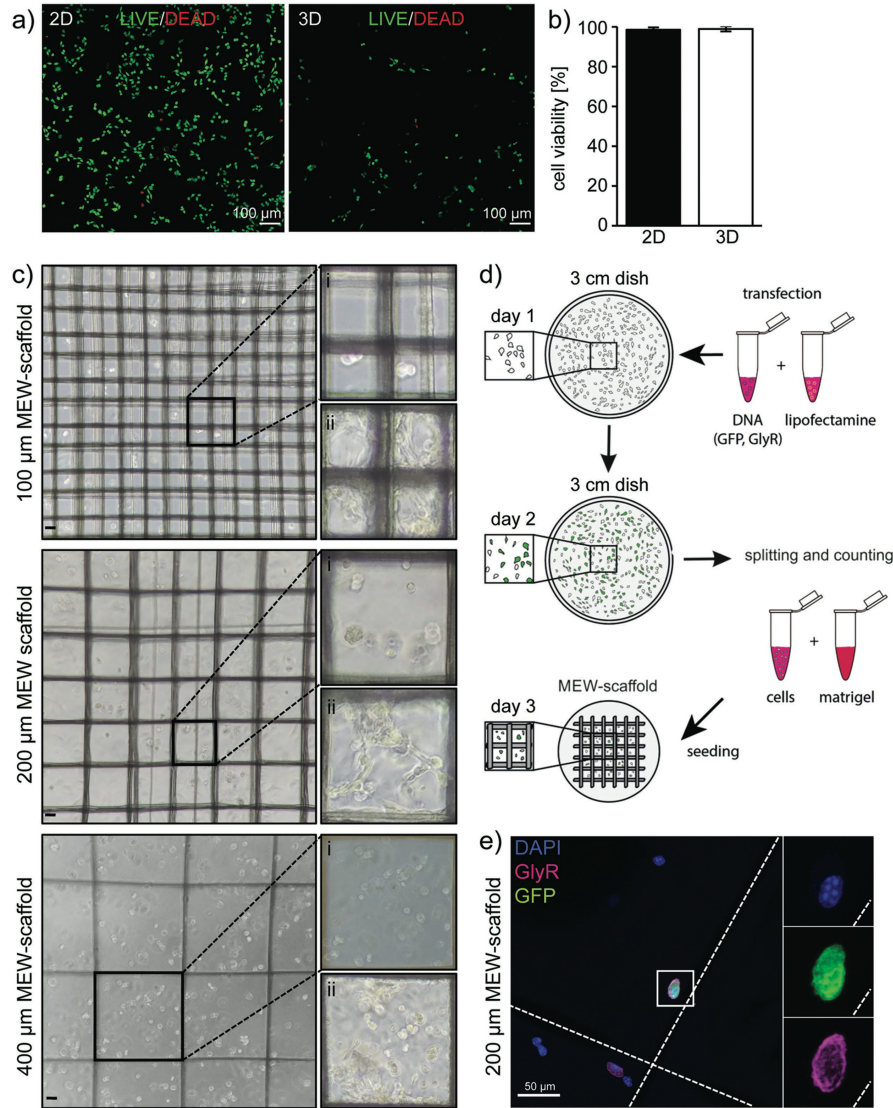


**Figure 2.** Ltk-11 cells embedded in Matrigel grow in different MEW scaffold sizes and express protein of interest. a) Live/dead assay in 2D cultures and 3D cultures of Ltk-11 cells: live, green; dead, red; scale bar refers to 100 μm; three independent experiments were performed for 2D and 3D cultures, 15 images with 5 images per experiment were counted with a total number of counted cells in 2D = 10115, 3D = 1955, b) quantification of cell viability in 2D and 3D, and c) 100, 200, and 400 μm scaffolds side chain length at day 1 after seeding with Ltk-11 cells. A representative pore is shown in magnification at the right with i) 24 h after seeding, lower magnified image day 9 after seeding ii). Scale bar in each picture resembles 50 μm. d) Exemplary working schedule: day 1—Ltk-11 cell seeding and transfection with eGFP and GlyR using lipofectamine; day 2—proof for eGFP positive cells, mixing with Matrigel, and seeding into MEW scaffold; day 3—scaffold with transfected Ltk-11 cells. e) Immunocytochemical staining of transfected Ltk-11 cells 24 h after seeding in 3D, 200 μm scaffold expressing eGFP (green) and GlyR α1 (magenta). Cell nuclei were stained with Hoechst. Scale bar in each picture resembles 50 μm. All experiments have been performed at least three times. Representative images are shown.

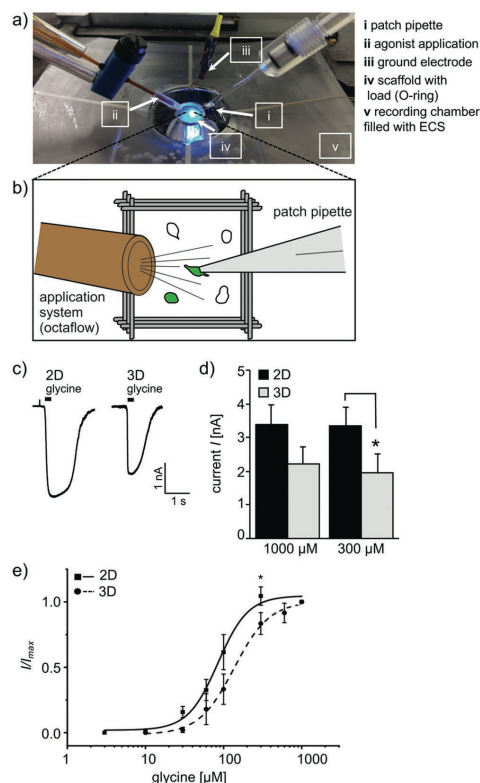


**Figure 3.** 3D electrophysiological recordings from Ltk-11 cells grown in Matrigel reinforced with MEW scaffolds. a) Image of the electrophysiological recording chamber with labeled i–v. b) Cartoon of the recording from transfected Ltk-11 cells (cotransfected with eGFP, green) grown in MEW scaffolds. c) Representative current traces from 2D and 3D recordings. d) Bar diagram representing  $I$  values at  $300 \times 10^{-6}$  M glycine  $\pm$  standard error of the mean (S.E.M.) (2D black with  $n = 10$ , 3D grey with  $n = 8$ ;  $*p \leq 0.05$ ). e) Dose-response curves obtained from 2D (black squares and full line;  $n = 10$ ) and 3D (black circles and dotted line;  $n = 8$ ) measurements to determine the  $EC_{50}$ . Cells used for data analysis ( $n = 8$ – $10$ ) have been recorded within three independent experiments.

transfected Ltk-11 cells revealed a significant reduction in current amplitudes following application of  $300 \times 10^{-6}$  M glycine but similar current values for all other glycine concentrations applied. Differences in glycine potency determined by the  $EC_{50}$

**Table 1.** Electrophysiological properties of GlyRs determined from reinforced MEW scaffolds (Values are presented  $\pm$  standard error of the mean (S.E.M.)).

	$EC_{50}$ [ $\times 10^{-6}$ M]	$n_H$	$I_{max}$ [nA]	$n$
2D	$110.5 \pm 17.6$	$3.9 \pm 0.5$	$3.3 \pm 0.6$	10
3D	$174.7 \pm 34.3$	$4.1 \pm 0.7$	$2.2 \pm 0.5$	8

value exhibited a slight rightward shift (magnitude shift is less than twice) of the dose-response curve in 3D compared to 2D. For whole-cell recordings from 2D cell cultures of transfected HEK293 cells, glycine  $EC_{50}$  values between  $20$  and  $120 \times 10^{-6}$  M have been documented from different labs.<sup>[34]</sup> Differences in cell number, number of transiently transfected cells, promoter of DNA plasmid used, and state or passage of the culture have been pointed out to underlie those values. The decrease in glycine potency from  $110 \times 10^{-6}$  M in 2D toward  $175 \times 10^{-6}$  M in 3D is however not significant and might result from differences in surrounding matrix density decelerating glycine from fast approaching the cell. Recently, Frega et al. also compared 3D to 2D electrophysiology using hippocampal neurons coupled to a microelectrode array.<sup>[35]</sup> Significant differences with respect to mean burst rates and network burst duration times compared to 2D electrophysiological measurements were observed.<sup>[35]</sup> Xu et al. could not observe differences in the firing rates and spontaneous inhibitory postsynaptic currents in hippocampal neurons cultured in a 3D collagen hydrogel but slight changes in the resting membrane potential and the duration of the after-hyperpolarization differed to 2D cultures.<sup>[33]</sup> Thus, the physiological properties of cells differ between 2D and 3D cultures arguing for a requirement of 3D techniques, which are closer to the natural situation than planar cell growth in 2D cell cultures.

The electrophysiological measurements of transfected cells embedded within fiber-reinforced Matrigel harbors all advantages of a 3D system such as the mimicking of a physiological tissue environment including the ability to grow in all three dimensions, better access to nutrients and suitability to describe the physiological properties of the cells used. The fiber-reinforcement using MEW scaffolds could in future provide physical cues for cell migration<sup>[36]</sup> or process guidance.<sup>[7]</sup> Such fiber-reinforced matrices provide a systematic, composite platform that can be adapted to other cell systems comprising multiple circuit information to study the electrophysiological properties of ion channels in a 3D environment.

## Experimental Section

**MEW Process:** MEW scaffolds were fabricated by a previously described custom-built MEW<sup>[37]</sup> Medical-grade poly( $\epsilon$ -Caprolacton) (PCL) (Corbion Inc, Netherlands, PURASORB PC12, Lot# 1412000249, 03/2015) was used to fabricate the MEW scaffolds. All MEW printing was performed at  $21 \pm 2$  °C environment temperature and a humidity of  $35 \pm 10\%$ . PCL was heated at  $80$  °C in 3 mL syringe and air pressure was set to 3 bar. A high voltage was applied and after an electrified jet was generated, the G-code that drives the collector was initiated. A large  $48 \times 96$  mm rectangular mesh with 100, 200 or 400  $\mu$ m spacing fiber was direct-written and then cut with an infrared laser to 9 mm circular disks for use in 24-well plates for in vitro experiments. MEW scaffolds were produced using the following parameters: 25 G nozzle and a 6 kV voltage applied across a 4 mm collector distance.

**Scanning Electron Microscopy (SEM):** SEM (Crossbeam 340, Carl Zeiss AG Oberkochen, Germany) was used to image the MEW scaffolds, sputter-coated with a 4 nm platinum layer. Software from Zeiss (Zeiss SmartSEM Version 6.03) was used for measurement of fiber size.

**Handling Test:** MEW scaffolds with and without Matrigel were photographed using forceps to determine the extent of folding. Prior to embedding, the scaffolds were washed with 70% ethanol, sterile water, and phosphate-buffered saline (PBS) then dried at room temperature ( $21 \pm 2$  °C). 120  $\mu$ L Matrigel-Dulbecco's modified Eagle medium (DMEM) mixtures were added on top of scaffolds and left for gelation for 30 min.

**Mechanical Behavior:** The frequency and amplitude sweep of Matrigel ( $n = 4$ ) was measured using a controlled stress rheometer (Physica MCR301, Anton Paar GmbH, Germany) with a plate–plate configuration (diameter = 25 mm). 4.5 mg mL<sup>-1</sup> Matrigel (500  $\mu$ L) samples were added to the center of the lower plate at 4 °C. The upper plate was placed on samples with 0.5 mm gap. The temperature was increased from 4 to 37 °C and kept at 37 °C for 45 min. All the measurements were done at 37 °C. The amplitude sweep was performed between 0.01% and 100% strain at 1 Hz. Frequency sweep was performed between 1 and 50 Hz at 0.1% strain.

**Cell Culture:** Ltk-11 mouse fibroblast cells (CRL-10422; ATCC, Manassas, VA, United States) were cultured in DMEM supplemented with 10% fetal calf serum,  $4 \times 10^{-3}$  M GlutaMAX,  $1 \times 10^{-3}$  M sodium pyruvate, and 50 U mL<sup>-1</sup> penicillin/streptomycin (Thermo Fisher Scientific, Waltham, United States) under standard growth conditions at 37 °C and 5% CO<sub>2</sub>.

**Transfection:** Ltk-11 cells were transiently transfected using Lipofectamine 2000 reagent (Thermo Fisher Scientific, Waltham, United States) according to the manufacturer's protocol. In brief, Opti-Mem (Life Technologies, Darmstadt, Germany) was mixed with either 6  $\mu$ L of lipofectamine or 2  $\mu$ L (1  $\mu$ g  $\mu$ L<sup>-1</sup>) of plasmid DNA and incubated for 5 min at room temperature before combining. Following a second 15 min incubation period, the mixture was carefully pipetted onto the cells (3 cm dish). Cells were transfected with the GlyR  $\alpha$ 1 subunit and eGFP. eGFP was used as an internal transfection efficiency control and fluorescence of eGFP was controlled next day.

**Scaffold Preparation and Cell Seeding:** Scaffolds were placed into 24-well plates, washed once with 70% ethanol, three times with sterile water, and once with sterile PBS. Transfected Ltk-11 cells were detached 1 day after transfection and counted. Cells were either seeded onto four coverslips in a 3 cm dish (150 000 cells per dish) or 60–100  $\mu$ L cell suspension (100 000 cells) were mixed with Matrigel (Corning, NY, United States) using a final protein concentration of 4.5–4.8 mg mL<sup>-1</sup> and pipetted onto scaffolds. After 30 min incubation at 37 °C, 500  $\mu$ L DMEM was added.

**Immunocytochemical Staining:** Glycine receptors were stained to assess cell transfection efficiency. All steps were performed at room temperature. Cells in MEW scaffolds were fixed for 5 min with 2% paraformaldehyde, washed three times with PBS and blocked/permeabilized for 30 min with 5% (v/v) goat serum and 0.2% Triton X-100 in PBS. Afterward, cells were incubated for 1 h with the GlyR  $\alpha$ 1-specific primary antibody mAb2b (1:500 in blocking solution; Synaptic Systems, Göttingen, Germany, Cat. No: 146 111). Cells were washed three times with PBS and incubated for 45 min with the secondary Cy3-coupled goat–antimouse antibody (1:500 in blocking solution; Dianova, Hamburg, Germany). Cells were washed three times with PBS, once with dH<sub>2</sub>O, and mounted on glass slides with ProLong Glass Antifade Mountant (Thermo Fisher Scientific, Waltham, United States). Mounting Medium contains Hoechst 33342.

**Cell Viability:** The viability of transfected Ltk-11 cells was measured 1 day after seeding in 2D and 3D cultures. Briefly, cells were incubated for 30 min with  $2 \times 10^{-6}$  M Calcein-AM (green/living cells; Thermo Fisher Scientific, Waltham, United States) and  $2 \times 10^{-6}$  M ethidium homodimer I (red/dead cells; Sigma-Aldrich, St. Louis, United States) in PBS. Five images each of three independent samples were used for measuring the live/dead ratio.

**Confocal Microscopy and Image Acquisition:** Fluorescence and cell viability images were acquired with an inverted Olympus IX81 microscope equipped with an Olympus FV1000 confocal laser scanning system, a FVD10 SPD spectral detector, and diode lasers of 405 nm (Hoechst), 495 nm (Alexa488), and 550 nm (Cy3) (Olympus, Tokyo, Japan). All images shown were acquired using an Olympus UPLFLN 40x (oil, numerical aperture: 1.3) or UPLSAPO 10x (air, numerical aperture: 0.4) objective. Phase-contrast images were acquired using a Leica DM IL LED (Leica, Wetzlar, Germany) microscope equipped with a HTC 10 (HTC, New Taipei City, Taiwan). Images were processed with ImageJ (1.52)/Fiji.<sup>[38]</sup>

**Electrophysiology:** The patch clamp technique was used to measure current amplitudes ( $I$ ) of transfected Ltk-11 cells in 2D (coverslips)

and 3D (Matrigel reinforced with MEW scaffolds) conditions for 48 h after transfection in a whole-cell configuration mode. Currents were amplified using an EPC10 amplifier and the software Patchmaster NEXT (HEKA, Lambrecht, Germany). For dose-response curves to determine the glycine EC<sub>50</sub>, seven glycine concentrations were used (2D: 3, 10, 30, 60, 100, 300, and 1000  $\times 10^{-6}$  M; and 3D: 10, 30, 60, 100, 300, 600, and 1000  $\times 10^{-6}$  M) were applied for 250 ms with a pressure of 1 bar, followed by application of ECS for 7250 ms using an Octaflo II system (ALA Scientific Instruments, Farmingdale, NY, United States). The extracellular buffer consisted of (in  $\times 10^{-3}$  M): 137 NaCl, 5.4 KCl, 1.8 CaCl<sub>2</sub>, 1 MgCl<sub>2</sub>, 5 HEPES; pH adjusted to 7.4 with NaOH. The intracellular buffer contained (in  $\times 10^{-3}$  M): 120 CsCl, 20 N(Et)<sub>3</sub>Cl, 1 CaCl<sub>2</sub>, 2 MgCl<sub>2</sub>, 11 EGTA, 10 HEPES; pH adjusted to 7.2 with CsOH. Cells were held at –60 mV. Recording pipettes were manufactured from borosilicate capillaries and were pulled with the help of a P97 horizontal puller (Sutter Instrument, Novato, CA, United States). Recording pipettes had an open resistance of 4–6 M $\Omega$ . All measurements were performed at 21 °C.

**Statistical Analysis:** Electrophysiological data was analyzed using OriginPro 2018b (OriginLab, Northampton, MA, United States). A nonlinear algorithm was used to construct dose-response curves from peak current amplitudes obtained with seven appropriately spaced concentrations in the range of 10–1000  $\times 10^{-6}$  M glycine. The following Hill equation was used:  $I = I_{max} \times c^{n_H} / (c^{n_H} + EC_{50}^{n_H})$ .  $I$  refers to the current amplitude at the given agonist concentration  $c$ ,  $I_{max}$  is the current amplitude at a saturating agonist concentration, EC<sub>50</sub> refers to the agonist concentration evoking half-maximal current responses and  $n_H$  is the Hill coefficient.

Statistical analysis was performed using calculation of mean values, followed by determination of the standard deviation (S.D.) or standard error of the mean (S.E.M.) (electrophysiological measurements—calculation from 8 to 10 measured cells out of three or more independent transfections were performed; amplitude and frequency sweep—calculated from four independent replicates). Subsequent Student's *t*-test was used to evaluate the probability values—*p*-values: *p*-values were set as follows: \**p* < 0.05; \*\**p* < 0.01; and \*\*\**p* < 0.001.

## Acknowledgements

N.S. and D.J. contributed equally to this work. This work was supported by the German Research Foundation (DFG) as part of the Collaborative Research Centre SFB TRR225 (B01). INST 93/940-1 and the State Major Instrumentation Program, which financed the Scanning electron microscope used in this study (INST 105022/58-1 FUGG), is gratefully acknowledged. The MEW 3D printer used for this study was built by A.H. The authors appreciate the assistance in initial scaffold manufacture by Almoatbellah Youssef.

## Conflict of Interest

The authors declare no conflict of interest.

## Keywords

3D electrophysiology, glycine receptors, melt electrowriting

Received: September 30, 2018  
Revised: November 23, 2018  
Published online: January 13, 2019

[1] N. Annabi, K. Tsang, S. M. Mithieux, M. Nikkhal, A. Ameri, A. Khademhosseini, A. S. Weiss, *Adv. Funct. Mater.* **2013**, 23.

- [2] D. W. Huttmacher, R. E. Horch, D. Loessner, S. Rizzi, S. Sieh, J. C. Reichert, J. A. Clements, J. P. Beier, A. Arkudas, O. Bleiziffer, U. Kneser, *J. Cell. Mol. Med.* **2009**, *13*, 1417.
- [3] B. Delalat, F. Harding, B. Gundsambuu, E. M. De-Juan-Pardo, F. M. Wunner, M. L. Wille, M. Jasieniak, K. A. L. Malatesta, H. J. Griesser, A. Simula, D. W. Huttmacher, N. H. Voelcker, S. C. Barry, *Biomaterials* **2017**, *140*, 58.
- [4] R. A. Marklein, J. A. Burdick, *Adv. Mater.* **2010**, *22*, 175.
- [5] J. Groll, T. Boland, T. Blunk, J. A. Burdick, D. W. Cho, P. D. Dalton, B. Derby, G. Forgacs, Q. Li, V. A. Mironov, L. Moroni, M. Nakamura, W. Shu, S. Takeuchi, G. Vozzi, T. B. Woodfield, T. Xu, J. J. Yoo, J. Malda, *Biofabrication* **2016**, *8*, 013001.
- [6] X. Cao, M. S. Shoichet, *Neuroscience* **2001**, *103*, 831.
- [7] P. D. Dalton, J. Mey, *Front. Biosci., Landmark Ed.* **2009**, *14*, 769.
- [8] Y. Luo, M. S. Shoichet, *Biomacromolecules* **2004**, *5*, 2315.
- [9] G. Palazzolo, N. Broguiere, O. Cenciarelli, H. Dermutz, M. Zenobi-Wong, *Tissue Eng., Part A* **2015**, *21*, 2177.
- [10] S. H. Oh, D. B. An, T. H. Kim, J. H. Lee, *Acta Biomater.* **2016**, *35*, 23.
- [11] A. Youssef, S. J. Hollister, P. D. Dalton, *Biofabrication* **2017**, *9*, 012002.
- [12] P. Fattahi, A. Borhan, M.-R. Abidian, presented at *2013 6th Int. IEEE/EMBS Conf. Neural Eng. (NER)*, CA, Los Angeles, November **2013**.
- [13] P. Fattahi, A. Borhan, M. R. Abidian, *Adv. Mater.* **2013**, *25*, 4555.
- [14] T. J. Sill, H. A. von Recum, *Biomaterials* **2008**, *29*, 1989.
- [15] P. D. Dalton, *Curr. Opin. Biomed. Eng.* **2017**, *2*, 49.
- [16] J. Malda, J. Visser, F. P. Melchels, T. Jungst, W. E. Hennink, W. J. Dhert, J. Groll, D. W. Huttmacher, *Adv. Mater.* **2013**, *25*, 5011.
- [17] N. V. Mekhileri, K. S. Lim, G. C. J. Brown, I. Mutreja, B. S. Schon, G. J. Hooper, T. B. F. Woodfield, *Biofabrication* **2018**, *10*, 024103.
- [18] O. Bas, D. D'Angella, J. G. Baldwin, N. J. Castro, F. M. Wunner, N. T. Saïdy, S. Kollmannsberger, A. Reali, E. Rank, E. M. De-Juan-Pardo, D. W. Huttmacher, *ACS Appl. Mater. Interfaces* **2017**, *9*, 29430.
- [19] J. Visser, F. P. Melchels, J. E. Jeon, E. M. van Bussel, L. S. Kimpton, H. M. Byrne, W. J. Dhert, P. D. Dalton, D. W. Huttmacher, J. Malda, *Nat. Commun.* **2015**, *6*, 6933.
- [20] a) O. Bas, E. M. De-Juan-Pardo, M. P. Chhaya, F. M. Wunner, J. E. Jeon, T. J. Klein, D. W. Huttmacher, *Eur. Polym. J.* **2015**, *72*, 451; b) M. de Ruijter, A. Hrynevich, J. N. Haigh, G. Hochleitner, M. Castilho, J. Groll, J. Malda, P. D. Dalton, *Small* **2018**, *14*.
- [21] A. Hrynevich, B. S. Elci, J. N. Haigh, R. McMaster, A. Youssef, C. Blum, T. Blunk, G. Hochleitner, J. Groll, P. D. Dalton, *Small* **2018**, *14*, e1800232.
- [22] B. M. Baker, C. S. Chen, *J. Cell Sci.* **2012**, *125*, 3015.
- [23] R. M. Smeal, R. Rabbitt, R. Biran, P. A. Tresco, *Ann. Biomed. Eng.* **2005**, *33*, 376.
- [24] J. W. Lynch, *Physiol. Rev.* **2004**, *84*, 1051.
- [25] J. Du, W. Lu, S. Wu, Y. Cheng, E. Gouaux, *Nature* **2015**, *526*, 224.
- [26] a) N. Schaefer, A. Berger, J. van Brederode, F. Zheng, Y. Zhang, S. Leacock, L. Littau, S. Jablonka, S. Malhotra, M. Topf, F. Winter, D. Davydova, J. W. Lynch, C. J. Paige, C. Alzheimer, R. J. Harvey, C. Villmann, *J. Neurosci.* **2017**, *37*, 7948; b) N. Schaefer, C. J. Kluck, K. L. Price, H. Meiselbach, N. Vornberger, S. Schwarzinger, S. Hartmann, G. Langlhofer, S. Schulz, N. Schlegel, K. Brockmann, B. Lynch, C. M. Becker, S. C. Lummis, C. Villmann, *J. Neurosci.* **2015**, *35*, 422.
- [27] B. L. Farrugia, T. D. Brown, Z. Upton, D. W. Huttmacher, P. D. Dalton, T. R. Dargaville, *Biofabrication* **2013**, *5*, 025001.
- [28] C. F. Valenzuela, R. A. Cardoso, M. J. Wick, J. L. Weiner, T. V. Dunwiddie, R. A. Harris, *Alcohol: Clin. Exp. Res.* **1998**, *22*, 1132.
- [29] A. S. Hoffman, *Adv. Drug Delivery Rev.* **2002**, *54*, 3.
- [30] Y. Hong, T. V. Chirila, S. Vijayasekaran, P. D. Dalton, S. G. Tahija, M. J. Cuypers, I. J. Constable, *J. Biomed. Mater. Res.* **1996**, *30*, 441.
- [31] M. Natoli, B. D. Leoni, I. D'Agnano, M. D'Onofrio, R. Brandi, I. Arisi, F. Zucco, A. Felsani, *J. Cell. Physiol.* **2011**, *226*, 1531.
- [32] a) C. Chen, H. Okayama, *Mol. Cell. Biol.* **1987**, *7*, 2745; b) P. L. Felgner, T. R. Gadek, M. Holm, R. Roman, H. W. Chan, M. Wenz, J. P. Northrop, G. M. Ringold, M. Danielsen, *Proc. Natl. Acad. Sci. USA* **1987**, *84*, 7413; c) P. L. Felgner, G. M. Ringold, *Nature* **1989**, *337*, 387.
- [33] T. Xu, P. Molnar, C. Gregory, M. Das, T. Boland, J. J. Hickman, *Biomaterials* **2009**, *30*, 4377.
- [34] S. Fucile, D. de Saint Jan, B. David-Watine, H. Korn, P. Bregestovski, *J. Physiol.* **1999**, *517*, 369.
- [35] M. Frega, M. Tedesco, P. Massobrio, M. Pesce, S. Martinoia, *Sci. Rep.* **2014**, *4*, 5489.
- [36] H. G. Sundararaghavan, J. A. Burdick, *Biomacromolecules* **2011**, *12*, 2344.
- [37] T. D. Brown, P. D. Dalton, D. W. Huttmacher, *Adv. Mater.* **2011**, *23*, 5651.
- [38] a) J. Schindelin, I. Arganda-Carreras, E. Frise, V. Kaynig, M. Longair, T. Pietzsch, S. Preibisch, C. Rueden, S. Saalfeld, B. Schmid, J. Y. Tinevez, D. J. White, V. Hartenstein, K. Eliceiri, P. Tomancak, A. Cardona, *Nat. Methods* **2012**, *9*, 676; b) J. Schindelin, C. T. Rueden, M. C. Hiner, K. W. Eliceiri, *Mol. Reprod. Dev.* **2015**, *82*, 518; c) C. A. Schneider, W. S. Rasband, K. W. Eliceiri, *Nat. Methods* **2012**, *9*, 671.



# **Cortical Neurons Form a Functional Neuronal Network in a 3D Printed Reinforced Matrix**

Dieter Janzen<sup>1</sup>, Ezgi Bakirci<sup>2</sup>, Annalena Wieland<sup>3</sup>, Corinna Martin<sup>1</sup>,  
Paul D. Dalton<sup>2</sup>, Carmen Villmann<sup>1</sup>

<sup>1</sup> Institute for Clinical Neurobiology, University Hospital Würzburg,  
Würzburg, Germany

<sup>2</sup> Department of Functional Materials in Medicine and Dentistry,  
University Hospital Würzburg, Würzburg, Germany

<sup>3</sup> Department of Obstetrics and Gynecology, University Hospital Erlangen,  
Erlangen, Germany

Published in  
**Advanced Healthcare Materials**  
March 17, 2020

## Cortical Neurons form a Functional Neuronal Network in a 3D Printed Reinforced Matrix

Dieter Janzen, Ezgi Bakirci, Annalena Wieland, Corinna Martin, Paul D. Dalton, and Carmen Villmann\*


Impairments in neuronal circuits underly multiple neurodevelopmental and neurodegenerative disorders. 3D cell culture models enhance the complexity of *in vitro* systems and provide a microenvironment closer to the native situation than with 2D cultures. Such novel model systems will allow the assessment of neuronal network formation and their dysfunction under disease conditions. Here, mouse cortical neurons are cultured from embryonic day E17 within in a fiber-reinforced matrix. A soft Matrigel with a shear modulus of  $31 \pm 5.6$  Pa is reinforced with scaffolds created by melt electrowriting, improving its mechanical properties and facilitating the handling. Cortical neurons display enhanced cell viability and the neuronal network maturation in 3D, estimated by staining of dendrites and synapses over 21 days *in vitro*, is faster in 3D compared to 2D cultures. Using functional readouts with electrophysiological recordings, different firing patterns of action potentials are observed, which are absent in the presence of the sodium channel blocker, tetrodotoxin. Voltage-gated sodium currents display a current–voltage relationship with a maximum peak current at  $-25$  mV. With its high customizability in terms of scaffold reinforcement and soft matrix formulation, this approach represents a new tool to study neuronal networks in 3D under normal and, potentially, disease conditions.

3D *in vitro* cell culture models are becoming more and more important as they attempt to recreate the *in vivo* microenvironment of cells. The field of neuroscience is no exception with

D. Janzen, Dr. C. Martin, Prof. C. Villmann  
Institute for Clinical Neurobiology  
University Hospital Würzburg  
Versbacherstr. 5, Würzburg 97078, Germany  
E-mail: Villmann\_C@ukw.de

E. Bakirci, Prof. P. D. Dalton  
Department of Functional Materials in Medicine and Dentistry  
and Bavarian Polymer Institute  
University Hospital Würzburg  
Pleicherwall 2, Würzburg 97070, Germany

A. Wieland  
Department of Obstetrics and Gynecology  
University Hospital Erlangen  
Laboratory for Molecular Medicine  
FAU Erlangen-Nürnberg  
Universitätsstrasse, 21–23, Erlangen 91054, Germany

 The ORCID identification number(s) for the author(s) of this article can be found under <https://doi.org/10.1002/adhm.201901630>.

© 2020 The Authors. Published by WILEY-VCH Verlag GmbH & Co. KGaA, Weinheim. This is an open access article under the terms of the Creative Commons Attribution-NonCommercial License, which permits use, distribution and reproduction in any medium, provided the original work is properly cited and is not used for commercial purposes.

DOI: 10.1002/adhm.201901630

the third dimension especially important for neuronal outgrowth and thus dendritic arborization. Such 3D neuronal cultures have been described in various hydrogels/matrices and scaffolds.<sup>[1]</sup> Some common matrices are agarose,<sup>[2]</sup> alginate,<sup>[3,4]</sup> collagen,<sup>[5,6]</sup> and Matrigel<sup>[7]</sup> while peptides derived from extracellular matrix (ECM) proteins such as laminin (RGD, YIGSR, IKVAV) are often used to influence cell behavior.<sup>[8]</sup> Alongside variables like growth factors and ECM proteins, matrix stiffness is an important factor when trying to create an *in vitro* 3D neuronal model that is intended to mimic the *in vivo* situation.<sup>[9]</sup> Brain tissue is extremely soft, with reported elastic moduli ranging from 30–500 Pa, depending on brain region and developmental stage.<sup>[10]</sup> Stiffness gradients are detected by neurons and used as guidance cues, affecting growth direction and neurite length.<sup>[3,11]</sup> Mimicking soft brain tissue requires equally soft matrices, which are difficult to handle and easily destroyed, for example, when performing immunocytochemical staining. One solution to this problem is the fiber-reinforcement of soft matrices.

Melt electrowriting (MEW) is a relatively new additive manufacturing technology<sup>[12]</sup> and can fabricate highly porous (>90 vol%) reinforcing frames.<sup>[13]</sup> Such MEW-reinforced cell-containing matrices have been used in strong and tough biomaterials for cartilage<sup>[13]</sup> and vascular applications.<sup>[14]</sup> The placement of the fibers, and whether they are linear or sinusoidal can significantly influence the mechanics and porosity of the hydrogel composite.<sup>[15]</sup> Mechanical properties and biological response to the scaffolds could therefore be adjusted with the internal architecture and hybrid scaffold design.<sup>[12,14]</sup> Additionally, MEW uses no toxic solvents and scaffolds can be used almost immediately within the biological framework.

Previously, we described how poly( $\epsilon$ -caprolactone) (PCL) scaffolds made via MEW could be used for reinforcement of Matrigel.<sup>[16]</sup> Using this technique, we created a 3D model that allowed 3D electrophysiology of a transfected fibroblast cell line.<sup>[16]</sup> This study expands on this, to incorporate and perform 3D electrophysiology of neurons. Techniques were developed to prevent blockage of the patch pipette by the Matrigel, and to direct it toward a neuron to take recordings. Reinforcing PCL MEW frames with ten layers and a hatch spacing of 200  $\mu$ m were fabricated and used as 9 mm discs that fit into 24-well

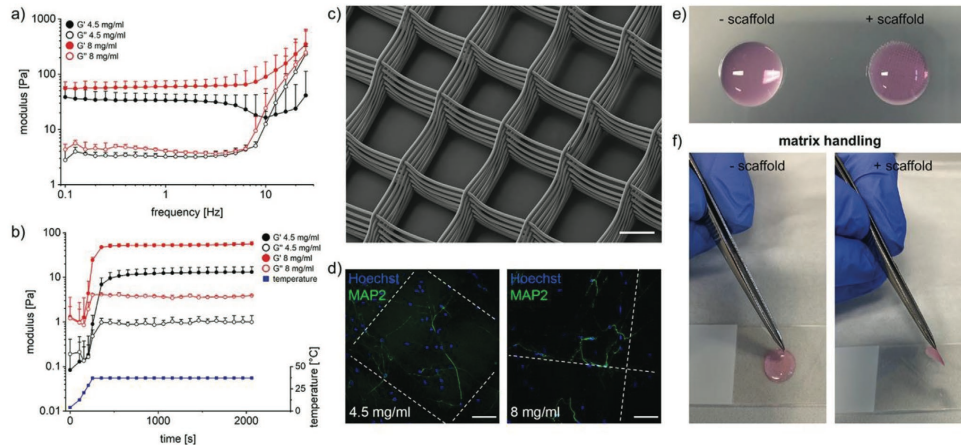


**Figure 1.** Rheological characterization of Matrigel at different concentrations. a) Frequency sweep and b) time sweep data comparing rheological storage ( $G'$ ) and loss moduli ( $G''$ ) of 4.5 and 8 mg mL<sup>-1</sup> Matrigel. Error bars indicate standard deviation ( $n = 3$  independent experiments). Lower graph exhibits the temperature plot (blue curve). c) Scanning electron microscopy image of MEW-scaffold with a hatch spacing of 200  $\mu\text{m}$ , diameter of scaffolds is 9 mm. d) Cortical neurons at DIV7 using 4.5 and 8 mg mL<sup>-1</sup> Matrigel-scaffold composites ( $n = 3$ ). Neurons were stained for MAP2 (green) and the nucleus (Hoechst, blue). White dotted lines indicate MEW fibers. Scale bar = 50  $\mu\text{m}$ . e) Drop-like hydrogel (Matrigel 4.5 mg mL<sup>-1</sup>) without (left) and with (right) scaffold. f) Handling properties of soft Matrigel without (left) and with (right) MEW scaffold. Note, the matrix without scaffold cannot be lifted with forceps. Presence of scaffold allows easy transfer with forceps.

plates. Since PCL is a slowly degrading polymer (2–3 years),<sup>[17]</sup> it can be considered stable for the periods used in this study.

Rheological measurements of Matrigel with concentrations of 4.5 and 8 mg mL<sup>-1</sup> were performed without the MEW scaffold. Using an amplitude sweep at 1 Hz, the linear viscoelastic region of Matrigel was identified up to 1% strain (data not shown), therefore a lower strain of 0.1% was used to ensure deformation remains within the linear region. A frequency sweep of 0.1–30 Hz confirms crosslinking of Matrigel at both concentrations (Figure 1a). Values obtained from amplitude and frequency sweep were used for a time sweep to get a gelation profile of Matrigel at concentrations of 4.5 and 8 mg mL<sup>-1</sup> (Figure 1b, blue line). The final storage modulus of Matrigel was  $31 \pm 5.6$  Pa for 4.5 mg mL<sup>-1</sup> and  $66 \pm 4.4$  Pa for 8 mg mL<sup>-1</sup> concentrations, shown in Figure 1b with corresponding temperature profile used for gelation.

To exhibit neuronal network formation, mouse cortical neurons taken from embryonic stage E17 were seeded into MEW (Figure 1c) reinforced Matrigel of both concentrations (Figure 1d). The presence of MEW had no obvious impact on dendrite extend, orientation, and neuronal network formation within 21 days in vitro (DIV) of growth in 4.5 mg mL<sup>-1</sup> compared to 8 mg mL<sup>-1</sup> of Matrigel. Since embryonic neurons come from a rather soft environment, the following experiments were performed at the lower Matrigel concentration of 4.5 mg mL<sup>-1</sup>. The presence of MEW, however enabled handling and easy transfer of the formed neuronal network in reinforced Matrigel for various experimental purposes (Figure 1e,f and Video S1, Supporting Information).

The cell viability of cortical neurons in reinforced Matrigel was measured at DIV1, 7, 14, and 21, Figure 2a). Viability was

high in 3D at DIV1 ( $85 \pm 7\%$ ) and DIV7 ( $83 \pm 6\%$ ) and significantly decreased after 2 (DIV14,  $65 \pm 7\%$ ) and 3 (DIV21,  $54 \pm 8\%$ ) weeks in culture (Figure 2b). Living cells also reduce over time in 2D neuronal cultures,<sup>[18,19]</sup> however the number in 2D culture was already lower after 1 week (DIV7,  $50 \pm 8\%$ ) than in 3D cultures after 3 weeks (Figure 2b). Immunocytochemical staining of cortical neurons was performed to visualize neuronal network formation in MEW scaffold reinforced Matrigel (Figure 2c). The dendritic marker MAP2 as well as the synaptic marker synaptophysin<sup>[20]</sup> were used to specifically concentrate on synapse formation as an estimate of neuronal maturation. At DIV1, MAP2 and synaptophysin signals were limited to a few cells and located close to nuclei, as neurite formation was just beginning (Figure 2c,d). A widespread neuronal network with strong MAP2 and synaptophysin signal has been formed by DIV7 with further increased network density at DIV14 and DIV21. The 3D reconstruction of neurons within the fiber-reinforced matrix revealed a close proximity of both markers (Figure 2d and Video S2, Supporting Information). The quantification of the synaptophysin signal as an estimate for the number of synapses formed demonstrated a larger increase of synapse formation within the first 7 days in 3D compared to 2D cultures (3D: synaptophysin density/100  $\mu\text{m}$  dendrite  $15 \pm 10$ ,  $n = 26$ ; 2D  $7.5 \pm 7.5$ ,  $n = 17$ ; Figure 2e). Furthermore, dendrites grew longer within the first week in 3D cultures compared to 2D cultures (3D:  $86 \pm 40$   $\mu\text{m}$ ,  $n = 39$ ); 2D:  $56 \pm 25$   $\mu\text{m}$ ,  $n = 25$ , Figure 2f). Our results indicate that cortical neurons start to form a structural network after only DIV7 in 3D cultures.

To investigate the maturation level of the 3D neural network, calcium imaging was performed (Figure 3a and Video S3,

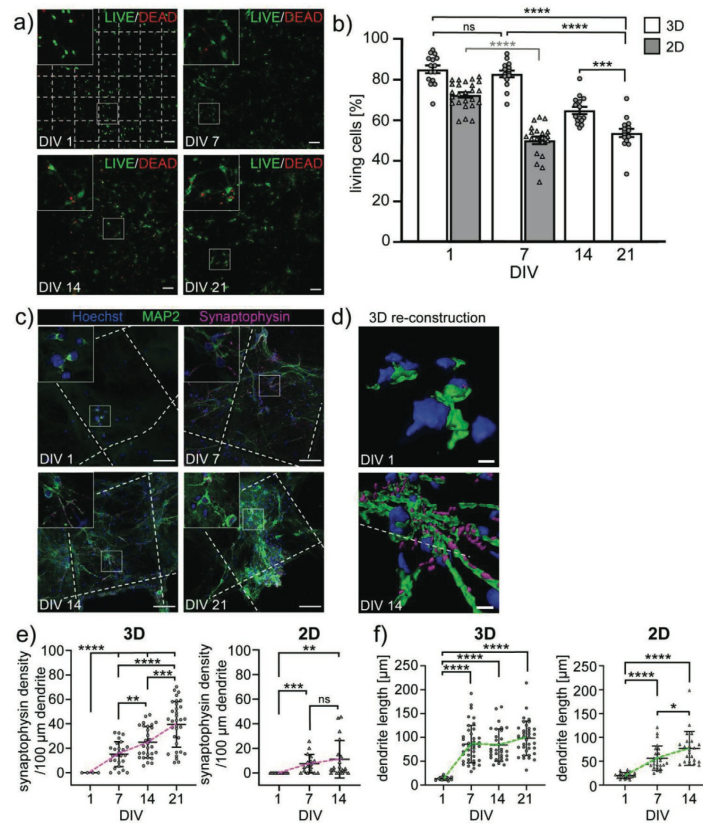


**Figure 2.** Cortical neurons commence network formation around DIV7 in 3D cultures. a) Cell viability assay of cortical neurons in 3D after DIV1, 7, 14, 21. Live cells are shown green; dead cells, red. Scale bar = 100  $\mu\text{m}$ ; three independent experiments were performed  $n = 3$ . b) Cell viability was quantified by cell counting in five images per experiment. Living cells: white bars 3D, gray bars 2D. Note, the cell viability at DIV7 in 2D is lower compared to 3D cultures after 3 weeks in culture. Black asterisks refer to 3D viability, gray asterisks to 2D living cells,  $***p < 0.001$ ,  $****p < 0.0001$ . c) Immunocytochemical staining of 3D cortical neurons in  $4.5 \text{ mg mL}^{-1}$  Matrigel-scaffold composites (MAP2, green; synaptophysin, magenta; nuclei (Hoechst), blue). White dotted lines indicate MEW fibers. Insets show a single  $1 \mu\text{m}$  slice of the highlighted areas (white box). Scale bar = 50  $\mu\text{m}$ . d) 3D reconstruction of magnified areas from DIV1 and 14 seen in (c). e) Quantification of synaptophysin as a synaptic marker in 3D (circles) and 2D (triangles) cultures, pink dotted lines connect mean values,  $n = 3$ . f) Comparison of neurite length in 3D (circles) and 2D (triangles) cultures, green dotted lines connect mean values,  $n = 3$ . Values of significance in (e) and (f)  $**p < 0.01$ ,  $***p < 0.001$ ,  $****p < 0.0001$ , ns = non significant, error bars indicate standard deviation.

Supporting Information). Between DIV13–16 in 2D neuronal cultures, neuronal networks show synchronized network activity.<sup>[21,22]</sup> At DIV14, spontaneous action potential firing was primarily observed which could be blocked by application of the sodium channel blocker TTX (Figure 3b). Hence, we used the time window between DIV14–18 to perform electrophysiological measurements from cortical neurons in 3D using the whole-cell configuration either in current or voltage-clamp mode.<sup>[23]</sup> Neuronal cultures in scaffold reinforced Matrigel were transferred to a recording chamber and fixed with an O-ring.<sup>[6]</sup> We used MEW fibers with a frame size of 200  $\mu\text{m}$  which

displayed enough space for the recording pipette mounted in a  $45^\circ$  angle to reach cortical neurons not only at the top but also in deeper layers of the reinforced matrix.<sup>[16]</sup> Positive pressure was applied to the patch pipette to prevent clogging with matrix while approaching a cell (Figure 3c). Occasionally, pressure was increased even further in short bursts to clear the cell of matrix (Video S4, Supporting Information). The rapid transmission of electrical signals and their conversion into chemical signals depends on the action of voltage-gated sodium channels (VGSCs). Voltage-gated sodium currents were recorded using 10 mV steps from  $-80 \text{ mV}$  to  $+40 \text{ mV}$  ( $n = 6$ , Figure 3d). The

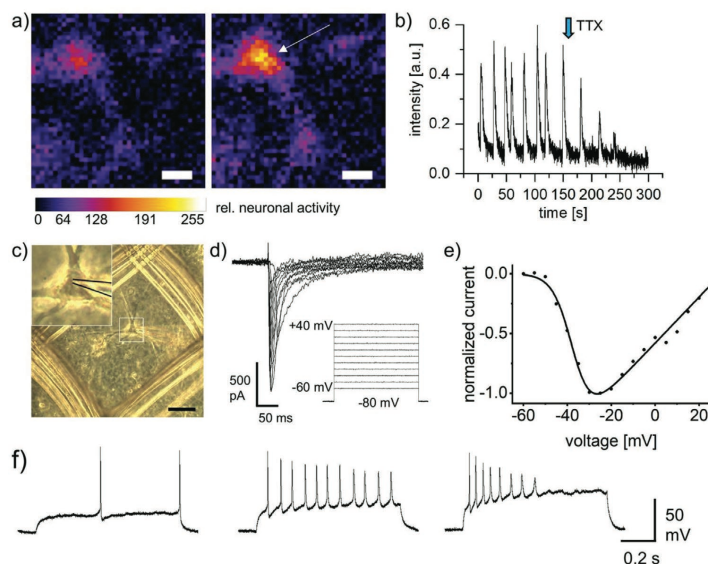


**Figure 3.** Cortical neurons grown in scaffold reinforced Matrigel exhibit neuronal network activity. a) Calcium imaging of cortical neurons in reinforced matrix at DIV14. Same cell without (left) and with (right) neuronal activity. Relative neuronal activity is shown by color code from dark blue (no activity) to yellow (high activity). White bar refers to 10  $\mu\text{m}$ . b) Spontaneous action potential firing of cortical neurons in reinforced Matrigel over a time course of 300 s. Application of the sodium channel blocker tetrodotoxin (TTX) to block neuronal activity is marked by blue arrow. c) Cortical neuron in MEW scaffold reinforced Matrigel. Inset shows magnification with the patch pipette (traced in black) approaching the cell. Scale bar = 50  $\mu\text{m}$ . d) Representative traces of voltage-gated sodium channel recordings at voltages from  $-80$  to  $+40$  mV,  $n = 6$ . e) Typical current–voltage relationship of voltage-gated sodium channels with the largest amplitude at  $-25$  mV. f) Current clamp recordings of action potentials from DIV18 cortical neurons. An increasing current was injected for 800 ms in 10 pA steps. Depolarization above threshold evokes single APs (top). Strong depolarization results in repetitive firing (middle) and eventually a complete blockage (bottom).

current–voltage relationship showed maximum sodium currents at  $-25$  mV (Figure 3e).<sup>[24]</sup>

After achieving the whole-cell configuration, action potentials were recorded in current clamp mode by injection of 10 pA current steps starting at a membrane potential of  $-80$  mV. Current injection to a near-threshold potential evoked single action potentials (Figure 3f, left trace). Further current injection resulted in repetitive firing and eventually, blockage of action potentials (Figure 3f, middle and right trace). Similar firing patterns have been reported before for cortical pyramidal neurons.<sup>[25]</sup>

Action potential firing argues for functional neuronal network formation.<sup>[19,22,26]</sup> To exhibit functional neuronal networks with synchronized activity, the initial cell density during seeding is important.<sup>[27]</sup> While we have tested densities of 5400–16200 cells  $\text{mm}^{-3}$ , the optimal cell density was estimated to 10 800 cells  $\text{mm}^{-3}$ .

Previously, we described a transfected cell line embedded in MEW scaffold reinforced Matrigel and electrophysiological recordings of a transfected ligand-gated ion channel.<sup>[16]</sup> Here, we successfully used this 3D cell culture approach to study primary cortical neurons, demonstrating that this model achieves the state of a mature functional neuronal network after 2 weeks

in culture with better cell survival, faster dendrite growth and synapse formation within the first week in culture compared to 2D cultures. This model could be further improved by replacing Matrigel with matrices specifically tailored for the desired cell type. Full control over mechanical support and matrix formulation will allow creation of an optimal environment for studying growth and electrophysiological properties of cells of the central nervous system. The MEW scaffolds used here provide mechanical support for weak matrices comparable to the native embryonic brain environment and allow sufficient handling to study neuronal cell types under healthy and, potentially, disease conditions.

## Experimental Section

**MEW Process:** A custom-built MEW printer<sup>[28]</sup> was used to fabricate scaffolds as previously described.<sup>[16]</sup> Briefly, MEW was performed using medical-grade PCL (PURASORB PC 12, Lot#1712002224, 05/2018; Corbion Inc, Amsterdam, Netherlands) at  $21 \pm 2$  °C and a humidity of  $35 \pm 10\%$ . The following parameters were used: heating to 80 °C; 3 bar of air pressure; 25G nozzle; 6 kV voltage applied across a 4 mm collector distance. A  $48 \times 96$  mm rectangular mesh with ten layers and 200  $\mu\text{m}$  fiber spacing was direct-written and cut to 9 mm disks with an infrared laser.

**Mechanical Behavior:** Rheological characterization of Matrigel was performed using a Physica MCR 301 rheometer (Anton Paar, Graz, Austria) with a parallel plate configuration (25 mm diameter, 0.5 mm gap size). Matrigel samples (500  $\mu\text{L}$ ; 4.5 or 8  $\text{mg mL}^{-1}$ ) were loaded onto the lower plate at 4  $^{\circ}\text{C}$ .<sup>[6]</sup> The amplitude sweep was performed between 0.01% and 100% strain at 1 Hz. According to amplitude sweep results, linear viscoelastic regions were defined, and the frequency sweep was performed between 1 and 30 Hz at 0.1% strain. Samples were exposed to 1 Hz frequency and 0.1% strain to understand time and temperature dependent behavior during heating from 4 to 37  $^{\circ}\text{C}$  at a rate of 10  $^{\circ}\text{C min}^{-1}$  and setting at 37  $^{\circ}\text{C}$  for 30 min. All experiments were performed in triplicates.

**Isolation of Cortical Neurons:** Primary cortical neuronal cultures were prepared at E17 from CD1 mouse embryos. Experiments were authorized by the local veterinary authority and Committee on the Ethics of Animal Experiments (Regierung von Unterfranken). Briefly, cortices were incubated with 0.5  $\text{mg mL}^{-1}$  trypsin, 0.2  $\text{mg mL}^{-1}$  EDTA, and 10  $\mu\text{g mL}^{-1}$  DNase I in PBS for 30 min at 37  $^{\circ}\text{C}$ . Trypsinization was stopped by adding 10% fetal calf serum. Cells were dissociated by trituration and counted.

**Scaffold Preparation, Cell Seeding, and Culture:** MEW scaffolds in 24-well plates were washed once with 70% ethanol, three times with  $\text{ddH}_2\text{O}$ , and once with PBS. A cell suspension containing 200 000 cells and Matrigel (Corning, NY, USA) were mixed to a final volume of 180  $\mu\text{L}$  and a protein concentration of 4.5 or 8  $\text{mg mL}^{-1}$  and pipetted onto scaffolds. After 30 min of incubation at 37  $^{\circ}\text{C}$ , 500  $\mu\text{L}$  Neurobasal medium containing  $2 \times 10^{-3}$  M GlutaMAX and 2% (v/v) B27 supplement was added (Thermo Fisher Scientific, Waltham, MA, USA). For 2D cultures, 150 000 cells were seeded on poly-D-lysine coated glass cover slips. Cortical neurons were cultured in 2D and 3D under standard growth conditions at 37  $^{\circ}\text{C}$  and 5%  $\text{CO}_2$ . As neurons secrete growth factors by themselves into the cell culture medium and thus promote their growth, only 50% of fresh medium was added every week.<sup>[29]</sup>

**Cell Viability:** The viability of cortical neurons was assessed 1, 7, 14, and 21 DIV after seeding. In brief, cells were incubated for 30 min at 21  $^{\circ}\text{C}$  for 30 min with  $2 \times 10^{-6}$  M Calcein-AM (green/living cells; Thermo Fisher Scientific, Waltham, MA, USA) and  $2 \times 10^{-6}$  M ethidium homodimer I (red/dead cells; Sigma-Aldrich, St. Louis, MO, USA) in PBS. Per time point, five images of at least three independent samples were used for determining the live/dead ratio. Cell viability numbers were acquired using the Spots modal of Imaris 7.7.2 (Oxford Instruments, Abingdon, UK).

**Immunocytochemical Staining:** Cortical neurons were stained for microtubule-associated protein 2 (MAP2) and synaptophysin to assess network formation. All steps were performed at 21  $^{\circ}\text{C}$ . Cells were fixed for 10 min with 2% formaldehyde, washed with PBS, and blocked/permeabilized for 3 min with 5% goat serum and 0.2% Triton X-100 in PBS. Cells were incubated with primary antibodies Anti-MAP2 and Anti-Synaptophysin for 1h (both 1:500; MAB3418, AB9272, Merck Millipore, Burlington, MA, USA). Following washing, cells were incubated for 45 min with secondary Alexa488-goat-anti-mouse and Cy3-goat-anti-rabbit antibodies (both 1:500; Dianova, Hamburg, Germany). Cells were mounted on glass slides with Hoechst 33342-containing Prolong Glass Antifade Mountant (Thermo Fisher Scientific, Waltham, MA, USA). Synaptophysin density was determined by tracing dendrites with the ImageJ plugin Neuron and subsequent counting of synaptophysin signal close to traced dendrites using SynapCountJ.<sup>[30]</sup> Dendrite length was measured with the FilamentTracer of Imaris (Oxford Instruments, Abingdon, UK). Only the longest and fully traceable dendrites in each image were analyzed.

**Confocal Microscopy and Image Acquisition:** Cell viability and fluorescence images were acquired using an Olympus IX81 microscope equipped with a FV1000 confocal laser scanning system, a FVD10 SPD spectral detector, and diode lasers of 405, 495, 550, and 635 nm (Olympus, Tokyo, Japan). Olympus UPLSAPO 10 $\times$  (air, numerical aperture 0.4) and UPLFLN 40 $\times$  (oil, numerical aperture 1.3) objectives were used. Phase-contrast images were acquired using a Zeiss Axio Observer D1 microscope (Carl Zeiss AG, Oberkochen, Germany)

equipped with a Moticam 3+ (Motic Europe, Wetzlar, Germany). Images were processed with ImageJ/Fiji 1.52n using maximum intensity projection and display range adjustment.<sup>[31]</sup> Imaris was used for 3D reconstruction (Oxford Instruments, Abingdon, UK).

**Calcium Imaging:** For cell calcium analysis, cortical neurons were labeled with the high affinity calcium indicator Oregon Green 488 BAPTA-1AM (Thermo Fischer Scientific, Waltham, MA, USA). 0.5  $\mu\text{L}$  of a 5 mM stock solution in 20% Pluronic F-127 in DMSO was solved in 500  $\mu\text{L}$  imaging solution for 30 min at 37  $^{\circ}\text{C}$  and 5%  $\text{CO}_2$ . The imaging solution consisted of (in  $\times 10^{-3}$  M) 119 NaCl, 4.5 KCl, 1  $\text{MgCl}_2$ , 2  $\text{CaCl}_2$ , 1.2  $\text{NaH}_2\text{PO}_4$ , 26  $\text{NaHCO}_3$ , 10 glucose, 10 HEPES, pH7.4, adjusted with NaOH. Calcium imaging was performed under continuous perfusion with the imaging solution and TTX (550 nM) was applied using this perfusion system. Image series were captured at 10 Hz with a Rolera XR Mono fast 1394 CCD camera (Qimaging, Surrey, Canada) and StreamPix4 Software (Norpix, Montreal, Canada) under continuous illumination with a cooled epifluorescent light source for 470 nm (Visitron Systems, Puchheim, Germany) and analyzed by ImageJ.

**Electrophysiology:** The patch clamp technique was used to obtain whole-cell recordings of cortical neurons cultured in 3D for 14–21 days. Recording pipettes (2–3 M $\Omega$ ) were pulled from thin-walled borosilicate capillaries (TW150F-4; World Precision Instruments, Sarasota, FL, USA) using a Sutter P97 horizontal puller (Sutter Instrument, Novato, CA, USA). Recordings were obtained with an EPC10 USB amplifier controlled by Patchmaster software (HEKA Elektronik, Lambrecht, Germany). Currents were low-pass filtered at 2.9 kHz and digitized at 20 kHz. For measurement of action potentials, the intracellular solution consisted of (in  $\times 10^{-3}$  M) 130 KCl, 1  $\text{CaCl}_2$ , 1  $\text{MgCl}_2$ , 10 HEPES, 11 EGTA; pH 7.3, adjusted with KOH ( $294 \pm 1.5$  mOsm  $\text{L}^{-1}$ ) and extracellular solution contained (in  $\times 10^{-3}$  M): 140 NaCl, 1  $\text{CaCl}_2$ , 1  $\text{MgCl}_2$ , 10 HEPES; pH 7.3, adjusted with NaOH ( $305 \pm 1.5$  mOsm  $\text{L}^{-1}$ ). A liquid junction potential of 5 mV was corrected, and cells were held at  $-70$  mV. For measuring voltage-gated sodium channels, the intracellular solution contained (in  $\times 10^{-3}$  M) 120 CsF, 5 NaCl, 1  $\text{CaCl}_2$ , 1  $\text{MgCl}_2$ , 10 HEPES, 11 EGTA, 2 Mg-ATP, 5 TEA-Cl; pH 7.3, adjusted with CsOH ( $303 \pm 1.5$  mOsm  $\text{L}^{-1}$ ) and the extracellular solution consisted of (in  $\times 10^{-3}$  M): 140 NaCl, 1  $\text{CaCl}_2$ , 1  $\text{MgCl}_2$ , 10 HEPES, 0.5  $\text{CdCl}_2$ ; pH 7.3, adjusted with NaOH ( $310 \pm 1.5$  mOsm  $\text{L}^{-1}$ ). A liquid junction potential of 9 mV was corrected, and cells were held at  $-80$  mV.  $R_s$  was compensated 80% to minimize voltage errors. The P/5 protocol was used to subtract leak currents and voltage.

**Statistical Analysis:** GraphPad Prism 8.3.0 (Graphpad Software, San Diego, CA, USA) was used to calculate mean values, standard deviation (SD), standard error of the mean, and values for statistical significance. Statistical significance was estimated using an unpaired *t* test with Welch's correction with \**p* < 0.05, \*\**p* < 0.01, \*\*\**p* < 0.001, \*\*\*\**p* < 0.0001.

## Supporting Information

Supporting Information is available from the Wiley Online Library or from the author.

## Acknowledgements

This work was funded by the Deutsche Forschungsgemeinschaft (DFG, German Research Foundation)—Project number 326998133—TRR 225 (subproject B01). The technical assistance of Mr. Andrei Hrynevich is greatly appreciated.

## Conflict of Interest

The authors declare no conflict of interest.

## Keywords

3D electrophysiology, 3D neuronal networks, cortical neurons, melt electrowriting

Received: November 15, 2019  
Revised: February 17, 2020  
Published online:

- [1] a) K. Chwalek, M. D. Tang-Schomer, F. G. Omenetto, D. L. Kaplan, *Nat. Protoc.* **2015**, *10*, 1362; b) M. F. Daud, K. C. Pawar, F. Claeysens, A. J. Ryan, J. W. Haycock, *Biomaterials* **2012**, *33*, 5901; c) A. R. Murphy, J. M. Haynes, A. L. Laslett, N. R. Cameron, C. M. O'Brien, *Acta Biomater.* **2019**, *101*, 102; d) S. K. Seidlits, J. Liang, R. D. Bierman, A. Sohrabi, J. Karam, S. M. Holley, C. Cepeda, C. M. Walthers, *J. Biomed. Mater. Res., Part A* **2019**, *107*, 704.
- [2] a) A. P. Balgude, X. Yu, A. Szymanski, R. V. Bellamkonda, *Biomaterials* **2001**, *22*, 1077; b) R. Bellamkonda, J. P. Ranieri, N. Bouche, P. Aebischer, *J. Biomed. Mater. Res.* **1995**, *29*, 663.
- [3] G. Palazzolo, N. Brogiere, O. Cenciarelli, H. Dermutz, M. Zenobi-Wong, *Tissue Eng., Part A* **2015**, *21*, 2177.
- [4] J. P. Frampton, M. R. Hynd, M. L. Shuler, W. Shain, *Biomed. Mater.* **2011**, *6*, 015002.
- [5] N. Dubey, P. C. Letourneau, R. T. Tranquillo, *Exp. Neurol.* **1999**, *158*, 338.
- [6] T. Xu, P. Molnar, C. Gregory, M. Das, T. Boland, J. J. Hickman, *Biomaterials* **2009**, *30*, 4377.
- [7] J. Park, I. Wetzel, I. Marriott, D. Dreau, C. D'Avanzo, D. Y. Kim, R. E. Tanzi, H. Cho, *Nat. Neurosci.* **2018**, *21*, 941.
- [8] a) P. D. Dalton, J. Mey, *Front. Biosci.* **2009**, *14*, 769; b) J. C. Schense, J. Bloch, P. Aebischer, J. A. Hubbell, *Nat. Biotechnol.* **2000**, *18*, 415; c) J. C. Schense, J. A. Hubbell, *J. Biol. Chem.* **2000**, *275*, 6813.
- [9] a) E. H. Barriga, K. Franze, G. Charras, R. Mayor, *Nature* **2018**, *554*, 523; b) E. Moeendarbary, I. P. Weber, G. K. Sheridan, D. E. Koser, S. Soleman, B. Haenzi, E. J. Bradbury, J. Fawcett, K. Franze, *Nat. Commun.* **2017**, *8*, 14787.
- [10] a) A. F. Christ, K. Franze, H. Gautier, P. Moshayedi, J. Fawcett, R. J. Franklin, R. T. Karadottir, J. Guck, *J. Biomech.* **2010**, *43*, 2986; b) M. Iwashita, N. Kataoka, K. Toida, Y. Kosodo, *Development* **2014**, *141*, 3793.
- [11] D. E. Koser, A. J. Thompson, S. K. Foster, A. Dwivedy, E. K. Pillai, G. K. Sheridan, H. Svoboda, M. Viana, L. D. Costa, J. Guck, C. E. Holt, K. Franze, *Nat. Neurosci.* **2016**, *19*, 1592.
- [12] T. M. Robinson, D. W. Huttmacher, P. D. Dalton, *Adv. Funct. Mater.* **2019**, *29*, 1904664.
- [13] J. Visser, F. P. Melchels, J. E. Jeon, E. M. van Bussel, L. S. Kimpton, H. M. Byrne, W. J. Dhert, P. D. Dalton, D. W. Huttmacher, J. Malda, *Nat. Commun.* **2015**, *6*, 6933.
- [14] N. T. Saïdy, F. Wolf, O. Bas, H. Keijndener, D. W. Huttmacher, P. Mela, E. M. De-Juan-Pardo, *Small* **2019**, *15*, 1900873.
- [15] O. Bas, D. D'Angella, J. G. Baldwin, N. J. Castro, F. M. Wunner, N. T. Saïdy, S. Kollmannsberger, A. Reali, E. Rank, E. M. De-Juan-Pardo, D. W. Huttmacher, *ACS Appl. Mater. Interfaces* **2017**, *9*, 29430.
- [16] N. Schaefer, D. Janzen, E. Bakirci, A. Hrynevich, P. D. Dalton, C. Villmann, *Adv. Healthcare Mater.* **2019**, *8*, 1801226.
- [17] M. Bartnikowski, T. R. Dargaville, S. Ivanovski, D. W. Huttmacher, *Prog. Polym. Sci.* **2019**, *96*, 1.
- [18] T. Voigt, H. Baier, A. Dolabela de Lima, *Eur. J. Neurosci.* **1997**, *9*, 990.
- [19] T. Opitz, A. D. De Lima, T. Voigt, *J. Neurophysiol.* **2002**, *88*, 2196.
- [20] G. Kierstein, K. Obst, P. Wahle, *Dev. Brain Res.* **1996**, *92*, 39.
- [21] a) T. A. Basarsky, V. Parpura, P. G. Haydon, *J. Neurosci.* **1994**, *14*, 6402; b) R. Blum, C. Heinrich, R. Sanchez, A. Lepier, E. D. Gundelfinger, B. Berninger, M. Gotz, *Cereb. Cortex* **2011**, *21*, 413; c) T. L. Fletcher, P. De Camilli, G. Banker, *J. Neurosci.* **1994**, *14*, 6695.
- [22] T. Voigt, T. Opitz, A. D. de Lima, *J. Neurosci.* **2005**, *25*, 4605.
- [23] M. Lindau, E. Neher, *Pflügers Arch.* **1988**, *411*, 137.
- [24] a) L. S. Milescu, B. P. Bean, J. C. Smith, *J. Neurosci.* **2010**, *30*, 7740; b) T. R. Cummins, F. Aglieco, M. Renganathan, R. I. Herzog, S. D. Dib-Hajji, S. G. Waxman, *J. Neurosci.* **2001**, *21*, 5952.
- [25] O. P. Hamill, J. R. Huguenard, D. A. Prince, *Cereb. Cortex* **1991**, *1*, 48.
- [26] D. Lam, H. A. Enright, J. Cadena, S. K. G. Peters, A. P. Sales, J. J. Osburn, D. A. Soscia, K. S. Kulp, E. K. Wheeler, N. O. Fischer, *Sci. Rep.* **2019**, *9*, 4159.
- [27] a) M. Chiappalone, M. Bove, A. Vato, M. Tedesco, S. Martinoia, *Brain Res.* **2006**, *1093*, 41; b) R. Madhavan, Z. C. Chao, S. M. Potter, *Phys. Biol.* **2007**, *4*, 181.
- [28] T. D. Brown, P. D. Dalton, D. W. Huttmacher, *Adv. Mater.* **2011**, *23*, 5651.
- [29] S. Majd, A. Zarifkar, K. Rastegar, M. A. Takshid, *Iran. Biomed. J.* **2008**, *12*, 101.
- [30] E. Meijering, M. Jacob, J. C. Sarria, P. Steiner, H. Hirling, M. Unser, *Cytometry* **2004**, *58A*, 167.
- [31] J. Schindelin, I. Arganda-Carreras, E. Frise, V. Kaynig, M. Longair, T. Pietzsch, S. Preibisch, C. Rueden, S. Saalfeld, B. Schmid, J. Y. Tinevez, D. J. White, V. Hartenstein, K. Eliceiri, P. Tomancak, A. Cardona, *Nat. Methods* **2012**, *9*, 676.

# Discussion

## The GlyR Extracellular $\beta 8$ - $\beta 9$ Loop

Previously, residues involved in the signal transduction process of GlyRs translating ligand-binding into channel opening have been mainly defined by studies on point mutations found in human patients suffering from startle disease following generation and functional characterization of such GlyR variants (Bode & Lynch 2014). Initial structural data based on X-ray crystallographic structures of CLRs of lower organisms, e.g., acetylcholine-choline binding protein from *Lymnaea stagnalis* and *Aplysia californica* (Brejc et al. 2001; Hansen et al. 2005), the bacterial ELIC and GLIC (Hilf & Dutzler 2008; Bocquet et al. 2009), and the glutamate-gated chloride channel from *Caenorhabditis elegans* (Hibbs & Gouaux 2011). Since the structure of the GlyR has been solved, several regions of the extracellular domain (ECD) participating in this process have been identified. The ECD is formed by a short  $\alpha$ -helix followed by 10  $\beta$ -sheets connected by short loop structures. The preM1-M1 region, the M2, the Cys-loop,  $\beta 10$ , the M2-3 loop, the  $\beta 1$ -2 loop, as well as the  $\beta 8$ - $\beta 9$  loop are suggested to undergo structural transitions as a prerequisite for signal transduction processes. This transduction unit enables the receptor to switch between the closed and open states (Hassaine et al. 2014; Du et al. 2015; Morales-Perez et al. 2016). Mutations in these structurally important regions underlie disease mechanisms, e.g., mutations of residue R65 resulted into an up to 1250-fold decrease in glycine EC<sub>50</sub> as well as significant decrease in surface protein expression (Grudzinska et al. 2005; Chung et al. 2010).

The  $\beta 8$ - $\beta 9$  loop is highly flexible and moves into varying orientations depending on the receptor state. Moreover, the  $\beta 8$ - $\beta 9$  loop contributes to a hydrogen bond network close to the ligand binding site that is important for receptor state transition (Padgett & Lummis 2008; Nys et al. 2013). A very recent structural model of the GlyR confirmed the importance of this hydrogen bond network. In particular, the hydrogen-bond between residues Q219 in the pre-M1 and Q186 in the  $\beta 8$ - $\beta 9$  loop stabilizes the receptor in the open and desensitized states (Yu et al. 2021). The human mutation GlyR $\alpha 1^{W170S}$ , localized in the  $\beta 8$ - $\beta 9$  loop, displayed accelerated decay, rise times, and a complete abolishment of Zn<sup>2+</sup> enhancement (Al-Futaisi et al. 2012; Zhou et al. 2013; Zhang et al. 2016; Cornelison et al. 2017). Another mutation, GlyR $\alpha 3^{P185L}$ , increased glycine potency *in vitro* (Meier et al. 2005). In the startle disease mouse model *shaky*, the underlying mutation GlyR $\alpha 1^{Q177K}$  decreased synaptic



localization, as well as reduced glycine potency, current amplitudes, frequencies, and decay times. Residue Q177 was shown to be part of a functionally important hydrogen network together with the aforementioned residue R65 (Schaefer et al. 2017).

The aim of the publication entitled “**The GlyR Extracellular  $\beta$ 8– $\beta$ 9 Loop – A Functional Determinant of Agonist Potency**” was to investigate how charge, volume, and side chain length at position 177 of the GlyR $\alpha$ 1 subunit affect expression, localization, and function of the receptor and thus gain new knowledge on the importance of  $\beta$ 8– $\beta$ 9 loop for proper ion channel function. Nine mutations were generated and analyzed in HEK293 cells: The original *shaky* mutation Q177K; Q177R, which also has a positively charged but larger side chain; Q177D and Q177E, both having a negatively charged side chain; the conservative exchange Q177N; Q177A and Q177G, which introduce very small or no side chain; Q177C, containing a thiolated side chain; and Q177W, which is the largest amino acid and contains an aromatic indole ring.

GlyR mutations commonly affect either expression and trafficking or ion channel function (Chung et al. 2010). Previous experiments could show a reduced overall expression for GlyR $\alpha$ 1<sup>Q177K</sup> (Schaefer et al. 2017). In the present study, whole-cell lysates and immunocytochemical surface staining of the nine Q177 variants in HEK293 cells revealed no differences in expression or surface localization compared to wild-type GlyR $\alpha$ 1, with and without co-expression of the  $\beta$  subunit. Biotinylation of surface proteins allowed separation and quantification of both whole-cell and surface protein levels. No significant differences in expression could be detected for whole-cell expression of the Q177 variants. However, significant reductions of surface expression for all variants except Q177E, Q177G, and Q177N could be detected, when expressed without the  $\beta$  subunit. Q177K displayed the lowest surface expression level, confirming previous data on this mutant (Schaefer et al. 2017). Co-expression with GlyR $\beta$  further decreased surface expression levels for all mutants. This effect may be explained by the low amount of GlyR $\beta$  DNA used during cell transfection, as in the presence of GlyR $\beta$  the formation of heteromeric  $\alpha$ 1 $\beta$  receptors and their co-transport to the cellular surface is promoted over homomeric receptor assemblies. It has been shown before that co-expression of GlyR $\beta$  promotes surface expression (Chung et al. 2010). Protein degradation was visible in the surface fractions of some variants, hinting at maturation deficits, which have been described before for other GlyR $\alpha$ 1 mutations (Schaefer et al. 2015). Interestingly, the *shaky* mutation Q177K resulted in significantly reduced surface expression, while expression levels of Q177R and the structurally similar Q177E were unchanged.

A reduced ion channel surface expression is commonly associated with reduced maximal currents at saturating agonist concentrations and corresponding electrophysiological data on GlyR mutants have been published before (Villmann et al. 2009b; Chung et al. 2010). However, none of the Q177 variants displayed reduced maximal currents at saturating glycine concentrations, thus indicating that the reduced surface expression of some variants is not sufficient to change maximal currents. These results are in line with previous results for Q177K demonstrating no change in maximal currents despite reduced surface expression *in vitro* (Schaefer et al. 2017). An earlier publication has already exhibited that a reduced surface expression of GlyR $\alpha$ 1 loop B mutants not necessarily resulted in reduced maximal currents (Schaefer et al. 2015). Furthermore, the dramatic neuromotor phenotype of GlyR $\beta$ -deficient *spastic* mice could be rescued by increasing GlyR $\beta$  expression to just 25%, indicating that low GlyR expression can still be sufficient to ensure proper inhibition, even *in vivo* (Hartenstein et al. 1996). However, all Q177 variants displayed significantly decreased currents at a low non-saturating glycine concentration, hinting at a reduced glycine potency. All Q177 variants exhibited a decreased glycine potency. While mutation Q177C and Q177N decreased potency around 1.5-fold, Q177K, Q177R, Q177G, and Q177A decreased it 3 to 5-fold. As it was previously shown that glycine and strychnine binding efficiency are unchanged for Q177K, those reductions in glycine potency of the Q177 variants most probably seemed to result from changes in the hydrogen bond network around residue Q177.

Modelling was performed using structural data obtained by Huang et al. (2017b) (PDB code 5TIN) to analyze how the Q177 variants affect this hydrogen bond network. In the wild type GlyR $\alpha$ 1, the oxygen of the amide side chain of glutamine acts as the hydrogen bond acceptor for residue R65, which directly participates in glycine binding (Grudzinska et al. 2005; Du et al. 2015). Variants Q177K and Q177R do not form this bond with R65 as the side chains of both amino acids lysine and arginine lack oxygen. Q177G and Q177W are also unable to form this bond, albeit because of different reasons. Glycine is the smallest amino acid and does not have a side chain. In contrast, the large volume of the indole ring of tryptophane makes a hydrogen bond with R65 impossible. The human mutation GlyR $\alpha$ 1<sup>R65W</sup> resulted in disturbed GlyR trafficking to the cell surface, indicating that tryptophane may also disrupt the hydrogen network on the opposite site of Q177 (Chung et al. 2010). Alanine, having the shortest side chain lacking oxygen, makes R65 binding also impossible in the Q177A variant. The asparagine of the mutant Q177N lacks one methylene unit compared to the original glutamine. This results in a weaker hydrogen bond with R65 and possibly affects the glycine

binding pocket, which would explain the slightly decreased glycine potency. Aspartic acid and glutamic acid both feature a carboxyl group which enable the formation of a hydrogen bond. However, most likely due to the negative charge, both Q177D and Q177E are oriented towards N203, preventing a hydrogen bond with R65. The cysteine of variant Q177C also seems to disturb the hydrogen bond network, which was confirmed by decreased glycine potency. Other effects, like formation of a disulfide bridge with a nearby free cysteine are unlikely, as the nearby residues C138-C152 and C198-209 already form stable bonds (James et al. 2013). Cysteines and their disulfide bridges have been shown to be important for GlyR maturation and folding, with their disruption leading to partial or complete intracellular retention (Vogel et al. 2009). Although we could observe reduced glycine potency in the Q177 variants, no obvious changes in receptor kinetics could be detected. Breitingner et al. (2001) performed a similar study in analyzing the effect of volume and charge of amino acids at GlyR $\alpha$ 1 residue P250, located in the M1-2 loop, which ensures correct ion channel shape. While surface expression levels were not quantified, the authors observed rapid desensitization and decreased glycine potency for amino acids carrying bulky, hydrophobic side chains, in particular P250V/I/L/F (Breitingner et al. 2001). These amino acids were not analyzed in our study, however due to the location of Q177 in the  $\beta$ 8- $\beta$ 9 loop, which is not part of the ion channel pore, an impact on receptor kinetics seems unlikely. In summary, our results show that mutations of residue Q177 does decreased surface expression in some cases, but not enough to affect maximum currents, as well as glycine potency. This seems to be the results of a disrupted hydrogen bond network with nearby residues like R65.

As previously described, the GlyR  $\beta$ 8- $\beta$ 9 loop undergoes large movements as part of a complex signal transduction process together with other structures (Du et al. 2015). Together with the results obtained by Schaefer et al. (2017) regarding the *shaky* mouse model, we could successfully demonstrate the importance of residue Q177 and the  $\beta$ 8- $\beta$ 9 loop in regard to correct receptor function (Schaefer et al. 2017). The hydrogen bond with R65 is critical for stabilization of the glycine binding pocket. New structural models could confirm the movement of the  $\beta$ 8- $\beta$ 9 loop during state transition (Kumar et al. 2020; Yu et al. 2021). Another hydrogen bond between residues Q186 ( $\beta$ 8- $\beta$ 9 loop) and Q219 (pre-M1) was identified to stabilize the receptor in the open and desensitized states (Yu et al. 2021). Islam et al. (2018) created a GlyR $\alpha$ 2 chimera containing the GlyR $\alpha$ 1  $\beta$ 8- $\beta$ 9 loop, resulting in an exchange of five amino acids. Q177 was not within the exchanged stretch between  $\alpha$ 1 and  $\alpha$ 2. No change in receptor function was observed when comparing the chimera to wild type

GlyR $\alpha$ 2 (Islam et al. 2018). It has been shown for the CLR ELIC, that the antipsychotic compound chlorpromazine was localized in the extracellular ligand-binding domain behind the  $\beta$ 8- $\beta$ 9 loop instead of in the ion channel pore. Chlorpromazine bound to this position inhibited receptor function, arguing for the existence of an allosteric binding site involving the  $\beta$ 8- $\beta$ 9 loop (Nys et al. 2016). A recent publication confirms the existence of a binding site by demonstrating allosteric modulation of the prokaryotic CLR ELIC by nanobodies bound to the  $\beta$ 8- $\beta$ 9 loop (Brams et al. 2020). This allosteric binding site may also exist in other CLRs, including the GlyR, and thus make the  $\beta$ 8- $\beta$ 9 loop a potential target for yet unknown, possibly clinically relevant modulators.

## GABA<sub>A</sub>R Modulation by Sesquiterpenes and Sesquiterpenoids

GABA<sub>A</sub>Rs are major inhibitory ion channels in the central nervous system and are popular targets for treatment of, e.g., epilepsy, insomnia, and anxiety (Lavery et al. 2017). Commonly used agonists with a positive modulatory effect are benzodiazepines, barbiturates, and propofol (Olsen 2018). Neurosteroids, like pregnanolone, are endogenous steroids synthesized in the brain, adrenals, and gonads. They are important modulators of the stress response and anxiety and have their own binding site at GABA<sub>A</sub>Rs located between the transmembrane domains (Miller et al. 2017). GABA<sub>A</sub>Rs are also able to be modulated by various natural compounds, such as flavonoids and terpenoids, originating from plants, that are being used in traditional medicine (Johnston et al. 2006; Manayi et al. 2016). For the publication **“Sesquiterpenes and sesquiterpenoids harbor modulatory allosteric potential and affect inhibitory GABA<sub>A</sub> receptor function in vitro”** we investigated the modulatory effect of 11 sesquiterpenes and sesquiterpenoids (SQTs) on GABA<sub>A</sub>R function. Our hypothesis was that SQTs taken up by nutrition even if biotransformed by digestive processes gain or retain modulatory effects similar to findings on essential oils demonstrated before (Heinlein & Buettner 2012).

The first SQTs we investigated were the monocyclic  $\alpha$ -humulene and the bicyclic  $\beta$ -caryophyllene, which are part of the volatile fraction of hop and other plants. At low pH during digestion, both compounds are hydroxylated, thus creating their secondary metabolites humulol and  $\beta$ -caryolanol. In transfected HEK293 cells overexpressing  $\alpha$ 1 $\beta$ 2 GABA<sub>A</sub>Rs, both metabolites significantly increased GABAergic currents upon co-application with a low GABA concentration, while  $\alpha$ -humulene and  $\beta$ -caryophyllene did not have any effect on current amplitude. This confirms previous reports demonstrating positive

allosteric modulation by hydroxylated terpenes and terpenoids (Kessler et al. 2014). However, other SQTs harboring a hydroxy group, namely guaiol,  $\alpha$ -bisabolone oxide A,  $\alpha$ -bisabolol oxide B, and spathulenol, did not follow this pattern and instead significantly reduced GABAergic currents. Co-application of two SQTs at the same time was performed to find any additive or neutralizing effects, albeit unsuccessful. Varying affinity, subtype-specific, and even cell-specific effects have been reported for substances before, e.g., bilobalide and ethanol (Kiewert et al. 2007; Forstera et al. 2016).

Next, SQT modulation was examined on dissociated hippocampal primary neurons in culture. The GABA<sub>A</sub>R  $\alpha 1\beta 2\gamma 2$  is the most common subtype in brain (Olsen & Sieghart 2008), so an effect of the presence of the  $\gamma 2$  subunit had to be evaluated. Previous data on monoterpenoids suggested that the observed positive modulatory effects were independent of the  $\gamma 2$  subunit (Kessler et al. 2014). However, in this study, different results in hippocampal neurons with the  $\gamma 2$  subunit present were found compared to  $\alpha 1\beta 2$  overexpressed in HEK293 cells. In hippocampal neurons  $\beta$ -caryolanol lost its modulatory effect, humulol acted as a negative modulator and guaiol as a positive allosteric modulator. Measurements using the benzodiazepine agonist diazepam and the superagonist gaboxadol confirmed the presence of phasic  $\gamma$ -containing and tonic  $\delta$ -containing receptors, respectively. The observed different effect of SQTs in hippocampal neurons could be influenced by presence of the  $\gamma$  subunit, the  $\delta$  subunit, or both. Thus,  $\alpha 1\beta 2\gamma 2$  receptors overexpressed in HEK293 cells were analyzed next. Again, humulol acted as a significant negative allosteric modulator, speaking for an active role of the  $\gamma$  subunit in modulation by some SQTs. However, no effects for guaiol were observed, which made an analysis of  $\delta$ -containing receptor configurations necessary. At tonic  $\alpha 4\beta 3\delta$  GABA<sub>A</sub>Rs,  $\beta$ -caryophyllene,  $\alpha$ -humulene,  $\beta$ -caryolanol, humulol, and guaiol all displayed significant negative allosteric modulation. In contrast, at  $\alpha 6\beta 3\delta$  receptors only  $\beta$ -caryophyllene exhibited significant negative modulation. These results indicate that the difference between these receptor subtypes must arise from the  $\alpha$  subunit, as  $\beta$  and  $\delta$  subunits used were identical. A similar mechanism of subunit specificity was reported for valerenic acid, which modulation is dependent on the  $\beta$  subunit type (Khom et al. 2007). However, our measurements on tonic  $\delta$ -containing GABA<sub>A</sub>R were obtained at saturating GABA concentrations, which could result in reduced current responses after repeated agonist applications (Mortensen et al. 2012; Karim et al. 2013). Hence, under non-saturating conditions, differences in the modulatory effects of SQTs at tonic GABA<sub>A</sub>Rs might become visible and have to be evaluated in the future.

So far, no binding site for SQTs at the GABA<sub>A</sub>R has been described. Due to their high hydrophobicity, SQTs may bind to the low-affinity diazepam and/or the neurosteroid binding site, both of which are located between the transmembrane domains of GABA<sub>A</sub>Rs (Miller et al. 2017; Masiulis et al. 2019). We performed modeling and docking studies of SQTs to the complete  $\alpha\beta$  or  $\alpha\alpha$  interfaces to find out which binding site is preferred. Two interfaces are possible between the  $\alpha$  and  $\beta$  subunits and were studied together:  $\beta^3+\alpha^1-$  (diazepam site) and  $\alpha^1+\beta^3-$  (alternative site). All five SQTs used for this analysis ( $\beta$ -caryophyllene,  $\alpha$ -humulene,  $\beta$ -caryolanol, humulol, and guaiol) were found in the diazepam site. However,  $\beta$ -caryophyllene and  $\alpha$ -humulene did not bind to several hydrogen groups of the binding pocket. In contrast, the hydroxylated  $\beta$ -caryolanol, humulol, and guaiol formed hydrogen bonds and overall displayed a good fit. This may explain the difference in modulatory potential observed for SQTs at GABA<sub>A</sub>Rs. Docking studies for the  $\alpha\alpha$  interface produced similar results, but with a lower score. However, the diazepam binding pocket is filled with water molecules in an unbound state, causing a strong desolvation penalty for the hydrophobic SQTs. The neurosteroid binding site is composed mostly of lipophilic amino acids, which should favor the hydroxylated SQTs. Also, it was shown before that the hydroxy group of neurosteroids plays a critical role in their ability to modulate GABA<sub>A</sub>Rs (Miller et al. 2017). Therefore, binding of hydroxylated SQTs may be more likely at the neurosteroid binding site than at the diazepam site.

SQTs may also bind to intracellular targets and regulate enzymatic activities. The sesquiterpene bilobalide has been shown to not just antagonize GABA<sub>A</sub>Rs but also to maintain glutamate decarboxylase (GAD) activity in presynaptic neurons of the hippocampus and cerebral cortex (Sasaki et al. 2000). Another group of SQTs are the artemisinins which are commonly used as antimalarial medication. Artemisinins bind to the GABA<sub>A</sub>R binding site of the scaffolding protein gephyrin which is critical for correct anchoring of GABA<sub>A</sub>Rs in synapses. Hindrance of the interaction between GABA<sub>A</sub>Rs and gephyrin results in fewer synaptic GABA<sub>A</sub>Rs and therefore decreased GABAergic inhibition (Kasaragod et al. 2019). Furthermore, artemisinins interfere presynaptically with GABAergic signaling by binding to the metabolic enzyme pyridoxal kinase, which regulates the synthesis of GABA via GAD (Kasaragod et al. 2020). However, modulation of these mechanisms requires long incubation times as uptake of SQTs into the cell is required. During our electrophysiological measurements, SQTs were applied onto the cells for only 50 ms and washed away immediately after, so only extracellular modulation of the GABA<sub>A</sub>Rs was

observed. Modulation of intracellular targets by the SQTs used in this study might be possible and should be investigated in the future.

In summary, we could successfully demonstrate the modulatory effect of some SQTs and their metabolic products via electrophysiological measurements on different GABA<sub>A</sub>R subtypes. Docking studies revealed that binding of hydroxylated SQTs should be possible at both the neurosteroid and diazepam binding sites of the receptor. The experimental setup only allowed for analysis of short-term effects of SQTs on GABA<sub>A</sub>R-generated currents. Recent results on other SQTs demonstrating their ability to modulate GABAergic inhibition both pre- and postsynaptically in neurons argue in favor of continued research on possible long-term effects of SQTs at GABAergic synapses. Doing so may unlock new therapeutic approaches for diseases of the central nervous system as well as help to further understand the structure and function of GABA<sub>A</sub>Rs.

### 3D Cell Culture in Fiber-Reinforced Hydrogel

In recent years, 3D *in vitro* cell culture models gained more and more importance. The third dimension allows for more complex models and brings the microenvironment of cells closer to the *in vivo* situation, which is especially of interest to clinical application studies. 3D *in vitro* cultures commonly use hydrogels as a matrix. Cells are encapsulated in the matrix, thus turning it into their microenvironment and making it necessary to choose a matrix with mechanical and biological properties similar to the native tissue of the encapsulated cells. These decisions complicate the development of certain 3D tissue models. This is especially the case for 3D *in vitro* cultures of the brain using primary neurons and astrocytes, being aware of the fact that the brain is one of the softest tissues found in the body (Spedden et al. 2012; Iwashita et al. 2014). 3D cultures that use hydrogels with similar mechanical properties can be challenging due to their difficult handling. One solution to this problem is to reinforce soft hydrogels with 3D printed thermoplastic fibers.

For the publication “**3D Electrophysiological Measurements on Cells Embedded within Fiber-Reinforced Matrigel**”, we cultured a transfected fibroblast cell line in fiber-reinforced matrigel and successfully performed 3D electrophysiological measurements. Matrigel is an ECM mixture secreted by Engelbreth-Holm-Swarm mouse sarcoma cells, which supports the growth of almost all cell types (Hughes et al. 2010). PCL scaffolds with 100 µm, 200 µm, and 400 µm pore size were designed and printed using MEW, an additive manufacturing technique that allows for placement of ordered low-micrometer diameter fibers. PCL is a biodegradable, non-toxic polyester approved for use in the human body.

Handling tests with and without hydrogel revealed high mechanical stability for 100  $\mu\text{m}$  and 200  $\mu\text{m}$  scaffolds, while matrigel reinforced by 400  $\mu\text{m}$  scaffolds collapsed when picked up. Disintegration of scaffolds with large fiber spacings was also observed (Visser et al. 2015). The Ltk-11 mouse fibroblast cell line was used as a cheap and less labor-intensive alternative to murine neurons to establish the methods necessary for analysis of such 3D scaffold-matrix composites. Furthermore, fibroblasts have been shown to infiltrate MEW scaffolds (Farrugia et al. 2013). Ltk-11 cells were seeded in matrigel reinforced by all three scaffolds designs and cultured for up to 9 days. Fewer cells were present in matrix composites containing scaffolds with 100  $\mu\text{m}$  pore size. Cells proliferated well in all three conditions and were also interacting with MEW fibers, which is in line with previous data that demonstrated growth of fibroblasts on PCL fibers (Farrugia et al. 2013). No significant change in cell viability was detected when comparing 2D cultures to 3D cultures in matrix composites. However, a delay in proliferation after seeding was observed for 3D cells (48 h vs 24 h), which may be due slow adjustment of cells to their new microenvironment. Taken together, 200  $\mu\text{m}$  scaffolds performed best and were chosen for all further experiments.

Using this system of 200  $\mu\text{m}$  spaced PCL fibers printed in a box-like structure, methods for further structural and functional analysis of neuronal networks in 3D matrix composites, e.g., immunocytochemistry or patch clamp recordings were established. Common fibroblast or endothelial cell lines usually do not express ligand-gated ion channels, which makes them suitable hosts for transfection, expression, and analysis of ion channels by electrophysiological techniques (Estacion 1991; Varghese et al. 2006). Here, the GlyR $\alpha$ 1 subunit was chosen as it forms homomeric ligand-gated ion channels. In 2D cultures, Ltk-11 cells can easily be transfected by common techniques, e.g., the calcium phosphate precipitation method or cationic lipid mediated transfection. Both techniques were unable to reliably transfect cells in fiber-reinforced matrigel. The calcium phosphate precipitates or DNA-lipid complexes could not enter or diffuse into the matrigel and therefore not reach the cells. To circumvent this problem, cells were transfected with a cationic lipid-based approach in 2D cultures 24 h before seeding into 3D matrix composites. Other possible approaches could have been electroporation or transduction of cells using viral vectors, which have been successfully used in 3D matrigel cultures (Maru et al. 2016; Laperrousaz et al. 2018). Cells were transfected with GlyR $\alpha$ 1 and enhanced green fluorescent protein to easily verify successful transfection. Additionally, intracellular and surface-expressed GlyR $\alpha$ 1 was verified by immunocytochemical stainings and was comparable to expression observed



in 2D cultures (Langlhofer et al. 2015). Stainings could easily be performed with 3D matrix composites due to the mechanical stability provided by scaffolds.

Next, patch-clamp recordings were performed on Ltk-11 cells in both 2D and 3D cultures. 3D matrix composites could easily be transferred to the recording chamber but had to be fixed in place with an O-ring, as described in a previous publication that performed patch-clamp in 3D cultures (Xu et al. 2009). 3D recordings were performed with slight adjustments to the protocol, e.g., positive pressure to prevent the pipette from clogging and longer applications as well as wash-in time of the agonists via the application system to overcome the matrigel surrounding the cells. Patch-clamp measurements verified a decrease in whole-cell maximal glycine-gated currents and a slightly decreased glycine potency for 3D cultures compared to cells grown on coverslips in monolayers. This is most likely due to the matrigel blocking access to the whole cellular membrane, thus only a part of the glycine receptors at the surface can be reached by the application of the agonist glycine by the external application system. However, differences of electrophysiological properties between 2D and 3D independent of an application system have previously been reported for neuronal cultures, arguing for not just blocked physical access but also physiological changes in cells cultured in 3D (Frega et al. 2014; Xu et al. 2009). These changes in physiological properties of the cell may be closer to the *in vivo* situation, making 3D cultures more attractive for future research. In sum, we successfully created a 3D matrix composite consisting of fiber-reinforced ultra-soft matrigel, allowing easy handling for common methods like structural detection of expressed proteins and functional recordings using the patch-clamp technique. Using the Ltk-11 mouse fibroblast cell line, we established the methods necessary for analysis of such 3D scaffold-matrix composites.

Based on these results, we further developed the 3D model for the formation of a neuronal network and published our data in a follow-up publication entitled “**Cortical Neurons Form a Functional Neuronal Network in a 3D Printed Reinforced Matrix**”. Here, murine embryonic cortical neurons were isolated and cultured for up to 21 days in matrigel reinforced by MEW scaffolds with 200  $\mu\text{m}$  pore size. First, rheological measurements were performed for two concentrations of matrigel. Although a matrigel concentration of 4.5 mg/ml was exhibited as suitable for cellular survival in the mouse fibroblast cell line Ltk-11, we analyzed a concentration of 8 mg/ml as well as previous studies showed that hydrogel stiffness affects neuronal network formation in 3D cultures (Palazzolo et al. 2015). Storage moduli for both 4.5 mg/ml and 8.5 mg/ml were in the range of ultra-soft stiffness, with 31 Pa and 66 Pa, respectively. No difference in neuronal network density could be

detected between the two matrigel concentrations used. Further experiments were performed with the 4.5 mg/ml concentration to closer resemble the softness of the embryonic brain. The MEW scaffolds used here increased the overall mechanical stability of the hydrogel, thus allowing proper handling of the composites. Dendrite extension and orientation seemed not to be affected by the presence of the scaffold. Cell viability remained high for 3D cultures during the first week in culture but dropped after two weeks. However, viability in 2D cultures was lower than in 3D cultures and significantly decreased already after one week, similar to previous findings demonstrating approx. 50% viability for cortical neurons in 6 day-old 2D cultures (Voigt et al. 1997).

Immunocytochemical stainings of one-week-old 3D cultures with dendritic and synaptic markers revealed fully formed neuronal networks that increased in complexity until week three. Quantification of the number of synapses showed a large increase in synapse formation during the first 7 days in 3D compared to 2D cultures. Also, dendrites had increased length in 3D cultures. Ichikawa et al. previously demonstrated that network formation in 2D neuronal cultures was slow during the first 7 days and significantly increased up to day 14 (Ichikawa et al. 1993). These results argue for an accelerated network formation of cortical neurons in our 3D matrix composites. After confirming network formation, calcium imaging was performed to test if the neuronal networks were functional. Spontaneous network activity was observed in two weeks old 3D cultures, which is comparable to data available for 2D cultures (Basarsky et al. 1994; Fletcher et al. 1994; Blum et al. 2011). Application of the voltage-gated sodium channel blocker tetrodotoxin did completely block neuronal activity in 3D cultures (Lee & Ruben 2008). Due to these results, we proceeded with patch-clamp measurement in 14-18-day old 3D cultures. As already pointed out, 3D matrix composites could easily be transferred to the recording chamber but had to be fixed by an O-ring. The 200  $\mu\text{m}$  pore size of the scaffold did not hinder pipette movement. Voltage-gated sodium currents were obtained by voltage-clamp recordings, confirming their function as indicated by calcium imaging. Voltage-gated sodium channels open upon membrane depolarization and initiate and propagate action potentials (de Lera Ruiz & Kraus 2015). Action potentials were recorded in current-clamp mode and were evoked by near-threshold current injection. Increased current injection led to repetitive firing and, ultimately, to a block of action potentials. Previously, such action potential firing patterns had been reported for dissociated cortical pyramidal neurons (Hamill et al. 1991).

Taken together, we successfully adapted our previously established 3D cell culture model for the use with primary neurons suitable for future work, e.g., on cell-cell interactions in glioma

where pseudo-synaptic structures are formed between primary cells of the brain and tumor cells using the same ECM. Ultra-soft matrigel provides an optimal microenvironment for neurons, with both excellent nutrition supply and appropriate mechanical properties. Reinforcement with MEW scaffolds supplies overall stability necessary for handling and thus investigating the composite in the context of various analyses depending on the research question behind. The 3D culture displayed multiple advantages compared to standard 2D culture of primary neurons, e.g., higher cell viability, increased dendrite growth, and faster synapse formation. However, matrigel is not approved for medical uses, which argues for replacing it with a synthetic matrix. This would ensure high reproducibility over multiple batches and allow for full customization of the matrix. Mechanical properties as well as nutritional factors could be tailored for specific cell types, which would be especially important when considering 3D co-cultures of multiple cell types, e.g., neurons, astrocytes, and brain tumor cells. One candidate for such a matrix is hyaluronic acid, a natural component of the brain extracellular matrix. Hyaluronic-acid-based hydrogels have been successfully used for many biomedical applications, including cartilage tissue engineering and cardiac repair (Burdick & Prestwich 2011; Nettles et al. 2004; Ifkovits et al. 2010). Neuronal 3D cultures using hyaluronic acid have so far mainly focused on neuronal stem and progenitor cells (Seidlits et al. 2010; Seidlits et al. 2019). However, recently established cross-linking strategies for hyaluronic acid will help to modify this attractive matrix for different neuronal 3D cultures and regenerative medicine (Jensen et al. 2020). For example, a thiolated hyaluronic acid may provide further options for modifications of the matrix (Hauptstein et al. 2020).

Using aimed matrix modifications is a prerequisite for studying and understanding of cell-matrix, cell-scaffold, as well as cell-cell interaction in co-cultures of various cell types, e.g., neurons, astrocytes, and brain tumor cells in the context of glioblastoma. These developments will help to further elucidate the molecular pathology of these aggressive tumors affecting healthy cells of the CNS but will also be suitable to model other disease mechanisms. 3D matrix composites could be used for drug screening as replacement for animal experiments. Primary cells could be entirely replaced by induced pluripotent stem cells, thus eliminating the need for animals. With further development, our 3D matrix composites could be used in an organ-on-a-chip model as brain compartment together with other tissue models to study, e.g., the gut-brain axis. Taken together, we developed a flexible 3D cell culture model that can be used as a base for a wide range of further developments.

# References

- Adams, T. B., Gavin, C. L., McGowen, M. M. et al. (2011) The FEMA GRAS assessment of aliphatic and aromatic terpene hydrocarbons used as flavor ingredients. *Food Chem Toxicol* 49, 2471-2494.
- Aisenbrey, E. A. and Murphy, W. L. (2020) Synthetic alternatives to Matrigel. *Nature Reviews Materials*.
- Al-Futaisi, A. M., Al-Kindi, M. N., Al-Mawali, A. M., Koul, R. L., Al-Adawi, S. and Al-Yahyaee, S. A. (2012) Novel mutation of GLRA1 in Omani families with hyperekplexia and mild mental retardation. *Pediatr Neurol* 46, 89-93.
- Althoff, T., Hibbs, R. E., Banerjee, S. and Gouaux, E. (2014) X-ray structures of GluCl in apo states reveal a gating mechanism of Cys-loop receptors. *Nature* 512, 333-337.
- Alvarez, L. D. and Estrin, D. A. (2015) Exploring the molecular basis of neurosteroid binding to the beta3 homopentameric GABAA receptor. *J Steroid Biochem Mol Biol* 154, 159-167.
- Alvarez, L. D. and Pecci, A. (2018) Structure and dynamics of neurosteroid binding to the alpha1beta2gamma2 GABAA receptor. *J Steroid Biochem Mol Biol* 182, 72-80.
- Annabi, N., Tsang, K., Mithieux, S. M., Nikkhah, M., Ameri, A., Khademhosseini, A. and Weiss, A. S. (2013) Highly Elastic Micropatterned Hydrogel for Engineering Functional Cardiac Tissue. *Adv Funct Mater* 23.
- Atak, S., Langlhofer, G., Schaefer, N., Kessler, D., Meiselbach, H., Delto, C., Schindelin, H. and Villmann, C. (2015) Disturbances of Ligand Potency and Enhanced Degradation of the Human Glycine Receptor at Affected Positions G160 and T162 Originally Identified in Patients Suffering from Hyperekplexia. *Front Mol Neurosci* 8, 79.
- Avila, A., Vidal, P. M., Dear, T. N., Harvey, R. J., Rigo, J. M. and Nguyen, L. (2013) Glycine receptor alpha2 subunit activation promotes cortical interneuron migration. *Cell Rep* 4, 738-750.
- Baker, B. M. and Chen, C. S. (2012) Deconstructing the third dimension: how 3D culture microenvironments alter cellular cues. *J Cell Sci* 125, 3015-3024.
- Balgude, A. P., Yu, X., Szymanski, A. and Bellamkonda, R. V. (2001) Agarose gel stiffness determines rate of DRG neurite extension in 3D cultures. *Biomaterials* 22, 1077-1084.

- Barriga, E. H., Franze, K., Charras, G. and Mayor, R. (2018) Tissue stiffening coordinates morphogenesis by triggering collective cell migration in vivo. *Nature* 554, 523-527.
- Barros, C. S., Franco, S. J. and Muller, U. (2011) Extracellular matrix: functions in the nervous system. *Cold Spring Harb Perspect Biol* 3, a005108.
- Bartnikowski, M., Dargaville, T. R., Ivanovski, S. and Hutmacher, D. W. (2019) Degradation mechanisms of polycaprolactone in the context of chemistry, geometry and environment. *Progress in Polymer Science* 96, 1-20.
- Bártolo, P. J., Chua, C. K., Almeida, H. A., Chou, S. M. and Lim, A. S. C. (2009) Biomanufacturing for tissue engineering: Present and future trends. *Virtual and Physical Prototyping* 4, 203-216.
- Bas, O., D'Angella, D., Baldwin, J. G. et al. (2017) An Integrated Design, Material, and Fabrication Platform for Engineering Biomechanically and Biologically Functional Soft Tissues. *ACS Appl Mater Interfaces* 9, 29430-29437.
- Bas, O., De-Juan-Pardo, E. M., Chhaya, M. P., Wunner, F. M., Jeon, J. E., Klein, T. J. and Hutmacher, D. W. (2015) Enhancing structural integrity of hydrogels by using highly organised melt electrospun fibre constructs. *European Polymer Journal* 72, 451-463.
- Basarsky, T. A., Parpura, V. and Haydon, P. G. (1994) Hippocampal synaptogenesis in cell culture: developmental time course of synapse formation, calcium influx, and synaptic protein distribution. *J Neurosci* 14, 6402-6411.
- Becker, C. M., Hoch, W. and Betz, H. (1988) Glycine receptor heterogeneity in rat spinal cord during postnatal development. *EMBO J* 7, 3717-3726.
- Bellamkonda, R., Ranieri, J. P., Bouche, N. and Aebischer, P. (1995) Hydrogel-based three-dimensional matrix for neural cells. *J Biomed Mater Res* 29, 663-671.
- Bemelmans, J. (1979) Progress in Flavour Research. *Applied Science Publishers Ltd: London*, 79-98.
- Berthiaume, F., Maguire, T. J. and Yarmush, M. L. (2011) Tissue engineering and regenerative medicine: history, progress, and challenges. *Annu Rev Chem Biomol Eng* 2, 403-430.
- Blaeser, A., Duarte Campos, D. F., Puster, U., Richtering, W., Stevens, M. M. and Fischer, H. (2016) Controlling Shear Stress in 3D Bioprinting is a Key Factor to Balance Printing Resolution and Stem Cell Integrity. *Adv Healthc Mater* 5, 326-333.
- Blum, R., Heinrich, C., Sanchez, R., Lepier, A., Gundelfinger, E. D., Berninger, B. and Gotz, M. (2011) Neuronal network formation from reprogrammed early postnatal rat cortical glial cells. *Cereb Cortex* 21, 413-424.

- Bocquet, N., Nury, H., Baaden, M., Le Poupon, C., Changeux, J. P., Delarue, M. and Corringer, P. J. (2009) X-ray structure of a pentameric ligand-gated ion channel in an apparently open conformation. *Nature* 457, 111-114.
- Bode, A. and Lynch, J. W. (2014) The impact of human hyperekplexia mutations on glycine receptor structure and function. *Mol Brain* 7, 2.
- Bonneh-Barkay, D. and Wiley, C. A. (2009) Brain extracellular matrix in neurodegeneration. *Brain Pathol* 19, 573-585.
- Brams, M., Govaerts, C., Kambara, K. et al. (2020) Modulation of the Erwinia ligand-gated ion channel (ELIC) and the 5-HT<sub>3</sub> receptor via a common vestibule site. *Elife* 9.
- Brams, M., Pandya, A., Kuzmin, D., van Elk, R., Krijnen, L., Yakel, J. L., Tsetlin, V., Smit, A. B. and Ulens, C. (2011) A structural and mutagenic blueprint for molecular recognition of strychnine and d-tubocurarine by different cys-loop receptors. *PLoS Biol* 9, e1001034.
- Breitinger, H. G. and Becker, C. M. (1998) The inhibitory glycine receptor: prospects for a therapeutic orphan? *Curr Pharm Des* 4, 315-334.
- Breitinger, H. G., Villmann, C., Becker, K. and Becker, C. M. (2001) Opposing effects of molecular volume and charge at the hyperekplexia site alpha 1(P250) govern glycine receptor activation and desensitization. *J Biol Chem* 276, 29657-29663.
- Breitinger, U., Raafat, K. M. and Breitinger, H. G. (2015) Glucose is a positive modulator for the activation of human recombinant glycine receptors. *J Neurochem* 134, 1055-1066.
- Brejc, K., van Dijk, W. J., Klaassen, R. V., Schuurmans, M., van Der Oost, J., Smit, A. B. and Sixma, T. K. (2001) Crystal structure of an ACh-binding protein reveals the ligand-binding domain of nicotinic receptors. *Nature* 411, 269-276.
- Brickley, S. G. and Mody, I. (2012) Extrasynaptic GABA(A) receptors: their function in the CNS and implications for disease. *Neuron* 73, 23-34.
- Brown, T. D., Dalton, P. D. and Hutmacher, D. W. (2011) Direct writing by way of melt electrospinning. *Adv Mater* 23, 5651-5657.
- Burdick, J. A. and Prestwich, G. D. (2011) Hyaluronic acid hydrogels for biomedical applications. *Adv Mater* 23, H41-56.
- Cao, X. and Shoichet, M. S. (2001) Defining the concentration gradient of nerve growth factor for guided neurite outgrowth. *Neuroscience* 103, 831-840.
- Chen, C. and Okayama, H. (1987) High-efficiency transformation of mammalian cells by plasmid DNA. *Mol Cell Biol* 7, 2745-2752.

- Chiappalone, M., Bove, M., Vato, A., Tedesco, M. and Martinoia, S. (2006) Dissociated cortical networks show spontaneously correlated activity patterns during in vitro development. *Brain Res* 1093, 41-53.
- Choi, Y. J., Kim, M. C., Lim, Y. J., Yoon, S. Z., Yoon, S. M. and Yoon, H. R. (2014) Propofol infusion associated metabolic acidosis in patients undergoing neurosurgical anesthesia: a retrospective study. *J Korean Neurosurg Soc* 56, 135-140.
- Christ, A. F., Franze, K., Gautier, H., Moshayedi, P., Fawcett, J., Franklin, R. J., Karadottir, R. T. and Guck, J. (2010) Mechanical difference between white and gray matter in the rat cerebellum measured by scanning force microscopy. *J Biomech* 43, 2986-2992.
- Chua, H. C. and Chebib, M. (2017) GABAA Receptors and the Diversity in their Structure and Pharmacology. *Adv Pharmacol* 79, 1-34.
- Chung, S. K., Vanbellinghen, J. F., Mullins, J. G. et al. (2010) Pathophysiological mechanisms of dominant and recessive GLRA1 mutations in hyperekplexia. *J Neurosci* 30, 9612-9620.
- Chwalek, K., Tang-Schomer, M. D., Omenetto, F. G. and Kaplan, D. L. (2015) In vitro bioengineered model of cortical brain tissue. *Nat Protoc* 10, 1362-1373.
- Cipitria, A., Skelton, A., Dargaville, T. R., Dalton, P. D. and Hutmacher, D. W. (2011) Design, fabrication and characterization of PCL electrospun scaffolds—a review. *Journal of Materials Chemistry* 21, 9419-9453.
- Cornelison, G. L., Daszkowski, A. W., Pflanz, N. C. and Mihic, S. J. (2017) Interactions between Zinc and Allosteric Modulators of the Glycine Receptor. *J Pharmacol Exp Ther* 361, 1-8.
- Cuddapah, V. A., Robel, S., Watkins, S. and Sontheimer, H. (2014) A neurocentric perspective on glioma invasion. *Nat Rev Neurosci* 15, 455-465.
- Cummins, T. R., Aglieco, F., Renganathan, M., Herzog, R. I., Dib-Hajj, S. D. and Waxman, S. G. (2001) Nav1.3 sodium channels: rapid repriming and slow closed-state inactivation display quantitative differences after expression in a mammalian cell line and in spinal sensory neurons. *J Neurosci* 21, 5952-5961.
- Dalton, P. D. (2017) Melt electrowriting with additive manufacturing principles. *Current Opinion in Biomedical Engineering* 2, 49-57.
- Dalton, P. D. and Mey, J. (2009) Neural interactions with materials. *Front Biosci (Landmark Ed)* 14, 769-795.

- Daud, M. F., Pawar, K. C., Claeysens, F., Ryan, A. J. and Haycock, J. W. (2012) An aligned 3D neuronal-glia co-culture model for peripheral nerve studies. *Biomaterials* 33, 5901-5913.
- de Lera Ruiz, M. and Kraus, R. L. (2015) Voltage-Gated Sodium Channels: Structure, Function, Pharmacology, and Clinical Indications. *J Med Chem* 58, 7093-7118.
- de Ruijter, M., Hrynevich, A., Haigh, J. N., Hochleitner, G., Castilho, M., Groll, J., Malda, J. and Dalton, P. D. (2018) Out-of-Plane 3D-Printed Microfibers Improve the Shear Properties of Hydrogel Composites. *Small* 14.
- Deckert, J., Weber, H., Villmann, C. et al. (2017) GLRB allelic variation associated with agoraphobic cognitions, increased startle response and fear network activation: a potential neurogenetic pathway to panic disorder. *Mol Psychiatry* 22, 1431-1439.
- Delalat, B., Harding, F., Gundsambuu, B. et al. (2017) 3D printed lattices as an activation and expansion platform for T cell therapy. *Biomaterials* 140, 58-68.
- Distler, T., Lauria, I., Detsch, R., Sauter, C. M., Bendt, F., Kapr, J., Rutten, S., Boccaccini, A. R. and Fritsche, E. (2021) Neuronal Differentiation from Induced Pluripotent Stem Cell-Derived Neurospheres by the Application of Oxidized Alginate-Gelatin-Laminin Hydrogels. *Biomedicine* 9.
- Długaiczek, J., Singer, W., Schick, B., Iro, H., Becker, K., Becker, C. M., Zimmermann, U., Rohbock, K. and Knipper, M. (2008) Expression of glycine receptors and gephyrin in the rat cochlea. *Histochem Cell Biol* 129, 513-523.
- Du, J., Lu, W., Wu, S., Cheng, Y. and Gouaux, E. (2015) Glycine receptor mechanism elucidated by electron cryo-microscopy. *Nature* 526, 224-229.
- Dubey, N., Letourneau, P. C. and Tranquillo, R. T. (1999) Guided neurite elongation and Schwann cell invasion into magnetically aligned collagen in simulated peripheral nerve regeneration. *Experimental Neurology* 158, 338-350.
- Duricic, N., Godin, A. G., Wever, C. M., Heyes, C. D., Lakadamyali, M. and Dent, J. A. (2012) Stoichiometry of the human glycine receptor revealed by direct subunit counting. *J Neurosci* 32, 12915-12920.
- Edmondson, R., Broglie, J. J., Adcock, A. F. and Yang, L. (2014) Three-dimensional cell culture systems and their applications in drug discovery and cell-based biosensors. *Assay Drug Dev Technol* 12, 207-218.
- Eichler, S. A., Forstera, B., Smolinsky, B., Juttner, R., Lehmann, T. N., Fahling, M., Schwarz, G., Legendre, P. and Meier, J. C. (2009) Splice-specific roles of glycine receptor alpha3 in the hippocampus. *Eur J Neurosci* 30, 1077-1091.



- Emsley, P., Lohkamp, B., Scott, W. G. and Cowtan, K. (2010) Features and development of Coot. *Acta Crystallogr D Biol Crystallogr* 66, 486-501.
- Engel, W., Bahr, W. and Schieberle, P. (1999) Solvent assisted flavour evaporation – a new and versatile technique for the careful and direct isolation of aroma compounds from complex food matrices. *European Food Research and Technology* 209, 237-241.
- Estacion, M. (1991) Characterization of ion channels seen in subconfluent human dermal fibroblasts. *J Physiol* 436, 579-601.
- Eyckmans, J., Boudou, T., Yu, X. and Chen, C. S. (2011) A hitchhiker's guide to mechanobiology. *Dev Cell* 21, 35-47.
- Farrugia, B. L., Brown, T. D., Upton, Z., Hutmacher, D. W., Dalton, P. D. and Dargaville, T. R. (2013) Dermal fibroblast infiltration of poly(epsilon-caprolactone) scaffolds fabricated by melt electrospinning in a direct writing mode. *Biofabrication* 5, 025001.
- Fattahi, P., Borhan, A. and Abidian, M. R. (2013a) Characterization of the size, shape, and drug encapsulation efficiency of PLGA microcapsules produced via electrojetting for drug delivery to brain tumors. In: *2013 6th International IEEE/EMBS Conference on Neural Engineering (NER)*, pp. 953-956.
- Fattahi, P., Borhan, A. and Abidian, M. R. (2013b) Microencapsulation of chemotherapeutics into monodisperse and tunable biodegradable polymers via electrified liquid jets: control of size, shape, and drug release. *Adv Mater* 25, 4555-4560.
- Fawcett, J. W., Oohashi, T. and Pizzorusso, T. (2019) The roles of perineuronal nets and the perinodal extracellular matrix in neuronal function. *Nat Rev Neurosci* 20, 451-465.
- Felgner, P. L., Gadek, T. R., Holm, M., Roman, R., Chan, H. W., Wenz, M., Northrop, J. P., Ringold, G. M. and Danielsen, M. (1987) Lipofection: a highly efficient, lipid-mediated DNA-transfection procedure. *Proc Natl Acad Sci U S A* 84, 7413-7417.
- Felgner, P. L. and Ringold, G. M. (1989) Cationic liposome-mediated transfection. *Nature* 337, 387-388.
- Fletcher, T. L., De Camilli, P. and Banker, G. (1994) Synaptogenesis in hippocampal cultures: evidence indicating that axons and dendrites become competent to form synapses at different stages of neuronal development. *J Neurosci* 14, 6695-6706.
- Forstera, B., Castro, P. A., Moraga-Cid, G. and Aguayo, L. G. (2016) Potentiation of Gamma Aminobutyric Acid Receptors (GABAAR) by Ethanol: How Are Inhibitory Receptors Affected? *Front Cell Neurosci* 10, 114.

- Frampton, J. P., Hynd, M. R., Shuler, M. L. and Shain, W. (2011) Fabrication and optimization of alginate hydrogel constructs for use in 3D neural cell culture. *Biomed Mater* 6, 015002.
- Frega, M., Tedesco, M., Massobrio, P., Pesce, M. and Martinoia, S. (2014) Network dynamics of 3D engineered neuronal cultures: a new experimental model for in-vitro electrophysiology. *Sci Rep* 4, 5489.
- Fritschy, J. M., Harvey, R. J. and Schwarz, G. (2008) Gephyrin: where do we stand, where do we go? *Trends Neurosci* 31, 257-264.
- Fritschy, J. M. and Mohler, H. (1995) GABAA-receptor heterogeneity in the adult rat brain: differential regional and cellular distribution of seven major subunits. *J Comp Neurol* 359, 154-194.
- Fucile, S., de Saint Jan, D., David-Watine, B., Korn, H. and Bregestovski, P. (1999) Comparison of glycine and GABA actions on the zebrafish homomeric glycine receptor. *J Physiol* 517 ( Pt 2), 369-383.
- Groll, J., Boland, T., Blunk, T. et al. (2016) Biofabrication: reappraising the definition of an evolving field. *Biofabrication* 8, 013001.
- Grudzinska, J., Schemm, R., Haeger, S., Nicke, A., Schmalzing, G., Betz, H. and Laube, B. (2005) The beta subunit determines the ligand binding properties of synaptic glycine receptors. *Neuron* 45, 727-739.
- Haeger, S., Kuzmin, D., Detro-Dassen, S., Lang, N., Kilb, M., Tsetlin, V., Betz, H., Laube, B. and Schmalzing, G. (2010) An intramembrane aromatic network determines pentameric assembly of Cys-loop receptors. *Nat Struct Mol Biol* 17, 90-98.
- Hamill, O. P., Huguenard, J. R. and Prince, D. A. (1991) Patch-clamp studies of voltage-gated currents in identified neurons of the rat cerebral cortex. *Cereb Cortex* 1, 48-61.
- Hansen, S. B., Sulzenbacher, G., Huxford, T., Marchot, P., Taylor, P. and Bourne, Y. (2005) Structures of Aplysia AChBP complexes with nicotinic agonists and antagonists reveal distinctive binding interfaces and conformations. *EMBO J* 24, 3635-3646.
- Hartenstein, B., Schenkel, J., Kuhse, J., Besenbeck, B., Kling, C., Becker, C. M., Betz, H. and Weiher, H. (1996) Low level expression of glycine receptor beta subunit transgene is sufficient for phenotype correction in spastic mice. *EMBO J* 15, 1275-1282.
- Harvey, R. J., Depner, U. B., Wassle, H. et al. (2004) GlyR alpha3: an essential target for spinal PGE2-mediated inflammatory pain sensitization. *Science* 304, 884-887.

- Harvey, R. J., Schmieden, V., Von Holst, A., Laube, B., Rohrer, H. and Betz, H. (2000) Glycine receptors containing the alpha4 subunit in the embryonic sympathetic nervous system, spinal cord and male genital ridge. *Eur J Neurosci* 12, 994-1001.
- Harvey, R. J., Topf, M., Harvey, K. and Rees, M. I. (2008) The genetics of hyperekplexia: more than startle! *Trends Genet* 24, 439-447.
- Harvey, R. J. and Yee, B. K. (2013) Glycine transporters as novel therapeutic targets in schizophrenia, alcohol dependence and pain. *Nat Rev Drug Discov* 12, 866-885.
- Harvey, V. L., Caley, A., Muller, U. C., Harvey, R. J. and Dickenson, A. H. (2009) A Selective Role for alpha3 Subunit Glycine Receptors in Inflammatory Pain. *Front Mol Neurosci* 2, 14.
- Hassaine, G., Deluz, C., Grasso, L. et al. (2014) X-ray structure of the mouse serotonin 5-HT3 receptor. *Nature* 512, 276-281.
- Hauptstein, J., Bock, T., Bartolf-Kopp, M. et al. (2020) Hyaluronic Acid-Based Bioink Composition Enabling 3D Bioprinting and Improving Quality of Deposited Cartilaginous Extracellular Matrix. *Adv Healthc Mater* 9, e2000737.
- Haverkamp, S., Muller, U., Harvey, K., Harvey, R. J., Betz, H. and Wassle, H. (2003) Diversity of glycine receptors in the mouse retina: localization of the alpha3 subunit. *J Comp Neurol* 465, 524-539.
- Haverkamp, S., Muller, U., Zeilhofer, H. U., Harvey, R. J. and Wassle, H. (2004) Diversity of glycine receptors in the mouse retina: localization of the alpha2 subunit. *J Comp Neurol* 477, 399-411.
- Heinlein, A. and Buettner, A. (2012) Monitoring of biotransformation of hop aroma compounds in an in vitro digestion model. *Food Funct* 3, 1059-1067.
- Heinlein, A., Metzger, M., Walles, H. and Buettner, A. (2014) Transport of hop aroma compounds across Caco-2 monolayers. *Food Funct* 5, 2719-2730.
- Heinze, L., Harvey, R. J., Haverkamp, S. and Wassle, H. (2007) Diversity of glycine receptors in the mouse retina: localization of the alpha4 subunit. *J Comp Neurol* 500, 693-707.
- Hibbs, R. E. and Gouaux, E. (2011) Principles of activation and permeation in an anion-selective Cys-loop receptor. *Nature* 474, 54-60.
- Hibbs, R. E., Sulzenbacher, G., Shi, J., Talley, T. T., Conrod, S., Kem, W. R., Taylor, P., Marchot, P. and Bourne, Y. (2009) Structural determinants for interaction of partial agonists with acetylcholine binding protein and neuronal alpha7 nicotinic acetylcholine receptor. *EMBO J* 28, 3040-3051.

- Hilf, R. J. and Dutzler, R. (2008) X-ray structure of a prokaryotic pentameric ligand-gated ion channel. *Nature* 452, 375-379.
- Hoerbelt, P., Lindsley, T. A. and Fleck, M. W. (2015) Dopamine directly modulates GABAA receptors. *J Neurosci* 35, 3525-3536.
- Hoffman, A. S. (2002) Hydrogels for biomedical applications. *Adv Drug Deliv Rev* 54, 3-12.
- Holland, E. C. (2000) Glioblastoma multiforme: the terminator. *Proc Natl Acad Sci U S A* 97, 6242-6244.
- Hong, Y., Chirila, T. V., Vijayasekaran, S., Dalton, P. D., Tahija, S. G., Cuypers, M. J. and Constable, I. J. (1996) Crosslinked poly(1-vinyl-2-pyrrolidinone) as a vitreous substitute. *J Biomed Mater Res* 30, 441-448.
- Hoshihara, T., Chen, G., Endo, C., Maruyama, H., Wakui, M., Nemoto, E., Kawazoe, N. and Tanaka, M. (2016) Decellularized Extracellular Matrix as an In Vitro Model to Study the Comprehensive Roles of the ECM in Stem Cell Differentiation. *Stem Cells Int* 2016, 6397820.
- Hossain, S. J., Hamamoto, K., Aoshima, H. and Hara, Y. (2002) Effects of tea components on the response of GABA(A) receptors expressed in *Xenopus* Oocytes. *J Agric Food Chem* 50, 3954-3960.
- Hrynevich, A., Elci, B. S., Haigh, J. N. et al. (2018) Dimension-Based Design of Melt Electrowritten Scaffolds. *Small* 14, e1800232.
- Huang, S. H., Duke, R. K., Chebib, M., Sasaki, K., Wada, K. and Johnston, G. A. (2003) Bilobalide, a sesquiterpene trilactone from *Ginkgo biloba*, is an antagonist at recombinant  $\alpha 1\beta 2\gamma 2\text{L}$  GABA(A) receptors. *Eur J Pharmacol* 464, 1-8.
- Huang, X., Chen, H., Michelsen, K., Schneider, S. and Shaffer, P. L. (2015) Crystal structure of human glycine receptor- $\alpha 3$  bound to antagonist strychnine. *Nature* 526, 277-280.
- Huang, X., Chen, H. and Shaffer, P. L. (2017a) Crystal Structures of Human GlyR $\alpha 3$  Bound to Ivermectin. *Structure* 25, 945-950 e942.
- Huang, X., Shaffer, P. L., Ayube, S. et al. (2017b) Crystal structures of human glycine receptor  $\alpha 3$  bound to a novel class of analgesic potentiators. *Nat Struct Mol Biol* 24, 108-113.
- Hughes, C. S., Postovit, L. M. and Lajoie, G. A. (2010) Matrigel: a complex protein mixture required for optimal growth of cell culture. *Proteomics* 10, 1886-1890.
- Hutmacher, D. W., Horch, R. E., Loessner, D. et al. (2009) Translating tissue engineering technology platforms into cancer research. *J Cell Mol Med* 13, 1417-1427.

- Ichikawa, M., Muramoto, K., Kobayashi, K., Kawahara, M. and Kuroda, Y. (1993) Formation and maturation of synapses in primary cultures of rat cerebral cortical cells: an electron microscopic study. *Neurosci Res* 16, 95-103.
- Ifkovits, J. L., Tous, E., Minakawa, M., Morita, M., Robb, J. D., Koomalsingh, K. J., Gorman, J. H., 3rd, Gorman, R. C. and Burdick, J. A. (2010) Injectable hydrogel properties influence infarct expansion and extent of postinfarction left ventricular remodeling in an ovine model. *Proc Natl Acad Sci U S A* 107, 11507-11512.
- Ikada, Y. (2006) Challenges in tissue engineering. *J R Soc Interface* 3, 589-601.
- Islam, S., Chen, X., Estrada-Mondragon, A. and Lynch, J. W. (2018) Phosphorylation of the  $\alpha 2$  glycine receptor induces an extracellular conformational change and slows the rise and decay rates of glycinergic synaptic currents. *bioRxiv*, 434357.
- Ivica, J., Lape, R., Jazbec, V., Yu, J., Zhu, H., Gouaux, E., Gold, M. G. and Sivilotti, L. G. (2021) The intracellular domain of homomeric glycine receptors modulates agonist efficacy. *J Biol Chem* 296, 100387.
- Iwashita, M., Kataoka, N., Toida, K. and Kosodo, Y. (2014) Systematic profiling of spatiotemporal tissue and cellular stiffness in the developing brain. *Development* 141, 3793-3798.
- James, V. M., Bode, A., Chung, S. K. et al. (2013) Novel missense mutations in the glycine receptor beta subunit gene (GLRB) in startle disease. *Neurobiol Dis* 52, 137-149.
- Janhsen, K., Roser, P. and Hoffmann, K. (2015) The problems of long-term treatment with benzodiazepines and related substances. *Dtsch Arztebl Int* 112, 1-7.
- Janzen, D., Bakirci, E., Wieland, A., Martin, C., Dalton, P. D. and Villmann, C. (2020) Cortical Neurons form a Functional Neuronal Network in a 3D Printed Reinforced Matrix. *Adv Healthc Mater*, e1901630.
- Janzen, D., Schaefer, N., Delto, C., Schindelin, H. and Villmann, C. (2017) The GlyR Extracellular beta 8-beta 9 Loop - A Functional Determinant of Agonist Potency. *Frontiers in Molecular Neuroscience* 10.
- Janzen, D., Slavik, B., Zehe, M., Sotriuffer, C., Loos, H. M., Buettner, A. and Villmann, C. (2021) Sesquiterpenes and sesquiterpenoids harbor modulatory allosteric potential and affect inhibitory GABAA receptor function in vitro. *Journal of Neurochemistry* n/a.
- Jensen, G., Holloway, J. L. and Stabenfeldt, S. E. (2020) Hyaluronic Acid Biomaterials for Central Nervous System Regenerative Medicine. *Cells* 9.

- Johnston, G. A., Hanrahan, J. R., Chebib, M., Duke, R. K. and Mewett, K. N. (2006) Modulation of ionotropic GABA receptors by natural products of plant origin. *Adv Pharmacol* 54, 285-316.
- Karim, N., Wellendorph, P., Absalom, N., Johnston, G. A., Hanrahan, J. R. and Chebib, M. (2013) Potency of GABA at human recombinant GABA(A) receptors expressed in *Xenopus* oocytes: a mini review. *Amino Acids* 44, 1139-1149.
- Kasaragod, V. B., Hausrat, T. J., Schaefer, N. et al. (2019) Elucidating the Molecular Basis for Inhibitory Neurotransmission Regulation by Artemisinins. *Neuron* 101, 673-689 e611.
- Kasaragod, V. B., Pacios-Michelena, A., Schaefer, N., Zheng, F., Bader, N., Alzheimer, C., Villmann, C. and Schindelin, H. (2020) Pyridoxal kinase inhibition by artemisinins down-regulates inhibitory neurotransmission. *Proc Natl Acad Sci U S A*.
- Kasaragod, V. B. and Schindelin, H. (2019) Structure of Heteropentameric GABAA Receptors and Receptor-Anchoring Properties of Gephyrin. *Front Mol Neurosci* 12, 191.
- Kessler, A., Sahin-Nadeem, H., Lummis, S. C., Weigel, I., Pischetsrieder, M., Buettner, A. and Villmann, C. (2014) GABA(A) receptor modulation by terpenoids from *Sideritis* extracts. *Mol Nutr Food Res* 58, 851-862.
- Kessler, A., Villmann, C., Sahin-Nadeem, H., Pischetsrieder, M. and Buettner, A. (2012) GABAA receptor modulation by the volatile fractions of *Sideritis* species used as 'Greek' or 'Turkish' mountain tea. *Flavour and Fragrance Journal* 27, 297-303.
- Khatri, A. and Weiss, D. S. (2010) The role of Loop F in the activation of the GABA receptor. *J Physiol* 588, 59-66.
- Khom, S., Baburin, I., Timin, E., Hohaus, A., Trauner, G., Kopp, B. and Hering, S. (2007) Valerenic acid potentiates and inhibits GABA(A) receptors: molecular mechanism and subunit specificity. *Neuropharmacology* 53, 178-187.
- Kierstein, G., Obst, K. and Wahle, P. (1996) Development and activity-dependent expression of neuronal marker proteins in organotypic cultures of rat visual cortex. *Brain Res Dev Brain Res* 92, 39-48.
- Kiewert, C., Kumar, V., Hildmann, O., Rueda, M., Hartmann, J., Naik, R. S. and Klein, J. (2007) Role of GABAergic antagonism in the neuroprotective effects of bilobalide. *Brain Res* 1128, 70-78.

- Kim, Y., Meade, S. M., Chen, K., Feng, H., Rayyan, J., Hess-Dunning, A. and Ereifej, E. S. (2018) Nano-Architectural Approaches for Improved Intracortical Interface Technologies. *Front Neurosci* 12, 456.
- Koser, D. E., Thompson, A. J., Foster, S. K. et al. (2016) Mechanosensing is critical for axon growth in the developing brain. *Nat Neurosci* 19, 1592-1598.
- Krall, J., Balle, T., Krogsgaard-Larsen, N., Sorensen, T. E., Krogsgaard-Larsen, P., Kristiansen, U. and Frolund, B. (2015) GABAA receptor partial agonists and antagonists: structure, binding mode, and pharmacology. *Adv Pharmacol* 72, 201-227.
- Kreuzer, M., Garcia, P. S., Brucklacher-Waldert, V., Claassen, R., Schneider, G., Antkowiak, B. and Drexler, B. (2019) Diazepam and ethanol differently modulate neuronal activity in organotypic cortical cultures. *BMC Neurosci* 20, 58.
- Krissinel, E. and Henrick, K. (2004) Secondary-structure matching (SSM), a new tool for fast protein structure alignment in three dimensions. *Acta Crystallogr D Biol Crystallogr* 60, 2256-2268.
- Kuhse, J., Kuryatov, A., Maulet, Y., Malosio, M. L., Schmieden, V. and Betz, H. (1991) Alternative splicing generates two isoforms of the alpha 2 subunit of the inhibitory glycine receptor. *FEBS Lett* 283, 73-77.
- Kumar, A., Basak, S., Rao, S., Gicheru, Y., Mayer, M. L., Sansom, M. S. P. and Chakrapani, S. (2020) Mechanisms of activation and desensitization of full-length glycine receptor in lipid nanodiscs. *Nat Commun* 11, 3752.
- Lam, D., Enright, H. A., Cadena, J. et al. (2019) Tissue-specific extracellular matrix accelerates the formation of neural networks and communities in a neuron-glia co-culture on a multi-electrode array. *Sci Rep* 9, 4159.
- Langhans, S. A. (2018) Three-Dimensional in Vitro Cell Culture Models in Drug Discovery and Drug Repositioning. *Front Pharmacol* 9, 6.
- Langlhofer, G., Janzen, D., Meiselbach, H. and Villmann, C. (2015) Length of the TM3-4 loop of the glycine receptor modulates receptor desensitization. *Neuroscience Letters*.
- Langosch, D., Thomas, L. and Betz, H. (1988) Conserved quaternary structure of ligand-gated ion channels: the postsynaptic glycine receptor is a pentamer. *Proc Natl Acad Sci USA* 85, 7394-7398.
- Laperrousaz, B., Porte, S., Gerbaud, S., Harma, V., Kermarrec, F., Hourtane, V., Bottausci, F., Gidrol, X. and Picollet-D'hahan, N. (2018) Direct transfection of clonal organoids in Matrigel microbeads: a promising approach toward organoid-based genetic screens. *Nucleic Acids Res* 46, e70.

- Lau, L. W., Cua, R., Keough, M. B., Haylock-Jacobs, S. and Yong, V. W. (2013) Pathophysiology of the brain extracellular matrix: a new target for remyelination. *Nat Rev Neurosci* 14, 722-729.
- Laube, B., Kuhse, J. and Betz, H. (2000) Kinetic and mutational analysis of Zn<sup>2+</sup> modulation of recombinant human inhibitory glycine receptors. *J Physiol* 522 Pt 2, 215-230.
- Lavery, D., Desai, R., Uchanski, T. et al. (2019) Cryo-EM structure of the human alpha1beta3gamma2 GABAA receptor in a lipid bilayer. *Nature* 565, 516-520.
- Lavery, D., Thomas, P., Field, M., Andersen, O. J., Gold, M. G., Biggin, P. C., Gielen, M. and Smart, T. G. (2017) Crystal structures of a GABAA-receptor chimera reveal new endogenous neurosteroid-binding sites. *Nat Struct Mol Biol* 24, 977-985.
- Leacock, S., Syed, P., James, V. M., Bode, A., Kawakami, K., Keramidias, A., Suster, M., Lynch, J. W. and Harvey, R. J. (2018) Structure/Function Studies of the alpha4 Subunit Reveal Evolutionary Loss of a GlyR Subtype Involved in Startle and Escape Responses. *Front Mol Neurosci* 11, 23.
- LeBleu, V. S., Macdonald, B. and Kalluri, R. (2007) Structure and function of basement membranes. *Exp Biol Med (Maywood)* 232, 1121-1129.
- Lee, C. H. and Ruben, P. C. (2008) Interaction between voltage-gated sodium channels and the neurotoxin, tetrodotoxin. *Channels (Austin)* 2, 407-412.
- Lee, V. and Maguire, J. (2014) The impact of tonic GABAA receptor-mediated inhibition on neuronal excitability varies across brain region and cell type. *Front Neural Circuits* 8, 3.
- Lei, Y., Han, H., Yuan, F., Javeed, A. and Zhao, Y. (2017) The brain interstitial system: Anatomy, modeling, in vivo measurement, and applications. *Prog Neurobiol* 157, 230-246.
- Lewis, T. M., Schofield, P. R. and McClellan, A. M. (2003) Kinetic determinants of agonist action at the recombinant human glycine receptor. *J Physiol* 549, 361-374.
- Lindau, M. and Neher, E. (1988) Patch-clamp techniques for time-resolved capacitance measurements in single cells. *Pflugers Arch* 411, 137-146.
- Low, K., Crestani, F., Keist, R. et al. (2000) Molecular and neuronal substrate for the selective attenuation of anxiety. *Science* 290, 131-134.
- Luo, Y. and Shoichet, M. S. (2004) Light-activated immobilization of biomolecules to agarose hydrogels for controlled cellular response. *Biomacromolecules* 5, 2315-2323.



- Lynch, J. W. (2004) Molecular structure and function of the glycine receptor chloride channel. *Physiol Rev* 84, 1051-1095.
- Lynch, J. W. (2009) Native glycine receptor subtypes and their physiological roles. *Neuropharmacology* 56, 303-309.
- Madhavan, R., Chao, Z. C. and Potter, S. M. (2007) Plasticity of recurring spatiotemporal activity patterns in cortical networks. *Phys Biol* 4, 181-193.
- Majd, S., Zarifkar, A., Rastegar, K. and Takhshid, M. A. (2008) Culturing adult rat hippocampal neurons with long-interval changing media. *Iran Biomed J* 12, 101-107.
- Malda, J., Visser, J., Melchels, F. P., Jungst, T., Hennink, W. E., Dhert, W. J., Groll, J. and Hutmacher, D. W. (2013) 25th anniversary article: Engineering hydrogels for biofabrication. *Adv Mater* 25, 5011-5028.
- Malosio, M. L., Marqueze-Pouey, B., Kuhse, J. and Betz, H. (1991) Widespread expression of glycine receptor subunit mRNAs in the adult and developing rat brain. *EMBO J* 10, 2401-2409.
- Manayi, A., Nabavi, S. M., Daglia, M. and Jafari, S. (2016) Natural terpenoids as a promising source for modulation of GABAergic system and treatment of neurological diseases. *Pharmacol Rep* 68, 671-679.
- Marklein, R. A. and Burdick, J. A. (2010) Controlling stem cell fate with material design. *Adv Mater* 22, 175-189.
- Maru, Y., Orihashi, K. and Hippo, Y. (2016) Lentivirus-Based Stable Gene Delivery into Intestinal Organoids. *Methods Mol Biol* 1422, 13-21.
- Masiulis, S., Desai, R., Uchanski, T. et al. (2019) GABAA receptor signalling mechanisms revealed by structural pharmacology. *Nature* 565, 454-459.
- McCull, E., Groll, J., Jungst, T. and Dalton, P. D. (2018) Design and fabrication of melt electrowritten tubes using intuitive software. *Materials & Design* 155, 46-58.
- McKernan, R. M., Rosahl, T. W., Reynolds, D. S. et al. (2000) Sedative but not anxiolytic properties of benzodiazepines are mediated by the GABA(A) receptor alpha1 subtype. *Nat Neurosci* 3, 587-592.
- Medberry, C. J., Crapo, P. M., Siu, B. F. et al. (2013) Hydrogels derived from central nervous system extracellular matrix. *Biomaterials* 34, 1033-1040.
- Meera, P., Wallner, M. and Otis, T. S. (2011) Molecular basis for the high THIP/gaboxadol sensitivity of extrasynaptic GABA(A) receptors. *J Neurophysiol* 106, 2057-2064.

- Meier, J. C., Henneberger, C., Melnick, I., Racca, C., Harvey, R. J., Heinemann, U., Schmieden, V. and Grantyn, R. (2005) RNA editing produces glycine receptor alpha3(P185L), resulting in high agonist potency. *Nat Neurosci* 8, 736-744.
- Meijering, E., Jacob, M., Sarria, J. C., Steiner, P., Hirling, H. and Unser, M. (2004) Design and validation of a tool for neurite tracing and analysis in fluorescence microscopy images. *Cytometry A* 58, 167-176.
- Mekhileri, N. V., Lim, K. S., Brown, G. C. J., Mutreja, I., Schon, B. S., Hooper, G. J. and Woodfield, T. B. F. (2018) Automated 3D bioassembly of micro-tissues for biofabrication of hybrid tissue engineered constructs. *Biofabrication* 10, 024103.
- Mihalik, B., Palvolgyi, A., Bogar, F. et al. (2017) Loop-F of the alpha-subunit determines the pharmacologic profile of novel competitive inhibitors of GABAA receptors. *Eur J Pharmacol* 798, 129-136.
- Mihic, S. J., Ye, Q., Wick, M. J. et al. (1997) Sites of alcohol and volatile anaesthetic action on GABA(A) and glycine receptors. *Nature* 389, 385-389.
- Milanos, S., Kuenzel, K., Gilbert, D. F., Janzen, D., Sasi, M., Buettner, A., Frimurer, T. M. and Villmann, C. (2018) Structural changes at the myrtenol backbone reverse its positive allosteric potential into inhibitory GABA(A) receptor modulation. *Biological Chemistry* 399, 549-563.
- Milescu, L. S., Bean, B. P. and Smith, J. C. (2010) Isolation of somatic Na<sup>+</sup> currents by selective inactivation of axonal channels with a voltage prepulse. *J Neurosci* 30, 7740-7748.
- Miller, P. S. and Aricescu, A. R. (2014) Crystal structure of a human GABAA receptor. *Nature* 512, 270-275.
- Miller, P. S., Scott, S., Masiulis, S., De Colibus, L., Pardon, E., Steyaert, J. and Aricescu, A. R. (2017) Structural basis for GABAA receptor potentiation by neurosteroids. *Nat Struct Mol Biol* 24, 986-992.
- Miroshnikova, Y. A., Mouw, J. K., Barnes, J. M. et al. (2016) Tissue mechanics promote IDH1-dependent HIF1alpha-tenascin C feedback to regulate glioblastoma aggression. *Nat Cell Biol* 18, 1336-1345.
- Moendarbary, E., Weber, I. P., Sheridan, G. K., Koser, D. E., Soleman, S., Haenzi, B., Bradbury, E. J., Fawcett, J. and Franze, K. (2017) The soft mechanical signature of glial scars in the central nervous system. *Nat Commun* 8, 14787.
- Mohler, H. (2006) GABAA receptors in central nervous system disease: anxiety, epilepsy, and insomnia. *J Recept Signal Transduct Res* 26, 731-740.

- Moraga-Cid, G., Sauguet, L., Huon, C. et al. (2015) Allosteric and hyperekplexic mutant phenotypes investigated on an alpha1 glycine receptor transmembrane structure. *Proc Natl Acad Sci U S A* 112, 2865-2870.
- Morales-Perez, C. L., Noviello, C. M. and Hibbs, R. E. (2016) X-ray structure of the human alpha4beta2 nicotinic receptor. *Nature* 538, 411-415.
- Morris, G. M., Goodsell, D. S., Halliday, R. S., Huey, R., Hart, W. E., Belew, R. K. and Olson, A. J. (1998) Automated docking using a Lamarckian genetic algorithm and an empirical binding free energy function. *Journal of Computational Chemistry* 19, 1639-1662.
- Mortensen, M., Patel, B. and Smart, T. G. (2012) GABA Potency at GABA(A) Receptors Found in Synaptic and Extrasynaptic Zones. *Front Cell Neurosci* 6, 1.
- Murphy, A. R., Haynes, J. M., Laslett, A. L., Cameron, N. R. and O'Brien, C. M. (2020) Three-dimensional differentiation of human pluripotent stem cell-derived neural precursor cells using tailored porous polymer scaffolds. *Acta Biomater* 101, 102-116.
- Nakane, T., Kotecha, A., Sente, A. et al. (2020) Single-particle cryo-EM at atomic resolution. *Nature* 587, 152-156.
- Natoli, M., Leoni, B. D., D'Agnano, I., D'Onofrio, M., Brandi, R., Arisi, I., Zucco, F. and Felsani, A. (2011) Cell growing density affects the structural and functional properties of Caco-2 differentiated monolayer. *J Cell Physiol* 226, 1531-1543.
- Nettles, D. L., Vail, T. P., Morgan, M. T., Grinstaff, M. W. and Setton, L. A. (2004) Photocrosslinkable hyaluronan as a scaffold for articular cartilage repair. *Ann Biomed Eng* 32, 391-397.
- Nikolic, Z., Laube, B., Weber, R. G., Lichter, P., Kioschis, P., Poustka, A., Mulhardt, C. and Becker, C. M. (1998) The human glycine receptor subunit alpha3. Glra3 gene structure, chromosomal localization, and functional characterization of alternative transcripts. *J Biol Chem* 273, 19708-19714.
- Nobles, R. D., Zhang, C., Muller, U., Betz, H. and McCall, M. A. (2012) Selective glycine receptor alpha2 subunit control of crossover inhibition between the on and off retinal pathways. *J Neurosci* 32, 3321-3332.
- Nys, M., Kesters, D. and Ulens, C. (2013) Structural insights into Cys-loop receptor function and ligand recognition. *Biochem Pharmacol* 86, 1042-1053.
- Nys, M., Wijckmans, E., Farinha, A. et al. (2016) Allosteric binding site in a Cys-loop receptor ligand-binding domain unveiled in the crystal structure of ELIC in complex with chlorpromazine. *Proc Natl Acad Sci U S A* 113, E6696-E6703.

- Oh, S. H., An, D. B., Kim, T. H. and Lee, J. H. (2016) Wide-range stiffness gradient PVA/HA hydrogel to investigate stem cell differentiation behavior. *Acta Biomater* 35, 23-31.
- Olsen, R. W. (2018) GABAA receptor: Positive and negative allosteric modulators. *Neuropharmacology* 136, 10-22.
- Olsen, R. W. and Sieghart, W. (2008) International Union of Pharmacology. LXX. Subtypes of gamma-aminobutyric acid(A) receptors: classification on the basis of subunit composition, pharmacology, and function. Update. *Pharmacol Rev* 60, 243-260.
- Olsen, R. W. and Sieghart, W. (2009) GABA A receptors: subtypes provide diversity of function and pharmacology. *Neuropharmacology* 56, 141-148.
- Opitz, T., De Lima, A. D. and Voigt, T. (2002) Spontaneous development of synchronous oscillatory activity during maturation of cortical networks in vitro. *J Neurophysiol* 88, 2196-2206.
- Padgett, C. L. and Lummis, S. C. (2008) The F-loop of the GABA A receptor gamma2 subunit contributes to benzodiazepine modulation. *J Biol Chem* 283, 2702-2708.
- Palazzolo, G., Broguiere, N., Cenciarelli, O., Dermutz, H. and Zenobi-Wong, M. (2015) Ultrasoft Alginate Hydrogels Support Long-Term Three-Dimensional Functional Neuronal Networks. *Tissue Eng Part A* 21, 2177-2185.
- Park, J., Wetzel, I., Marriott, I., Dreau, D., D'Avanzo, C., Kim, D. Y., Tanzi, R. E. and Cho, H. (2018) A 3D human triculture system modeling neurodegeneration and neuroinflammation in Alzheimer's disease. *Nat Neurosci* 21, 941-951.
- Patrizio, A., Renner, M., Pizzarelli, R., Triller, A. and Specht, C. G. (2017) Alpha subunit-dependent glycine receptor clustering and regulation of synaptic receptor numbers. *Sci Rep* 7, 10899.
- Pelkey, K. A., Chittajallu, R., Craig, M. T., Tricoire, L., Wester, J. C. and McBain, C. J. (2017) Hippocampal GABAergic Inhibitory Interneurons. *Physiol Rev* 97, 1619-1747.
- Piechotta, K., Weth, F., Harvey, R. J. and Friauf, E. (2001) Localization of rat glycine receptor alpha1 and alpha2 subunit transcripts in the developing auditory brainstem. *J Comp Neurol* 438, 336-352.
- Pilorge, M., Fassier, C., Le Corrionc, H. et al. (2016) Genetic and functional analyses demonstrate a role for abnormal glycinergic signaling in autism. *Mol Psychiatry* 21, 936-945.

- Pless, S. A., Hanek, A. P., Price, K. L., Lynch, J. W., Lester, H. A., Dougherty, D. A. and Lummis, S. C. (2011) A cation-pi interaction at a phenylalanine residue in the glycine receptor binding site is conserved for different agonists. *Mol Pharmacol* 79, 742-748.
- Pribilla, I., Takagi, T., Langosch, D., Bormann, J. and Betz, H. (1992) The atypical M2 segment of the beta subunit confers picrotoxinin resistance to inhibitory glycine receptor channels. *EMBO J* 11, 4305-4311.
- Rajendra, S., Lynch, J. W. and Schofield, P. R. (1997) The glycine receptor. *Pharmacol Ther* 73, 121-146.
- Robinson, T. M., Hutmacher, D. W. and Dalton, P. D. (2019) The Next Frontier in Melt Electrospinning: Taming the Jet. *Advanced Functional Materials*.
- Rudolph, U. and Knoflach, F. (2011) Beyond classical benzodiazepines: novel therapeutic potential of GABAA receptor subtypes. *Nat Rev Drug Discov* 10, 685-697.
- Sadtler, S., Laube, B., Lashub, A., Nicke, A., Betz, H. and Schmalzing, G. (2003) A basic cluster determines topology of the cytoplasmic M3-M4 loop of the glycine receptor alpha1 subunit. *J Biol Chem* 278, 16782-16790.
- Saidy, N. T., Wolf, F., Bas, O., Keijdener, H., Hutmacher, D. W., Mela, P. and De-Juan-Pardo, E. M. (2019) Biologically Inspired Scaffolds for Heart Valve Tissue Engineering via Melt Electrowriting. *Small* 15, e1900873.
- Sasaki, K., Hatta, S., Wada, K., Ohshika, H. and Haga, M. (2000) Bilobalide prevents reduction of gamma-aminobutyric acid levels and glutamic acid decarboxylase activity induced by 4-O-methylpyridoxine in mouse hippocampus. *Life Sci* 67, 709-715.
- Sato, K., Zhang, J. H., Saika, T., Sato, M., Tada, K. and Tohyama, M. (1991) Localization of glycine receptor alpha 1 subunit mRNA-containing neurons in the rat brain: an analysis using in situ hybridization histochemistry. *Neuroscience* 43, 381-395.
- Schaefer, N., Berger, A., van Brederode, J. et al. (2017) Disruption of a Structurally Important Extracellular Element in the Glycine Receptor Leads to Decreased Synaptic Integration and Signaling Resulting in Severe Startle Disease. *J Neurosci* 37, 7948-7961.
- Schaefer, N., Janzen, D., Bakirci, E., Hrynevich, A., Dalton, P. D. and Villmann, C. (2019) 3D Electrophysiological Measurements on Cells Embedded within Fiber-Reinforced Matrigel. *Advanced Healthcare Materials* 8.

- Schaefer, N., Kluck, C. J., Price, K. L. et al. (2015) Disturbed neuronal ER-Golgi sorting of unassembled glycine receptors suggests altered subcellular processing is a cause of human hyperekplexia. *J Neurosci* 35, 422-437.
- Schense, J. C., Bloch, J., Aebischer, P. and Hubbell, J. A. (2000) Enzymatic incorporation of bioactive peptides into fibrin matrices enhances neurite extension. *Nat Biotechnol* 18, 415-419.
- Schense, J. C. and Hubbell, J. A. (2000) Three-dimensional migration of neurites is mediated by adhesion site density and affinity. *J Biol Chem* 275, 6813-6818.
- Schindelin, J., Arganda-Carreras, I., Frise, E. et al. (2012) Fiji: an open-source platform for biological-image analysis. *Nat Methods* 9, 676-682.
- Schindelin, J., Rueden, C. T., Hiner, M. C. and Eliceiri, K. W. (2015) The ImageJ ecosystem: An open platform for biomedical image analysis. *Mol Reprod Dev* 82, 518-529.
- Schneider, C. A., Rasband, W. S. and Eliceiri, K. W. (2012) NIH Image to ImageJ: 25 years of image analysis. *Nat Methods* 9, 671-675.
- Seidlits, S. K., Khaing, Z. Z., Petersen, R. R., Nickels, J. D., Vanscoy, J. E., Shear, J. B. and Schmidt, C. E. (2010) The effects of hyaluronic acid hydrogels with tunable mechanical properties on neural progenitor cell differentiation. *Biomaterials* 31, 3930-3940.
- Seidlits, S. K., Liang, J., Bierman, R. D., Sohrabi, A., Karam, J., Holley, S. M., Cepeda, C. and Walthers, C. M. (2019) Peptide-modified, hyaluronic acid-based hydrogels as a 3D culture platform for neural stem/progenitor cell engineering. *J Biomed Mater Res A* 107, 704-718.
- Shan, Q., Haddrill, J. L. and Lynch, J. W. (2001) Ivermectin, an unconventional agonist of the glycine receptor chloride channel. *J Biol Chem* 276, 12556-12564.
- Sieghart, W. (2006) Structure, pharmacology, and function of GABAA receptor subtypes. *Adv Pharmacol* 54, 231-263.
- Sievers, F., Wilm, A., Dineen, D. et al. (2011) Fast, scalable generation of high-quality protein multiple sequence alignments using Clustal Omega. *Mol Syst Biol* 7, 539.
- Sill, T. J. and von Recum, H. A. (2008) Electrospinning: applications in drug delivery and tissue engineering. *Biomaterials* 29, 1989-2006.
- Silva, A. R., Grosso, C., Delerue-Matos, C. and Rocha, J. M. (2019) Comprehensive review on the interaction between natural compounds and brain receptors: Benefits and toxicity. *Eur J Med Chem* 174, 87-115.

- Simon, J., Wakimoto, H., Fujita, N., Lalande, M. and Barnard, E. A. (2004) Analysis of the set of GABA(A) receptor genes in the human genome. *J Biol Chem* 279, 41422-41435.
- Smeal, R. M., Rabbitt, R., Biran, R. and Tresco, P. A. (2005) Substrate curvature influences the direction of nerve outgrowth. *Ann Biomed Eng* 33, 376-382.
- Spedden, E., White, J. D., Naumova, E. N., Kaplan, D. L. and Staii, C. (2012) Elasticity maps of living neurons measured by combined fluorescence and atomic force microscopy. *Biophys J* 103, 868-877.
- Sundararaghavan, H. G. and Burdick, J. A. (2011) Gradients with depth in electrospun fibrous scaffolds for directed cell behavior. *Biomacromolecules* 12, 2344-2350.
- Thompson, A. J., Lester, H. A. and Lummis, S. C. (2010) The structural basis of function in Cys-loop receptors. *Q Rev Biophys* 43, 449-499.
- Thompson, A. J., Padgett, C. L. and Lummis, S. C. (2006) Mutagenesis and molecular modeling reveal the importance of the 5-HT<sub>3</sub> receptor F-loop. *J Biol Chem* 281, 16576-16582.
- Traynelis, S. F., Wollmuth, L. P., McBain, C. J. et al. (2010) Glutamate receptor ion channels: structure, regulation, and function. *Pharmacol Rev* 62, 405-496.
- Tziridis, K., Buerbank, S., Eulenburg, V., Długaiczek, J. and Schulze, H. (2017) Deficit in acoustic signal-in-noise detection in glycine receptor alpha3 subunit knockout mice. *Eur J Neurosci* 45, 581-586.
- Valenzuela, C. F., Cardoso, R. A., Wick, M. J., Weiner, J. L., Dunwiddie, T. V. and Harris, R. A. (1998) Effects of ethanol on recombinant glycine receptors expressed in mammalian cell lines. *Alcohol Clin Exp Res* 22, 1132-1136.
- van Brederode, J., Atak, S., Kessler, A., Pischetsrieder, M., Villmann, C. and Alzheimer, C. (2016) The terpenoids Myrtenol and Verbenol act on delta subunit-containing GABAA receptors and enhance tonic inhibition in dentate gyrus granule cells. *Neurosci Lett* 628, 91-97.
- Varghese, A., Tenbroek, E. M., Coles, J., Jr. and Sigg, D. C. (2006) Endogenous channels in HEK cells and potential roles in HCN ionic current measurements. *Prog Biophys Mol Biol* 90, 26-37.
- Venkataramani, V., Tanev, D. I., Strahle, C. et al. (2019) Glutamatergic synaptic input to glioma cells drives brain tumour progression. *Nature* 573, 532-538.
- Villmann, C., Oertel, J., Ma-Hogemeier, Z. L., Hollmann, M., Sprengel, R., Becker, K., Breiteringer, H. G. and Becker, C. M. (2009a) Functional complementation of

- Glra1(spdl-ot), a glycine receptor subunit mutant, by independently expressed C-terminal domains. *J Neurosci* 29, 2440-2452.
- Villmann, C., Oertel, J., Melzer, N. and Becker, C. M. (2009b) Recessive hyperekplexia mutations of the glycine receptor alpha1 subunit affect cell surface integration and stability. *J Neurochem* 111, 837-847.
- Visser, J., Melchels, F. P., Jeon, J. E. et al. (2015) Reinforcement of hydrogels using three-dimensionally printed microfibres. *Nat Commun* 6, 6933.
- Vogel, N., Kluck, C. J., Melzer, N., Schwarzinger, S., Breiting, U., Seeber, S. and Becker, C. M. (2009) Mapping of disulfide bonds within the amino-terminal extracellular domain of the inhibitory glycine receptor. *J Biol Chem* 284, 36128-36136.
- Voigt, T., Baier, H. and Dolabela de Lima, A. (1997) Synchronization of neuronal activity promotes survival of individual rat neocortical neurons in early development. *Eur J Neurosci* 9, 990-999.
- Voigt, T., Opitz, T. and de Lima, A. D. (2005) Activation of early silent synapses by spontaneous synchronous network activity limits the range of neocortical connections. *J Neurosci* 25, 4605-4615.
- Wagoner, K. R. and Czajkowski, C. (2010) Stoichiometry of expressed alpha(4)beta(2)delta gamma-aminobutyric acid type A receptors depends on the ratio of subunit cDNA transfected. *J Biol Chem* 285, 14187-14194.
- Walters, R. J., Hadley, S. H., Morris, K. D. and Amin, J. (2000) Benzodiazepines act on GABAA receptors via two distinct and separable mechanisms. *Nat Neurosci* 3, 1274-1281.
- Whiting, P. J. (2003) GABA-A receptor subtypes in the brain: a paradigm for CNS drug discovery? *Drug Discov Today* 8, 445-450.
- Whiting, P. J., McKernan, R. M. and Wafford, K. A. (1995) Structure and pharmacology of vertebrate GABAA receptor subtypes. *Int Rev Neurobiol* 38, 95-138.
- Xu, T., Molnar, P., Gregory, C., Das, M., Boland, T. and Hickman, J. J. (2009) Electrophysiological characterization of embryonic hippocampal neurons cultured in a 3D collagen hydrogel. *Biomaterials* 30, 4377-4383.
- Yang, Z., Taran, E., Webb, T. I. and Lynch, J. W. (2012) Stoichiometry and subunit arrangement of alpha1beta glycine receptors as determined by atomic force microscopy. *Biochemistry* 51, 5229-5231.
- Yevenes, G. E. and Zeilhofer, H. U. (2011) Molecular sites for the positive allosteric modulation of glycine receptors by endocannabinoids. *PLoS One* 6, e23886.



- Young, A. B. and Snyder, S. H. (1974) The glycine synaptic receptor: evidence that strychnine binding is associated with the ionic conductance mechanism. *Proc Natl Acad Sci U S A* 71, 4002-4005.
- Youssef, A., Hollister, S. J. and Dalton, P. D. (2017) Additive manufacturing of polymer melts for implantable medical devices and scaffolds. *Biofabrication* 9, 012002.
- Yu, J., Zhu, H., Lape, R., Greiner, T., Du, J., Lu, W., Sivilotti, L. and Gouaux, E. (2021) Mechanism of gating and partial agonist action in the glycine receptor. *Cell* 184, 957-968 e921.
- Yu, R., Hurdiss, E., Greiner, T., Lape, R., Sivilotti, L. and Biggin, P. C. (2014) Agonist and antagonist binding in human glycine receptors. *Biochemistry* 53, 6041-6051.
- Zhang, Y., Bode, A., Nguyen, B., Keramidis, A. and Lynch, J. W. (2016) Investigating the Mechanism by Which Gain-of-function Mutations to the alpha1 Glycine Receptor Cause Hyperekplexia. *J Biol Chem* 291, 15332-15341.
- Zhou, L., Chillag, K. L. and Nigro, M. A. (2002) Hyperekplexia: a treatable neurogenetic disease. *Brain Dev* 24, 669-674.
- Zhou, N., Wang, C. H., Zhang, S. and Wu, D. C. (2013) The GLRA1 missense mutation W170S associates lack of Zn<sup>2+</sup> potentiation with human hyperekplexia. *J Neurosci* 33, 17675-17681.
- Zhu, S., Noviello, C. M., Teng, J., Walsh, R. M., Jr., Kim, J. J. and Hibbs, R. E. (2018) Structure of a human synaptic GABAA receptor. *Nature* 559, 67-72.







# Declaration of Authorship

Statement of individual author contributions and of legal second publication rights:

<i>The GlyR Extracellular beta 8-beta 9 Loop - A Functional Determinant of Agonist Potency</i> <b>D. Janzen*</b> , N. Schaefer*, C. Delto, H. Schindelin, C. Villmann (* shared first authorship) Frontiers in Molecular Neuroscience 2017, DOI: 10.3389/fnmol.2017.00322					
Participated in	Author initials, responsibility decreasing from left to right				
Study Design	CV	NS	DJ	HS	
Methods Development	DJ	NS			
Data Collection	DJ	CD			
Data Analysis and Interpretation	DJ	CD	NS	CV	HS
Manuscript Writing					
Writing of Introduction	NS	DJ	CV	HS	
Writing of Materials & Methods	DJ	CD			
Writing of Discussion	NS	DJ	CV		
Writing of First Draft	DJ				

<i>Sesquiterpenes and sesquiterpenoids harbor modulatory allosteric potential and affect inhibitory GABAA receptor function in vitro</i> <b>D. Janzen</b> , B. Slavik, M. Zehe, C. Sotriffer, H.M. Loos, A. Buettner, C. Villmann Journal of Neurochemistry 2021, DOI: 10.1111/jnc.15469					
Participated in	Author initials, responsibility decreasing from left to right				
Study Design	CV	DJ	AB	CS	
Methods Development	DJ	BS	HL		
Data Collection	DJ	BS	HL		
Data Analysis and Interpretation	DJ	BS	CV	MZ	CS
Manuscript Writing					
Writing of Introduction	DJ	CV			
Writing of Materials & Methods	DJ	BS	MZ		
Writing of Discussion	DJ	CV	CS		
Writing of First Draft	DJ				

*3D Electrophysiological Measurements on Cells Embedded within Fiber-Reinforced Matrigel*  
 N. Schaefer\*, **D. Janzen\***, E. Bakirci, A. Hrynevich, P.D. Dalton, C. Villmann (\* shared first authorship)  
 Advanced Healthcare Materials 2019, DOI: 10.1002/adhm.201801226

<b>Participated in</b>	<b>Author initials</b> , responsibility decreasing from left to right				
Study Design	CV	NS	DJ	PD	
Methods Development	DJ	EB	NS	AH	
Data Collection	DJ	EB			
Data Analysis and Interpretation	DJ	EB	NS	CV	PD
Manuscript Writing					
Writing of Introduction	NS	DJ	CV	PD	
Writing of Materials & Methods	DJ	EB			
Writing of Discussion	NS	DJ	CV		
Writing of First Draft	DJ				

*Cortical Neurons form a Functional Neuronal Network in a 3D Printed Reinforced Matrix*  
**D. Janzen**, E. Bakirci, A. Wieland, C. Martin, P.D. Dalton, C. Villmann  
 Advanced Healthcare Materials 2020, DOI: 10.1002/adhm.201901630

<b>Participated in</b>	<b>Author initials</b> , responsibility decreasing from left to right				
Study Design	CV	DJ	PD		
Methods Development	DJ	EB			
Data Collection	DJ	EB	AW	CM	
Data Analysis and Interpretation	DJ	EB	CV	PD	
Manuscript Writing					
Writing of Introduction	DJ	CV	PD		
Writing of Materials & Methods	DJ	EB			
Writing of Discussion	DJ	CV			
Writing of First Draft	DJ				

The doctoral researcher confirms that he has obtained permission from both the publishers and the co-authors for legal second publication.

The doctoral researcher and the primary supervisor confirm the correctness of the above-mentioned assessment.

Dieter Janzen

\_\_\_\_\_  
 Doctoral Researcher's Name

\_\_\_\_\_  
 Place, Date

\_\_\_\_\_  
 Signature

Prof. Dr. Carmen Villmann

\_\_\_\_\_  
 Primary Supervisor's Name

\_\_\_\_\_  
 Place, Date

\_\_\_\_\_  
 Signature

**Statement of individual author contributions to figures/tables/chapters included in the manuscripts**

*The GlyR Extracellular beta 8-beta 9 Loop - A Functional Determinant of Agonist Potency*  
**D. Janzen\***, N. Schaefer\*, C. Delto, H. Schindelin, C. Villmann (\* shared first authorship)  
 Frontiers in Molecular Neuroscience 2017, DOI: 10.3389/fnmol.2017.00322

Figure	Author initials, responsibility decreasing from left to right				
1-5	DJ				
6	CD				
Table 1-2	DJ				

*Sesquiterpenes and sesquiterpenoids harbor modulatory allosteric potential and affect inhibitory GABAA receptor function in vitro*  
**D. Janzen**, B. Slavik, M. Zehe, C. Sottriffer, H.M. Loos, A. Buettner, C. Villmann  
 Journal of Neurochemistry 2021, DOI: 10.1111/jnc.15469

Figure	Author initials, responsibility decreasing from left to right				
1	BS				
2-6	DJ				
7	MZ				
Supp. 1	BS				
Table 1-3	DJ				

*3D Electrophysiological Measurements on Cells Embedded within Fiber-Reinforced Matrigel*  
 N. Schaefer\*, **D. Janzen\***, E. Bakirci, A. Hrynevich, P.D. Dalton, C. Villmann (\* shared first authorship)  
 Advanced Healthcare Materials 2019, DOI: 10.1002/adhm.201801226

Figure	Author initials, responsibility decreasing from left to right				
1	EB	DJ			
2-3	DJ				
Table 1	DJ				

*Cortical Neurons form a Functional Neuronal Network in a 3D Printed Reinforced Matrix*

**D. Janzen**, E. Bakirci, A. Wieland, C. Martin, P.D. Dalton, C. Villmann

Advanced Healthcare Materials 2020, DOI: 10.1002/adhm.201901630

<b>Figure</b>	<b>Author initials</b> , responsibility decreasing from left to right				
1	EB	DJ	AW		
2	DJ				
3	DJ	CM			
Supp. 1	AW				
Supp. 2-4	DJ				

The doctoral researcher also confirms his primary supervisor's acceptance.

Dieter Janzen

\_\_\_\_\_  
Doctoral Researcher's Name

\_\_\_\_\_  
Place, Date

\_\_\_\_\_  
Signature



## **Affidavit**

I hereby confirm that my thesis entitled is the result of my own work. I did not receive any help or support from commercial consultants. All sources and / or materials applied are listed and specified in the thesis.

Furthermore, I confirm that this thesis has not yet been submitted as part of another examination process neither in identical nor in similar form.

Place, Date

Signature

## **Eidesstattliche Erklärung**

Hiermit erkläre ich an Eides statt, die Dissertation eigenständig, d.h. insbesondere selbständig und ohne Hilfe eines kommerziellen Promotionsberaters, angefertigt und keine anderen als die von mir angegebenen Quellen und Hilfsmittel verwendet zu haben.

Ich erkläre außerdem, dass die Dissertation weder in gleicher noch in ähnlicher Form bereits in einem anderen Prüfungsverfahren vorgelegen hat.

Ort, Datum

Unterschrift